DEVELOPMENT OF GUIDELINES FOR EXHAUST SYSTEM DESIGN FROM FUNDAMENTAL GAS DYNAMICS STUDIES

by

Phillip David Bush BEng(Hons)

A thesis submitted to the University of Strathclyde
for the degree of Doctor of Philosophy

Department of Mechanical Engineering

Glasgow
2000

ABSTRACT

This thesis details an experimental and computational investigation of the relationship between exhaust system geometry, the exhaust port pressure history and the gas exchange process in reciprocating four-stroke engines.

The study was conducted in four phases. In the first phase, an extensive experimental programme was undertaken, during which key engine performance indicators together with exhaust and intake system manifold pressure and temperature data were recorded on a Rover 1.4 litre 16-valve K series engine. Measured data from each test were used to validate computational predictions.

In the second phase the effect of the phasing of pressure waves at the exhaust port was systematically studied using a modified version of the validated model. The relationships between key engine performance indicators and the pressure at the exhaust port during specific periods of the exhaust event were identified.

In the third phase, exhaust system gas dynamics were studied and the effect of exhaust system junctions and components on the transmitted and reflected characteristics of pressure waves were investigated. A method was identified by which the dynamic pressure history at the exhaust port could be broken down into its principal incident and reflected pressure wave components.

In the fourth phase, using these findings, design criteria for exhaust system manifolds were proposed that, when satisfied, gave the optimum phasing of pressure waves at the exhaust port to assist cylinder gas exchange and reduce pumping losses. The effectiveness of the design guidelines was demonstrated with predicted and experimental results.

ACKNOWLEDGEMENTS

I would like to take this opportunity to extend my thanks to the following, without whom this research would not have been completed. I would like to thank my supervisors Denis Boam of the National Engineering Laboratory, East Kilbride and Dr. Chee Kong Lee of The University of Strathclyde, Glasgow for giving me the opportunity to complete this work and for their guidance, support and insight throughout the course of the project. Similarly I would like to thank Dr. John Bingham, also of the National Engineering Laboratory, East Kilbride, for his advice on gas dynamics matters and the general field of IC engines.

I would like to extend my thanks to Clive Telford and Nicolas Topping of Arvin Exhaust, Warton for their support of this project and for arranging the supply of the hardware for the experimental work.

I would like to thank the support staff, Harry Glendinning of the National Engineering Laboratory, East Kilbride and John Paton of Glasgow Caledonian University, for their meticulous installation work and I would also like to thank the Rover Group for the supply of the test engine.

The research was jointly funded by The National Engineering Laboratory, The University of Strathclyde and the Postgraduate Training Partnership (a joint initiative of the Department of Trade and Industry and the Engineering and Physical Sciences Research Council).

Finally, I would like to thank Valerie, my mother and especially my father, who sadly passed away before the project was completed, for their continual support and encouragement in the most difficult of circumstances.

LIST OF CONTENTS

NOTATION

Throughout this thesis some variable names are defined. Where local definitions are not given the notation below applies.

Symbol		Units
A	Non-dimensional speed of sound, a/a_0	-
A_a	Non-dimensional a_a, a_a/a_0	-
a	Speed of sound	m/s
a_a	Speed of sound after isentropic change of state to reference pressure p_o	m/s
c	Wave velocity	m/s
C_d	Discharge coefficient	-
C_p	Specific heat at constant pressure	J/KgK
C_v	Specific heat at constant volume	J/KgK
D	Diameter	m
f	Friction factor	-
f_0	Frequency	Hz
F	Cross sectional area	m^2
h	Enthalpy	j/kg
N	Engine speed	r/min
L	Length	m
m	Mass	kg
$\dot{m}$	Mass flow rate	kg/s
M	Mach number	-
p	Pressure	N/m^2
q	Specific energy flow rate	W/kg
Q	Energy flow rate	W
R	Specific gas constant	j/kgK
Re	Reynolds number	-
s	Entropy	j/kgK

t	Time	s
T	Temperature	K
u	Particle velocity	m/s
U	Non-dimensional particle velocity, u/a_0	-
V	Volume	m^3
V_{cl}	Clearance volume	m^3
V_s	Swept volume	m^3
x	Distance	m
X	Non-dimensional distance, x/L	-
Z	Non-dimensional time, $a_0 t/L$	-

Greek symbols

β	Leftward moving Riemann variable	-
γ	Ratio of specific heats, C_p/C_v	-
λ	Rightward moving Riemann variable	-
ρ	Density	kg/m^3

Subscripts

0	Reference conditions
p	Primary pipe
s	Secondary pipe
c, col	Collector or tertiary pipe

Operators

δ	Small increment of
Δ	Increment of
∂	Partial differential
d	Calculus differential

CHAPTER 1

INTRODUCTION AND LITERATURE SURVEY

CHAPTER 1

INTRODUCTION AND LITERATURE SURVEY

1.1 GENERAL INTRODUCTION

For the early part of its history, the development of the reciprocating internal combustion (IC) engine progressed employing mostly "trial and error" methods, a wholly unsatisfactory design procedure, and it is an admirable achievement that significant levels of performance gain and improvements in reliability were attained using these methods. Credit must be given to the engine designers and tuners of this period for their intuitive appreciation of the workings of internal combustion engines without necessarily appreciating the governing laws of mechanical, fluid and thermal dynamics of the system. Awareness and understanding of these laws subsequently led to further significant improvements and presently, the application of these laws to engine simulation computer programs to predict performance characteristics has dramatically reduced the time, cost and the number of prototype builds necessary to achieve an optimum design.

A fundamental design deliverable has always been good brake specific fuel consumption, which is influenced by the gas exchange mechanisms and the in-cylinder combustion process. Improvement of the gas exchange process has traditionally been achieved through careful design of the induction system from the air intake to the inlet valves. Particular attention has been focused on the design of the manifold pipes and plenums, since engine breathing in naturally aspirated engines can be enhanced at predetermined speeds by careful selection of the geometry of

individual pipes. The phasing of high amplitude pressure waves within the intake system, caused by the reflection of pressure depressions at certain pipe boundary conditions, can be controlled. These waves, if timed to arrive during the period following inlet valve open after bottom dead centre, cause an increased pressure differential to exist across the inlet valve, even though the piston is rising, giving a supercharging effect and improving volumetric efficiency. The careful design of the exhaust system, in particular the manifold pipes, can also yield worthwhile performance improvements by similarly utilising the pressure wave action. However, it is generally accepted that, in the case of naturally aspirated engines, the potential benefits are not as significant as those gained through optimisation of the induction system geometry. It is for this reason that research into improvement of the gas exchange processes has tended to concentrate on the optimisation of the intake system geometry.

The influence of the exhaust system on the gas exchange process results from the arrival of compression and expansion pressure reflections at the exhaust port during the exhaust period. A low pressure during this period can reduce piston pumping losses, improve cylinder scavenging and thus can improve fuel consumption and engine performance. If a low pressure at the exhaust port exists during the valve overlap period then the induction of fresh charge into the cylinder can be assisted, further improving engine performance. These performance improvements, resulting from the selection of either inlet or exhaust system geometry to best utilise manifold wave action, will only be realised for a limited range of operational speeds. The phasing of the waves, in relation to the exhaust and inlet events, is primarily a function of the local acoustic velocity and the manifold geometry, which in the case of

exhaust systems, is ordinarily fixed, whereas the engine speed varies constantly. Therefore, an engine manifold tuned for improved performance at a given speed range will often restrict engine breathing either side of this range as a consequence of the poor phasing of the pressure waves.

Design methodologies for intake manifold geometry have been proposed so that an optimum configuration, for a given engine application, can be iterated to rapidly. When used in conjunction with accurate engine simulation computer programs, significant savings in time, materials and labour become possible. Little similar work, however, has been undertaken in the area of exhaust system design even though the action of the pressure waves within the system has been understood for a number of years. Therefore, although the time taken to reach such designs can be considerably longer than for an inlet manifold system, an exhaust system that will perform relatively well from a gas-dynamics perspective has been a possibility for some time. In recent years, however, the exhaust system designer has been forced to consider emissions constraints in addition to overall engine performance parameters. Various strategies can be utilised to achieve the legal requirements for exhaust emissions such as strict control of engine fuelling, the use of environmentally friendly fuels or by careful design of combustion chamber and inlet tract geometry so as to promote thorough mixing of the inlet charge, thereby improving combustion characteristics. However, at present, the single most commonly utilised technique for meeting legal emissions requirements in modern four-stroke, spark ignition (SI), IC engines is the use of catalytic converters. The effect on engine performance of the inclusion of such devices within the exhaust system has not, as yet, been systematically studied.

The catalytic converter itself uses an active catalyst material, usually platinum and palladium, for CO and HC oxidation and NO reduction. Configurations of converter commonly employed use honeycomb or pelletized active monoliths, with the honeycomb configuration being used more commonly for small to medium capacity SI engines. Honeycomb monoliths, as the name implies, comprise a large number of small cross-sectional area passageways (usually < 1.0 mm^2), lined with a highly porous washcoat material into which the active catalyst material is impregnated. Pelletized catalysts utilise highly porous material formed into small diameter pellets (usually ≤ 3.0 mm) into which the active catalyst material is impregnated to a depth of approximately 250 μm. Each of these configurations of active catalyst bed has sufficiently high surface area/volume ratios such that the mass transfer characteristic between the exhaust gases and the active catalyst material approaches 100% when the catalyst has reached its optimum operating temperature (usually 400-800°C). Either of these catalyst beds is contained within a metal can located within the exhaust system through which the exhaust gases are directed.

The inclusion of a device such as a converter within the exhaust system clearly influences the flow of exhaust gases and the propagation of pressure waves to some degree, through both its physical location and due to the heat generated by the exothermic reactions taking place on the monolith surface, although to what degree has not been fully quantified. A gas temperature rise of 100 to 150°C is typically measured across a catalyst monolith when fully activated. As emissions regulations have become even more stringent, the design trend has been to locate the catalyst(s) as far upstream as possible to reduce catalyst light-off time; the time taken for the

catalyst to become more than 50% effective. Again, the real effect on engine performance of this design trend is not fully understood. When considering the necessary compromise between engine output and emissions requirements, the design of the optimum manifold and exhaust system configuration is not possible without a complete awareness and understanding of all the implications of relocating the catalyst and of modifying its geometry on engine performance.

Recent world-wide legislation [1, 2] has compelled designers to consider engine exhaust emissions to be a dependent design variable as important as general engine performance. Additionally, the physical design, operation and construction of the engine must be considered in conjunction with complex engine management systems controlling, for instance, the fuelling strategy, the valve timing and the inlet manifold geometry depending upon the current driving conditions. Thus, the engine designer is presented with a vast array of parameters to be considered at the initial design stage. Even with high-speed computers, to consider the effect of all these controlling parameters and their potential interactions on all of the results variables would be an enormous task. Therefore, during the draft design stage, the engine designer must make a subjective engineering decision to prioritise those dependent variables of particular interest. He must then identify those controlling parameters and any of their potential combinations that are likely to have a significant effect on each of the dependent variables being considered. During an initial limited parametric study, an optimum design may be identified but subsequently may have to be modified once, for instance, manufacturing limitations are considered. This methodology has been applied to exhaust manifold design for a number of years and, even with the use of modern high-speed computers, is still simply an extension of historical "cut and try"

design methods. Using an engine simulation program and inputting various input data for the exhaust manifold configuration, a design may be identified which gives a desirable performance characteristic but fails to meet emissions requirements. The inclusion or relocation of an emissions control device may amend this, but at the expense of performance. The geometry of the system is then further modified to retain the emissions characteristic and preserve performance; finally an optimum design may be iterated to.

This study has three primary objectives. The first is to identify the relationship between the geometry of the exhaust system, the pressure wave action within the system and its effect on engine performance. The second is to present a total design methodology, based on these fundamental gas dynamics studies, for the design of exhaust system manifolds, which may or may not incorporate catalytic converters, for the improvement of the engine torque characteristic. The third objective is to apply this methodology to design, build and test an optimum system for a typical automotive SI engine.

The study itself is conducted in four phases, which are expanded in Section 1.3. The first phase of the study involves the comprehensive validation of predicted results from an engine simulation computer program against measured results from an experimental test rig which was extensively instrumented to record engine performance characteristics, mean temperatures, mean pressures and dynamic pressure histories. In the second phase a detailed investigation is made into various exhaust system components and the effect of modification to their geometry on engine performance characteristics. The study is conducted using Taguchi design of

experiments analysis in conjunction with an engine simulation computer program and its purpose is to initially identify those exhaust system components and any interactions thereof, that have a significant effect on engine performance. Ongoing modelling studies form the third phase of the study. Modifications to engine simulation code used throughout the course of the study allow the relationship between exhaust design elements such as pipe lengths, pipe diameters, junction configurations, tapers, catalyst location and geometry, and the interactions of various individual parameters to be quantified in terms of their influence on the exhaust pressure wave action. In the fourth phase these results are used to define a total design methodology for exhaust systems, allowing the designer to identify optimum builds for systems without recourse to a full gas dynamics simulation.

1.2 LITERATURE SURVEY

To assist with the development of a design strategy for IC engine exhaust systems, relevant current and past studies and various generic topics were researched.

1.2.1 Finite pressure wave analysis and the application of the method of characteristics to engine gas dynamics problems

Pressure waves may be differentiated into two main groups:

i. Acoustic waves, or sound waves, which have a very low amplitude and hence all points on such a wave may be considered to propagate with equal velocity; and

ii. finite waves, generally considered to have an amplitude greater than ± 6 kPa. There is a change of wave profile during propagation and a complete analysis

requires the solution of a set of non-linear, hyperbolic, partial differential equations.

The pressure waves within exhaust and intake manifolds that influence gas exchange processes are finite waves and accurate prediction of the spatial and temporal variation of these waves throughout both manifold systems is a prerequisite for optimum engine performance design. It requires a detailed analysis that ideally includes the effects of friction, heat transfer, entropy, variations in area and the superimposition of finite pressure waves. The earliest studies of finite wave propagation were made by Lagrange [3] who, in 1760, proposed that the propagation velocity of finite waves depended on the nature of the wave. In 1807 Poisson [4] quantified this non-linear behaviour and presented a relationship that showed the wave velocity was the sum of the acoustic velocity and the particle velocity due to the wave passing. Further work by Stokes [5] and Challis in 1848 showed that a finite wave would ultimately form a shock and this was further confirmed in 1859 by Earnshaw [6] who also generalised the simple wave solution which formed the basis for all subsequent finite wave analysis. During this period Riemann [7] was amongst the first to apply a method of solution, which became known as the method of characteristics, to gas-dynamics problems.

One of the earliest applications of finite wave theory to IC engine analysis was made by Capetti [8] in his study of wave action in diesel engines. In 1940, Mucklow [9] also recognised the significance of pressure wave action on the breathing characteristics of engines in his study of the effects of valve timing and exhaust pipe lengths. The first application of the method of characteristics to the solution of

unsteady gas flow problems in IC engines was by Jenny [10, 11], based upon previous work by de Haller [12]. The second paper by Jenny was particularly important as it detailed the general analysis of the method of characteristics incorporating friction, heat transfer and area change. During this period Bannister and Mucklow [13] and Wallace and Stuart-Mitchell [14] published papers detailing the behaviour of finite pressure waves in engine ducts; the Wallace and Stuart-Mitchell paper including equations governing flow through engine ports. Complete analysis of separate manifold systems was now possible including the valve events and in 1954 Wallace and Nassif [15] investigated the effects of pressure wave action of both intake and exhaust manifold dimensions under motored conditions. Wallace [16] also studied unsteady fluid flow in diffusers and shortly after, Mucklow and Wilson [17] studied attenuation and reflection of pressure waves in pipe systems. Wallace and Boxer [18] continued working on the effect of diffusers and their work highlighted the laborious nature of the graphical solution of flow problems.

The advent of the digital computer provided the means for the rapid solution of the quasi-linear, hyperbolic, partial differential equations governing unsteady fluid flow. A key paper by Benson, Garg and Woollatt [19] adapted the well-established method of characteristics based solution technique into a form suitable for solution by computer. The new method required the superposition of a two dimensional grid onto the distance-time plane. The values of the dependent variables were then calculated at all the mesh nodes for each time-step as the calculation advanced. This technique became the basic method of solution for many engine gas-dynamics studies undertaken during following years and is still in widespread use today. It has been developed to a high level of detail and culminated in the production of several texts

[20, 21] that have become standard references for ongoing studies in this field. The new unsteady flow analysis method was further developed by Benson *et al* to include a more detailed analysis of the effects of area change and heat transfer [22, 23]. With this new solution technique for pipe gas dynamics, Benson *et al* applied the method to the simulation of single cylinder [24] and multi-cylinder, four-stroke, SI engines [25], compression ignition [26] and two-stroke engines [27].

During the same period an extensive research programme by Blair *et al* commenced at The Queen's University, Belfast. The studies applied the computer based unsteady flow analysis to four-stroke engines [28, 29] and with particular effect to the improvement of two-stroke engine performance [30-32]. The accuracy of an engine simulation model is invariably related to the accuracy with which it represents the various boundary conditions found throughout the system. Cahoon [33] solved the equations presented by Wallace and Stuart-Mitchell [14] governing flow through an open port. These solutions were stored in a matrix form suitable for inclusion in an engine simulation computer program and were used during the later two-stroke engine studies. Similarly, McConnell [34] applied such an analysis to the open port condition in four-stroke engines.

The natural progression following the accurate prediction of exhaust system gas-dynamics was the prediction of noise characteristics. Exhaust gas simulations were successfully applied to exhaust noise predictions by Blair, Spechko and Coates [35-37] who took finite wave pressure histories at the exhaust open end and then applied acoustic theory to predict sound pressure levels and the frequency spectrum.

Junctions within manifold systems were initially modelled assuming that the pressure at each pipe adjacent to the junction was equal [38]. Benson and Woolatt [39] published pressure loss coefficients, obtained directly from experimental studies, which were incorporated into models based on momentum theory. A detailed study by Bingham [40] offered a junction model based on an empirical form of the momentum equation and the application of loss coefficients. This enabled junctions of any configuration and any number of connected pipes to be modelled. Deckker, Male and Chelsom [41-43] had studied the flow regime and pressure wave action within junctions themselves in more detail. They showed that additional wave reflections could be generated, as a wave traversed a junction, which immediately followed the initial reflection.

Carburettors and other throttling valves can also have a significant influence on both the fluid flow and the pressure wave action in a system, particularly at low settings. Examples of studies into the effect of such components and various models can be found in [44-46].

Alternative solutions for the quasi-linear, hyperbolic, partial differential equations governing unsteady fluid flow in one-dimension have developed in parallel with the method of characteristics and these are now considered, along with other simplified methods of solving gas-dynamics problems.

1.2.2 Alternative one-dimensional gas-dynamics solution methods

Finite difference schemes

Ledger's [47] application of finite difference theory to flow problems in engine manifolds was one of the earliest. He claimed second order accuracy and results comparable to Benson's previous non-homentropic calculations. The "two-step Lax Wendroff method", described by Richtmyer and Morton [48], was compared by MacLaren *et al* [49] with other solution methods and they found the finite difference method to be superior, both in speed and accuracy. A research note published shortly after [50] proposed the application of an alternative method, the "leap-frog method", which was said to be faster still. Comparisons by researchers at Toyota [51] between the method of characteristics and the "two-step Lax Wendroff method" also offered evidence of the superiority of the latter method. Chapman *et al* [52,53] published the application of a method he called FRAM, which was similarly used by Morel *et al* [54]. Sato *et al* [55,56] applied a method called the "fluid in cell method"; both of these methods, again, offered improved accuracy and speed over the method of characteristics.

All of these methods however, required the inclusion of a term to damp out spurious oscillations. Since such a term is not a rigorous mathematical derivation from fundamentals, then, strictly speaking, these finite difference schemes are only first order accurate. In 1985 Bulaty and Niessner [57] considered this, and proposed a new method called "naive flux correction" which damped the spurious oscillations whilst, they claimed, maintaining the order of accuracy. Corberán and Gascón [58] reported on the application of a method known as TVD (total variation diminishing) to nozzle

flow problems and concluded that the method was free of numerical oscillations for this particular application.

More recently, Liu *et al* [59] and Pearson and Winterbone [60] reviewed a number of the principal finite difference schemes and the method of characteristics applied to engine gas dynamics problems. Liu concluded that the "two-step Lax Wendroff method" was the most suitable for this particular application in terms of the method's ability to handle area discontinuities and hence mass flow continuity was maintained. He recognised, however, that the method of characteristics did not require additional terms to damp spurious oscillations and handled pressure discontinuities better. Pearson and Winterbone assessed the performance of various flux limiters applied to the "two-step Lax Wendroff method" in greater detail.

Linear acoustic methods

These methods are used to rapidly identify pipe network characteristics and have been successfully applied to assist with the design of short pipe manifolds. The methods generally make the significant assumptions that the amplitudes of the pressure disturbances are small and that homentropic flow occurs without friction; they also have difficulty in handling area changes in pipes. The methods are based on the non-linear, one-dimensional momentum and continuity equations for the unsteady flow of a non-viscous fluid in pipes of constant cross sectional area:

$$\text{Momentum:} \quad \frac{\partial p}{\partial x} + \rho\left(\frac{\partial u}{\partial t} + u\frac{\partial u}{\partial x}\right) = 0 \qquad (1.1)$$

$$\text{Continuity:} \quad \frac{\partial \rho}{\partial t} + \rho\frac{\partial u}{\partial x} + u\frac{\partial \rho}{\partial x} = 0 \qquad (1.2)$$

By assuming that the amplitudes of the pressure disturbances are very small, then the pressure p and particle velocity u, at all points across a wave profile, can be assumed to remain constant. Thus, the equations can be linearised since all gas properties at all points along the wave profile remain constant. This gives:

$$\frac{\partial p}{\partial x}+\rho\frac{\partial(\Delta u)}{\partial t}=0 \qquad (1.3)$$

$$\frac{\partial \rho}{\partial t}+\rho\frac{\partial(\Delta u)}{\partial x}=0 \qquad (1.4)$$

Appendix A2.1 details the derivation of equations (1.3) and (1.4) and their manipulation into the following linear, partial differential equation:

$$\frac{\partial^2 p}{\partial t^2}-a_0{}^2\frac{\partial^2 p}{\partial x^2}=0 \qquad (1.5)$$

which can be represented in matrix form:

$$\begin{bmatrix} p|_{x=l} \\ \dot{m}|_{x=l} \end{bmatrix}=\begin{bmatrix} \cos kx & -jY_0\sin kx \\ -(j/Y_0)\sin kx & \cos kx \end{bmatrix}\times\begin{bmatrix} p|_{x=0} \\ \dot{m}|_{x=0} \end{bmatrix} \qquad (1.6)$$

and represents a solution in the frequency domain of pressure and mass flow characteristics at a pipe exit based on the entering pressure and mass flow characteristics and the pipe geometry. Equation (1.6) is commonly referred to as the transfer matrix of a pipe in acoustic theory. Appendix A2.1 and Munjal [61] detail the further application of equation (1.6) to calculate the natural resonant frequency of complex manifold systems.

Ohata and Ishida [62] applied this theory to intake manifold studies. Their analysis suggested the existence of two modes of resonance associated with intake system networks; one related to the dimensions of the intake runner only and one related to

the overall configuration of the intake system. Matsumoto and Ohata [63] applied equation (1.5) to derive a transfer function for an intake manifold that also considered the effect of fluid viscosity. The calculation gave a frequency response for the manifold that was then transferred into the time domain, by taking the inverse transform, enabling volumetric efficiency characteristics to be predicted. Pearson and Winterbone [64] similarly applied the linearised conservation equations to model intake systems and used empirically based coefficients to account for pipe friction, end losses and effective lengths. More recently Benajes *et al* [65, 66] applied the method when considering a design methodology for exhaust and intake systems.

Multi-dimensional methods

Multi-dimensional models have been available since the late 1970's. Such flow models are complex and demanding of computational time and effort. For this reason, they are presently generally not used for the modelling of complete engine systems and are more suited to specific problems such as valve flow optimisation and combustion chamber modelling.

In 1979 Chapman [67] employed a two-dimensional model which enabled him to optimise fuel-injection timing strategies and to examine the effects of the plenum chamber internal geometry on pressure wave action. Tosa *et al* [68] used a conventional one-dimensional model in pipes and a two-dimensional model in pipe junctions to study the flow field at these locations in detail. Dimitriadis *et al* [69] and Amsden *et al* [70] both used three dimensional models to study in greater detail the flow regime at specific locations.

Multi-dimensional flow models have not been used during the course of the study detailed in this work since their computational requirements render them impractical for full engine system simulation. They are, however, being used increasingly in conjunction with one-dimensional gas dynamics simulations, which provide the transient boundary conditions for three-dimensional simulation of flow regimes in complex components [71].

Other methods

Various other methods have been applied to the solution of unsteady gas flow problems in IC engines, some of which are completely new applications and others that are more subtle variations of existing solution techniques. The original graphical method-of-characteristics method has been successfully solved on a computer by Jones [72]. Kong and Woods [73] applied fluid transmission line dynamics to distributed parameter models of simple intake manifold systems and Margolis [74] applied the Bond graph technique to model two-stroke IC engines. Blair [75, 76] has also presented a hybrid finite volume method that will trace the variation of gas properties cell-by-cell.

At the present time, for the accurate prediction of pressure wave dynamics in engine cycle simulation models, within an acceptable time, one-dimensional method of characteristics or finite difference based solution schemes are most appropriate and both methods have been extensively validated. In this study a method of characteristics based solution scheme was utilised.

1.2.3 Concept of exhaust and intake system manifold tuning

Engine performance is influenced by the geometry of an exhaust system in one of two ways:

i. By the restriction that the exhaust system imposes on the free passage of exhaust gases to atmosphere, essentially a measure of the ΔP across the complete system where a low value is desirable to reduce piston pumping losses so improving brake mean effective pressure (bmep); and

ii. by harnessing the pressure wave action present within the exhaust system, which results from the unsteady nature of the flow in all engine manifolds, so that a low pressure exists at the exhaust port during particular periods of the exhaust cycle. This can encourage flow from the cylinder, further reducing piston pumping losses, and can also assist with cylinder filling, so improving cylinder volumetric efficiency.

It is usual to optimise the design parameters detailed in i. using multi-dimensional modelling codes, the objective being to achieve the optimum flow characteristics across a given component [77]. The design parameters detailed in ii., however, result from a complex interaction of all the system pipe lengths, pipe diameters, junction configurations and the configuration and location of any devices located within the exhaust stream, such as catalytic converters and silencer mufflers. Each of these design parameters has an influence on the propagation of pressure waves that exist in the exhaust system which themselves result from the unsteady flow nature of the exhaust process.

Considering the simple case of a single cylinder, four-stroke, two valve engine with a single, open ended exhaust pipe attached, then when the exhaust valve opens, high pressure, high temperature exhaust gases flow from the cylinder into the exhaust system because of the lower pressure that exists downstream of the exhaust valve. This sudden release of gases also causes a finite pressure wave to be generated, whose initial profile is a function of the in-cylinder and gas conditions downstream of the valve, the opening profile of the valve and of the geometry of the exhaust tract. This wave propagates along the exhaust pipe at the local acoustic velocity and as it does so, frictional effects and the theory of finite wave propagation, detailed in Chapter 2, causes the wave profile to modify. On reaching the open end of the exhaust pipe, a rarefaction wave is generated which then propagates back up the exhaust pipe to the exhaust valve. If the exhaust system geometry is selected so as to phase the arrival time of the rarefaction wave favourably with the exhaust event, then the resulting low pressure condition downstream of the exhaust valve can assist with flow from the cylinder, thus improving engine performance. This is the basic concept of exhaust system tuning and comprehensive introductions are given to this subject by Smith [78] and Annand and Roe [79]. In the case of a multi-cylinder engine, there are multiple sources of compressive waves that can interact with one another throughout the exhaust system. In addition, progressively decaying pressure oscillations occur within individual pipes as multiple reflections take place at the pipe boundaries. It is known that there are two types of these pressure oscillations that occur within engine manifold systems; these are organ pipe and Helmholtz resonances [80]. In the case of exhaust systems, the organ pipe resonance applies during the period from exhaust valve closed (EVC) to exhaust valve opening (EVO). It corresponds to the natural frequency of oscillation of the exhaust pipe network with fixed boundary conditions.

The Helmholtz resonance is considered to apply from the period EVO to EVC and is the frequency of oscillation of the exhaust pipe network with time varying boundary conditions; in this case the exhaust valve opening and closing. These phenomena are described in detail in sections 1.2.3.1 and 1.2.3.2.

The concept of intake system tuning is essentially identical to that for exhaust system tuning except that a rarefaction wave is generated by the opening of the intake valve and this results in a compressive reflection being generated at the open end of the intake system. If this compression wave is phased to arrive during the period from bottom-dead-centre (BDC) to inlet valve closure (IVC) then a supercharging effect occurs [62] and additional fresh charge is forced into the cylinder. Considerably more research has been dedicated to intake system design optimisation than that of exhaust systems since the potential benefits to engine performance are greater for four-stroke engines. Broome [81-83] and Prosser [84] both comprehensively detailed the principal features of intake system tuning effects.

The valve events are a function of engine speed whereas the relative phasing of the pressure waves is a function of the in-pipe gas conditions and the exhaust system geometry. Thus, any manifold system "tuned" for the optimum phasing of pressure waves at one speed may have poor phasing of the waves at speeds either side of the "tuned" speed, which may result in a drop in desired engine performance. This problem has been addressed, particularly in the case of intake manifold systems, by the use of variable-geometry element systems. Ohata and Ishida [62] showed that the inlet tract pressure history comprised of two distinct components; a long periodic component which is related to the geometry of the complete intake system and a

shorter periodic component which is related to the dimensions of the intake runner only. By incorporating variable-geometry elements into intake systems, it is possible to modify the resonance characteristics of the system [85]. As the engine speed changes, so the intake system switches between modes of operation. This is typically achieved by opening or closing valves, allowing pressure waves to interact or not as required. By this method, the phasing of pressure waves at the inlet valve can be maintained closer to the ideal than would be the case for a fixed geometry system. Improvements to volumetric efficiency can be observed over the whole engine operating range. Such systems are now commonplace in automotive engine applications [86-89] and apply a variety of methods to achieve the desired performance characteristic.

Compared with inlet systems, there have been relatively few applications of variable-geometry elements to exhaust system design. This is primarily due to the harshness of the environment within which such devices would be expected to operate. Over a typical automotive engine operating range, there is relatively little variation in the inlet charge temperature and the inlet charge itself will be either fresh air or a fresh air/fuel mixture. During the exhaust process, however, there is significant variation of the exhaust gas mass flow rate and its properties. Even during low speed operation the temperature of exhaust gases immediately downstream of the exhaust valve can typically exceed 900°K and this temperature will also vary significantly during the exhaust period itself. Steep temperature gradients, especially across dissimilar component materials, are a particular problem. In addition, the exhaust gas comprises highly corrosive gases and potentially particulates, such as carbon deposits from the combustion chamber, which can cause rapid failure of components located in the gas

stream. One of the main applications of variable-geometry elements in exhaust systems has been that of variable exhaust port geometry in performance two-stroke engines [90, 91]. These devices employ a mechanical valve, which can partially obstruct the exhaust port immediately adjacent to the piston face according to the operating speed of the engine. The valve is located in the top of the port and so when the valve is actuated, the port timing is effectively decreased. Thus, the pressure wave phasing is optimised by modifying the timing of the exhaust event rather than by modifying the geometry of the exhaust system itself.

Yamaha have used a variable-geometry exhaust element to great effect in their high performance, four-stroke, motorcycle engines. Known as the EXUP (EXhaust Ultimate Power) valve [92], it comprises a small rotary valve, actuated by a computer-controlled servomotor, that is located immediately downstream of a 4-into-1 exhaust collector and is activated according to engine speed. The exhaust is designed for high-speed power and in this condition the valve does not restrict gas flow through the exhaust. Below this speed, out-of-phase pressure waves during valve overlap result in a detrimental effect on volumetric efficiency. The exhaust valve then partially restricts the collector pipe and controls pressure reflections such that a high-pressure condition at the exhaust port during valve overlap is avoided.

Variable-geometry exhaust elements have been used to improve other engine operating characteristics. Krause *et al* [93] detail a variety of configurations of semi-active noise control systems. These systems utilise semi-active muffler mechanisms which modify the internal geometry of the muffler system according to the current driving conditions so as to give a reduction in noise emissions or an improvement in

perceived noise quality. Generally valves are used either to open and close tubes within the silencer box, or to open and close additional tailpipes. These valves can be operated by an engine management system or simply actuated by variations in exhaust back-pressure. At low engine speeds or during deceleration, where a relatively small gas volume flow exists, a small free cross-sectional area is sufficient to pass the gas volume with little increase in back-pressure. The small free cross-sectional area is beneficial to low frequency acoustic performance. At higher engine speeds the free cross-sectional area is increased, enhancing performance and reducing fluid flow noise. Mirosh [94] details the novel use of switching valves either side of catalytic converters. Their purpose is to alternate the direction of exhaust gas flow through the catalyst monolith so that a high temperature wave front resides in the monolith for a longer period, thus reducing its light-off time. Opel [95] proposed the use of dual pipes running to the catalytic converter. During cold-start conditions one of the pipes is throttled by a butterfly valve so that most of the exhaust gas flows down the second pipe, minimising heat transfer and rapidly bringing the catalyst to its light-off temperature. There is no mention of the effect of either of these devices on engine performance.

1.2.3.1 Organ pipe resonance

The wave action in pipe systems has been described using organ-pipe theory by a variety of researchers. The concept of the application of this theory to manifold systems is to calculate the time that it takes for a wave introduced at a pipe end to traverse the pipe and then for its generated reflection to return to the first pipe end. Consider the case of an open ended pipe. The organ pipe period corresponds to the period starting from the introduction of a wave at pipe end (1) until the inverse sign of

this wave, generated by the reflection of the original wave at the open end (2), arrives back at pipe end (1). In the case of an open ended pipe, this period corresponds to a half natural wave period for an open ended pipe and, in terms of crank-angle, is given by:

$$Crank\ angle\ period\ =\ \theta\ = \frac{12NL}{a} \qquad (1.7)$$

Equation (1.7) considers only the acoustic velocity in the pipe. An assumption is made that fluid in the pipe is flowing with a near steady velocity in one direction and that $a >> u$. Therefore, for a pressure wave traversing a pipe $2 \times n$ times, then the flow velocity will cancel. In determining the natural period of resonance of a pipe, it is usual to assume that equation (1.7) is applicable only during the period when any valves adjacent to the manifold are closed. Broome [83] uses this parameter in his description of the interaction of standing waves and of waves generated during the current cycle in induction systems. The application of equation (1.7) was further investigated by Winterbone *et al* [96] who confirmed that the parameter could be used to identify pipe geometry but to identify the magnitude of the effect a full gas dynamics simulation needed to be performed.

1.2.3.2 Helmholtz resonance

The cylinder and primary manifold pipes of an engine have been considered as a Helmholtz resonator to identify periods of wave oscillation during the current cycle. The model is analogous to a spring-mass system where, at its fundamental resonance, the mass of air in the pipe is the oscillating mass and the cylinder volume is the spring. Referring to Figure 1.1, the resonant frequency of the pipe-cylinder system is given by:

$$f_0 = \frac{a}{2\pi}\sqrt{\frac{F}{LV}} \qquad (1.8)$$

Thompson and Engelman [80] modelled the induction process of a single-cylinder engine using this method and considered the volume term in the equation as $V = \frac{V_s}{2} + V_{cl}$. Tuning peaks were identified when the pipe-cylinder system natural frequency was approximately twice that of the piston frequency.

Engelman [97] further expanded the application of this model to multi-cylinder engines and considered primary pipes not inducting fresh charge as additional volumes. Vorum [98, 99] and Tabaczynski [100] used the same model to analyse the exhaust and intake systems on multi-cylinder engines and, more recently, Jameson and Hodgins [101] successfully applied the model to the development of competition engines. The multi-cylinder model is shown in Figure 1.2 and is analogous to a parallel L-C electrical circuit. The tuned frequencies for this particular system are given by:

$$f_{\pm} = \frac{1}{2\pi}\sqrt{\frac{(ab+a+1) \pm \sqrt{(ab+a+1)^2 - 4ab}}{2abL_1C_1}} \qquad (1.8)$$

where:

$$a = \frac{L_2}{L_1} - \left[\frac{(L/F)_2}{(L/F)_1}\right]$$

$$b = \frac{C_2}{C_1} - \frac{2V_2}{V_1}\frac{R-1}{R+1} \qquad \text{(for intake systems)}$$

$$b = \frac{C_2}{C_1} - \frac{V_2}{V_1}\frac{R-1}{R} \qquad \text{(for exhaust systems)}$$

C_i = acoustic velocity

V_i = volume

R = compression ratio

1.2.4 Exhaust and intake system design methodologies

Historical "cut-and-try" methods for optimising manifold configurations have now been largely replaced by computational models of varying complexity to indicate the ideal manifold geometry for a given engine configuration and application. A convenient summary of the variety of mathematical models applied to general internal combustion engine design is given by Ramos [102]. Although these models can offer significant savings in materials and man-hours to arrive at an optimum design, they still have limitations. Specifically, in the case of four-stroke engine manifold design, accurate prediction of fluid flow and of the effects of pressure wave phenomena requires details of manifold geometry as input data. It may therefore take some considerable time, especially when incorporating a variable-geometry system, to iterate to a satisfactory final design. Recognising this, researchers have presented various design methodologies, incorporating detailed mathematical models only for the final stage of design optimisation, to offer further potential savings in man-hours and computational time.

Hall [103] details a design methodology for induction systems only, in which the optimum configuration of the manifolds for a specific application is indicated graphically. An intake system design chart defines an optimum pipe/cylinder volume ratio for a given operating condition from dimensionless inertia and acoustic wave parameters, the inlet valve closing point and the Mach number. Since the optimum pipe/cylinder volume ratio does not remain constant throughout the full range of

engine operating speeds, the method can be utilised for variable-geometry induction system design. The methodology is only intended to be indicative of the approximate ideal geometry and does not include effects such as exhaust scavenging, mechanical or combustion efficiency.

Payri *et al* [104] presented a design methodology for both intake and exhaust manifolds that incorporated five separate steps and three separate mathematical models of progressively increasing complexity. The initial input data required are engine specification details and volumetric efficiency requirements across a given speed range. General characteristics for the gas exchange processes are then defined as dimensionless numbers using a quasi-steady-flow model and an iterative search procedure for the optimum characteristics to satisfy the initial basic design requirements. The dimensionless numbers are then utilised in the second step by the acoustic wave model to define basic manifold geometry. At this stage restrictions are placed on the potential geometry configurations such as available free volume and maximum possible diameters of primary and secondary manifold pipes. This ensures that the iterative search time during the second and third steps is kept to a practical minimum. In the third step, a method-of-characteristics gas dynamics model simulates all potential manifold geometry indicated by previous steps in greater detail. The final two steps of the procedure are for results analysis and allow for modifications or designs that do not entirely satisfy the original design specification. Evaluations are made of designs and this may necessitate repeating either the first or second steps.

Liu [105] proposed a design procedure for inlet manifolds only in which he identified gas-dynamics similarity criteria for induction systems operating with engines of differing swept volumes. Using the defined criteria for gas-dynamics similarity to determine component dimensions, an induction system design can be transferred between engines of differing swept volume to provide similar volumetric efficiency characteristics. Volumetric efficiency and tuning peak requirements are initially defined and applied to a baseline design which is transferred from an existing optimised design according to the gas dynamics similarity criteria. An optimisation procedure was then presented for the individual induction system components based upon considerations of major or minor influence. The procedure also allowed for variable geometry designs.

Benajes *at al* [106, 107] presented design criteria for both intake and exhaust systems. Both methodologies were derived from the theory of distributed parameter acoustic models, detailed in Appendix 2.1, from which the natural frequency of manifold networks can be calculated. Non-dimensional frequency parameters were defined that considered the interaction of waves from each cylinder. Optimum values for these non-dimensional parameters represented tuning "peaks" and the geometry of the manifold systems should be selected to satisfy these criteria.

1.3 OBJECTIVES OF THE PRESENT STUDY

The preceding literature survey has indicated that considerable research has been undertaken in the area of engine manifold gas-dynamics prediction and manifold tuning principles. However, in the case of automotive exhaust system design, it also

shows that relatively few design strategies have been proposed for the design of an optimum system starting from a blank sheet of paper. Existing exhaust design methodologies have been found to be frequently based on the application of distributed parameter acoustic models and the application of equations (A2.1.50) to (A2.1.52) to a pipe network to find the natural frequency of a system. Assuming that the application of this method is correct and that the natural frequency of the system does not change during the exhaust event, then it is clear that there are an infinite number of solutions, in terms of pipe lengths, diameters and volumes, to achieve a desired natural frequency. Thus, the design of an optimum system using these methods remains an iterative process with significant assumptions and does not give any real insight into the effect of exhaust system geometry on the pressure wave action within.

This study will address this shortfall in knowledge and will investigate the following:

1. The effect of the configuration of exhaust systems on the interaction of pressure waves will be studied in detail. Conventional tuning wisdom suggests that 4:1 configuration systems are the optimum systems for high speed performance and yet there is no evidence, based on existing pressure wave tuning theories, to support why this should be so.
2. Existing design methodologies have tended only to consider constant area pipe lengths in terms of pressure wave phasing; the influence of pipe diameters or changes in cross-section are generally not considered in four-stroke engine applications. The variation of these parameters and their potential effect on pressure wave action will be quantified.

3. The effect of the inclusion of emissions control devices, particularly catalytic converters, in exhaust systems will be studied. To meet emissions requirements it is often necessary to close-couple such devices and include additional devices as components of the upstream manifold. Each of these devices will influence the flow of gases through the system. They also can potentially operate at a significantly higher temperature than the immediately adjacent upstream and downstream exhaust pipes, thus influencing local acoustic velocities. Existing design methodologies have not considered this and so the effect of these devices on pressure wave action must be studied in detail.
4. A detailed parametric study will be made of the effect of the exhaust port pressure history on engine breathing and performance characteristics. Although it is recognised that a reduction in exhaust port pressure throughout the exhaust period is desirable to reduce engine pumping losses, it is impossible to achieve in practical situations. Thus, a prerequisite for the derivation of a design methodology is the identification of the optimum achievable exhaust port pressure history.

The study has three principal objectives:

i. To identify and quantify the relationship between the geometry of the exhaust system, pressure wave action and engine performance;
ii. to present a total design methodology, based on these fundamental gas dynamics studies, for the design of exhaust system manifolds, which may or may not incorporate catalytic converters, for the improvement of the engine torque characteristic; and

iii. to apply the methodology to identify an optimum system for a Rover K series 1400 cc 16 valve engine.

The study is conducted in four principal phases. In the first phase, an extensive experimental programme is undertaken to validate a method-of-characteristics based engine simulation code that is used throughout the duration of the project. Comparisons are made between predicted results and the measured results from an experimental test rig extensively instrumented to record engine performance characteristics, mean temperatures, mean pressures and dynamic pressure histories. In the second phase a detailed investigation is made into various exhaust system components and the effect of modification to their geometry on engine performance characteristics. This investigation is conducted in the form of a design of experiments analysis using predicted results from engine simulation software. The purpose of the investigation is to initially identify those exhaust system components and any interactions thereof, that have a significant effect on engine performance. In the third phase, further modelling studies are conducted, which include 1. to 4. above, to identify the relationship between exhaust system geometry and engine performance characteristics in the speed domain. Modifications to the engine cycle simulation software allow the relationship between exhaust design elements such as pipe lengths, pipe diameters, junction configurations, tapers, catalyst location and geometry, and the interactions of various individual parameters to be quantified in terms of their influence on the exhaust pressure wave action. Then, in the fourth phase, a total exhaust system design methodology is derived, from the previous studies, that allows the rapid identification of an optimum system configuration from the point of view of the engine gas exchange process.

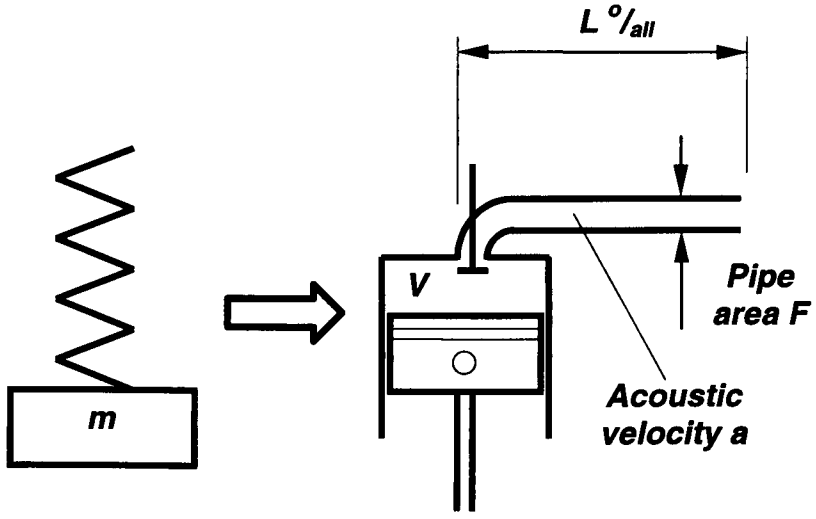

Figure 1.1 Helmholtz resonator model applied to single-cylinder engine manifolds

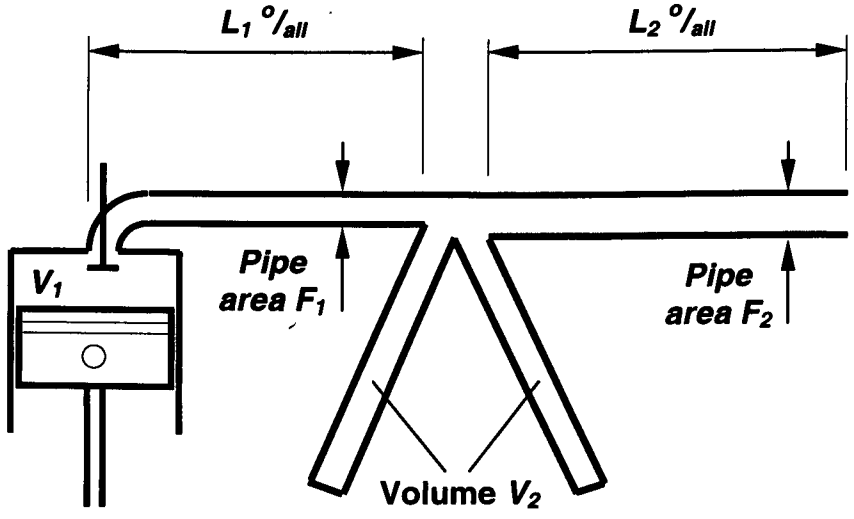

Figure 1.2 Helmholtz resonator model applied to multi-cylinder engine manifolds

CHAPTER 2

THEORY

CHAPTER 2

THEORY

2.1 INTRODUCTION

During this study, the NEL engine simulation computer code EMMA [108] was used extensively. An extended experimental programme was undertaken in which comparisons were made between a number of measured and predicted performance characteristics as the exhaust system geometry was modified. By performing this extensive validation, subsequent modifications could be made to the source code and confidence could be given to the accuracy of the ensuing results. These modifications permitted conditions to be imposed on a system that would be difficult, if not impossible, to achieve experimentally.

The software simulates in-cylinder events, flow across cylinder boundaries and gas-dynamic action within intake and exhaust systems. The unsteady, compressible flow within manifold pipes is assumed to be one-dimensional and dedicated solutions for flow across the various pipe boundaries typically encountered in these systems are included. At each calculation step the unsteady, compressible flow equations are solved using the method of characteristics, based on the method of application suitable for inclusion in a computer program originally implemented by Benson *et al* [19]. This method allows the definition of gas properties at every time-step and at any location within the pipe system. The version of the software used for the greater duration of the study was the homentropic version. The homentropic calculation assumes constant reference conditions in each pipe and thus entropy remains constant

throughout the whole flow field. True homentropic flow can only exist in frictionless, adiabatic flow conditions; the effects of area change and frictional effects are, however, included in the calculation. The non-homentropic version of the software became available during the latter stages of the project and comparisons were then made between the two versions.

Applied to exhaust flow, the homentropic version of the software has potential limitations. The software is not able to accurately predict the effects of temperature discontinuities on pressure wave action and such discontinuities exist in real exhaust system gas flow. Devices such as catalytic converters have a high thermal mass and generate an exotherm under normal operating conditions; the effect of this on gas flow are not included in the current version of the software. Despite these limitations the homentropic version of the software was shown to accurately predict pressure wave action in exhaust systems and comparisons of measured and predicted results are given in Chapter 3.

2.2 THE BASIS OF THE METHOD OF CHARACTERISTICS

To accurately predict in-cylinder events, it is essential to have knowledge of the temporal variation of the cylinder boundary conditions. The accurate prediction of these variable boundary conditions can only be achieved by the tracking of waves throughout the attached manifold and the knowledge of the gas flow behaviour across junctions, etc. EMMA uses the method of characteristics to simulate these gas dynamic processes within manifold systems.

The essential feature of the method of characteristics is that there exist two parameters that, if observed from a point moving with a given velocity, will remain constant. The method tracks the propagation of upstream and downstream moving waves, relative to the local fluid flow, and allows the evaluation of the spatial and temporal variation of fluid conditions. This information is derived from the two parameters which are called Riemann variables (usually written λ and β). By introducing these two variables the four governing partial differential equations of pipe flow, for which there are no direct solutions, can be simplified into ordinary differential form. These equations can then be solved at discrete time-steps.

2.2.1 Non-homentropic flow

Considering an elemental volume of gas as shown in Figure 2.1, the equations governing the element are:

1. Continuity

Net mass inflow rate = rate of change of mass in volume

$$\rho F u - \left[\rho \frac{\partial \rho}{\partial x} dx\right]\left[F + \frac{\partial F}{\partial x} dx\right]\left[u + \frac{\partial u}{\partial x} dx\right] =$$

$$\frac{\partial}{\partial t}\left[\rho \frac{F + \frac{\partial F}{\partial x} dx + F}{2} dx\right] \qquad (2.1)$$

Expanding and simplifying (2.1) gives:

$$\frac{\partial \rho}{\partial t} + u\frac{\partial \rho}{\partial x} + \rho\frac{\partial u}{\partial x} + \frac{\rho u}{F}\frac{\partial F}{\partial x} = 0 \qquad (2.2)$$

2. Momentum

Force = rate change of momentum

$$\rho F - \left(p + \frac{\partial p}{\partial x}dx\right)\left(F + \frac{\partial F}{\partial x}dx\right) + \left(p + \frac{\partial p}{\partial x}\frac{dx}{2}\right)\frac{\partial F}{\partial x}dx - \frac{\rho u^2}{2} f\pi D dx \frac{u}{|u|}$$

$$= \left[\left(\rho + \frac{\partial \rho}{\partial x}\frac{dx}{2}\right)\left(F + \frac{\partial F}{\partial x}\frac{dx}{2}\right)dx\right]\left[\frac{\partial u}{\partial t} + u\frac{\partial u}{\partial x}\right] \qquad (2.3)$$

By rearranging and simplifying (2.3) becomes:

$$\frac{\partial u}{\partial t} + u\frac{\partial u}{\partial x} + \frac{1}{\rho}\frac{\partial p}{\partial x} + \frac{4f}{D}\frac{u^2}{2}\frac{u}{|u|} = 0 \qquad (2.4)$$

3. Energy

Heat flow rate = rate of change of energy in control volume +

net rate of energy flow across boundaries

Assuming a perfect gas with constant specific heats:

$$q\rho F dx = \frac{\partial}{\partial t}\left[\rho F dx\left(C_v T + \frac{u^2}{2}\right)\right] + \frac{\partial}{\partial x}\left[\rho u F\left(C_v T + \frac{u^2}{2} + \frac{p}{\rho}\right)\right]dx \qquad (2.5)$$

4. State

Assuming a perfect gas:

$$p = \rho R T \qquad (2.6)$$

The solution to this set of quasi-linear, hyperbolic, partial differential equations contains information relating to the propagation of waves through a fluid. Inspection of equations (2.2), (2.4) and (2.5) indicates that the unknowns p, ρ and u must be evaluated for all x and t. Firstly the equations are arranged into their mathematically

"normal" form. Bingham [40] details these lengthy algebraic manipulations in full. The resulting equations are:

$$\frac{\partial p}{\partial t}+u\frac{\partial p}{\partial x}-a^2\left(\frac{\partial \rho}{\partial t}+u\frac{\partial \rho}{\partial x}\right)-(\gamma-1)\rho\left(q+u\frac{4f}{D}\frac{u^2}{2}\frac{u}{|u|}\right)=0 \quad (2.7)$$

$$\frac{\partial p}{\partial t}+(u+a)\frac{\partial p}{\partial x}+\rho a\left(\frac{\partial u}{\partial t}+(u+a)\frac{\partial u}{\partial x}\right)-(\gamma-1)\rho\left(q+u\frac{4f}{D}\frac{u^2}{2}\frac{u}{|u|}\right)$$

$$+\frac{a^2\rho u}{F}\frac{dF}{dx}+\frac{4f}{D}\frac{\rho a u^2}{2}\frac{u}{|u|}=0 \quad (2.8)$$

$$\frac{\partial p}{\partial t}+(u-a)\frac{\partial p}{\partial x}-\rho a\left(\frac{\partial u}{\partial t}+(u-a)\frac{\partial u}{\partial x}\right)-(\gamma-1)\rho\left(q+u\frac{4f}{D}\frac{u^2}{2}\frac{u}{|u|}\right)$$

$$+\frac{a^2\rho u}{F}\frac{dF}{dx}-\frac{4f}{D}\frac{\rho a u^2}{2}\frac{u}{|u|}=0 \quad (2.9)$$

2.2.2 Method of characteristics solution

The time derivative of any function $\varphi(x,t)$ in a flow moving with velocity u can be written:

$$\frac{d\varphi}{dt}=\frac{\partial \varphi}{\partial t}+u\frac{\partial \varphi}{\partial x} \quad (2.10)$$

Hence equation (2.7) can be written:

$$\frac{dp}{dt}-a^2\frac{d\rho}{dt}-(\gamma-1)\rho\left(q+u\frac{4f}{D}\frac{u^2}{2}\frac{u}{|u|}\right)=0 \quad (2.11)$$

which applies along a line in the t-x field with a gradient of $\frac{dx}{dt}=u$ (i.e. a gas particle path-line).

Equations (2.8) and (2.9) can be written:

$$\frac{dp}{dt} \pm \rho a \frac{du}{dt} - (\gamma - 1)\rho\left(q + u\frac{4f}{D}\frac{u^2}{2}\frac{u}{|u|}\right) + \frac{a^2 \rho u}{F}\frac{dF}{dx} \pm \frac{4f}{D}\frac{\rho a u^2}{2}\frac{u}{|u|} = 0 \qquad (2.12, 2.13)$$

which applies along lines with gradients of $\frac{dx}{dt} = u \pm a$ (i.e. a wavepoint velocity).

The wavepoint velocity equations define the λ and β characteristics which are defined as (see Appendix A2.3):

$$\lambda = A + \frac{(\gamma - 1)}{2}U \qquad \beta = A - \frac{(\gamma - 1)}{2}U \qquad (2.14, 2.15)$$

where $A = a/a_0$ and $U = u/a_0$.

2.2.3 Non-homentropic relationships

Referring to Figure 2.2, it can be shown that for an ideal gas undergoing an isentropic change of pressure:

$$\frac{p_1}{p_0} = \left(\frac{a_1}{a_0}\right)^{\frac{2\gamma}{\gamma - 1}} \qquad (2.16)$$

In the case of isentropic compression from p_0 to p_1 (0→1) followed by non-isentropic expansion to p_0 (1→2), the speed of sound following the expansion would be a_a. In this case the expansion relationship can be written:

$$\frac{p_1}{p_0} = \left(\frac{a_1}{a_a}\right)^{\frac{2\gamma}{\gamma - 1}} \qquad (2.17)$$

Referring to Figure 2.2, it would also be correct to say that:

$$\frac{p_1}{p_{01}} = \left(\frac{a_1}{a_0}\right)^{\frac{2\gamma}{\gamma - 1}} \qquad (2.18)$$

The calculation procedure used in EMMA requires a constant reference pressure p_0 and so the form of equation (2.17) is used. Appendix A2.2 shows how change from a_0 to a_a is related to the change in entropy by:

$$\frac{a_a}{a_0} = e^{\frac{(s_2 - s_1)}{2C_p}} \qquad (2.19)$$

Equation (2.19) shows that gas entropy can be determined by monitoring the value of a_a. The non-dimensional quantity $A_a = \frac{a_a}{a_0}$ is not gas entropy, but it is usual to refer to it as such in the case of method-of-characteristics based calculations.

2.3 ORGANISATION OF EQUATIONS FOR SOLUTION

To assist with the numerical solution of equations (2.11) to (2.13), various non-dimensional parameters are defined.

From (2.14) and (2.15):

$$A = \frac{a}{a_0} = \frac{\lambda + \beta}{2} \qquad (2.20)$$

$$A_a = \frac{a_a}{a_0} \qquad (2.21)$$

Thus:

$$\frac{p}{p_0} = \left(\frac{a}{a_a}\right)^{\frac{2\gamma}{(\gamma-1)}} = \left(\frac{A}{A_a}\right)^{\frac{2\gamma}{(\gamma-1)}} = \left(\frac{\lambda + \beta}{2A_a}\right)^{\frac{2\gamma}{(\gamma-1)}} \qquad (2.22)$$

Since for a perfect gas $p = \rho RT$, then:

$$\frac{p}{p_0} = \frac{\rho}{\rho_0}\frac{T}{T_0} \qquad (2.23)$$

Also since $a = \sqrt{\gamma RT}$, then:

$$\frac{T}{T_0} = \left(\frac{a}{a_0}\right)^2 = A^2 = \left(\frac{\lambda + \beta}{2}\right)^2 \qquad (2.24)$$

$$\frac{\rho}{\rho_0} = \frac{p}{p_0}\frac{T_0}{T} = \left(\frac{A}{A_a}\right)^{\frac{2\gamma}{\gamma-1}} \frac{1}{A^2} = \left(\frac{\lambda+\beta}{2A_a}\right)^{\frac{2}{\gamma-1}} \frac{1}{A_a{}^2} \qquad (2.25)$$

The parameters λ and β are modified to consider the effect of heat transfer and friction in pipes of varying cross sectional area. λ and β no longer remain constant (as is the case for homentropic flow) and thus, based on equations (2.14) and (2.15):

$$d\lambda = dA + \frac{(\gamma-1)}{2} dU \qquad d\beta = dA - \frac{(\gamma-1)}{2} dU \qquad (2.26, 2.27)$$

The lengthy algebraic manipulation to calculate the $d\lambda$ and $d\beta$ terms is detailed in full by Bingham [40]. With reference to Figure 2.3, the following equations can be defined:

<u>λ characteristic</u>

Direction condition:

$$\frac{dX}{dZ} = U + A \qquad (2.28)$$

where X = non-dimensional distance x/L and Z = non-dimensional time $a_0 t/L$.

$$\left.\frac{dX}{dZ}\right|_{\lambda} = \frac{\gamma+1}{2(\gamma-1)}\lambda - \frac{3-\gamma}{2(\gamma-1)}\beta \qquad (2.29)$$

Compatibility condition:

$$d\lambda = -\frac{(\gamma-1)}{2}\frac{AU}{F}\frac{dF}{dX}dZ + A\frac{dA_a}{A_a} - \frac{\gamma-1}{2}\frac{2fL}{D}U^2\frac{U}{|U|}\left[1-(\gamma-1)\frac{U}{A}\right]dZ$$

$$+\frac{(\gamma-1)^2}{2}\frac{qL}{a_0^3}\frac{1}{A}dZ \qquad (2.30)$$

<u>β characteristic</u>

Direction condition:

$$\frac{dX}{dZ} = U - A \qquad (2.31)$$

$$\left.\frac{dX}{dZ}\right|_\beta = \frac{3-\gamma}{2(\gamma-1)}\lambda - \frac{\gamma+1}{2(\gamma-1)}\beta \qquad (2.32)$$

Compatibility condition:

$$d\beta = -\frac{(\gamma-1)}{2}\frac{AU}{F}\frac{dF}{dX}dZ + A\frac{dA_a}{A_a} + \frac{\gamma-1}{2}\frac{2fL}{D}U^2\frac{U}{|U|}\left[1+(\gamma-1)\frac{U}{A}\right]dZ$$

$$+\frac{(\gamma-1)^2}{2}\frac{qL}{a_0^3}\frac{1}{A}dZ \qquad (2.33)$$

<u>Path-line characteristic:</u>

Direction condition:

$$\frac{dX}{dZ} = U = \frac{\lambda-\beta}{\gamma-1} \qquad (2.34)$$

Compatibility condition:

$$dA_a = \frac{\gamma-1}{2}\frac{A_a}{A^2}\left(\frac{qL}{a_0^3} + \frac{2fL}{D}|U^3|\right)dZ \qquad (2.35)$$

2.4 NUMERICAL OR MESH METHOD OF SOLUTION

The principal features of the numerical method of solution are the division of the pipes of interest into equal length meshes and the calculation of λ, β and A_a values at discrete time-steps. The superposition of this distance-time grid over the flow field facilitates the solution of the equations of continuity, energy, momentum and state with a computer program. The method of solution is illustrated with reference to Figure 2.4. The objective is to calculate the values of λ, β and A_a at the nodes of the distance-time grid (locations A, B, C and D). Characteristics with a positive gradient in the distance-time grid are λ characteristics and those with a negative gradient are β characteristics. From the values of λ, β and A_a, the fluid properties of interest can be calculated at each time-step and at every location. Assuming that the values of λ and β for all locations are known at the outset of the calculation and that the length of each mesh is known, it is first necessary to calculate the time increment for the next step of the calculation. This is found from the Courant-Friedrichs-Lewy criterion [109] and must be satisfied in order for the calculation to remain stable.

$$\frac{\Delta Z}{\Delta X} \leq \frac{1}{A+|U|} \qquad (2.36)$$

ΔZ and ΔX represent non-dimensional time and distance respectively. A value of ΔZ is calculated for every mesh length, based on the values of $\lambda 1$ and $\beta 1$, and the smallest value of ΔZ is used to advance the calculation. Considering only the λ characteristic, it is unlikely that such a characteristic passing through point A will also pass directly through point D. Similarly a β characteristic is unlikely to pass through both points B and C. Since the objective is to calculate the values of λ and β at time

Z2 then it is required to calculate values of λ_w, β_w and λ_r, β_r. Values at C and D are then given by:

$$\lambda 2(J+1) = \lambda_w + d\lambda \qquad (2.37)$$

$$\beta 2(J) = \beta_r + d\beta \qquad (2.38)$$

The calculation of the pairs of λ_w, β_w and λ_r, β_r are by linear interpolation and the solution of two sets of simultaneous equations, with unknowns λ_w, β_w, dX_w and λ_r, β_r, dX_r respectively.

2.5 SHOCKS

The equations presented in Sections 2.2 to 2.4 cannot be applied to wave propagation in pipe problems in conditions of sonic flow. This is not a common occurrence in manifold pipes but nevertheless can occur in specific circumstances. The National Engineering Laboratory engine simulation computer code handles the occurrence of this flow situation using an analysis applied by Blair and Johnston [30] that incorporated the Rankine-Hugoniot relationships. From (2.37) and (2.38), the values of the Riemann variables after time-step ΔZ are given by:

$$\lambda_n = \lambda 1 + d\lambda \qquad (2.39)$$

$$\beta_n = \beta 1 + d\beta \qquad (2.40)$$

The Mach number is then checked:

$$M_n = \left|\frac{U_n}{A_n}\right| = \left|\frac{\lambda_n - \beta_n}{\gamma - 1}\frac{2}{\lambda_n + \beta_n}\right| \qquad (2.41)$$

If $M_n > 1$, then it is assumed that a weak shock occurs and the velocity will again become subsonic. It is across this shock that the Rankine-Hugoniot relationships are applied. The Mach number after the shock, M_2, is given by.

$$M_2^{\,2} = \frac{M_n^{\,2} + \dfrac{2}{\gamma - 1}}{\left(\dfrac{2\gamma}{\gamma - 1}\right) M_n^{\,2} - 1} \qquad (2.42)$$

Downstream of the shock, the pressure p_2 is related to the pressure before the shock, p_n, by:

$$p_2 = p_n \left(\frac{2\gamma}{\gamma + 1} M_n^{\,2} - \frac{\gamma - 1}{\gamma + 1} \right) \qquad (2.43)$$

M_2 and p_2 can then be evaluated from (2.42) and (2.43) and can then be expressed in terms of λ_2 and β_2, the Riemann variables downstream of the shock.

$$M_2 = \left| \frac{\lambda 2 - \beta 2}{\gamma - 1} \frac{2}{\lambda 2 + \beta 2} \right| \qquad (2.44)$$

$$p_2 = \left(\frac{\lambda 2 + \beta 2}{2} \right)^{\frac{2\gamma}{\gamma + 1}} p_0 \qquad (2.45)$$

or:

$$\lambda 2 + \beta 2 = R_3 \qquad (2.46)$$

where:

$$R_3 = \left(\lambda_n + \beta_n\right) \left(\frac{2\gamma}{\gamma + 1} M_n^{\,2} - \frac{\gamma - 1}{\gamma + 1} \right)^{\frac{\gamma - 1}{2\gamma}} \qquad (2.47)$$

Solving (2.44) and (2.46) for $\lambda 2$ and $\beta 2$ gives:

$$\lambda_2 = \left(\frac{2}{\gamma - 1} \pm M_2 \right) \frac{(\gamma - 1) R_3}{4} \qquad (2.48)$$

$$\beta_2 = \left(\frac{2}{\gamma - 1} \pm M_2 \right) \frac{(\gamma - 1) R_3}{4} \qquad (2.49)$$

2.6 ENTROPY TRACING TECHNIQUES

2.6.1 Homentropic model

The homentropic version of the software requires the input of reference temperature and pressure conditions which characterise the conditions of the gas through which the pressure waves traverse. It implies constant entropy throughout the entire flow field although true homentropic flow can only exist in frictionless, adiabatic flow conditions. For the complete analysis of the flow field, expressions that account for the effects of friction, entropy, heat transfer and area changes are required. These terms are not wholly independent and the homentropic version of the software includes in its calculation the effects of area change and friction, neglecting entropy and heat transfer. Since an increase in entropy is possible as a result of any of these other factors, this calculation procedure is not strictly correct and in conditions of high heat transfer and friction, errors can result. It has been found however, that the errors resulting from these simplifications can be minimised with the appropriate selection of the reference gas conditions. There is also a significant saving in computational time and effort.

2.6.2 Modified Benson method

The non-homentropic version of the software, used for some of the work undertaken during the course of this study, uses the modified Benson method [21] for the tracking of entropy throughout pipe systems. Entropy tracking is required for the accurate

spatial and temporal definition of gas properties and is a particularly important consideration when modelling situations such as reverse flow through intake valves. It can be observed that throttled four-stroke engines, when at part load and at the instant of inlet valve opening, can have a cylinder pressure which is significantly higher than the manifold vacuum. This pressure differential causes the hot in-cylinder gases to be expelled into the inlet tract where they reside for a short period. As the in-cylinder pressure decreases, due to the increase in volume, the hot gas is drawn back into the cylinder where it is mixed with the incoming fresh charge reducing the trapped gas purity, volumetric efficiency and engine performance. Methods of entropy tracking used previously have included mesh and particle tracking methods. The mesh method uses a calculation procedure similar in approach to that for the calculation of the λ and β characteristics. It ultimately relies on the interpolated value of A_a between two meshes. Thus, in the case of a hot gas-cold gas interface, of the type illustrated in the above example, the location of the temperature discontinuity is not accurately defined and the condition of gas particles across single mesh lengths cannot be traced. Particle tracing techniques follow the path and entropy level of individual particles as they progress along the distance grid. Typically, at the outset of the calculation, particles are located between and at the intersection of every mesh, i.e. there are approximately twice as many particles as there are meshes. As the calculation progresses, new particles are introduced into the pipe as others leave. The tracking, updating and reorganising of old and new particle locations and entropy values have high computational memory requirements, but have the advantage over the mesh method of a shorter distance between particles containing entropy information. The interpolation for intermediate values of particle entropy gives a better representation of discontinuities over the mesh method, but there still remains

an entropy gradient rather than a single discontinuous step as expected. The modified Benson method recognises the importance of the tracking of the temperature discontinuity in particular circumstances and is a development of the particle tracking method.

The modified Benson method checks for cases of flow initiation or reversal at a pipe end. In such cases an additional particle is installed immediately adjacent to the end particle. The additional particle will contain the new entropy information and the existing end particle will contain the entropy information resident at the pipe end during the previous time-step. Thus, although the particles are immediately adjacent at the pipe end, the discontinuity information is retained and its location is defined exactly in space and time. A limit is placed on the number of particles allowed to exist in a given pipe length at any one time to ensure that the sizes of storage arrays do not exceed any pre-defined limits. This requires the removal of the least significant particle as another particle is introduced at a pipe end. The least significant particle is defined as one whose entropy value is nearest to the entropy value obtained by linear interpolation between the immediately adjacent particles.

2.7 BOUNDARY CONDITIONS

The previous sections have detailed the calculation methods applied to the solution of wave flow problems in pipes. Application of these methods will define gas properties throughout the pipe body and the characteristics of waves approaching the pipe ends. They do not consider the transmission or reflection of these waves across or from the various pipe boundaries that are typically encountered in engine systems, i.e.

volume/valve/pipe interfaces, pipe junctions, closed/open ends, turbines, etc. Specific gas dynamics equations must be set up for each of these boundary conditions and need to be defined in terms of λ and β for input into adjacent pipe systems. This section summarises the method of solution for each of the boundary conditions included in the model used during the course of this study.

2.7.1 Pipe/volume

Flow from a volume into a pipe, such as from the cylinder via the exhaust valve into the exhaust manifold or from atmosphere into the intake system, is modelled as an isentropic nozzle with sudden adiabatic expansion from the nozzle throat into the full pipe cross sectional area. Flow from a pipe into a volume, such as in the case of flow from the intake port via the intake valve into the cylinder is modelled as an isentropic nozzle with no pressure recovery from the nozzle throat to the volume. In either case the volume is assumed to be sufficiently large for stagnation conditions to exist. Flow to and from this volume is influenced by the pressure ratio across the restriction, the area of the restriction and the amplitude of any incident pressure waves. The equations that define these two flow conditions were originally presented by Wallace and Stuart Mitchell [14], with the assumption that the flow through the restriction was quasi-steady. They were then solved for a range of numerical values by Cahoon [33] and McConnell [34] who organised the results into a matrix form suitable for the solution of the pipe/volume boundary condition by computer. The main equations presented by McConnell are given here.

Figure 2.5 shows inflow and outflow conditions for the pipe/volume boundary. At the beginning of the time-step the cylinder pressure (p_1), the arriving characteristic (in

this case β) and the pipe/restriction area ratio are generally known. It is required to calculate the reflected characteristic (in this case λ). The calculation of the missing characteristic allows the derivation of mass flow at the mesh immediately adjacent to the restriction at any instant and represents the mass flow across the restriction at the same instant. To assist with the derivation of the pipe/volume boundary solution, the following non-dimensional parameters are introduced:

$$p_1 = \left(\frac{p_{volume}}{p_{reference}} \right)^{\frac{\gamma-1}{2\gamma}} \qquad (2.50)$$

$$p_2 = \left(\frac{p_{pipe}}{p_{reference}} \right)^{\frac{\gamma-1}{2\gamma}} \qquad (2.51)$$

$$p_i = \left(\frac{p_{incident}}{p_{reference}} \right)^{\frac{\gamma-1}{2\gamma}} \qquad (2.52)$$

$$p_r = \left(\frac{p_{reflected}}{p_{reference}} \right)^{\frac{\gamma-1}{2\gamma}} \qquad (2.53)$$

$$p_c = \left(\frac{p_{vena-contracta}}{p_{reference}} \right)^{\frac{\gamma-1}{2\gamma}} \qquad (2.54)$$

$$k = \textit{Effective port area/Pipe area} \qquad (2.55)$$

Where the subscripts refer to the following regions:

1	=	Volume conditions
2	=	Pipe conditions
i and *r*	=	Incident and reflected waves in pipes
c	=	Vena-contracta conditions

Considering the pipe pressure, it can be shown that (see Appendix 2.3):

$$p_2 = p_i + p_r - 1 = \frac{\lambda + \beta}{2} \qquad (2.56)$$

Which gives:

$$\lambda + \beta = 2p_i + 2p_r - 2 \qquad (2.57)$$

Considering pipe velocity, Appendix 2.3 also shows that for superposed incident and reflected waves:

$$u_2 = u_i + u_r = \frac{2a_0}{\gamma - 1}(p_r - p_i) \qquad (2.58)$$

Which in terms of λ and β is:

$$u_2 = a_0\left(\frac{\lambda - \beta}{\gamma - 1}\right) \qquad (2.59)$$

Therefore:

$$\lambda - \beta = 2p_r - 2p_i \qquad (2.60)$$

From (2.57) and (2.60):

$$\beta = 2p_i - 1 \qquad (2.61)$$

Dividing both (2.57) and (2.61) by p_1:

$$\frac{\lambda + \beta}{2p_1} = \frac{p_i + p_r - 1}{p_1} \qquad (2.62)$$

and:

$$\frac{\beta}{p_1} = \frac{2p_i - 1}{p_1} \qquad (2.63)$$

By expressing the boundary conditions in terms of k, $\frac{2p_i - 1}{p_1}$ and $\frac{p_i + p_r - 1}{p_1}$, then for specific values of k, p_i and β, so $\frac{p_i + p_r - 1}{p_1}$ is found and λ is then found from:

$$\lambda = 2\left(\frac{p_i + p_r - 1}{p_1}\right)p_1 - \beta \qquad (2.64)$$

The value of the $\frac{2p_i - 1}{p_1}$ term determines the flow direction. If $\frac{2p_i - 1}{p_1} > 1.0$, then inflow occurs. If $\frac{2p_i - 1}{p_1} < 1.0$, then outflow occurs. The four flow regimes of subsonic and sonic inflow and subsonic and sonic outflow are considered separately.

2.7.1.1 Subsonic inflow

From the energy equation, assuming isentropic flow from the pipe to the throat:

$$h_2 + \frac{u_2^2}{2} = h_c + \frac{u_c^2}{2} \qquad (2.65)$$

Therefore:

$$u_c^2 - u_2^2 = 2(h_2 - h_c) \qquad (2.66)$$

Also:

$$h = C_p T = \frac{\gamma R}{\gamma - 1} T = \frac{a_0^2}{\gamma - 1}\frac{T}{T_0} \qquad (2.67)$$

and:

$$\frac{p}{p_0} = \left(\frac{T}{T_0}\right)^{\frac{\gamma}{\gamma - 1}} \qquad (2.68)$$

Thus:

$$h = \frac{{a_0}^2}{\gamma - 1}\left(\frac{p}{p_0}\right)^{\frac{\gamma-1}{\gamma}} \qquad (2.69)$$

By substitution and using non-dimensional p_2 and p_c:

$${u_c}^2 - {u_2}^2 = \frac{2{a_0}^2}{\gamma - 1}\left({p_2}^2 - {p_c}^2\right) = \frac{2{a_0}^2}{\gamma - 1}\left[\left(p_i + p_r - 1\right)^2 - {p_c}^2\right] \qquad (2.70)$$

From the continuity equation:

$$\rho_2 F_2 u_2 = \rho_c F_c u_c \qquad (2.71)$$

Substituting for ρ in terms of non-dimensional pressure parameters:

$$\frac{u_2}{u_c} = k\left(\frac{P_c^{\frac{2\gamma}{\gamma-1}}}{p_2^{\frac{2\gamma}{\gamma-1}}}\right)^{\frac{1}{\gamma}} = k\left(\frac{p_c}{p_i + p_r - 1}\right)^{\frac{2}{\gamma-1}} \qquad (2.72)$$

Since no pressure recovery is assumed, then:

$$p_c = p_1 \qquad (2.73)$$

and the particle velocity is given by:

$$u_2 = \frac{2a_0}{\gamma - 1}\left(p_i - p_r\right) \qquad (2.74)$$

Rearranging and substituting (2.70), (2.72) and (2.74) gives the expression:

$$\left(\tfrac{2}{\gamma-1}\right)^2\left(A^2 - 2AB + B^2\right)B^{10} - \left(\tfrac{2}{\gamma-1}\right)^2 k^2\left(A^2 - 2AB + B^2\right) - \left(\tfrac{2}{\gamma-1}\right)B^2k^2 + \left(\tfrac{2}{\gamma-1}\right)k^2 = 0 \quad (2.75)$$

$$\text{where: } A = \frac{2p_i - 1}{p_1} \text{ and } B = \frac{p_i + p_r - 1}{p_1}$$

This equation can be solved for $\frac{p_i + p_r - 1}{p_1}$ for fixed values of k and $\frac{2p_i - 1}{p_1}$.

2.7.1.2 Sonic inflow

It can be shown that the mass flow per unit area through an isentropic nozzle is given by [110]:

$$\frac{\dot{m}}{F} = \frac{p_s}{\sqrt{T_s}}\left(\frac{\gamma}{R}\right)^{\frac{1}{2}}\left[\frac{M}{\left[1+\left(\frac{\gamma-1}{2}\right)M^2\right]^{\frac{\gamma+1}{2(\gamma-1)}}}\right] \tag{2.76}$$

where the subscript s = stagnation conditions.

Since in the case of sonic inflow at the throat $M = 1$, the flow per unit area is:

$$\frac{\dot{m}}{F_c} = \frac{p_s}{\sqrt{T_s}}\left(\frac{\gamma}{R}\right)^{\frac{1}{2}}\left[\frac{1}{\left(\frac{\gamma+1}{2}\right)^{\frac{\gamma+1}{2(\gamma-1)}}}\right] \tag{2.77}$$

Dividing (2.76) by (2.77) and noting that $\frac{F_c}{F} = k$ gives:

$$k = M\left[\frac{\frac{\gamma+1}{2}}{1+\frac{\gamma-1}{2}M^2}\right]^{\frac{\gamma+1}{2(\gamma-1)}} \tag{2.78}$$

Since the Mach number is the ratio of particle velocity to acoustic velocity, then:

$$M = \frac{\frac{2a_0}{\gamma-1}\left(p_i - p_r\right)}{a_0\left(p_i + p_r - 1\right)} \tag{2.79}$$

Substitution of (2.79) into (2.78) allows for the solution of the reflected pressure term based on fixed values of k and $\frac{2p_i - 1}{p_1}$.

2.7.1.3 Subsonic outflow

Application of the energy equation from the volume to the throat gives:

$$u_2^{\,2} = \frac{2a_0^{\,2}}{\gamma - 1}\left(p_1^{\,2} - p_c^{\,2}\right) \qquad (2.80)$$

and application of the energy and continuity equations from the throat to the pipe gives:

$$u_c^{\,2} - u_2^{\,2} = \frac{2a_0^{\,2}}{\gamma - 1} p_c^{\,2}\left[\frac{u_2}{u_c}\frac{1}{k}\left(\frac{p_1 + p_r - 1}{p_c}\right)^{\frac{2\gamma}{\gamma-1}} - 1\right] \qquad (2.81)$$

Applying and rearranging the momentum equation from the throat to the pipe gives:

$$u_c\left(u_c - u_2\right) = \frac{a_0^{\,2}}{\gamma k} p_c^{\,2}\left[\left(\frac{p_i + p_r - 1}{p_1}\right)^{\frac{2\gamma}{\gamma-1}} - 1\right] \qquad (2.82)$$

Equations (2.80) to (2.82) can be rearranged and solved to find the reflected pressure term based on fixed values of k and $\frac{2p_i - 1}{p_1}$.

2.7.1.4 Sonic outflow

In this case the momentum equation from the throat to the pipe (2.82) no longer applies. Since at the throat the particle velocity equals the local acoustic velocity and $a = \left(\frac{p}{p_0}\right)^{\frac{\gamma-1}{2\gamma}} a_0$, then:

$$u_c = a_0 p_c \qquad (2.83)$$

The solution for the reflected pressure term, based on fixed values of k and $\frac{2p_i - 1}{p_1}$, is obtained from equations (2.80), (2.81), (2.83) and the particle velocity equation (A2.3.2) given in Appendix 2.3.

The solutions to each of the preceding flow regimes, for any combination of incident pipe pressure wave, restriction free area and volume pressure condition, were organised by McConnell [34] into a matrix of solutions that are referred to when the appropriate boundary condition is met during the pipe gas dynamics calculation. The graphical format of this boundary solution array is shown in Figure 2.6. The flow direction is initially established and the appropriate matrix of solutions is then selected; one is calculated based on $\gamma = 1.4$ for intake system gases and one is calculated based on $\gamma = 1.35$ for exhaust system gases. These values of γ are representative of typical gas conditions in each system. Linear interpolation takes place to calculate the reflected pressure term based on incident pressure terms, volume pressures and restriction free areas that do not coincide with values contained within the solution matrix. It has been found that this method of solving the boundary condition equations loses little accuracy over the direct solution of the equations within the general code. The method outlined is used for the calculation of flow through intake and exhaust valves, flow into and out of large volumes (within which gas dynamics are not considered) and flow at air intakes and exhaust outlets.

2.7.2 Junctions

The simulation code used during this study uses two types of pipe junction model. The first of these is a constant pressure model that assumes that the pressures in all pipes at the junction are equal. The second is a generalised model, developed by Bingham and Blair [111], which allows for pressure differences between pipes at junctions with any number of branches. Both of these models assume zero volume at the junction location.

2.7.2.1 Constant pressure model

Referring to Figure 2.7 assuming that positive flow in each case is towards the junction and the pressure in each pipe at the junction is equal, then, using equation (2.59), the continuity equation can be written:

$$(\lambda_1 - \beta_1)F_1 + (\lambda_2 - \beta_2)F_2 + (\lambda_3 - \beta_3)F_3 + ... + (\lambda_n - \beta_n)F_n = 0 \qquad (2.84)$$

Since the pressures in each pipe at the junction are equal, then, applying equation (2.22), it can be written that:

$$(\lambda_1 + \beta_1) = (\lambda_2 + \beta_2) = (\lambda_3 + \beta_3) = ... = (\lambda_n + \beta_n) \qquad (2.85)$$

Substituting the β_1 term from (2.85) into (2.84) for $\beta_2 ..... \beta_n$, then β_1 can be solved directly by:

$$\beta_1 \left(\frac{F_1 \sum_2^n F_j}{\sum_1^n F_j} \right) \lambda_1 + 2 \left(\frac{\sum_2^n \lambda_j F_j}{\sum_1^n F_j} \right) \qquad (2.86)$$

Having found β_1, then the remaining β terms can be found. The solution for this junction type is demonstrated assuming λ is designated as the arriving characteristic in all pipes at the junction and the flow in all pipes is positive towards the junction. In practice the calculation of any reflected characteristic is possible as long as the arriving characteristic is correctly designated. This applies for any flow direction in any pipe.

2.7.2.2 Generalised model

The main features of this model are the solution of the continuity equation across the junction and the calculation of a pressure loss term across the junction. The calculation of this pressure loss term is based on the identification of the main flow

path through the junction and the geometric relationship between the connected pipes. Junctions are identified initially as either supplier or collector types, depending on the expected flow regime. In the event of the flow direction being the opposite of that expected, the model reverts to the constant pressure model, detailed in Section 2.7.2.1, for the duration of the reverse flow. The sign convention applied to supplier and collector type junctions for the calculation is shown in Figure 2.8. Considering each junction type in turn:

Supplier type

In the case of positive flow in supply pipe s and pipe n, then the pressure loss between these pipes is given by:

$$p_s - p_n = C_n\left(\rho_n u_n^2\right)_{previous\ time\ step} \qquad (2.87)$$

where C_n is an experimental loss coefficient and is a function of the angle between pipes s and n. Values of ρ_n and u_n are based on the λ and β values from the previous time-step to eliminate a lengthy iterative process.

In the case of positive flow in pipe s and negative flow in pipe n, then the pressure in both pipes will be equal, hence:

$$p_s - p_n = 0 \qquad (2.88)$$

Collector type

In the case of positive flow in collector pipe c and pipes 1 to n flowing towards the junction, then the velocities in pipes 1 to n are compared to find the pipe with the

highest velocity (pipe l). It is assumed that this is the main flow through the junction at that instant and the pressure loss is given by:

$$p_l - p_c = C_l\left(\rho_c u_c^{\,2}\right)_{previous\ \ time\ \ step} \qquad (2.89)$$

As previously, C_l is an experimental loss coefficient and is a function of the angle between pipes l and c. The values of ρ_n and u_n are again based on the λ and β values from the previous time-step.

In the case of flow in all pipes being towards the junction then it is again assumed that:

$$p_n - p_l = 0 \qquad (2.90)$$

The solution of each junction type model proceeds using the following non-dimensional parameters:

$$p = A^{\frac{2\gamma}{\gamma-1}} p_0 \qquad (2.91)$$

$$\rho = A^{\frac{2}{\gamma-1}} \rho_0 \qquad (2.92)$$

$$u = U a_0 \qquad (2.93)$$

Thus, equation (2.87) can be written:

$$A_s^{\frac{2\gamma}{\gamma-1}} p_0 - A_n^{\frac{2\gamma}{\gamma-1}} p_0 = C_n A_n^{\frac{2}{\gamma-1}} \rho_0 U_n^{\,2} a_0^{\,2} \qquad (2.94)$$

Since $dA_n = A_s - A_n$, then simplification of equation (2.94) yields:

$$dA_n = A_n\left[\left\{1 + C_n\gamma\left(\frac{U_n}{A_n}\right)^2\right\}^{\frac{\gamma-1}{2\gamma}} - 1\right] \qquad (2.95)$$

In the case of $p_s - p_n = 0$, then $dA_n = 0$.

Similarly, equation (2.89) can be rewritten:

$$dA_l = A_c\left[\left\{1 + C_l\gamma\left(\frac{U_c}{A_c}\right)^2\right\}^{\frac{\gamma-1}{2\gamma}} - 1\right] \qquad (2.96)$$

In the case of $p_n - p_l = 0$, then $dA_n = dA_l$, where $dA_n = A_c - A_n$.

The continuity equation for the supplier type junction is:

$$\rho_s F_s u_s - \Sigma \rho_n F_n u_n = 0 \qquad (2.97)$$

At any time, the arriving λ characteristic in the supplier pipe and the arriving β characteristic(s) in the other n pipes are known. Since $A_s = \frac{\lambda_s + \beta_s}{2}$, then from equation (2.93):

$$u_s = \frac{2(\lambda_s - A_s)}{\gamma - 1} a_0 \qquad (2.98)$$

Since $\rho_n = A_n^{\frac{2}{\gamma-1}}\rho_0 = (A_s - dA_n)^{\frac{2}{\gamma-1}}\rho_0$, then equation (2.93) can also be written as:

$$u_n = \frac{2[(A_s - dA_n) - \beta_n]}{\gamma - 1} a_0 \qquad (2.99)$$

Thus, equation (2.97) can be written as:

$$A_s^{\frac{2}{\gamma-1}} F_s(\lambda_s - A_s) - \Sigma(A_s - dA_n)^{\frac{2}{\gamma-1}} F_n(A_s - dA_n - \beta_n) = 0 \qquad (2.100)$$

and the collector type junction continuity equation can be written:

$$A_c^{\frac{2}{\gamma-1}} F_c(\beta_c - A_c) - \Sigma(A_c - dA_n)^{\frac{2}{\gamma-1}} F_n(A_c - dA_n - \lambda_n) = 0 \qquad (2.101)$$

Equations (2.100) and (2.101) are solved by Newton-Raphson iteration to find the values of A_s or A_c as based on the value of dA_n at the beginning of the time-step. Direct calculation of the missing reflected characteristics from all pipes adjacent to the junction is then possible from:

Supplier pipe

$$\beta_s = 2A_s - \lambda_s \qquad (2.102)$$

$$\lambda_n = 2(A_s - dA_n) - \beta_n \qquad (2.103)$$

Collector pipe

$$\lambda_c = 2A_c - \beta_c \qquad (2.104)$$

$$\beta_c = 2(A_c - dA_n) - \lambda_n \qquad (2.105)$$

2.7.3 Throttle

The simulation model used during the course of this study models the throttle, including butterfly valves and all carburettor components, as an isentropic restriction between two adjoining pipes. The model incorporates elements of the pipe-volume calculation procedure detailed in Section 2.7.1. As with all boundary condition subroutines used by this simulation model, the subroutine is called after the completion of all of the in-pipe calculations. The incident characteristics are therefore known at both adjacent pipe ends and the subroutine is required to calculate the value of both of the reflected characteristics.

At the outset of the throttle calculation, an initial guess is made of the current flow direction and the static pressure downstream of the throttle calculated. The array of isentropic nozzle restriction solutions are then accessed and the upstream reflected characteristic derived as detailed in Section 2.7.2, based upon the assumption that stagnation conditions exist downstream of the throttle. This, of course, is not actually the case but it has been found that this assumption gives acceptable results provided that an appropriate value of the throttle effective area is selected. The missing downstream characteristic is found by iterative solution of the continuity equation across the restriction.

Since:

$$\dot{m}_u = \rho_u F_u u_u \qquad (2.106)$$

where subscript u represents upstream conditions, then a mass flow parameter, x_u, can be defined as:

$$x_u = \left[\left(\frac{\lambda_u + \beta_u}{2} \right)^{\frac{2}{\gamma-1}} F_u \left(\frac{\lambda_u - \beta_u}{\gamma - 1} \right) \right] \qquad (2.107)$$

Since mass flow across the throttle is preserved, then it follows that:

$$x_u - \left[\left(\frac{\lambda_d + \beta_d}{2} \right)^{\frac{2}{\gamma-1}} F_d \left(\frac{\lambda_d - \beta_d}{\gamma - 1} \right) \right] = 0 \qquad (2.108)$$

where subscript d refers to downstream conditions. Equation (2.108) can then be solved for the missing characteristic by Newton-Raphson iteration.

2.8 IN-CYLINDER CALCULATION

The in-cylinder calculation is based on the application of the first law of thermodynamics to describe a homogenous gas contained within a simple, single zone volume. At each time-step the gas is described in terms of its purity, pressure and temperature and from these values the work output during each time-step can be calculated. The calculation proceeds considering the effect of heat transfer between the exposed cylinder walls, the piston crown and the cylinder head, the changing cylinder volume, heat release during combustion, the changing gas specific heats and gas flow to and from the cylinder.

There are three calculations that are common to the in-cylinder calculations at every time-step during the cycle. These are heat transfer, cylinder volume and gas specific heats.

2.8.1 Heat transfer calculation

Heat transfer during the cycle is calculated using the function proposed by Annand [112]:

$$\frac{q_c}{A_c} = a\frac{k}{D}\mathrm{Re}^b\left(T - T_w\right) + c\left(T^4 - T_w{}^4\right) \qquad (2.109)$$

where:

q_c = Heat transfer rate

A_c = Surface area exposed to heat transfer

a = Constant for convective heat transfer – typically 0.6 for SI engines

k = Thermal conductivity of the fluid

D = Cylinder bore

Re = Reynolds number, $V_p D / \upsilon$

V_p = Mean piston speed

υ = Viscocity of gas

b = Index relating Nu to Re – typically 0.7 for SI engines

T = Gas temperature

T_w = Combustion chamber surface temperature

c = Constant for radiative heat transfer – typically 0.431×10^{-11} for SI engines

2.8.2 Cylinder volume calculation

Referring to Figure 2.9, the cylinder volume can be calculated at each crank-angle, θ, by:

$$H = \left(\frac{S}{2} + L_R\right) - \left[\left(\frac{S}{2}\cos\theta\right) + \sqrt{\left\{L_R^{\,2} - \left(\frac{S}{2}\sin\theta\right)^2\right\}}\right] \qquad (2.110)$$

where:

H = Cylinder height

S = Crankshaft stroke

L_R = Connecting rod length

The cylinder volume is then given by:

$$V = \frac{\pi F_{bore}^{\,2}}{4} H + V_{cl} \qquad (2.111)$$

where:

F_{bore} = Cylinder bore

V_{cl} = Clearance volume

2.8.3 Gas specific heats calculation

Throughout the engine cycle, at every time-step, values of C_p, C_v, R and γ are calculated, based on the current values of gas temperature and purity. Gas purity is a parameter that varies between values of 0 and 1 and indicates the proportion of fresh air in the gas mixture. The value 0 indicates that only exhaust gas is present and 1 indicates that only fresh air is present. The relationships between gas specific heats, temperature and purity are given by Van Wylen and Sonntag [110].

2.8.4 In-cylinder calculation periods

The in-cylinder calculation applies the First Law of Thermodynamics to either an open system, from the period EVO to IVC, or a closed system for the remainder of the cycle. The closed system period can be further separated into three distinct phases. Thus, the four principal phases of the four-stroke cycle engine are:

1. Open cycle: EVO to IVC
2. Compression: IVO to the start of combustion
3. Combustion
4. Expansion: End of combustion to EVO

Each of these phases will be considered separately.

2.8.4.1 Open cycle

Application of the First Law of Thermodynamics gives:

$$\dot{Q}+\dot{m}_i\left(h_i+\frac{u_i^2}{2}\right)=\frac{d}{dt}\left(E_s\right)+\dot{m}_e\left(h_e+\frac{u_e^2}{2}\right)+\frac{pdV}{dt} \qquad (2.112)$$

where subscript i refers to the inlet and subscript e refers to the exhaust. The calculation advances in time-steps and so equation (2.113) must be expressed in incremental form:

$$dQ + dm_i\left(h_i + \frac{u_i^2}{2}\right) = d\left(E_s\right) + dm_e\left(h_e + \frac{u_e^2}{2}\right) + pdV \quad (2.113)$$

where: dQ = Heat transfer between the gas and the exposed combustion chamber surface during the time-step.

dm_i = Fresh charge flowing into the cylinder during the time-step (negative if flowing out).

$h_i + \frac{u_i^2}{2}$ = Stagnation enthalpy into cylinder with fresh charge = h_{0i}.

$d\left(E_s\right)$ = Change of cylinder gas internal energy.

dm_e = Exhaust gas flowing out of the cylinder during the time-step (positive if flowing in).

$h_e + \frac{u_e^2}{2}$ = Stagnation enthalpy out of cylinder with exhaust gas = h_{0e}.

Since $d\left(E_s\right) = \left(mC_vT\right)_{s"} - \left(mC_vT\right)_{s1}$ and $mT = pV/R$, then the energy term of equation (2.113) can be written:

$$d\left(E_s\right) = \frac{p_2V_2C_{v2}}{R} - \frac{p_1V_1C_{v1}}{R} \quad (2.114)$$

where subscripts *1* and *2* refer to the beginning and end of each time-step. Substituting equation (2.114) into equation (2.113) and rearranging enables the pressure at the end of each time-step to be found from:

$$p_2 = \frac{\left[dQ + dm_i h_{0i} - dm_e h_{0e} + p_1 \left(\frac{V_1 C_{v1}}{R} - \frac{dV}{2} \right) \right]}{\left(\frac{V_2 C_{v2}}{R} + \frac{dV}{2} \right)} \qquad (2.115)$$

Each of the individual terms in equation (2.115) can be determined from previously calculated parameters from other parts of the simulation. The dQ term is calculated from Annand's equation (2.109). The dm terms are given by the application of $m = \rho F u dt$ which can be written in terms of the λ and β characteristics in the pipe meshes immediately adjacent to the valves:

$$m = \left(\frac{\lambda + \beta}{2A_a} \right)^{\frac{2}{\gamma - 1}} \frac{1}{A_a{}^2} \rho_0 F \left(\frac{\lambda - \beta}{\gamma - 1} \right) a_0 dt \qquad (2.116)$$

Similarly the stagnation enthalpy terms are given by:

$$h_0 = h + \frac{u^2}{2} \qquad (2.117)$$

Since:

$$h = C_p T = \frac{C_p}{C_v} C_v T_0 \frac{T}{T_0} = \frac{\gamma R}{\gamma - 1} T_0 \frac{T}{T_0} \qquad (2.118)$$

then:

$$h = \frac{a_0{}^2}{\gamma - 1} \left(\frac{\lambda + \beta}{2} \right)^2 \qquad (2.119)$$

Also:

$$\frac{u^2}{2} = \left(\frac{\lambda + \beta}{\gamma - 1} \right)^2 \frac{a_0{}^2}{2} \qquad (2.120)$$

Substitution of equations (2.119) and (2.120) into (2.117) gives:

$$h_0 = \frac{a_0^2}{\gamma - 1}\left(\frac{\lambda + \beta}{2}\right)^2 + \left(\frac{\lambda - \beta}{\gamma - 1}\right)^2 \frac{a_0^2}{2} \qquad (2.121)$$

Finally the cylinder gas temperature at the end of the time-step is found from:

$$T_2 = \frac{p_2 V_2}{m_2 R_2} \qquad (2.122)$$

where $m_2 = m_1 + m_i - m_e$.

2.8.4.2 Compression and expansion

Since there is no flow to or from the cylinder during either of these events the application of the First Law equation gives:

$$Q = d(E_s) + pdV \qquad (2.123)$$

During compression the dV term is positive and during expansion it is negative.

Making similar substitutions as with the open cycle, in-cylinder pressure at the end of the time-step is given by:

$$p_2 = \frac{\left[dQ + p_1\left(\frac{V_1 C_{v1}}{R} - \frac{dV}{2}\right)\right]}{\left(\frac{V_2 C_{v2}}{R} + \frac{dV}{2}\right)} \qquad (2.124)$$

In this case the mass is constant and the temperature is again given by equation (2.122).

2.8.4.3 Combustion

At the point of IVC, the mass of air and fuel trapped in the cylinder is known. Combustion begins at a user-defined point during the cycle and is modelled using a

semi-empirical heat release calculation; the end of the combustion period is fixed at 41° ATDC. During this period, heat is released according to a defined function in terms of percent heat release over the duration of combustion. The quantity of heat released by the fuel during a time-step is given by:

$$dQ_f = dm_f \times (\textit{calorific value}) \times (\textit{combustion efficiency}) \qquad (2.125)$$

where: dQ_f = Heat release during time-step

dm_f = Mass of fuel burnt during time-step

The percent heat release vs. crank-angle data required to perform the calculation is supplied as input data at equal intervals during the combustion period. Interpolation is performed for the required values of percent heat release at intermediate time-steps. Combustion efficiency is a user-defined input. Additional refinements to the combustion calculation consider the effect of the equivalence ratio on the combustion characteristics. This is based on experimental data presented by Heywood [113] and is utilised during the combustion calculation with combustion efficiency as a function of air/fuel ratio.

The net heat transfer is given by:

$$dQ_{net} = dQ_f - dQ \qquad (2.126)$$

and the cylinder conditions are then given by:

$$p_2 = \frac{\left[dQ_{net} + p_1\left(\frac{V_1 C_{v1}}{R} - \frac{dV}{2}\right)\right]}{\left(\frac{V_2 C_{v2}}{R} + \frac{dV}{2}\right)} \qquad (2.127)$$

As previously, the temperature at the end of the time-step is given by equation (2.122), where:

$$m_2 = m_1 + dm_f \qquad (2.128)$$

2.8.5 Imep calculation

The imep calculation is performed by the summation of all the $\delta(imep)$ calculations during the engine cycle. For each time-step the incremental value of imep is given by:

$$\delta(imep) = \left[\frac{(p_2 - p_a) + (p_1 - p_a)}{2}\right]\frac{dV}{V_s} \qquad (2.130)$$

where:

p_1 = Pressure at the beginning of the time-step

p_2 = Pressure at the end of the time-step

p_a = Atmospheric pressure

dV = Change in volume during the time-step

V_s = Swept volume (one cylinder)

2.9 GAS PURITY

Gas purity can be tracked throughout the engine pipe systems and in the cylinders. The tracking of gas purity throughout the pipes is essential, particularly in the case of reverse flow, so that the in-cylinder purity is accurately predicted. The in-cylinder purity has a significant influence on the overall engine performance, which is largely a function of the mass flow rate of fresh air passing through it. Thus, the in-cylinder purity is an indicator of both volumetric efficiency and effective cylinder scavenging. The gas purity, ϕ, is defined as:

$$\phi = \frac{mass\ of\ air}{mass\ of\ mixture\ (air + exhaust)} \qquad (2.131)$$

The calculation procedure does not consider fuel, in either liquid or vapour form, but assumes that the fresh inlet charge contains the fuel at the appropriate ratio.

2.9.1 Gas purity in pipes

The pipe gas purity calculation is based on the designation of pipe volumes whose boundaries correspond to the locations of the pipe meshes. Referring to Figure 2.10, each volume is designated according to the mesh at its left-hand boundary. At the end of a time-step and assuming that flow is from left to right, the mass of gas contained within volume J can be given by:

$$m_2(J) = m_1(J) + \delta m(J) - \delta m(J+1) \qquad (2.132)$$

where $\delta m(J)$ and $\delta m(J+1)$ are the mass of gas entering and leaving volume J respectively. Since each mass δm will have the purity of the volume from which it has come then, at the end of the time-step, volume J will have its purity given by:

$$\phi_2(J) = \frac{m_1(J)\phi_1(J) + \delta m(J)\phi_1(J-1) - \delta m(J+1)\phi_1(J)}{m_2(J)} \qquad (2.133)$$

In cases where flow is across a boundary into a pipe then the purity is taken as that existing upstream of the pipe boundary.

2.9.2 Gas purity in the cylinder

There are four separate phases during a single engine cycle for the calculation of gas purity. These are detailed separately:

i. End of combustion to IVO

At the end of combustion it is assumed that there is no unburned fresh charge remaining in the cylinder and purity is therefore given a nominal value of 0.001. For the period from the end of combustion to IVO there is no mass flux to or from the cylinder and therefore the cylinder purity remains constant at this value.

ii. IVO to IVC

During this period mass flow will occur to and from the cylinder, via both the exhaust and inlet valves. Reverse flow is possible through both valves. Assuming positive flow is in the direction inlet → cylinder → exhaust, then the cylinder purity at the end of a time-step is given by:

$$\phi_{c2} = \frac{\phi_{c1} m_1 + \delta m_i \phi_i - \delta m_e \phi_{c1}}{m_2} \qquad (2.134)$$

where $m_2 = m_1 + \delta m_i - \delta m_e$ and subscript i = inlet port, e = exhaust port and c = cylinder.

iii. IVC to start of combustion

During this period there is no mass flux to or from the cylinder and therefore cylinder purity remains constant.

iv. Start of combustion to end of combustion

During this period an assumption is made that the cylinder purity falls linearly from the value in iii. to the nominal value of 0.001. In reality the cylinder purity should be related to the heat release rate.

2.10 SIMPLIFICATIONS AND LIMITATIONS OF THEORY

2.10.1 Order of accuracy

The method of characteristics is considered to be accurate to the first order. It is assumed that a linear variation of $d\lambda$ and $d\beta$ exists across time-step ΔZ, thus, referring to Figure 2.4:

$$\lambda 2 = \lambda_w + \frac{d\lambda}{dZ}\Delta Z \qquad (2.135)$$

where $\frac{d\lambda}{dZ} = f(\lambda_w, \beta_w)$. This is an approximation of the true integral solution that should account for the higher order variation as $d\lambda$ and $d\beta$ are attenuated. Equation (2.135) is analogous to the Taylor expansion to the first order:

$$f(x+h) = f(x) + h.f'(x) \qquad (2.136)$$

and hence the description of the method of characteristics being first order accurate. Generally, this solution scheme gives acceptable accuracy when applied to engine calculations although its application to unsteady flow problems in long pipes causes errors which manifest themselves as mass flow discontinuities between the entry and exit of the pipe. Some alternative solutions to pipe gas dynamics problems, detailed in Section 1.2.2 claim second order accuracy in at least one dimension.

2.10.2 Linear interpolation

Linear interpolation is used to calculate the values of characteristics at intermediate locations between meshes. This is not strictly correct but the selection of a suitably small mesh length minimises this error. There are particular instances where application of the linear interpolation procedure can cause cumulative errors that

ultimately lead to instability in the calculation. An example of this is the modelling of long single diffusers with sustained periods of high positive velocity. Bingham [40] demonstrates the generation of a progressively reflected rarefaction wave, which can ultimately result in a shock occurring near the diffuser entrance that may not otherwise have occurred. In practice these situations are rarely encountered and, having awareness of the potential problem, models can be assembled with suitable safeguards.

2.10.3 One-dimensional flow

The assumption of one-dimensional flow leads to a significant saving in computational time and effort. In practice the assumption is a valid one in the case of gas flow in pipes with a high length/diameter ratio such as those that are found in engine manifolds. Care must be taken when modelling "three dimensional" components such as air filters and plenums and it is important that the effective length of the component is maintained. Comparisons between measured and predicted results, shown in Chapter 3, provide evidence of the validity of this assumption.

2.11 ORGANISATION OF THE COMPUTER SIMULATION PROGRAM

Figure 2.11 shows a flow diagram indicating the main elements of the calculation procedure. The engine model is assembled as a number of cylinders and a series of pipes, representing each of the manifold systems, interconnected at various junction nodes, volumes, throttles, etc. Each component and junction is numbered and the manifold pipes are then further subdivided into mesh lengths. Arrays within the code keep track of the current gas properties at each component and at each mesh location,

which are then updated at the end of every time-step. Performance parameters for each cylinder are generally obtained by the summation of each time-step increment of the appropriate variable over the whole engine cycle. To stabilise the manifold gas dynamics, it is necessary to allow the simulation to run over a number of cycles. The summation of the performance parameters then occurs during the final cycle only. The following definitions for the principal engine performance indicators are used within the code:

$$\begin{aligned} &\textit{Brake mean effective pressure } (bmep) = \\ &\textit{indicated mep } (imep) - \textit{frictional mep } (fmep) \end{aligned} \qquad (2.137)$$

where the imep is given by equation (2.130) and fmep (frictional mean effective pressure) is given by:

$$fmep = \frac{97000 + 15RPM}{4} \qquad (2.138)$$

and RPM = engine speed in r/min.

$$Power = bmep \times \textit{ swept volume } \times \frac{RPM}{60} \times \frac{1}{2} \qquad (2.139)$$

$$Torque = \frac{power}{\left(\frac{2\pi \times RPM}{60}\right)} \qquad (2.140)$$

$$\textit{Volumetric efficiency} = \frac{\textit{mass of fresh air induced per cycle } \left(\textit{at inlet valve}\right)}{\textit{cylinder swept volume } \times \textit{ reference density}} \qquad (2.141)$$

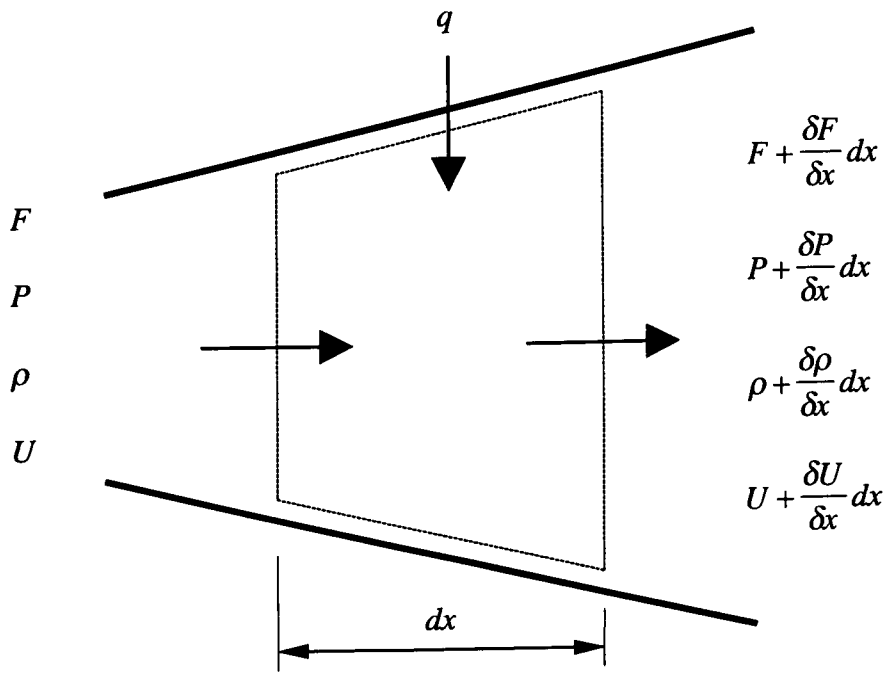

Figure 2.1 Control volume notation

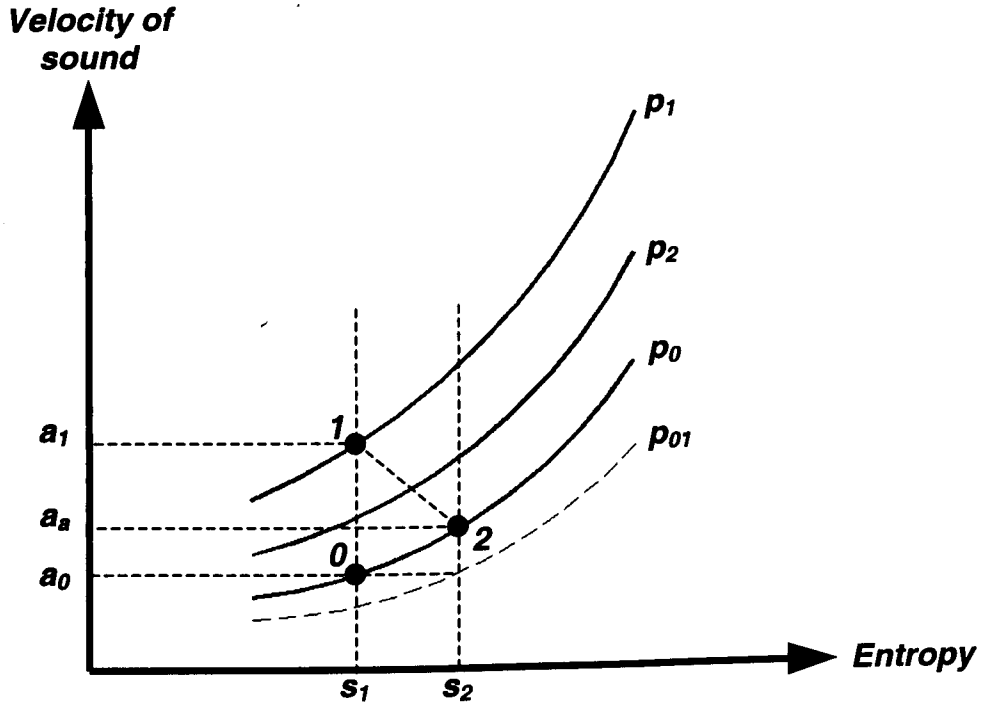

Figure 2.2 Non-homentropic relationships

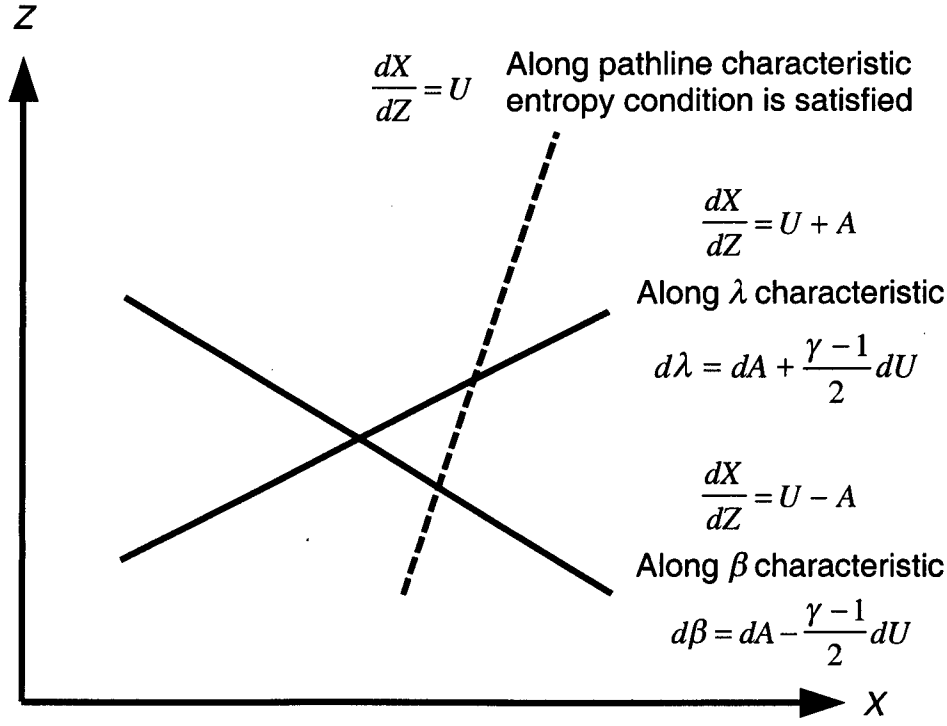

Figure 2.3 Direction and compatibility conditions

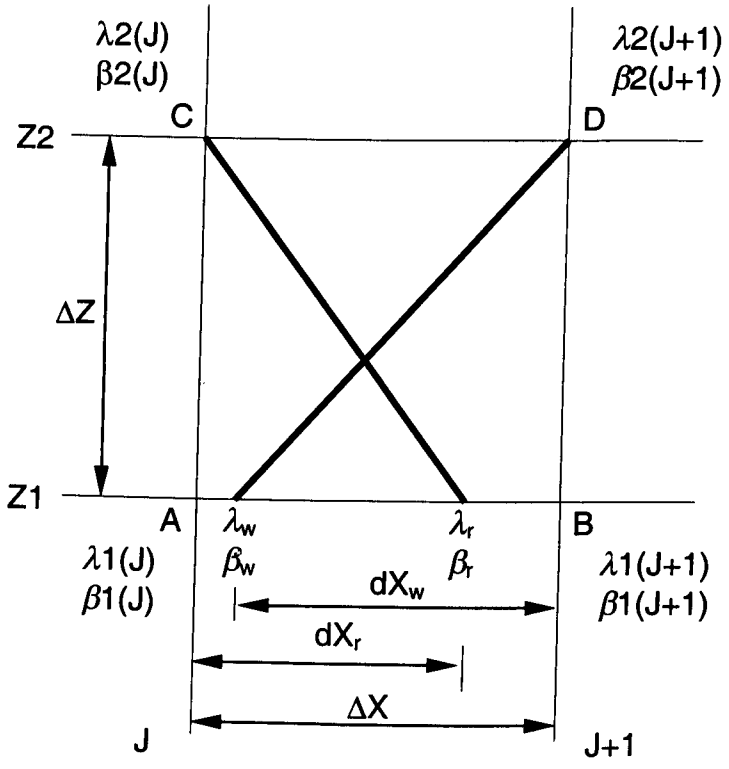

Figure 2.4 Distance-time mesh for numerical solution of λ and β characteristics

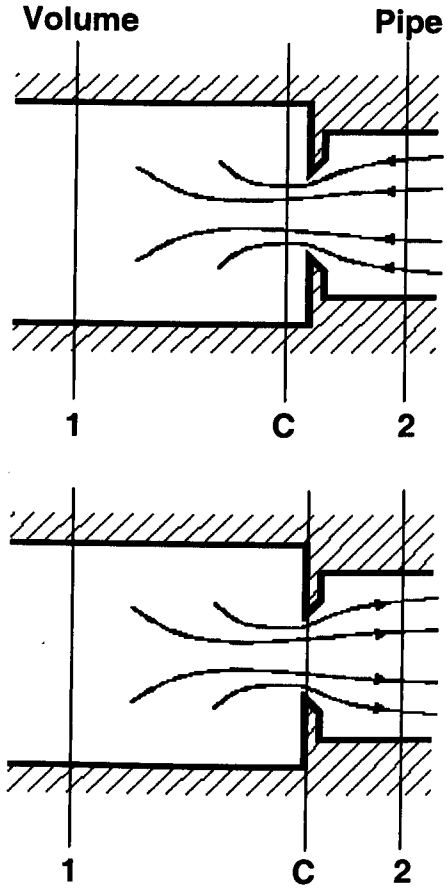

Figure 2.5 Volume inflow and outflow models

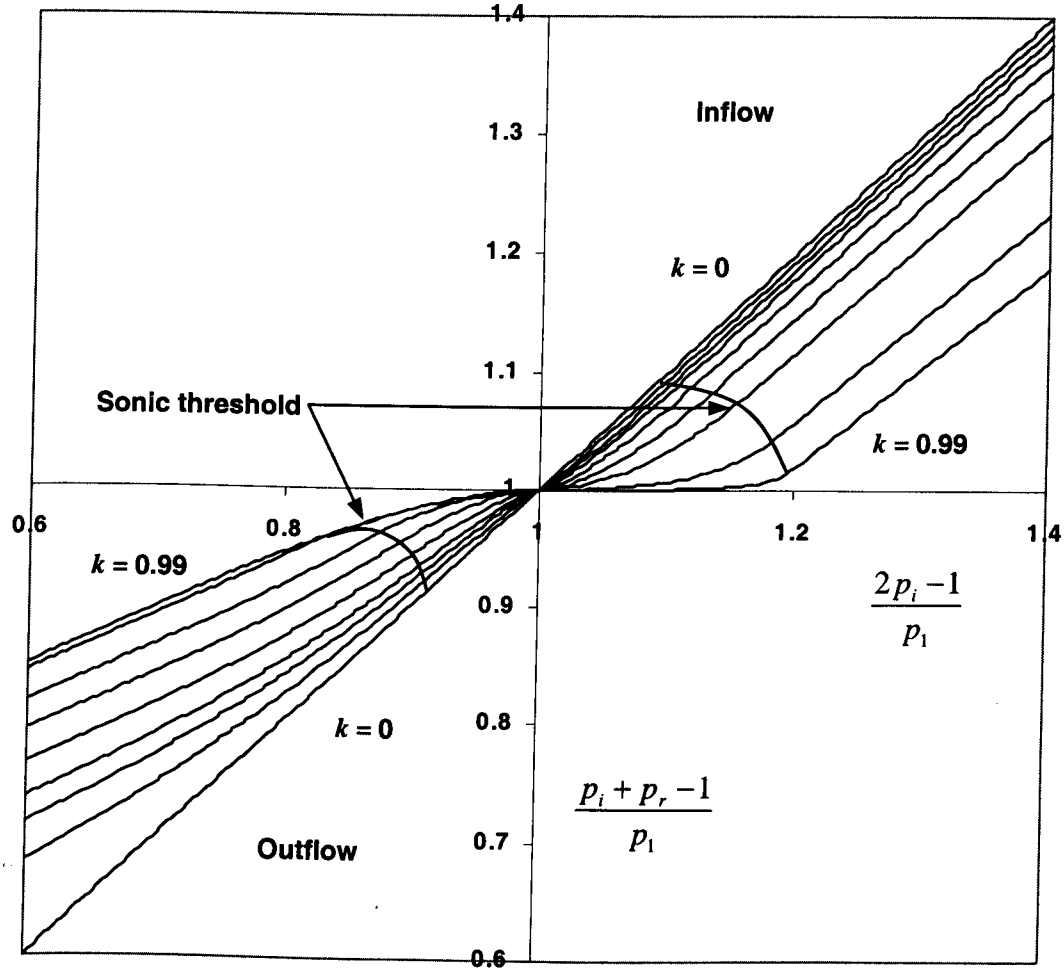

Figure 2.6 Boundary condition solution graph

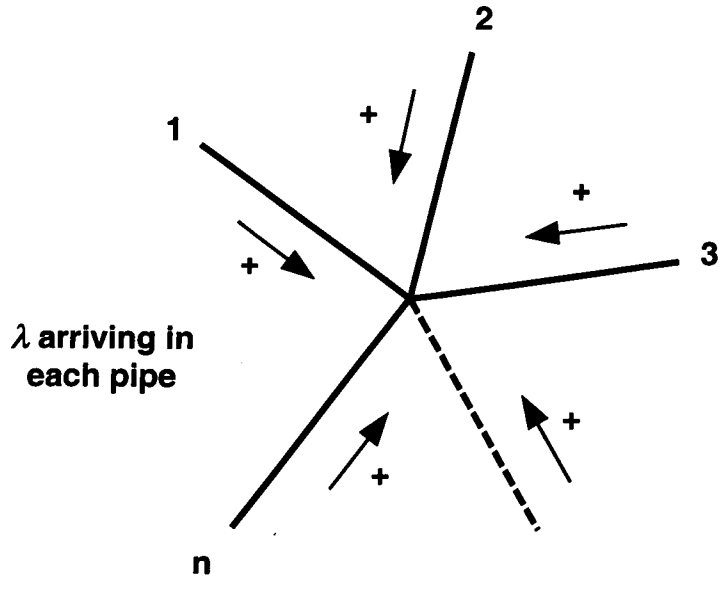

Figure 2.7 Pipe junction

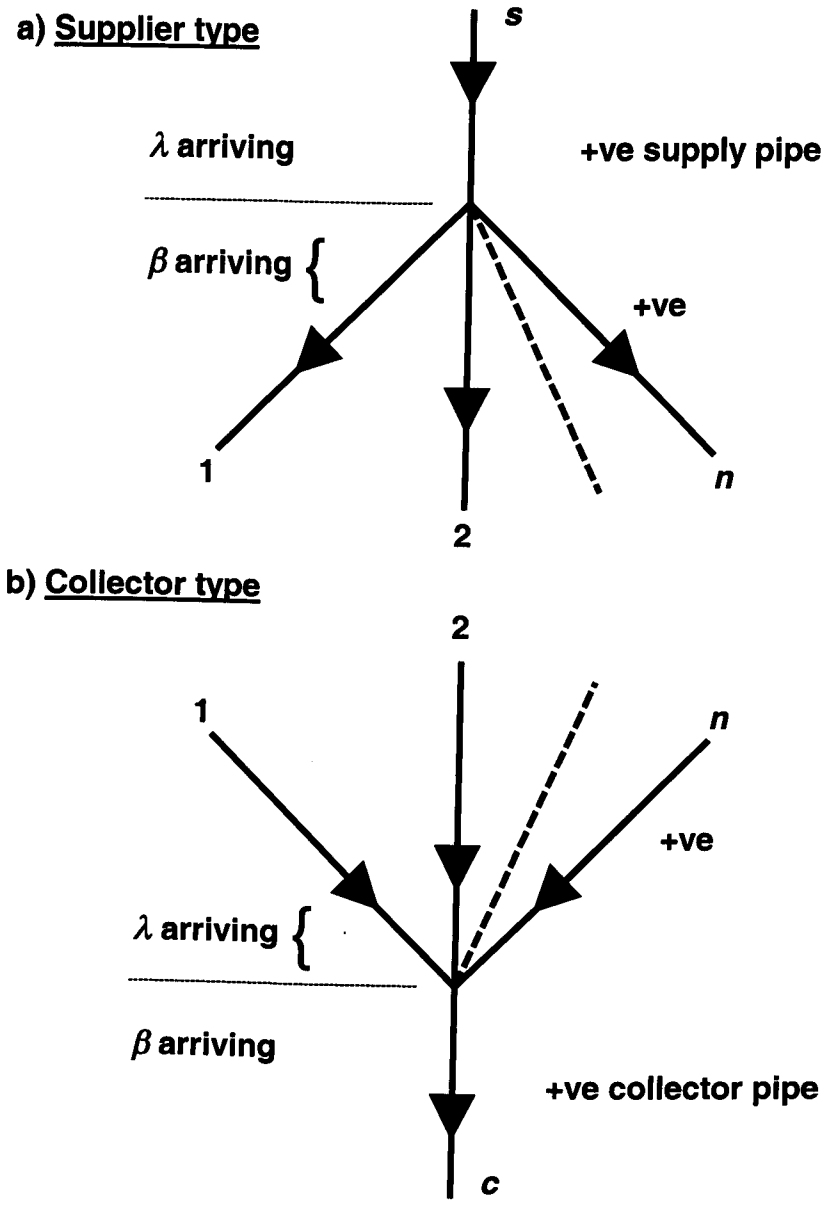

Figure 2.8 Sign convention for generalised junction model

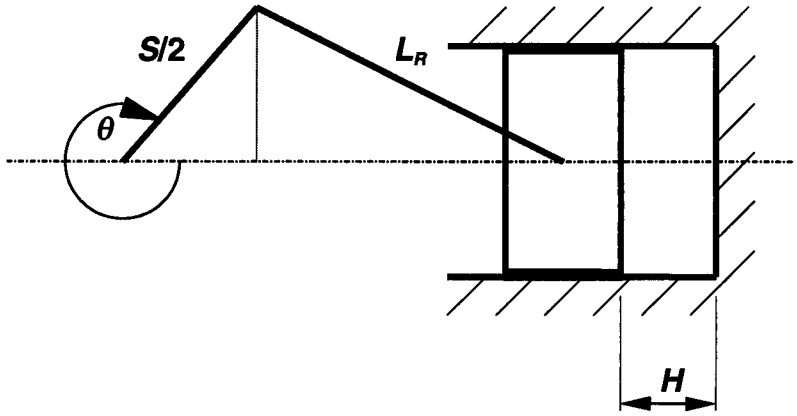

Figure 2.9 Cylinder height calculation

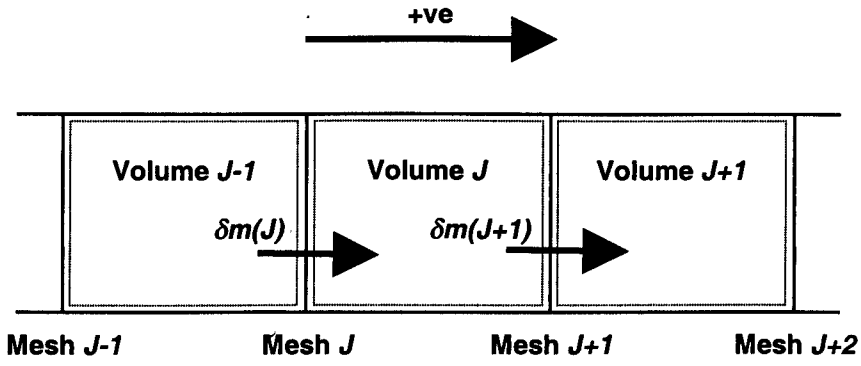

Figure 2.10 Pipe purity calculation

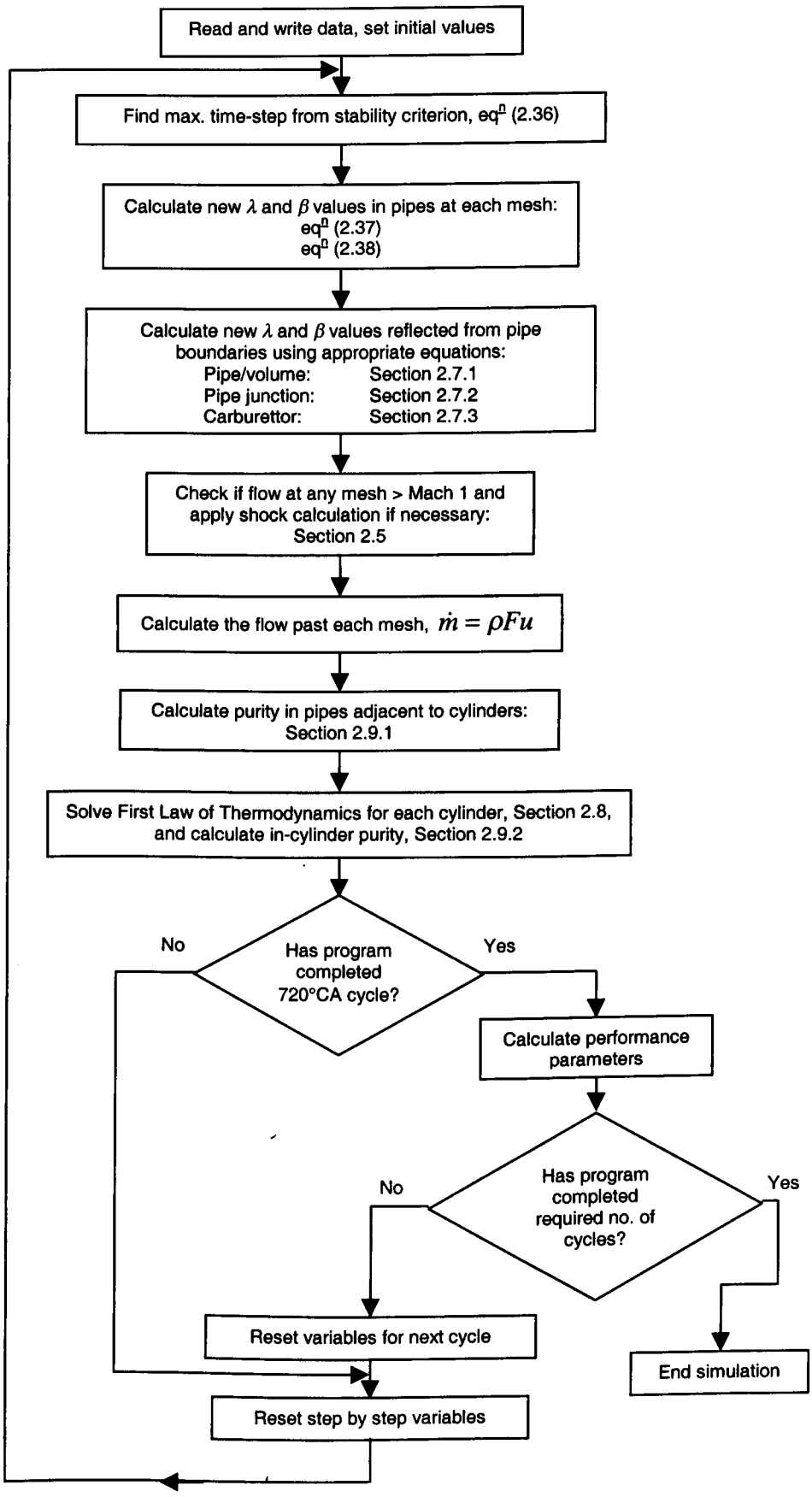

Figure 2.11 Flow diagram – engine simulation computer program

CHAPTER 3

EXPERIMENTAL TEST RIG AND COMPUTER SIMULATION VALIDATION

CHAPTER 3

EXPERIMENTAL TEST RIG AND COMPUTER SIMULATION VALIDATION

3.1 INTRODUCTION

The engine used throughout the experimental phase of this study was a Rover 1.4 litre 16 valve "K" series engine. The engine was operated in its conventional firing mode rather than being motored, since the focus of interest was the exhaust system gas dynamics and its influence on engine performance. The induction system gas dynamics are not greatly affected by either mode of operation since there is little variation of induction charge temperature across the engine operational speed range [105]. However, in a motored engine, the absence of high temperature, high pressure gases and the steep temperature gradients that exist in the exhaust manifolds of a typical firing engine has a significant influence on wave amplitudes and phasing.

Through the course of the test program a number of different configurations of exhaust system were installed and tested at WOT from approximately 1000-6000 r/min. Measurements were recorded of various engine performance parameters and of dynamic and static pressure histories and temperatures throughout the entire system. These results were used to correlate the various predicted performance characteristics of the homentropic engine simulation model that was to be used throughout the course of the project. The same results were also used to validate the non-homentropic model that became available during the latter stages of the project.

3.2 ENGINE TEST FACILITY

3.2.1 Engine installation

The engine used for the experimental phase of the study was a reconditioned Rover K series 1400 cc 16 valve engine. The main features of this engine are summarised in Table 3.1.

Table 3.1 Main features of Rover K series test engine

Capacity	1396 cc
Bore	75 mm
Stroke	79 mm
Connecting rod length	131.4 mm
Compression ratio	9.5:1
Combustion chamber	Pent-roof 4 valve central spark plug
Fuelling	Multi-point fuel injection
Valve timing: Exhaust open	128°
Exhaust close	372°
Inlet open	348°
Inlet close	592°

Figures 3.1 and 3.2 show the actual installed facility and Figure 3.3 shows a schematic of the test facility layout. Both the intake system and the main engine block were the standard Rover items, except for minor modifications to a number of components to facilitate the installation of various transducers. These modified components included the intake primary pipes, the intake system plenum, the intake filter housing, the engine oil filter housing and the thermostat housing, each of which had threaded transducer bosses fixed in suitable locations.

The engine oil and coolant systems were coupled to external, water-cooled heat exchangers with feedback-controlled circuits to maintain each fluid at specified

operating temperatures. The potential effect of the variation of coolant temperature on engine volumetric efficiency has been shown by Liu [105] and demonstrates the importance of close control of these parameters.

The engine was directly coupled, through a Bailey-Morris universal drive shaft, to a Schenk water-cooled, eddy-current, 130 kW dynamometer that was calibrated before commencement of the test programme.

The engine fuel consumption was monitored by a Hird Brown FM4 gravimetric measuring device while the air/fuel (A/F) ratio was measured using an NTK MO 1000 A/F ratio meter and MD 100 oxygen sensor on the exhaust side. Thus, the engine air consumption could be derived from the product of fuel flow rate and A/F ratio. This air consumption measurement was additional to that detailed in Section 3.2.2.

Due to a supply problem, the engine was run with the engine control unit (ECU) from the 1600 cc version of the engine. At part load conditions this did not cause a problem since the feedback control between the HEGO sensor and the ECU optimised the fuelling to maintain the combustion mixture at the stoichiometric A/F ratio. At WOT conditions however, the fuelling management switched to open loop control. The ECU therefore controlled the fuelling such that an A/F ratio of approximately 12-12.5:1, the optimum ratio for maximum torque at WOT, would be maintained if the engine was in fact 1600 cc capacity. Hence it could be observed during initial tests that the measured A/F ratio was richer than this optimum ratio at WOT. This problem was overcome by installing a selector valve in the pressure line between the fuel rail pressure relief valve and the inlet manifold. The fuel rail pressure relief valve usually

adjusts the fuel rail pressure to maintain a constant Δp across the injectors according to the intake manifold pressure. By imposing a pressure above or below that of the manifold, the fuelling could therefore be controlled externally at WOT to optimise the A/F ratio. This was achieved by installing a vacuum pump and a fine control bleed valve to the selector valve between fuel rail pressure relief valve and the inlet manifold. This fuelling control system is shown diagrammatically in Figure 3.4. Since the long term objective of the project was to rapidly identify exhaust manifold designs which improve torque performance by either reducing engine pumping work or by improving airflow through the engine, then, in the case of the latter, a facility would be required to optimise the A/F ratio at WOT if such an exhaust manifold were fitted. This validates the decision to continue with the use of a 1600 cc ECU at this stage of the project (note that the spark advance curves for both the 1400 cc and the 1600 cc engine are nearly identical).

Since the test engine was a newly reconditioned unit, a thorough bedding-in schedule had to be completed to ensure good repeatability for subsequent tests. Repeated corrected torque and airflow measurements after this bedding-in schedule had been completed are shown in Figures 3.5 and 3.6. The torque correction for reference atmospheric conditions [115] is given by:

$$E_c = \alpha E_m \qquad (3.1)$$

where:

E_c = Corrected torque (Nm)

E_m = Measured torque (Nm)

α = Correction factor

$$\alpha = \left(\frac{99}{P_s}\right)^{1.2}\left(\frac{T}{293}\right)^{0.6}$$

P_s = Dry atmospheric pressure (kPa)

T = Temperature (K)

This correction factor is only applicable for:

$$0.93 < \alpha < 1.07$$

The calculation of measured corrected airflow is detailed in Section 3.2.2

Figures 3.5 and 3.6 show good repeatability for both torque and airflow with the exception of the airflow measurement at 1000 r/min for one test which is significantly down on the other tests. This result can be attributed to the instability of the engine running at WOT at such low speeds and the associated difficulties of retrieving accurate results. There is no obvious time dependent variation in the results.

3.2.2 Measurement of air consumption

Air consumption by volume was measured by a Cussons Alcock type H viscous air flow meter. The volume air flow rate was derived from measurement of the pressure drop across the meter laminar flow elements. An additional pressure and thermocouple tapping at the meter exit allow for calculation of a temperature correction for the measured volume flow and of the engine intake air density. All viscous flow meter pressure measurements were made with paraffin filled manometers and temperatures were measured using 1.5 mm diameter type K NiCr/NiAl thermocouples. The engine volumetric efficiency calculation and correction calculation to standard atmospheric conditions is carried out as follows:

$$\eta_{volm} = \frac{\dot{m}_m}{V_s \frac{N}{120} \rho_a} \qquad (3.2)$$

where:

η_{volm} = Measured volumetric efficiency

$\dot{m}_m$ = Measured mass flow rate ($^{kg}/_{s}$)

V_s = Engine swept volume (m^3)

N = Engine speed ($^{rev}/_{\min}$)

ρ_a = Ambient air density ($^{kg}/_{m^3}$)

The corrected volumetric efficiency (η_{volc}) is calculated from:

$$\eta_{volc} = \frac{\dot{m}_c}{V_s \frac{N}{120} \rho_{ref}} \qquad (3.3)$$

where:

$\dot{m}_c$ = Corrected mass flow rate ($^{kg}/_{s}$)

$$\dot{m}_c = \dot{m}_m \frac{p_{ref}}{p_{amb}} \left(\frac{T_{amb}}{T_{ref}} \right)^{0.5}$$

p_{ref} = $101325\ ^{N}/_{m^2}$

T_{ref} = $293\ K$

p_{amb} = Ambient pressure ($^{N}/_{m^2}$)

T_{amb} = Ambient temperature (K)

ρ_{ref} = Reference density ($^{kg}/_{m^3}$)

$$\rho_{ref} = \frac{p_{ref}}{RT_{ref}}$$

R = Gas constant ($^{J}/_{kgK}$)

Located either side of the viscous air flow meter are large plenums, each of approximately 110 litres volume. The purpose of the plenum on the exit side of the meter was to minimise any dynamic pressure effects, resulting from the meter installation, within the engine intake system. Figure 3.7 to 3.9 show comparisons of measured cylinder 1 intake tract pressure histories from 2000-4000 r/min at WOT, with and without the airflow meter installed, measured using the method described in Section 3.2.3. Figure 3.10 shows comparisons of measured corrected air consumption at WOT with and without the airflow meter installed; in the later case airflow measurement is derived from fuel consumption and measured air/fuel ratio only. These results show that the installation of the air flow meter does not impose any significant additional pressure loss on the intake system and that engine air consumption is not unduly effected. They also show that the installation of the plenum downstream of the airflow meter attenuates wave reflections from the exit side of the meter and thus, there are no additional dynamic pressure effects resulting from the meter installation within the intake system.

3.2.3 Pressure measurement

Dynamic pressure measurement was made with Kistler type 6121 piezo-electric transducers. These were connected by high impedance leads to Fylde 128CA charge amplifiers, and the signals from these transferred to a Thorn SE2550 multi-channel transient recorder. The transient recorder was actuated by an optical trigger mounted on the end of the inlet camshaft whose trigger position corresponded to TDC of number 1 cylinder during combustion. The recorder operated on an external time-

base, which was generated by an encoder, coupled to the end of the crankshaft. This generated signals at 2° intervals. The digitised signals captured by the transient recorder were then transferred to a PC for processing. The pressure histories recorded were averaged over 20 cycles. This is less than an ideal sample (≥ 50 cycles) but was limited by the data acquisition equipment available. Therefore the standard deviation of the test data at each measurement point was also calculated to investigate if a limited sample size significantly affected the accuracy of the average measured pressure trace. This is discussed further in Section 3.4.1.

The signals generated by the piezo-electric transducers have to be referenced to a mean measured pressure at the same location and also have to be adjusted to the same reference pressure as the ambient pressure changes during the tests. The measured dynamic pressure was therefore modified as follows:

$$p'_{\varphi} = p_{\varphi} + (p_a + \Delta p) \qquad \varphi = 0 \ldots 720° \qquad (3.4)$$

where:

p'_{ϕ} = Corrected value of instantaneous pressure (N/m^2)

p_{ϕ} = Recorded dynamic pressure value (N/m^2)

p_a = Standard atmospheric pressure (=101325 N/m^2)

Δp = Difference between mean manifold pressure at transducer location and ambient pressure during test (N/m^2)

Mean pressure measurements of the exhaust and intake systems were made using Druck type 3800-K transducers and readouts. The pressure drop across the viscous air

flow meter and the pressure at its exit were measured using paraffin U-tube manometers.

3.2.4 Temperature measurement

Temperature measurement throughout the inlet and exhaust systems was made using 1.5 mm NiCr/NiAl thermocouples. Gas temperature measurement thermocouples were positioned using threaded compression glands screwed into welded threaded bosses. It was ensured that each thermocouple tip was located as close to the centreline of the pipe as possible. Surface temperature thermocouples were located using thin gauge, steel screw clips.

3.2.5 Test exhaust systems

The exhaust systems tested were manufactured by Arvin Exhaust Ltd. and were designed as modular, thin-walled, tubular systems. The principal dimensions of the baseline system and the locations of the various transducers are shown in Figure 3.11. This baseline system differs only slightly from the standard Rover supplied system. The primary pipes are slightly longer and the main silencer is a low pressure loss item, usually supplied with the 1.8 litre version of the engine. The modular system was manufactured to these dimensions to produce the shortest possible primary pipe length, given the manufacturing and physical restrictions of a composite, two-piece, 4-into-2 primary manifold. The exhaust exit is coupled to an induced draught exhaust extract system. The coupling to the extract remained open to atmosphere maintaining the exhaust exit at the ambient atmospheric pressure. This ensured that gas dynamic effects resulting from the additional extract pipe length were not imposed on the exhaust system.

The modular construction of all the test systems, utilising common flange dimensions for all components downstream of the primary manifolds, allowed rapid installation and testing of different systems. The systems tested included 4:1 and 4:2:1 configuration systems, each with various pipe lengths, pipe diameters, locations of catalyst(s) and configurations of catalyst(s). Tables 3.2 and 3.3 detail the configuration and overall principal dimensions of each of the systems tested and should be referenced to Figures 3.12 to 3.14, which show the locations to which the tabled dimensions apply. Transducer locations for each of the test systems were generally as the baseline test system shown in Figure 3.11. Junctions and catalyst dimensions are common throughout all of the test systems and transducers are dimensioned from upstream or downstream component flanges as applicable. These dimensions apply to all of the test systems, regardless of the overall pipe dimensions.

3.3 TEST PROCEDURE

Before each test the atmospheric pressure and dry and wet bulb temperatures were noted. The engine was then fully warmed up at WOT before any measurements were recorded.

When the operational temperatures were reached the A/F ratio was adjusted, using the A/F control system detailed in Section 3.2.1, so as to give optimum torque. This always corresponded to an A/F ratio of approximately 12.5:1, the optimum ratio for full load enrichment. For each exhaust build, data were recorded at speeds from 1000 r/min to at least 6000 r/min in approximately 500 r/min increments.

3.4 COMPARISON OF MEASURED AND PREDICTED RESULTS

The test schedule, detailed in Tables 3.2 and 3.3, was designed so as to separate, as far as possible, the effects of individual parameters on measured performance characteristics. Thus, the secondary pipe configuration is varied independently of primary pipe length during tests 1-4 and tests 5-8. Similarly, tests 7-12 fix the secondary pipe length and vary the primary pipe length and the starter catalyst location (if applicable) in a controlled manner. This test strategy is continued with the 4:1 systems tested.

3.4.1 Test 1 - Baseline 4:2:1 system

This is the baseline system against which all other systems were compared throughout the course of this study. Figures 3.15 to 3.17 show comparisons between the measured and predicted airflow, volumetric efficiency and torque characteristics from 1000-6000 r/min. Figure 3.15 shows that, during this test, the air mass flow rate measured by the viscous flow meter and that calculated indirectly from the measured A/F ratio follow closely. The viscous flow meter measurement was considered to be the more accurate of these measurement methods since the A/F ratio meter displayed a time-averaged measurement and also required frequent recalibration. For this first test however, the results indicate that there were no air leaks downstream of the viscous flow meter installation. The A/F ratio based airflow measurement is approximately 0.5% above that of the VFM measurement across the speed range. It would be expected that, because of leakage losses across the piston rings, the exhaust gas flow measurement (A/F ratio based) would be lower than the intake gas flow measurement (VFM based). The results indicate that piston leakage losses were too small for the

A/F ratio based air flow measurement to pick up; the apparent increase in airflow, from intake to exhaust, resulted from the error in the time averaged measurement of A/F ratio. It should be noted that intake and exhaust gas flow measurement on more modern engines should be identical since fresh charge that leaks past the pistons into the crankcase area are recirculated into the intake system to reduce unburned hydrocarbons emissions. The correlation with the predicted airflow is generally good across the speed range. However, the model can be seen to under-predict by some 5% at 6000 r/min. Since, as is shown later in this section, correlation between the measured and predicted inlet and exhaust port pressure histories were very good, the fall off in predicted airflow at high speeds were attributed to a small error in the model valve-flow data. This data was supplied by Rover from their own steady flow tests.

Figure 3.16 shows comparisons between the measured and predicted volumetric efficiency. The measured volumetric efficiency is calculated from both the viscous flow meter and A/F ratio measurements. Since the volumetric efficiency is calculated from a ratio of numbers it is a very sensitive indicator and this explains the apparent difference between the calculated values resulting from each of these measurements. It can be seen that although the model over-predicts the absolute value of volumetric efficiency up to 5500 r/min, where it begins to under-predict as a result of the valve-flow data error, the shape of the predicted curve is good. Mid-range peaks and troughs are captured by the model and the high-speed peak is reasonably well located.

Figure 3.17 shows the comparison between the measured and predicted torque for the baseline system. As with the volumetric efficiency there is a difference between absolute values but the shape of the curve is generally good up to 5500 r/min. The

divergence between the measured and predicted values for both torque and volumetric efficiency at 1000 r/min is partly a consequence of the poor correlation between the measured and predicted inlet and exhaust port pressure histories and is discussed later in this section.

Figures 3.18 to 3.23 show comparisons between the measured and predicted pressure histories immediately downstream of the exhaust valve and Figures 3.24 to 3.29 show comparisons between the measured and predicted pressure histories immediately upstream of the inlet valve. The instantaneous pressure at either of these locations, which define the cylinder flow boundary conditions, have a significant influence on both engine breathing and pumping losses. The measured plots are derived from recorded data over 20 cycles which are then averaged for each crank-angle position. Also shown on these plots are upper and lower bandwidths equal to the recorded mean pressure at that crank-angle position ± 2 standard deviations. These indicate the bands within which most of the measured data lie.

Considering the exhaust port pressure histories first, there are clear discrepancies between the measured and predicted profiles at 1000 r/min. Although the absolute magnitude of the pressure waves is relatively low, a phase difference of some 30°CA is evident and the model predicts some minor features on the profile which do not appear on the measured profile. At speeds from 2000 r/min upwards there is a great improvement in the predicted and measured correlation. Individual traits in the measured profiles are captured by the model and generally phased correctly although the model does sometimes over-predict the wave amplitudes. This over-prediction can be attributed to one of two factors; the equivalent valve areas and/or the cam data

used by the model may be incorrect which would effect the release profile, or there is an over-prediction of the amplitude of a wave travelling towards the exhaust valve. Figure 3.21 shows that at 4000 r/min the model predicts an excessively high release pressure at the exhaust port at the point of EVO. If such a profile resulted from an error in the valve and cam data, it is unlikely that the predicted pressure histories at other speeds would bear any resemblance to the measured histories during this period. Thus, the over prediction of wave amplitude is most likely caused by incorrect prediction of the amplitude of incident waves at the exhaust port. Correct wave amplitude and phasing prediction can only be achieved with knowledge of the temperature gradient along the system, and any errors resulting from the use of the homentropic model may be further magnified when modelling long exhaust systems.

As the speed increases it can be observed that the 2 standard deviations bandwidth increases, particularly during the blowdown process. This indicates an increasing cycle-to-cycle variation of the release pressure as the cylinder exhausts into the manifold which results primarily from the turbulent nature of the combustion process. The variation during the blowdown phase of measured data would still be observed if the sample size was increased above 20 cycles. The cycle-to-cycle variation accounts for the irregular nature of some of the measured pressure plots; these small irregularities are not manifold tuning effects. The consistency of the data recorded over the remainder of the cycle indicates that accurate pressure data could be captured over 20 cycles.

Figures 3.24 to 3.29 show that, with the exception of 1000 r/min, good agreement is shown between the measured and the predicted pressure histories immediately

upstream of the inlet valve although, as with the exhaust valve pressure histories, the model occasionally over-predicts the wave amplitude. There are two possible reasons for the poor low-speed pressure history correlation. Firstly the engine is not particularly stable running at such low speeds at WOT. Also, at low speeds, the volumetric efficiency is largely governed by the wave action throughout the entire intake system, including those components upstream of the plenum such as the filter and the throttle housing. Both models assume one-dimensional, compressible flow but in reality the filter used for this test engine is a complex shape that is difficult to model one-dimensionally with accuracy. The shortfalls of this filter model are inconsequential as the speed increases and the inlet tract pressure history becomes primarily influenced by the primary pipe and plenum wave action only.

Figures 3.30 to 3.32 show examples of measured and predicted pressure histories immediately downstream of the primary-secondary pipe junction. Most of the features of the pressure profile have been well captured by the model, although a small phasing error is apparent at 2000 r/min. At 6000 r/min there is a small offset between measured and predicted histories, which results from the use of the homentropic model and is caused by too high a selection of the mean exhaust system pressure. Figures 3.33 to 3.38 show examples of measured and predicted pressure histories immediately upstream and downstream of the catalytic; good agreement is similarly shown between both sets of results.

Since the measured and predicted exhaust and inlet port pressure histories are generally in good agreement, the discrepancy between the absolute values of measured and predicted torque and volumetric efficiency can be attributed to the model in-

cylinder calculation. The curve shapes, however, are well predicted and therefore, to aid with the analysis of other systems, the measured and predicted torque, airflow and volumetric efficiency are plotted relative to these baseline system results.

3.4.2 Tests 2 to 12 – 4:2:1 systems

Figures 3.39 to 3.60 show comparisons of the measured and predicted torque and volumetric efficiency for all of the 4:2:1 exhaust system tests relative to the baseline test system (test 1). The model generally correctly identifies tuned and untuned speeds for each system configuration tested. Figure 3.5 shows that repeated torque and airflow measurements fall within approximately a ±2.0% tolerance bandwidth across the speed range. Thus, correlation between relative measured and predicted effect amplitudes is also shown to be good. Figure 3.53 and 3.54 show an apparently spurious result at 1500 r/min. This is due to engine instability running at WOT at low engine speeds and the associated difficulty measuring accurate test data. It is not a failure of the model to identify a tuning characteristic of this particular exhaust build.

3.4.3 Tests 13 to 24 – 4:1 systems

Figures 3.61 to 3.84 show comparisons of the measured and predicted torque and volumetric efficiency for all of the 4:1 exhaust system tests relative to the baseline test system (test 1). As with the 4:2:1 system tests, generally good correlation is shown between both results sets. Performance trends are captured by the model, although, as with tests 2 to 12, the measured data bandwidth causes some straddling of the predicted data trend which is apparent in the results for tests 17, 19, 20 and 23.

Correlation between measured and predicted performance indicators and dynamic pressure histories was generally good for all of the systems tested. Specifically, for this study, the homentropic model was able to correctly predict the relative changes to engine performance characteristics when the exhaust system geometry was modified. The validated model was then used as a research tool to investigate the relationship between exhaust system geometry and engine breathing characteristics. The investigation of these relationships is detailed in the following chapters.

Table 3.2 Principal dimensions of 4:2:1 exhaust systems tested

System description	A	B	C	D	Starter Catalyst
Test 1 - baseline	389	760	-	481	-
2	389	306	-	935	-
3	389	574	-	667	-
4	389	574	182	667	Type 1
5	1234	574	182	667	Type 2
6	1234	574	-	667	-
7	1234	1023	636	667	Type 1 - downstream
8	1234	1023	182	667	Type 1 - upstream
9	389	1023	182	667	Type 1 - upstream
10	389	1023	182	667	Type 2 - upstream
11	389	1023	636	667	Type 1 - downstream
12	389	1023	-	667	-

Table 3.3 Principal dimensions of 4:1 exhaust systems tested

System description	A	B	C	D
Test 13	235	35	150	1606
14	235	35	1425	312
15	235	32	150	1587
16	235	32	1425	312
17	516	32	1425	312
18	516	32	150	1587
19	516	35	150	1587
20	516	35	1425	312
21	796	35	1425	312
22	796	35	150	1587
23	796	32	150	1587
24	796	32	1425	312

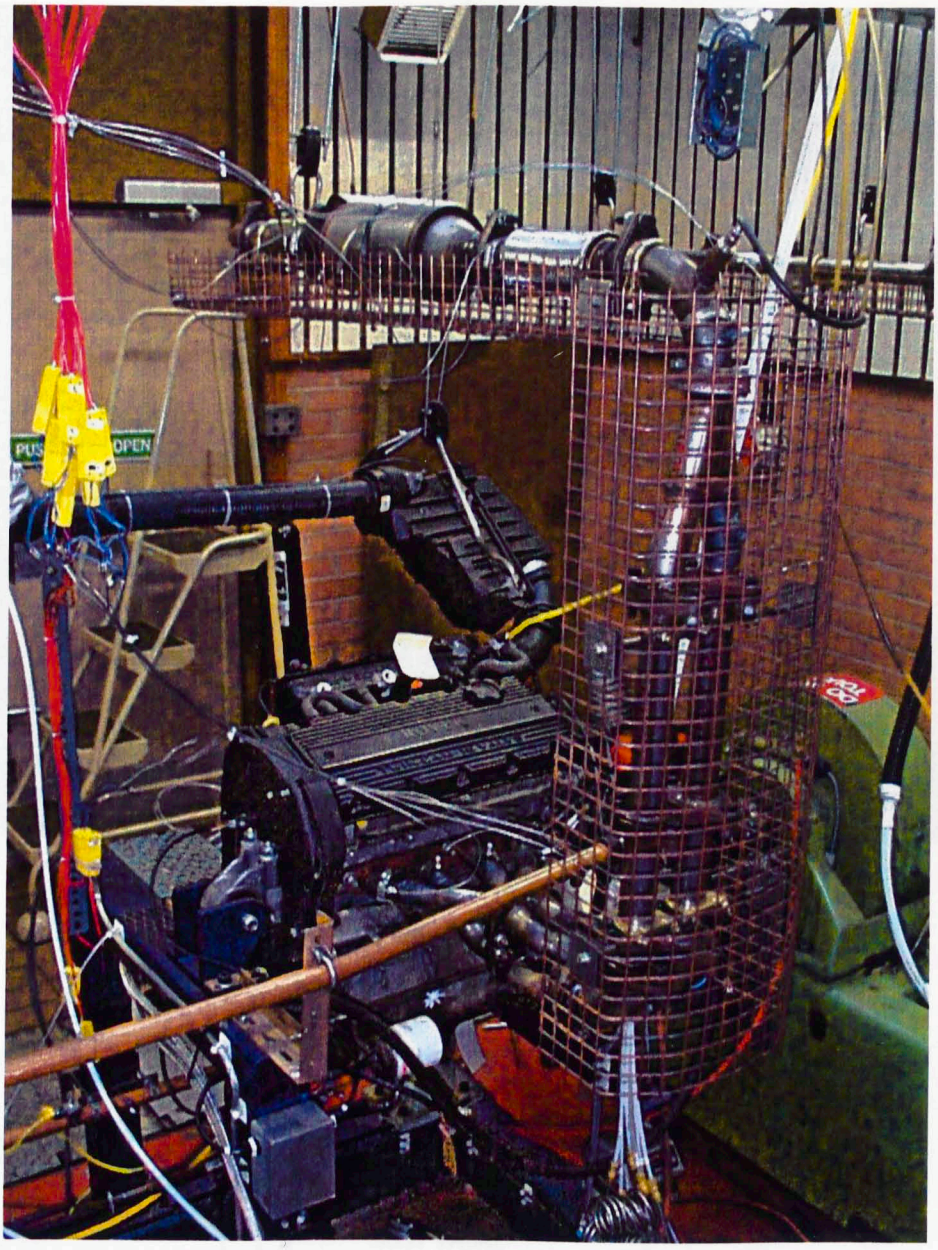

Figure 3.1 Rover 1400 cc 16 valve K series engine test cell installation

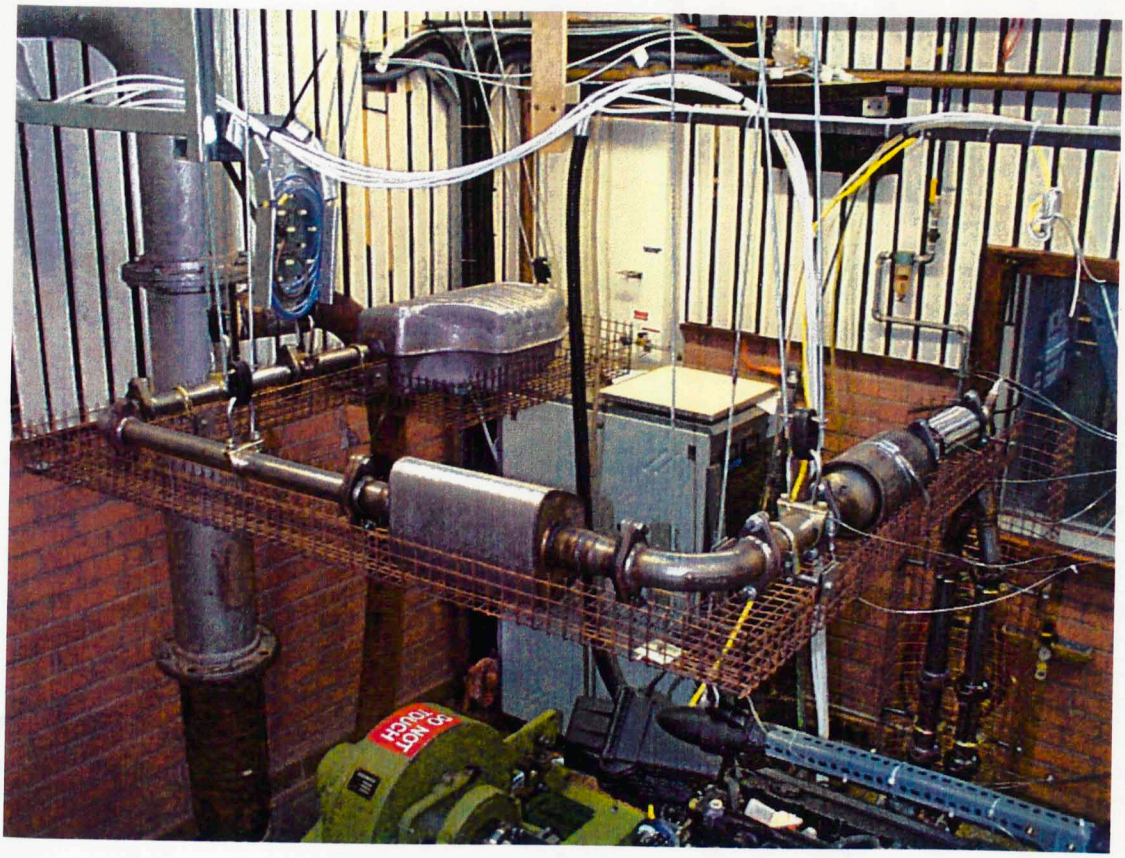

Figure 3.2 Rover 1400 cc 16 valve K series engine test cell installation showing exhaust system

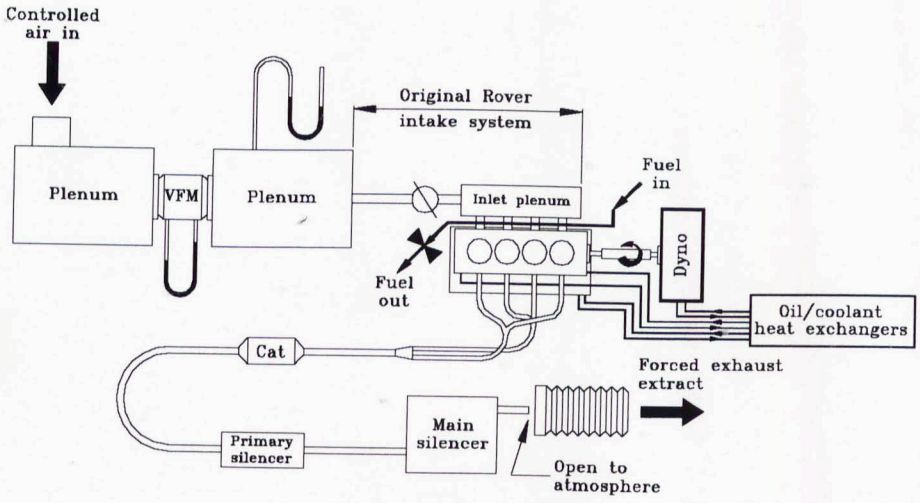

Figure 3.3 Test facility layout

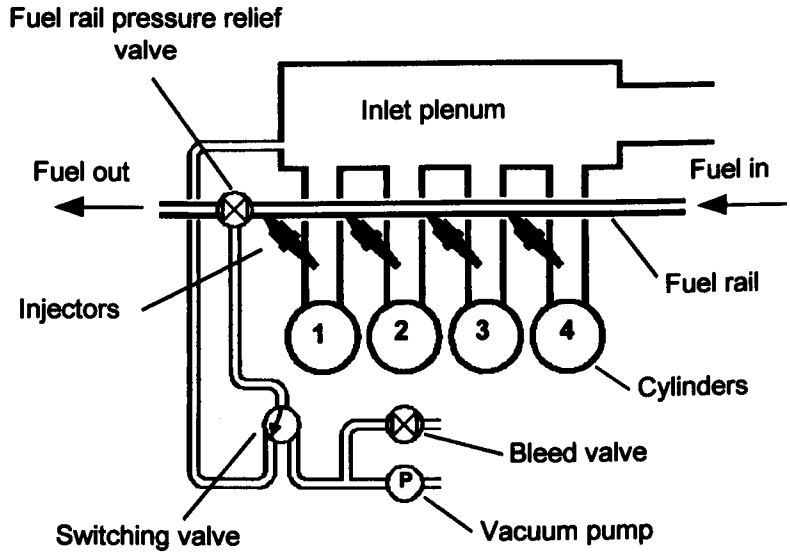

Figure 3.4 Fuel control system layout

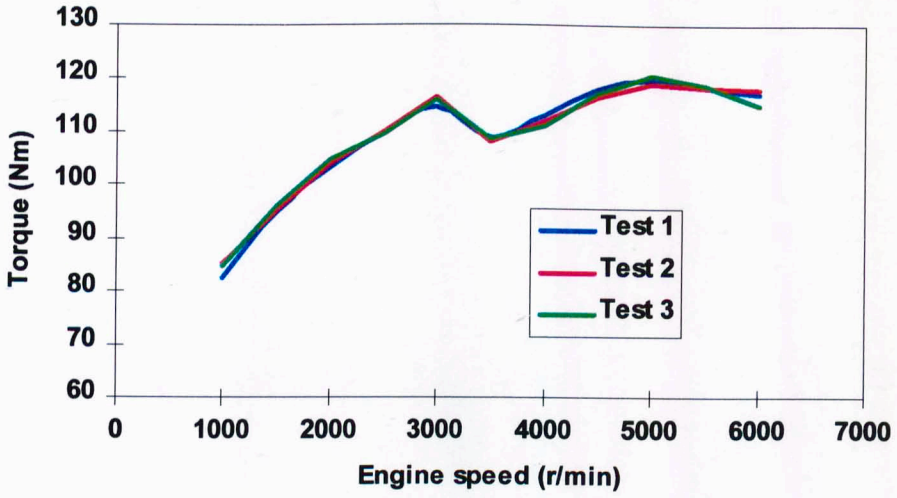

Figure 3.5 Repeatability of measured corrected torque

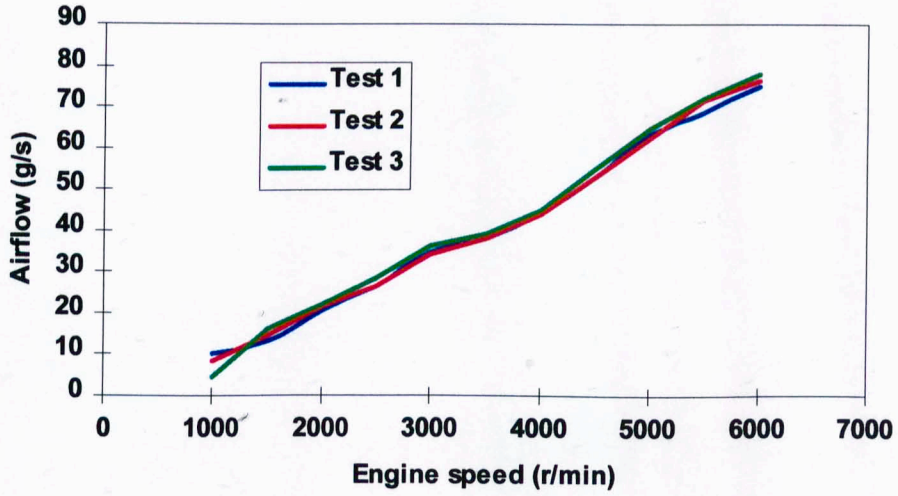

Figure 3.6 Repeatability of measured corrected airflow

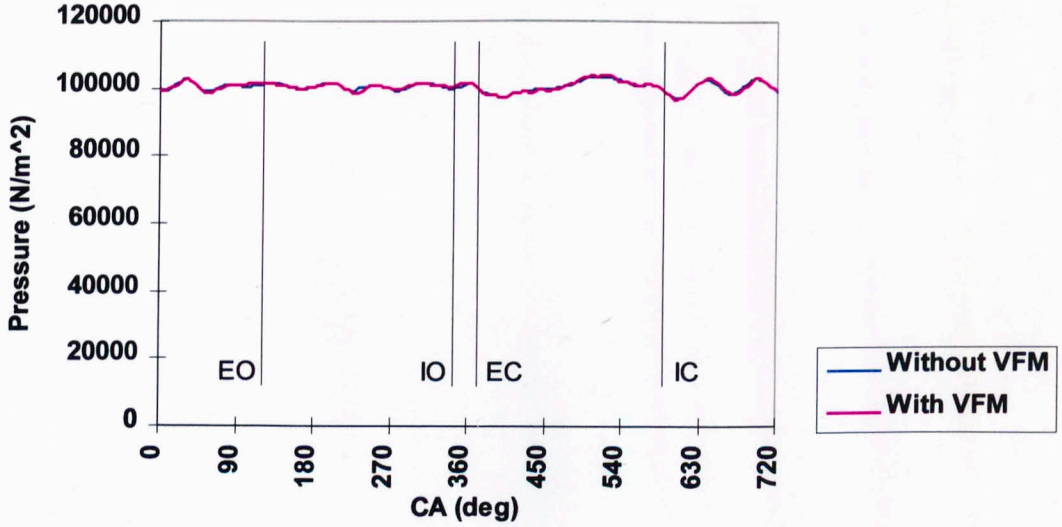

Figure 3.7 Measured inlet port pressure histories with and without viscous airflow meter installed at 2000 r/min

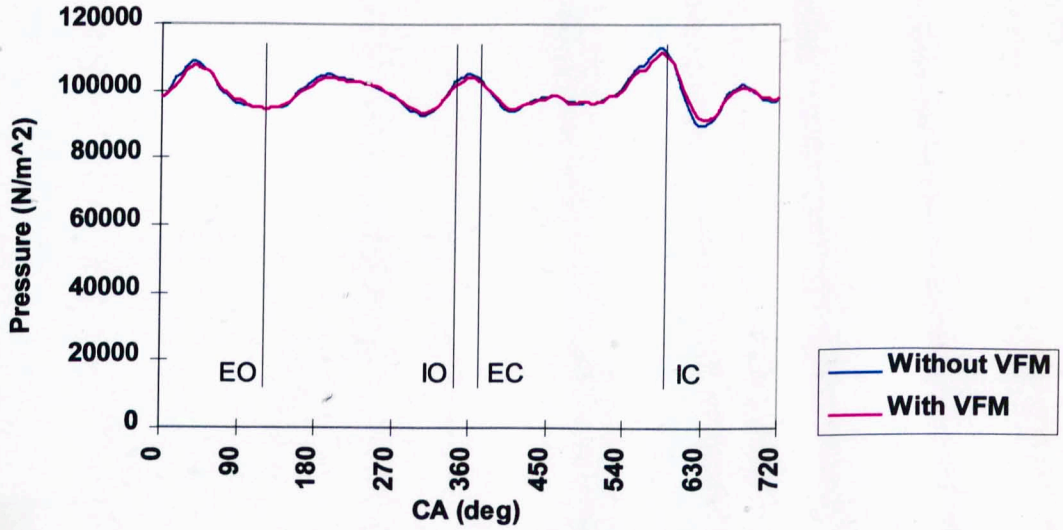

Figure 3.8 Measured inlet port pressure histories with and without viscous airflow meter installed at 3000 r/min

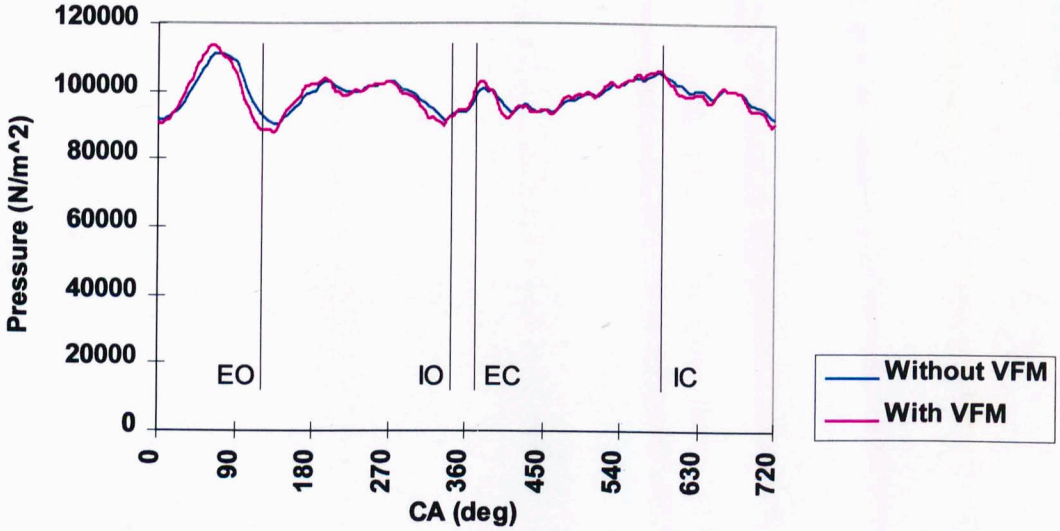

Figure 3.9 Measured inlet port pressure histories with and without viscous airflow meter installed at 4000 r/min

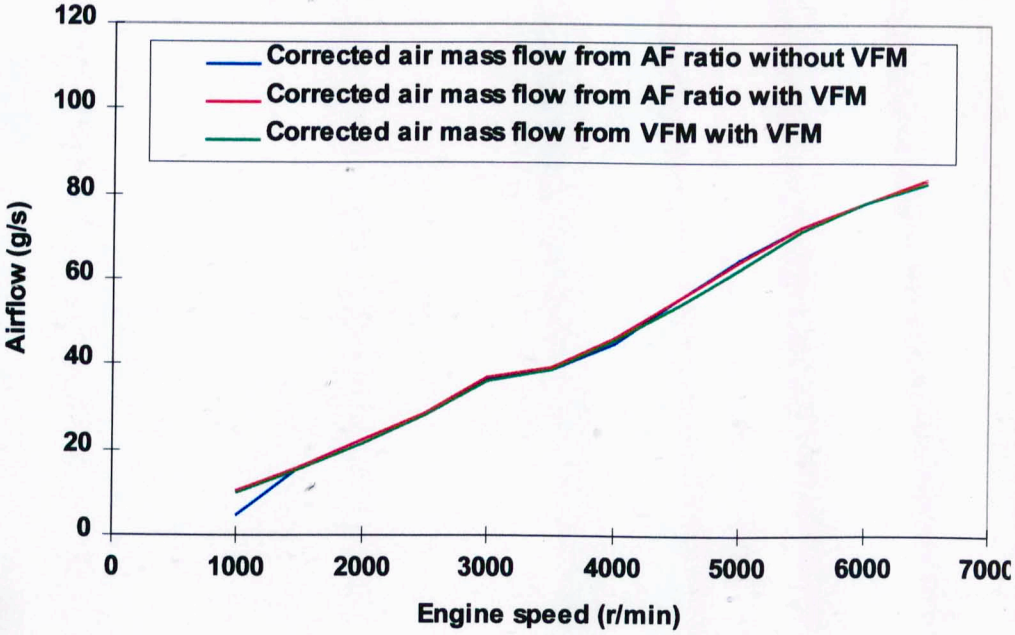

Figure 3.10 Measured corrected airflow with and without viscous airflow meter installed

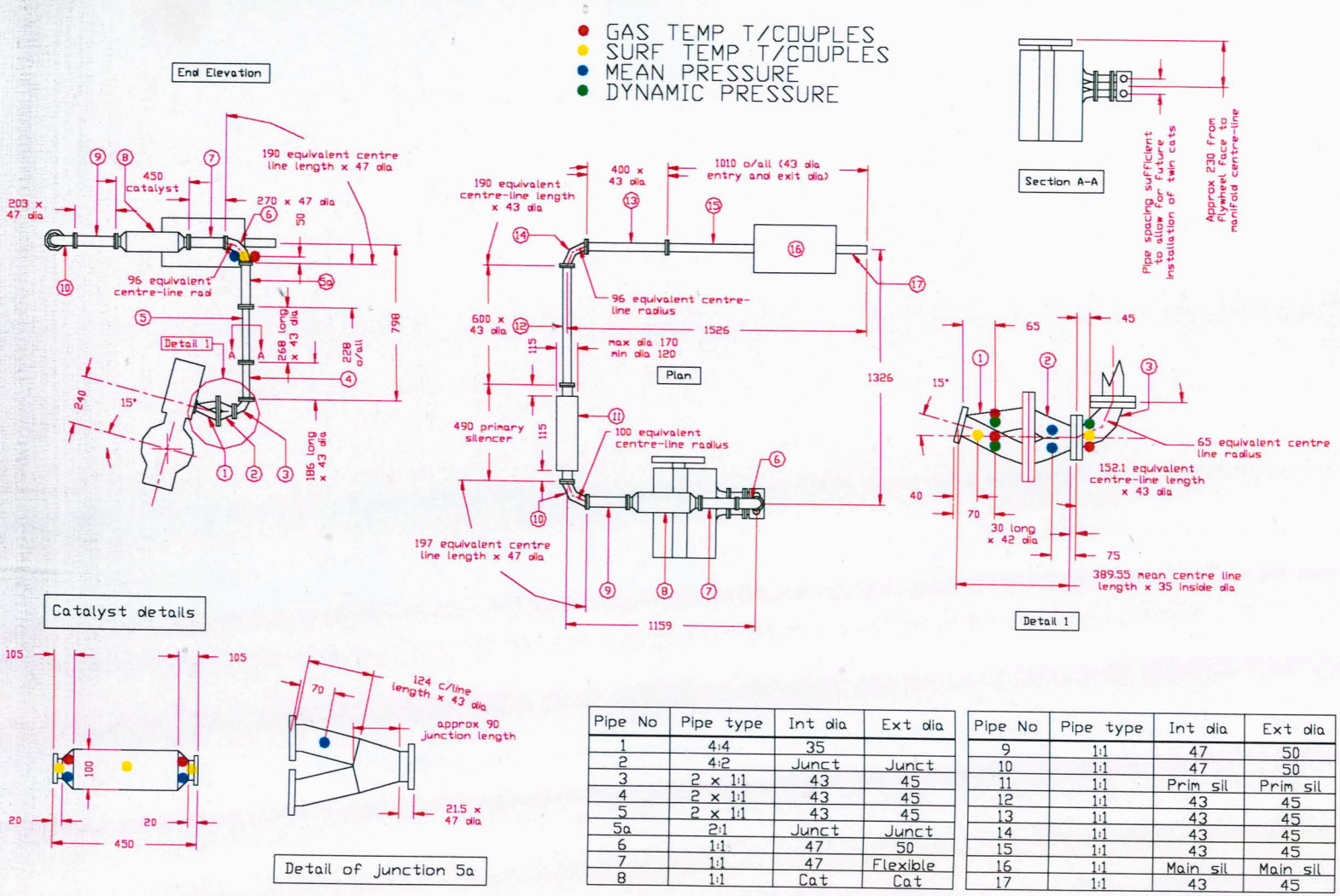

Pipe No	Pipe type	Int dia	Ext dia
1	4:4	35	
2	4:2	Junct	Junct
3	2 x 1:1	43	45
4	2 x 1:1	43	45
5	2 x 1:1	43	45
5a	2:1	Junct	Junct
6	1:1	47	50
7	1:1	47	Flexible
8	1:1	Cat	Cat

Pipe No	Pipe type	Int dia	Ext dia
9	1:1	47	50
10	1:1	47	50
11	1:1	Prim sil	Prim sil
12	1:1	43	45
13	1:1	43	45
14	1:1	43	45
15	1:1	43	45
16	1:1	Main sil	Main sil
17	1:1	43	45

Figure 3.11 Baseline exhaust system (system 1) dimensions and transducer locations

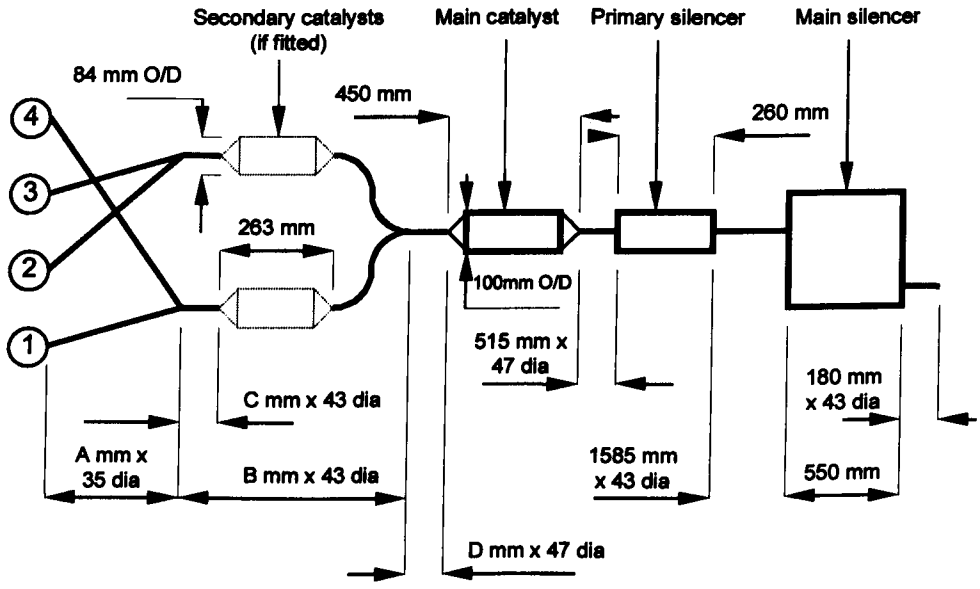

Figure 3.12 General configuration of 4:2:1 systems tested

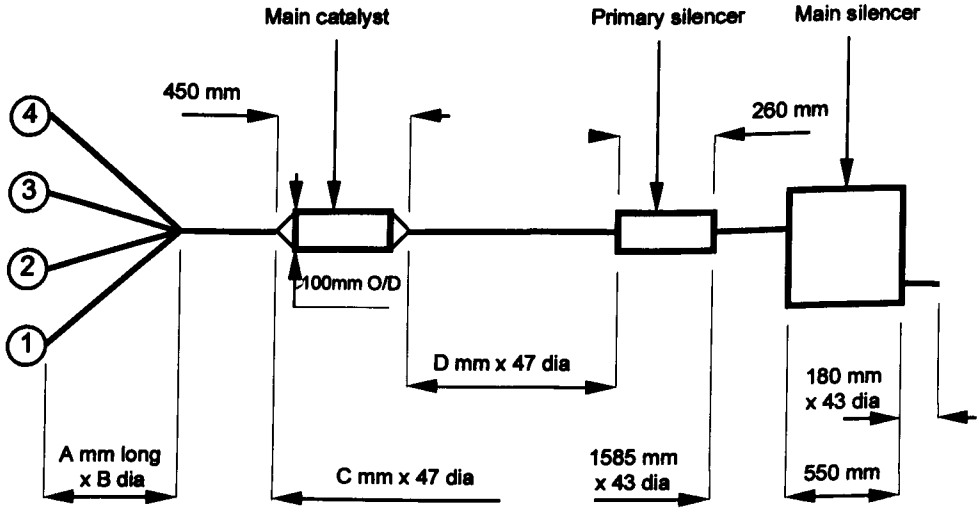

Figure 3.13 General configuration of 4:1 systems tested

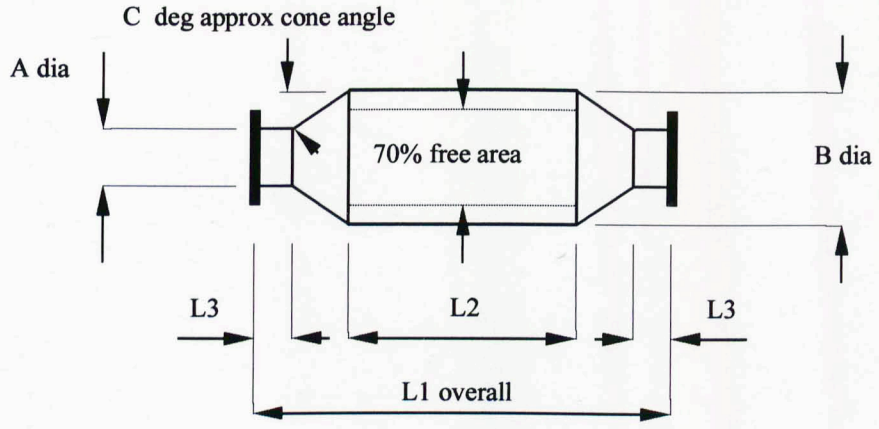

		A	B	C	L1	L2	L3
Main catalyst		47	100	17.3	450	240	20
Starter catalyst (type 1)	43	84	46	263	113.5	55	
Starter catalyst (type 2)	43	84	23.6	263	113.5	28	

Figure 3.14 General configuration of starter and main catalysts tested

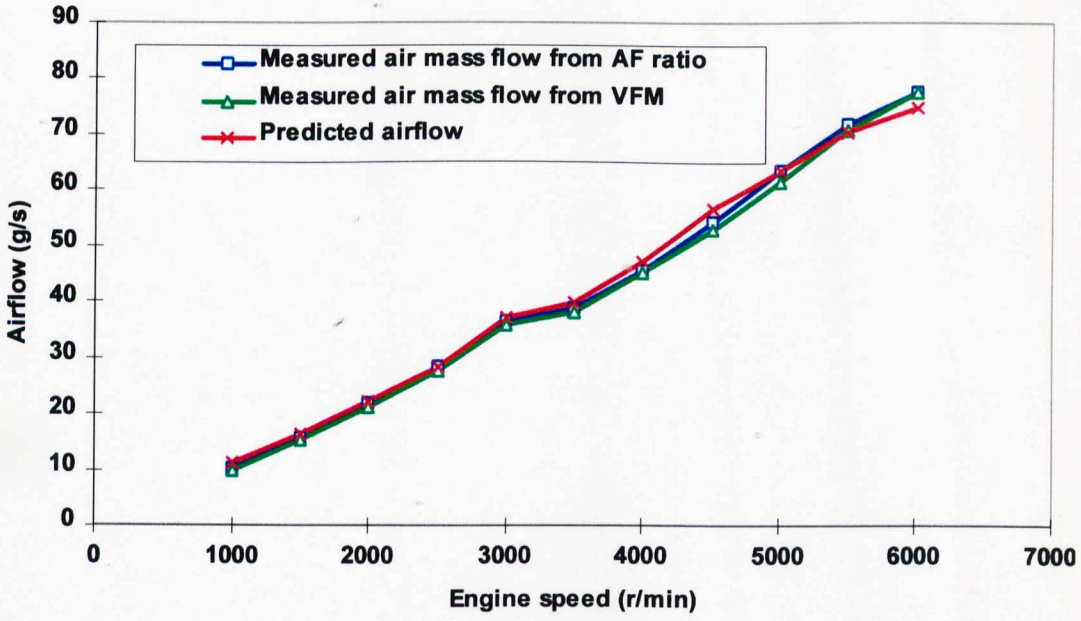

Figure 3.15 Test 1 - comparisons of measured and predicted airflow

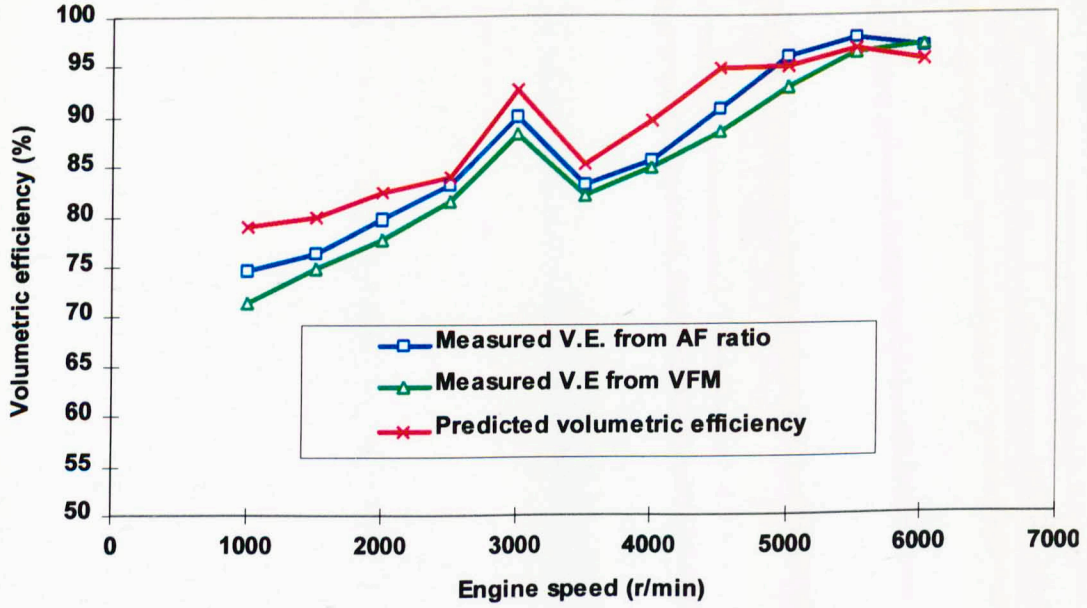

Figure 3.16 Test 1 - comparisons of measured and predicted volumetric efficiency

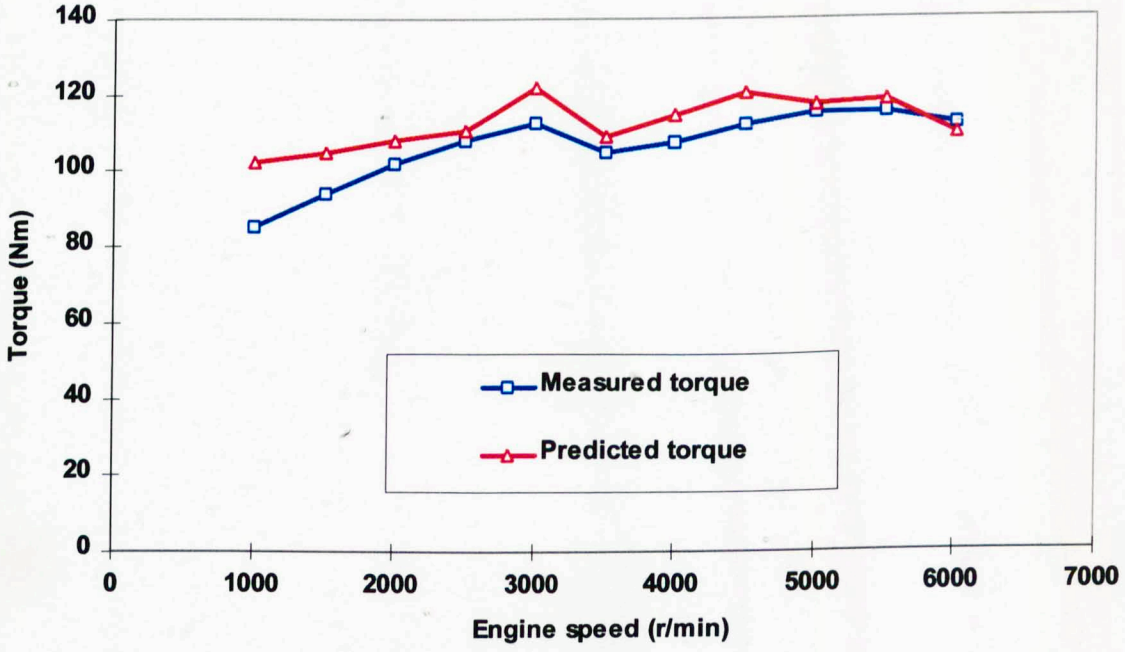

Figure 3.17 Test 1 - comparisons of measured and predicted torque

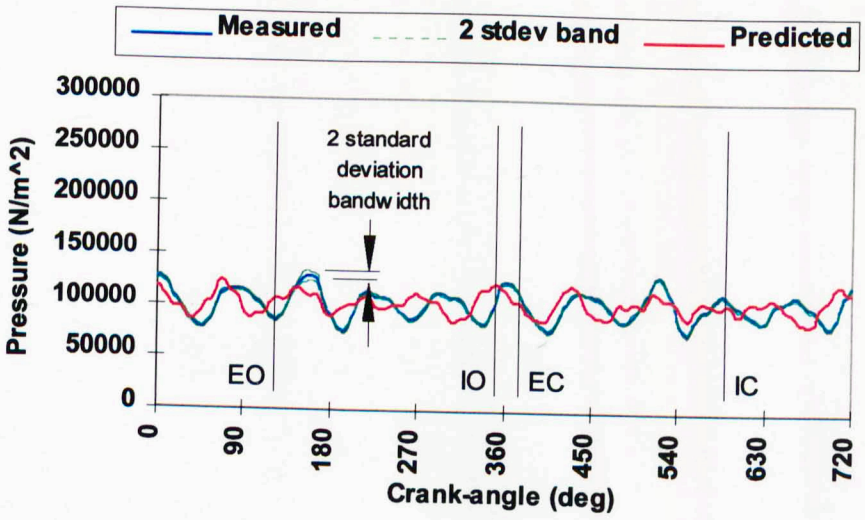

Figure 3.18 Test 1 - comparisons of measured and predicted exhaust port pressure histories at 1000 r/min

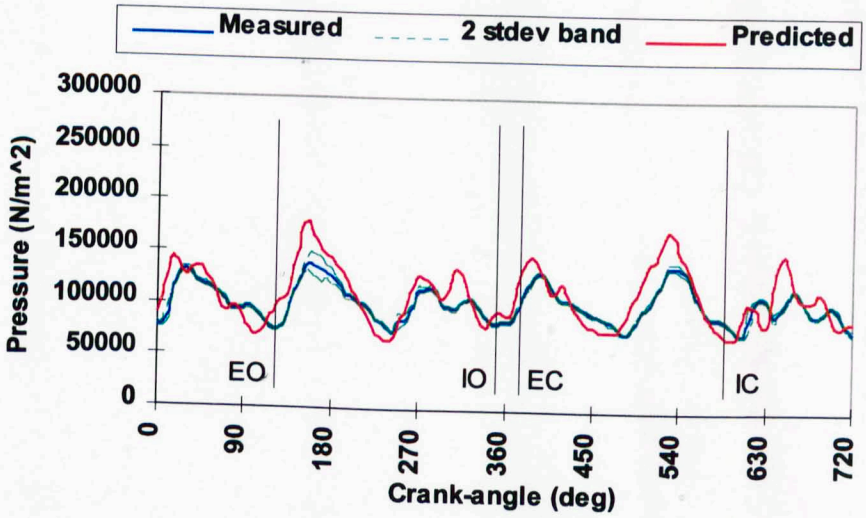

Figure 3.19 Test 1 - comparisons of measured and predicted exhaust port pressure histories at 2000 r/min

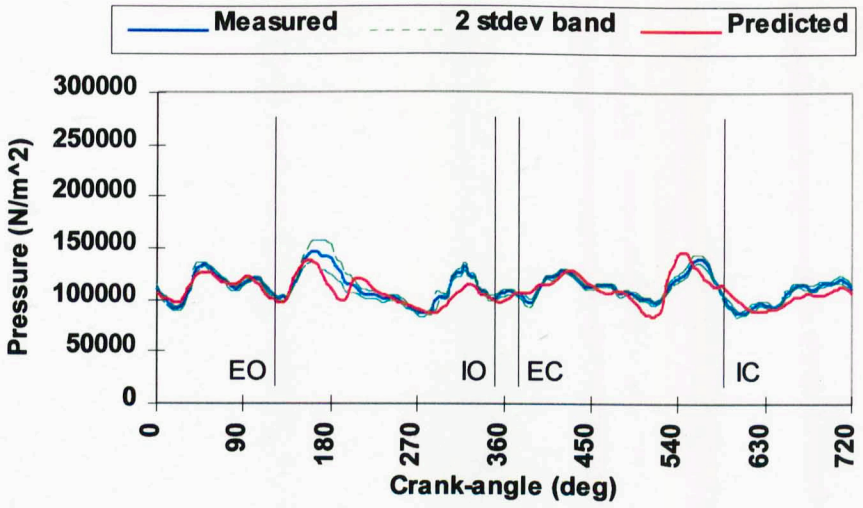

Figure 3.20 Test 1 - comparisons of measured and predicted exhaust port pressure histories at 3000 r/min

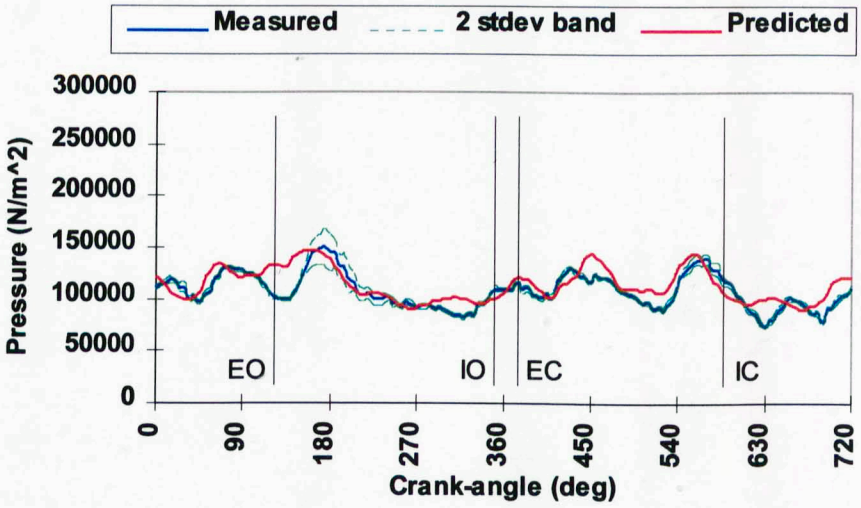

Figure 3.21 Test 1 - comparisons of measured and predicted exhaust port pressure histories at 4000 r/min

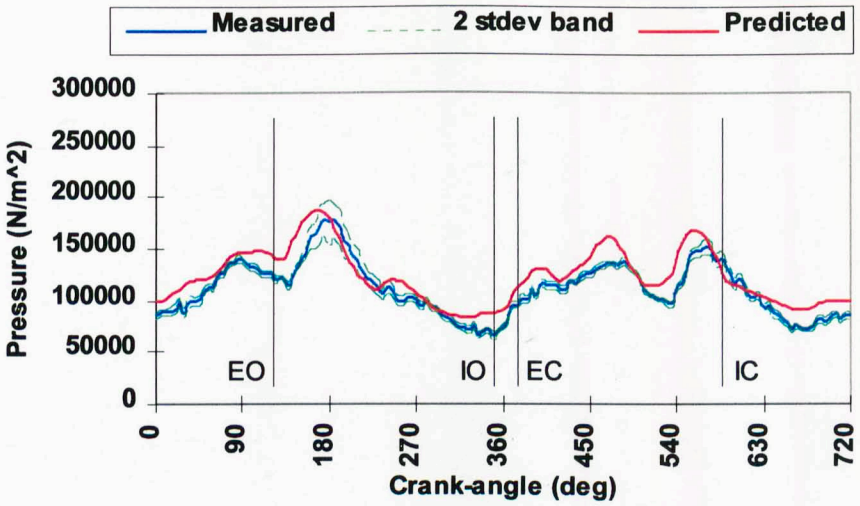

Figure 3.22 Test 1 - comparisons of measured and predicted exhaust port pressure histories at 5000 r/min

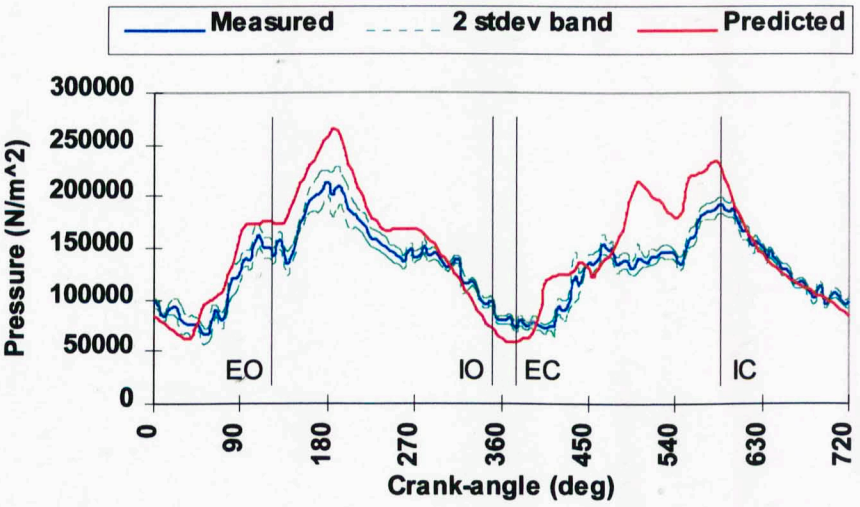

Figure 3.23 Test 1 - comparisons of measured and predicted exhaust port pressure histories at 6000 r/min

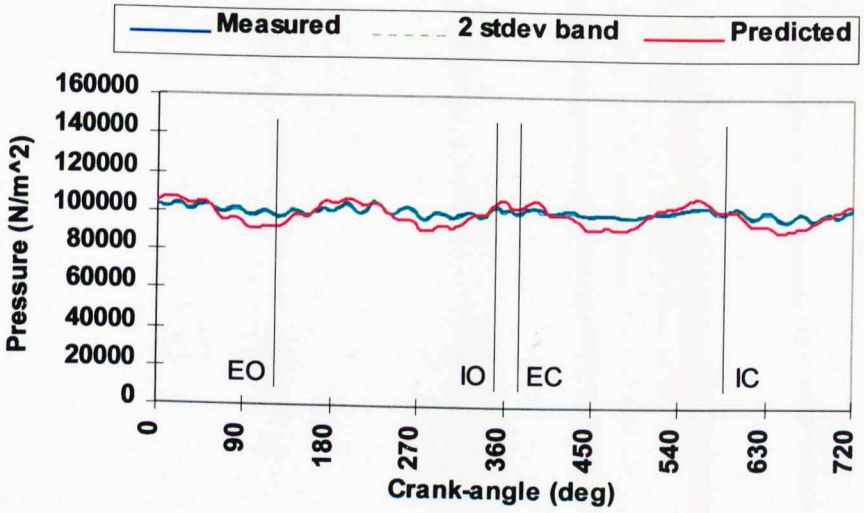

Figure 3.24 Test 1 - comparisons of measured and predicted inlet port pressure histories at 1000 r/min

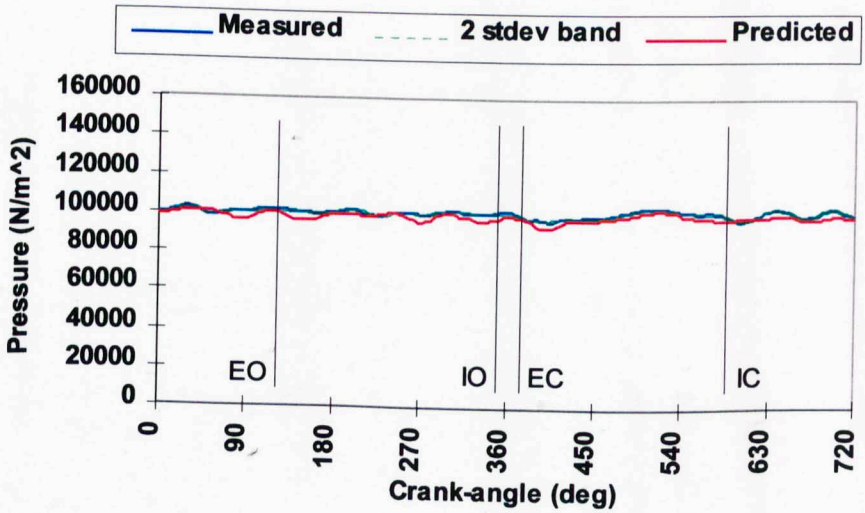

Figure 3.25 Test 1 - comparisons of measured and predicted inlet port pressure histories at 2000 r/min

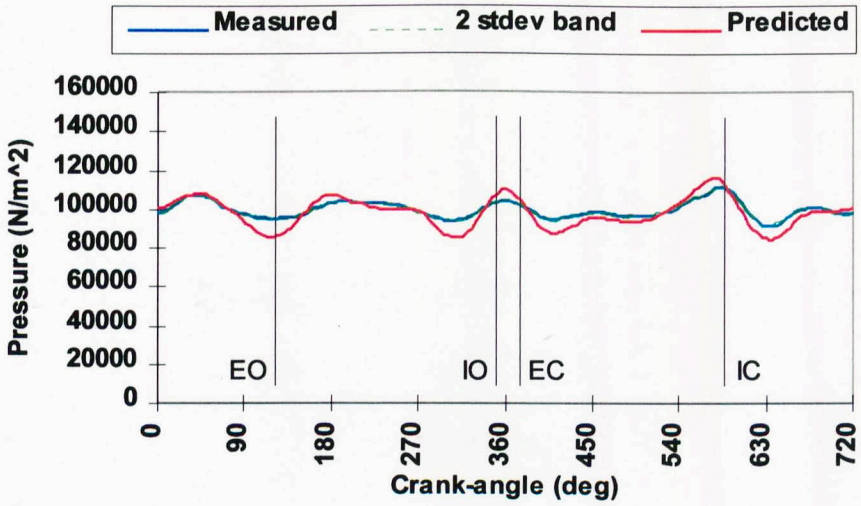

Figure 3.26 Test 1 - comparisons of measured and predicted inlet port pressure histories at 3000 r/min

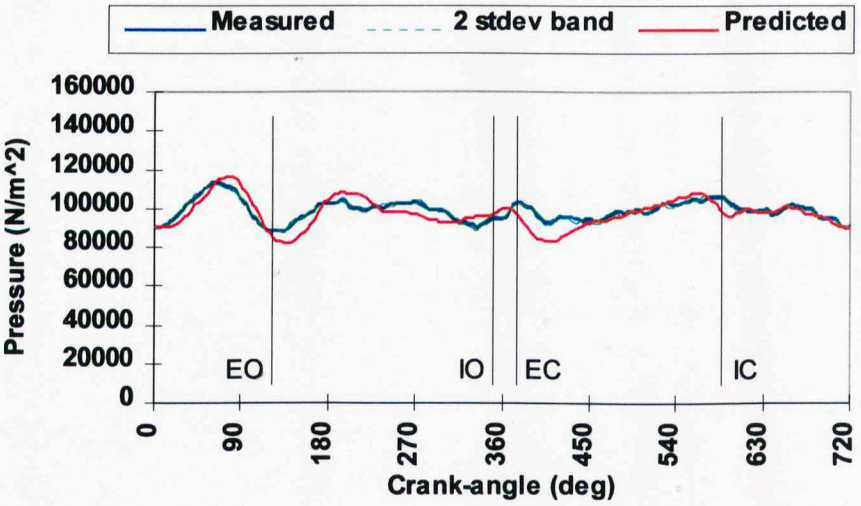

Figure 3.27 Test 1 - comparisons of measured and predicted inlet port pressure histories at 4000 r/min

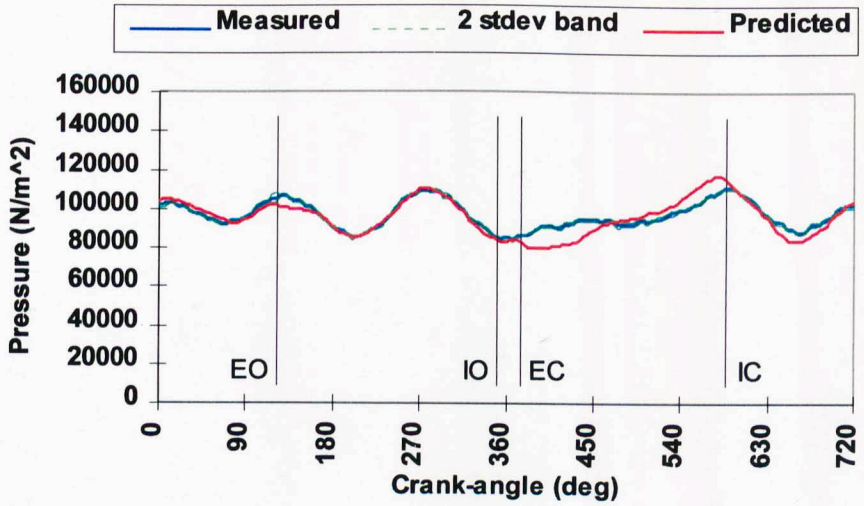

Figure 3.28 Test 1 - comparisons of measured and predicted inlet port pressure histories at 5000 r/min

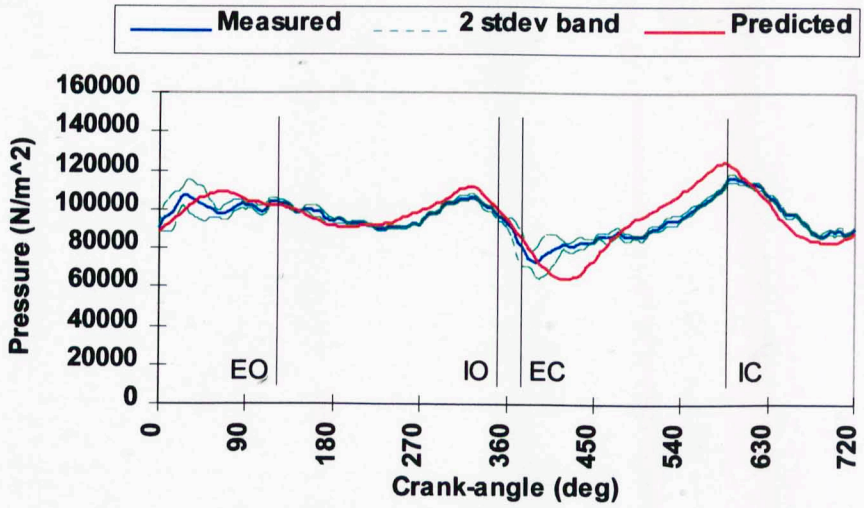

Figure 3.29 Test 1 - comparisons of measured and predicted inlet port pressure histories at 6000 r/min

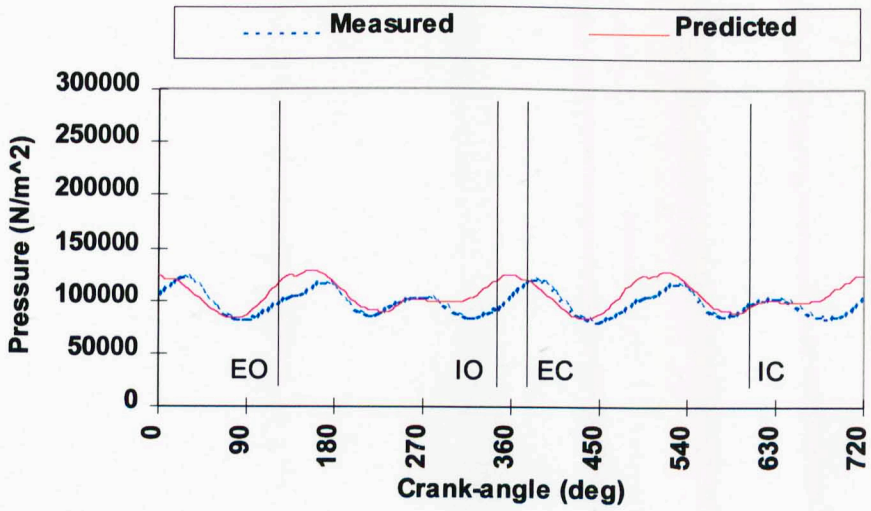

Figure 3.30 Test 1 - comparisons of measured and predicted downstream primary-secondary junction pressure histories at 2000 r/min

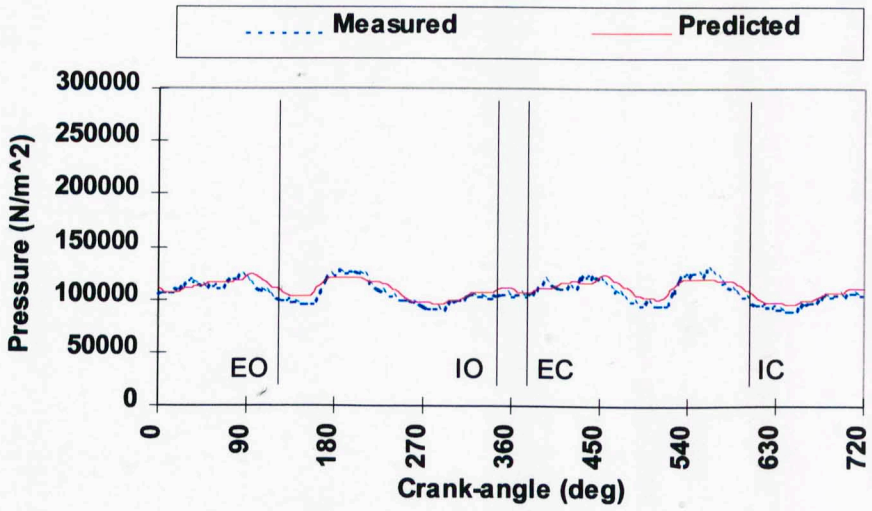

Figure 3.31 Test 1 - comparisons of measured and predicted downstream primary-secondary junction pressure histories at 4000 r/min

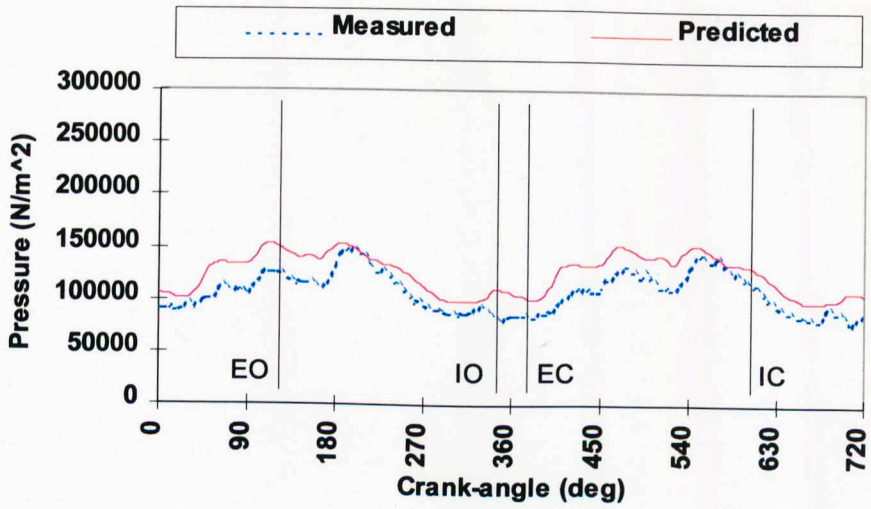

Figure 3.32 Test 1 - comparisons of measured and predicted downstream primary-secondary junction pressure histories at 6000 r/min

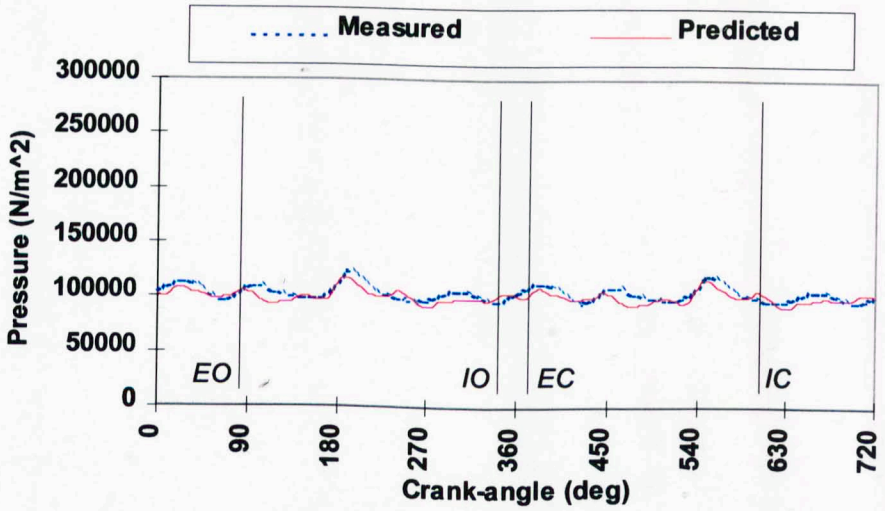

Figure 3.33 Test 1 - comparisons of measured and predicted upstream catalyst pressure histories at 2000 r/min

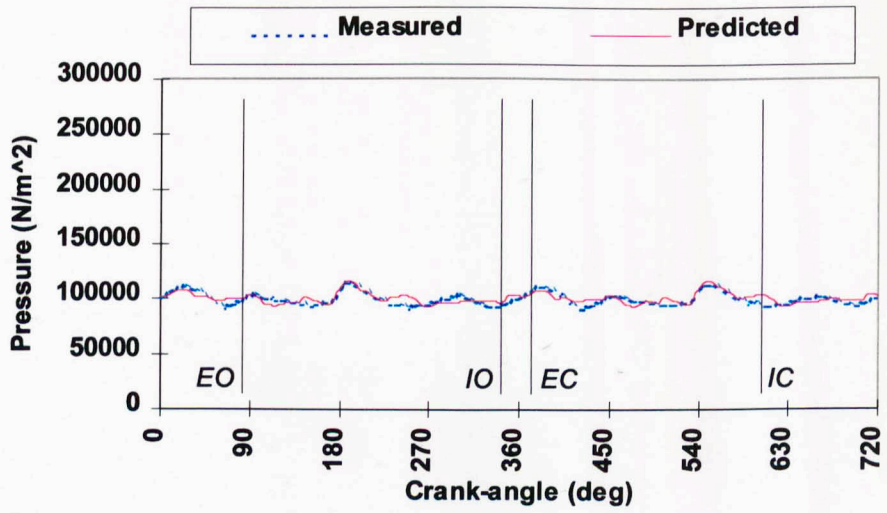

Figure 3.34 Test 1 - comparisons of measured and predicted downstream catalyst pressure histories at 2000 r/min

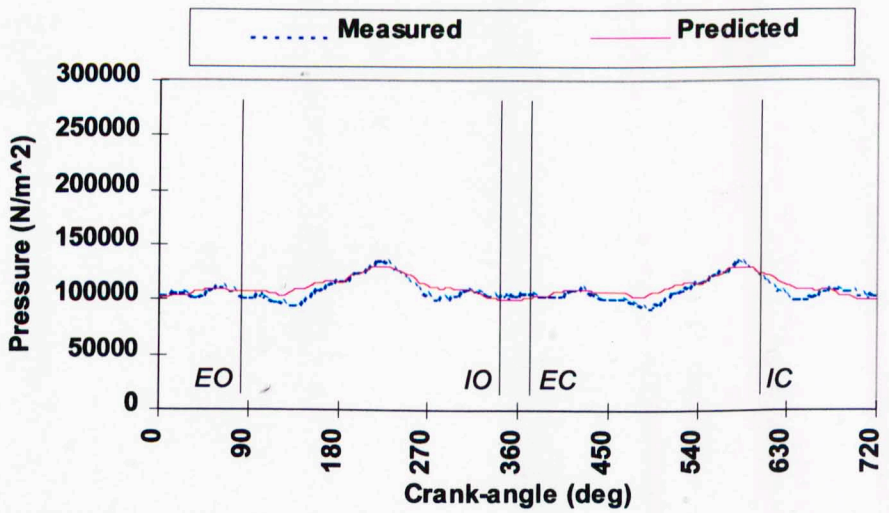

Figure 3.35 Test 1 - comparisons of measured and predicted upstream catalyst pressure histories at 4000 r/min

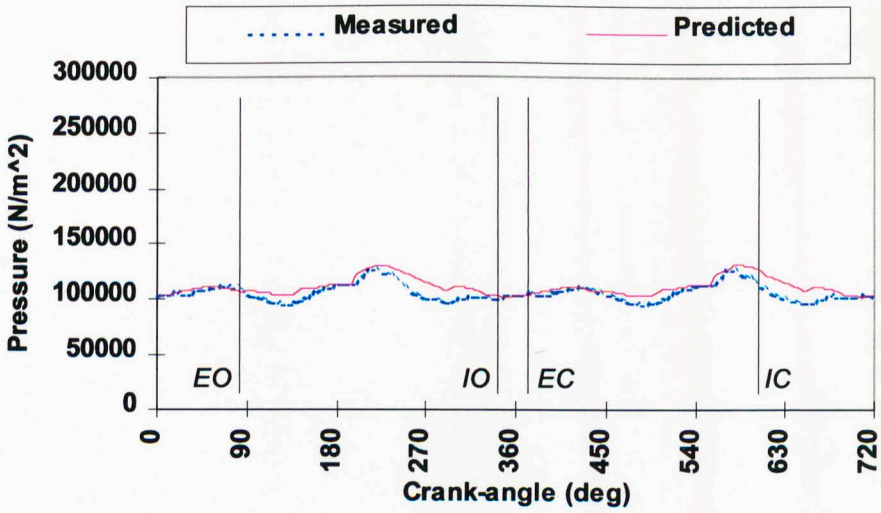

Figure 3.36 Test 1 - comparisons of measured and predicted downstream catalyst pressure histories at 4000 r/min

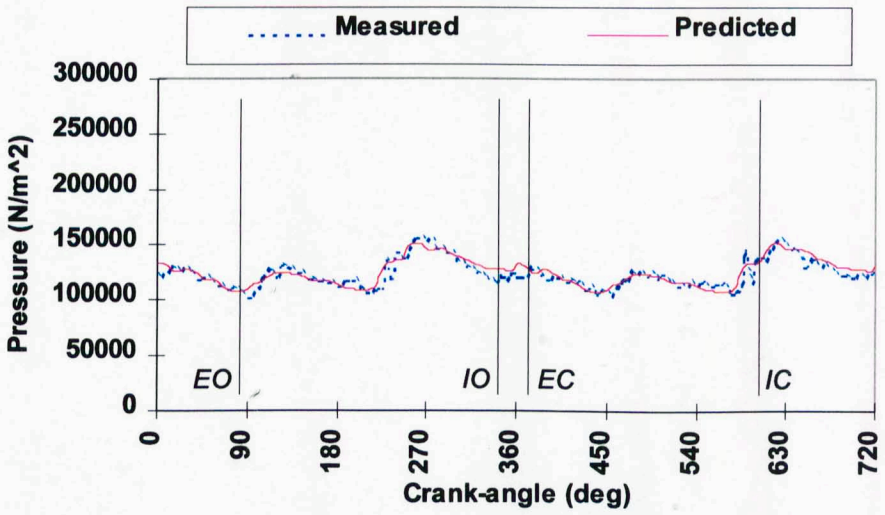

Figure 3.37 Test 1 - comparisons of measured and predicted upstream catalyst pressure histories at 6000 r/min

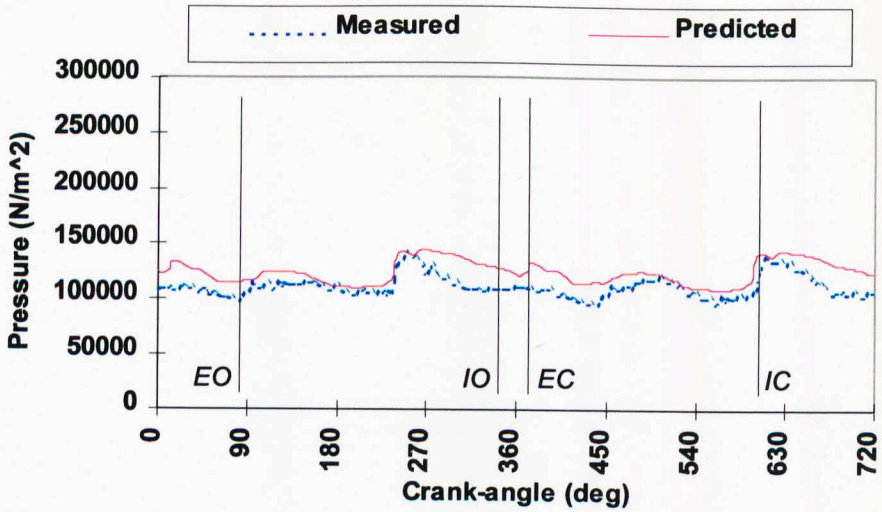

Figure 3.38 Test 1 - comparisons of measured and predicted downstream catalyst pressure histories at 6000 r/min

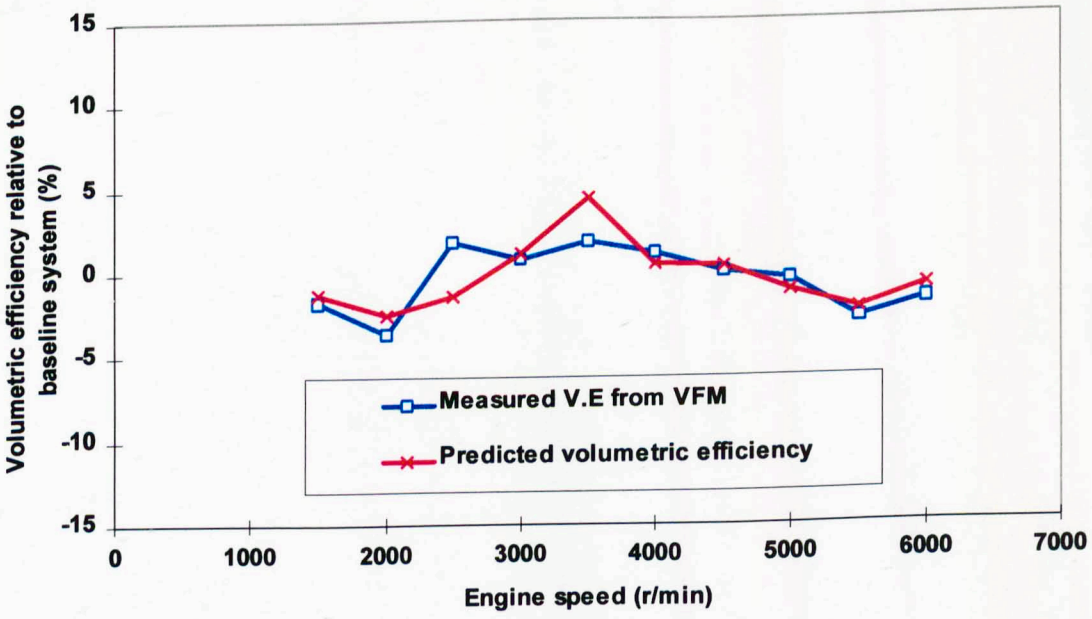

Figure 3.39 Comparisons of measured and predicted volumetric efficiency system test 2 relative to baseline system

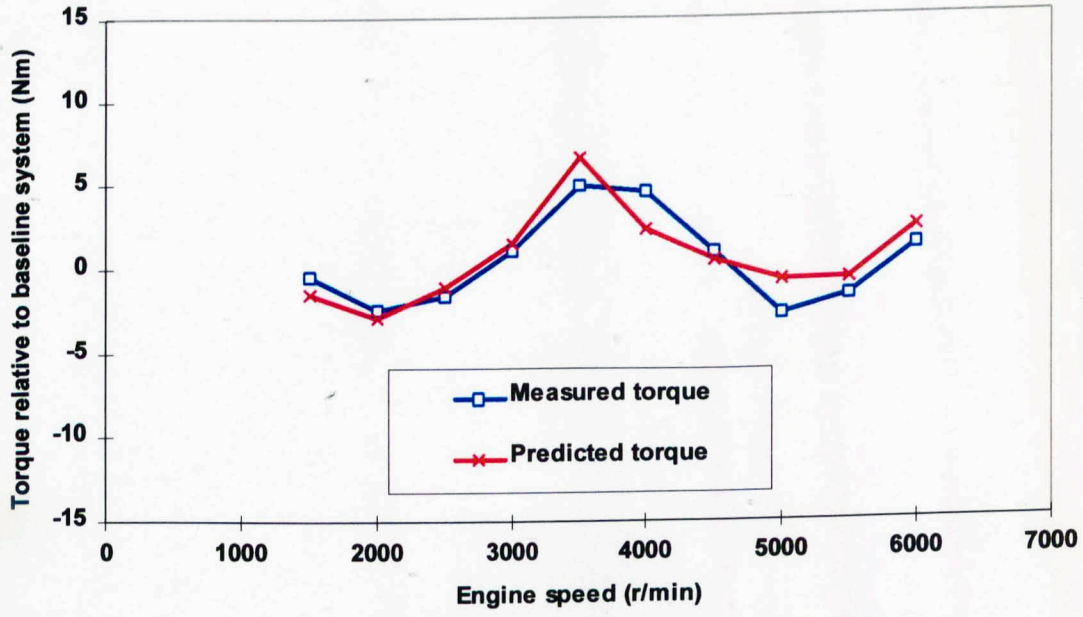

Figure 3.40 Comparisons of measured and predicted torque system test 2 relative to baseline system

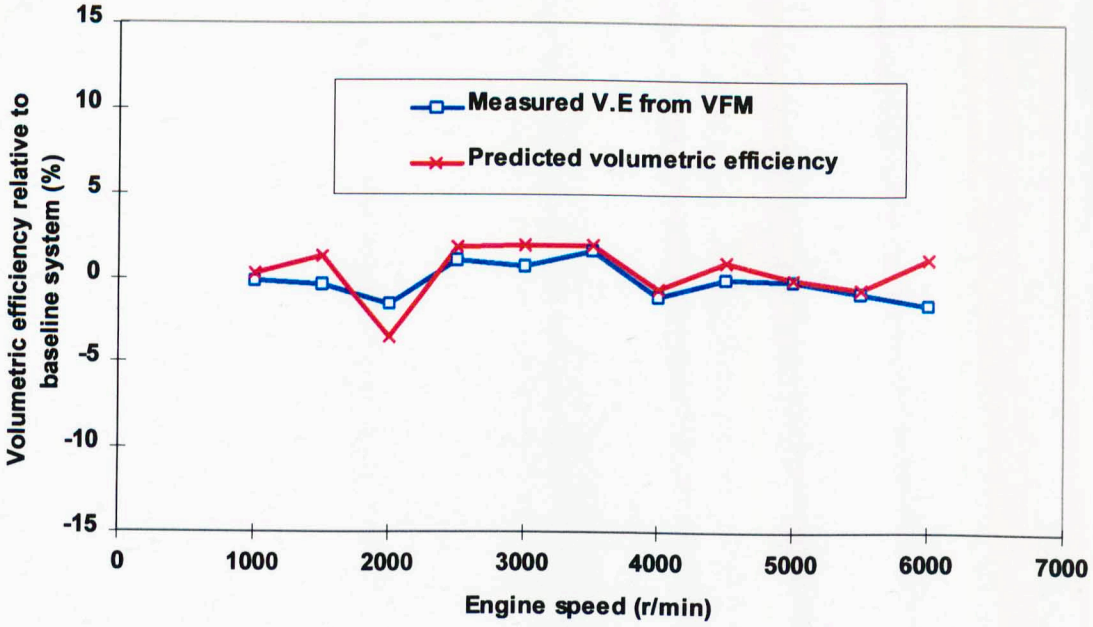

Figure 3.41 Comparisons of measured and predicted volumetric efficiency system test 3 relative to baseline system

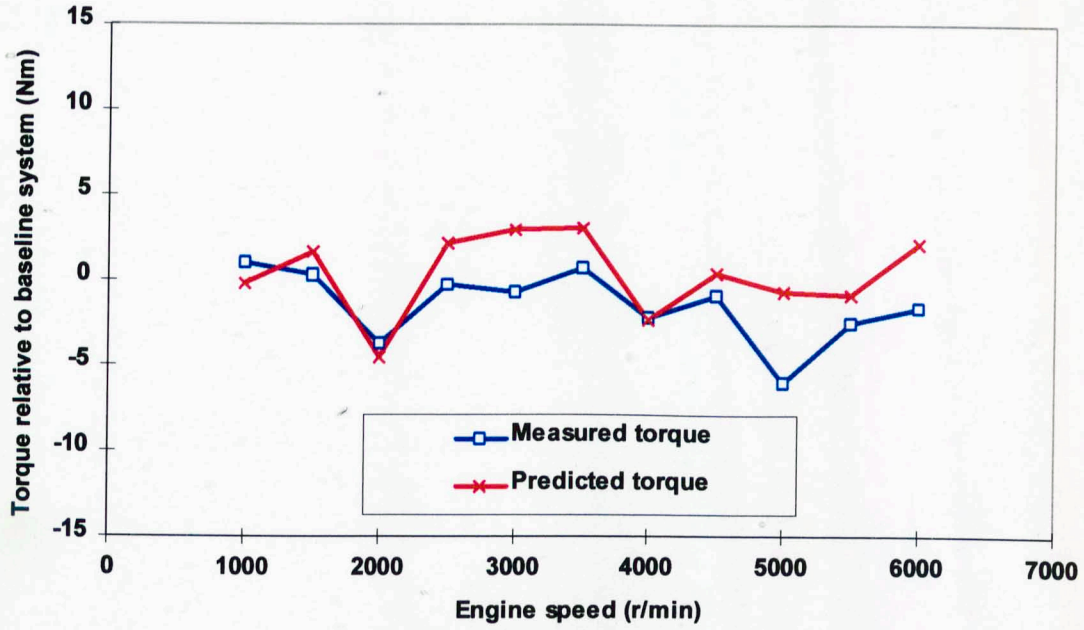

Figure 3.42 Comparisons of measured and predicted torque system test 3 relative to baseline system

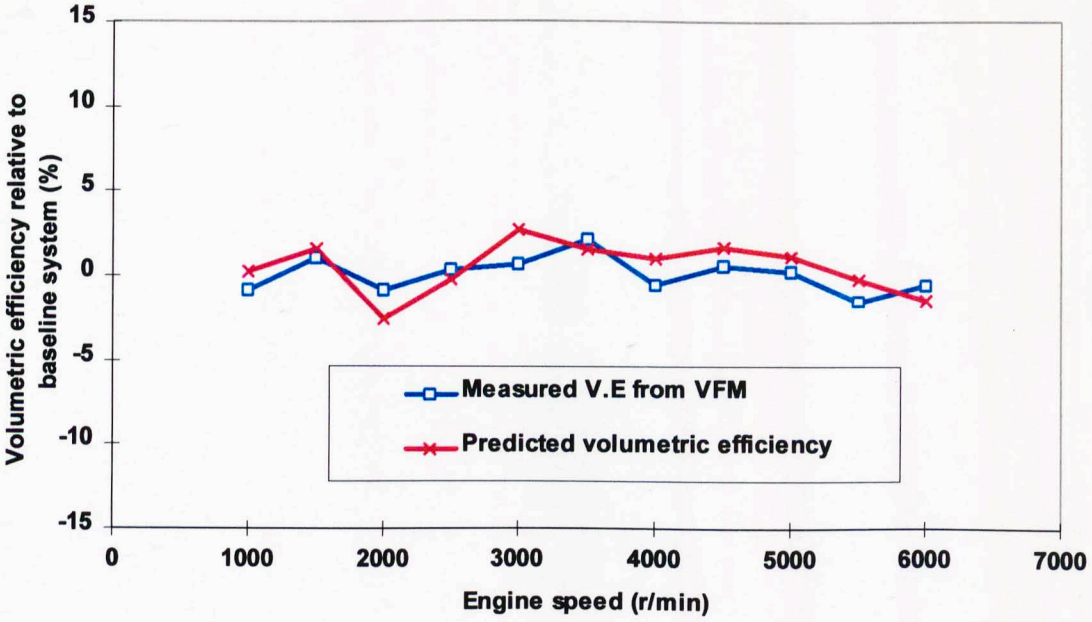

Figure 3.43 Comparisons of measured and predicted volumetric efficiency system test 4 relative to baseline system

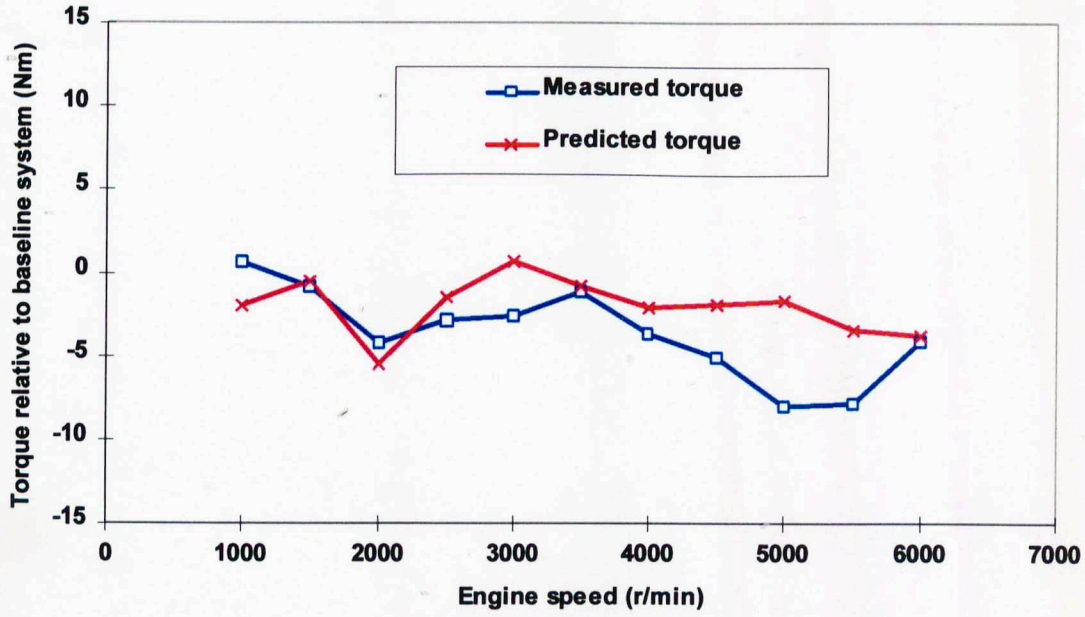

Figure 3.44 Comparisons of measured and predicted torque system test 4 relative to baseline system

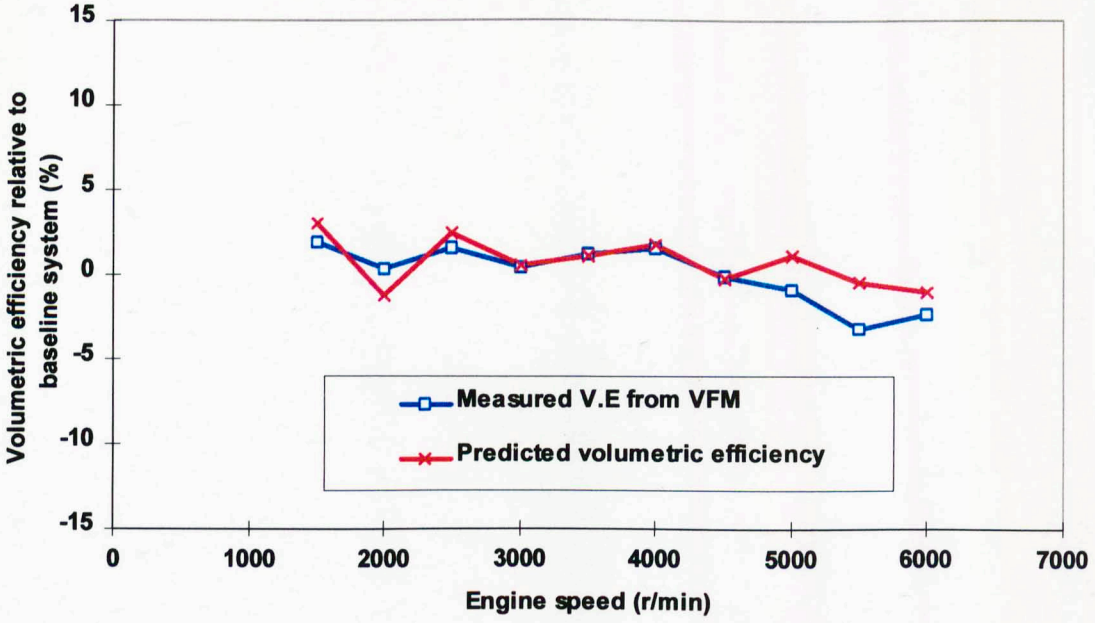

Figure 3.45 Comparisons of measured and predicted volumetric efficiency system test 5 relative to baseline system

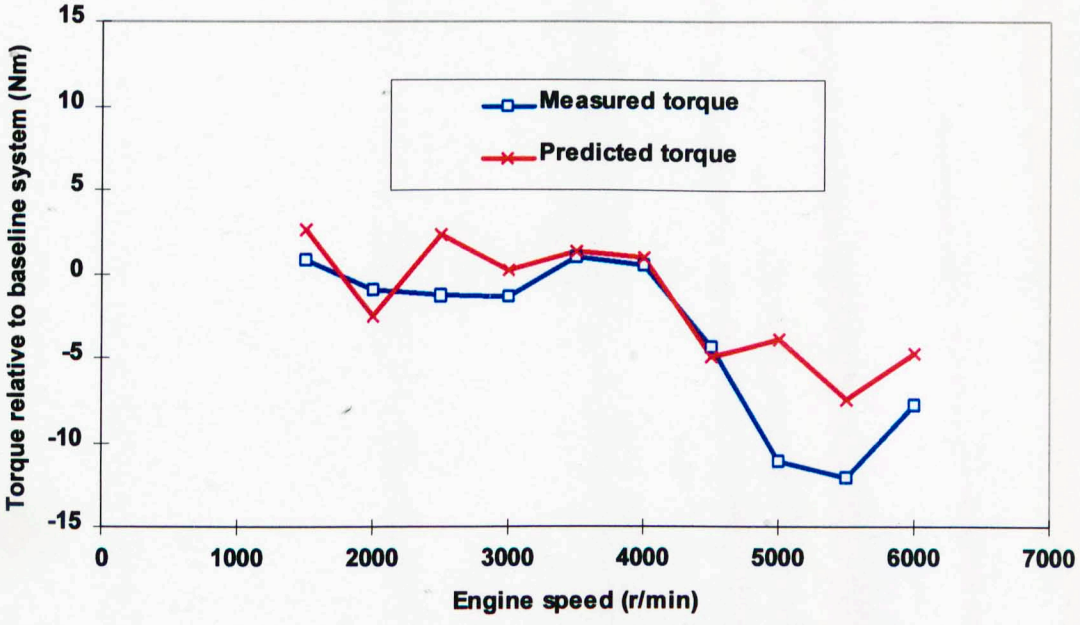

Figure 3.46 Comparisons of measured and predicted torque system test 5 relative to baseline system

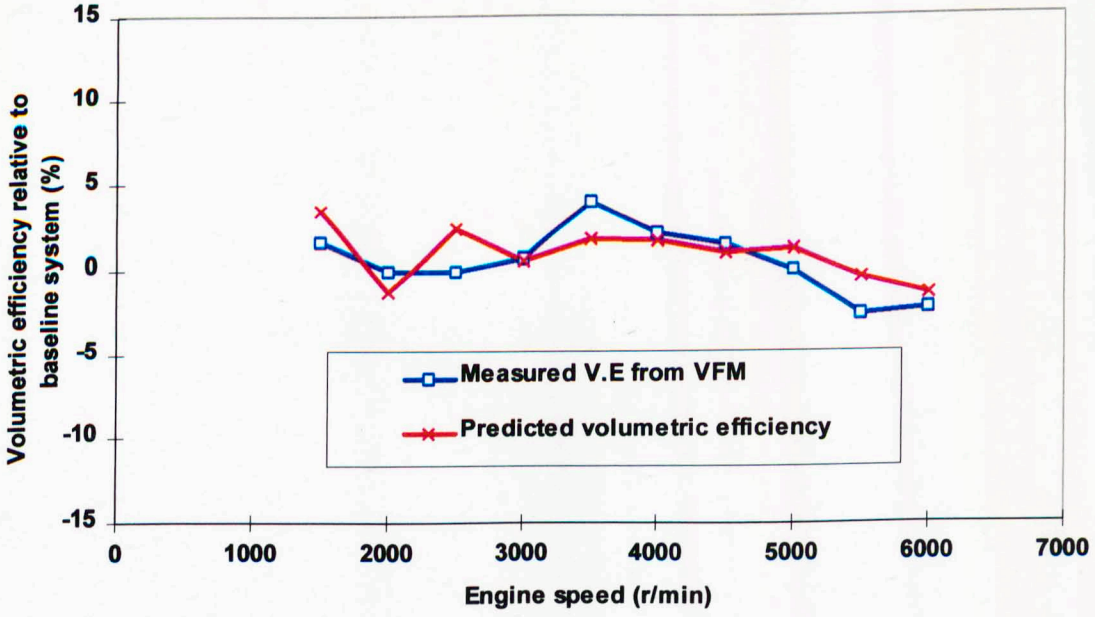

Figure 3.47 Comparisons of measured and predicted volumetric efficiency system test 6 relative to baseline system

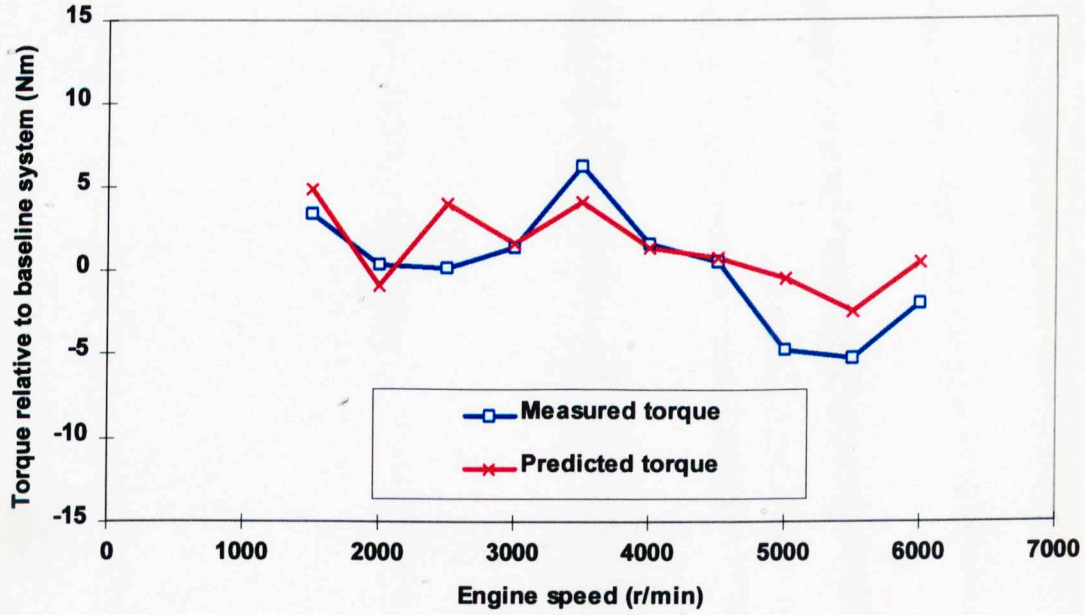

Figure 3.48 Comparisons of measured and predicted torque system test 6 relative to baseline system

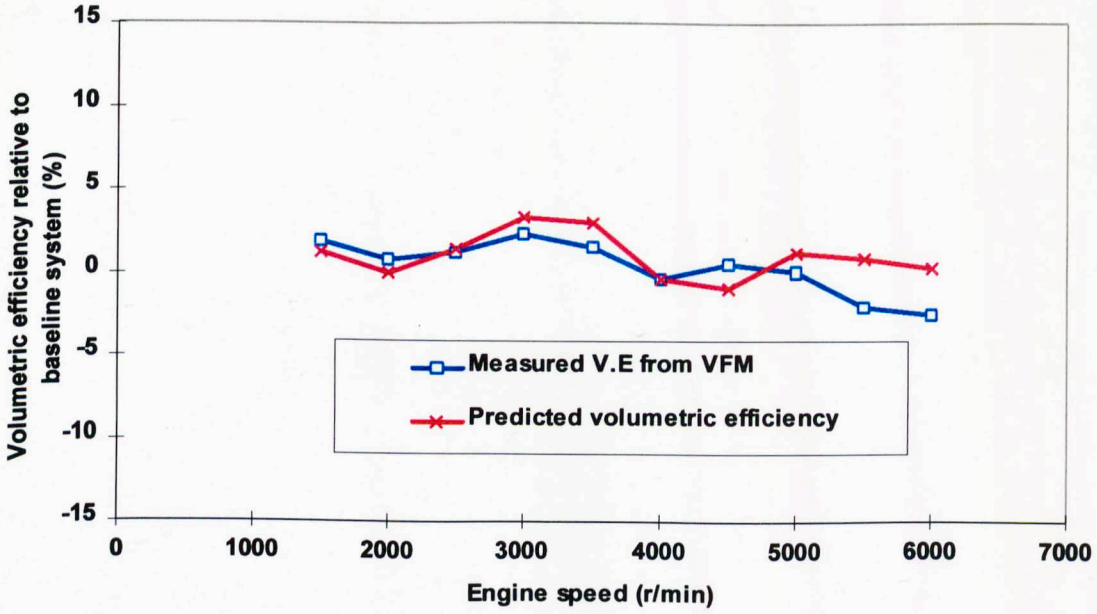

Figure 3.49 Comparisons of measured and predicted volumetric efficiency system test 7 relative to baseline system

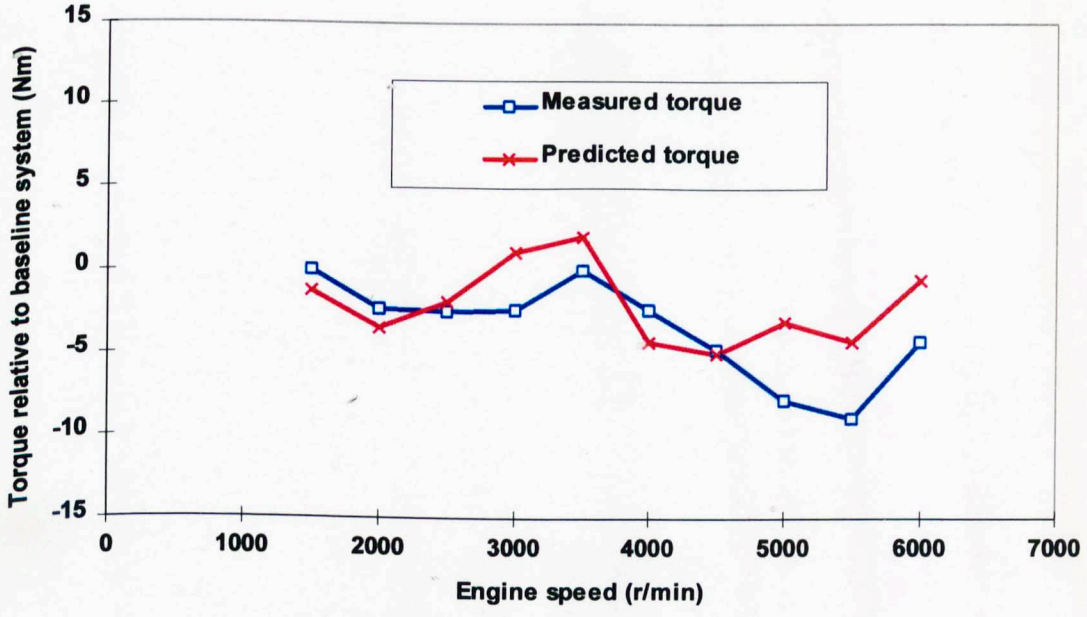

Figure 3.50 Comparisons of measured and predicted torque system test 7 relative to baseline system

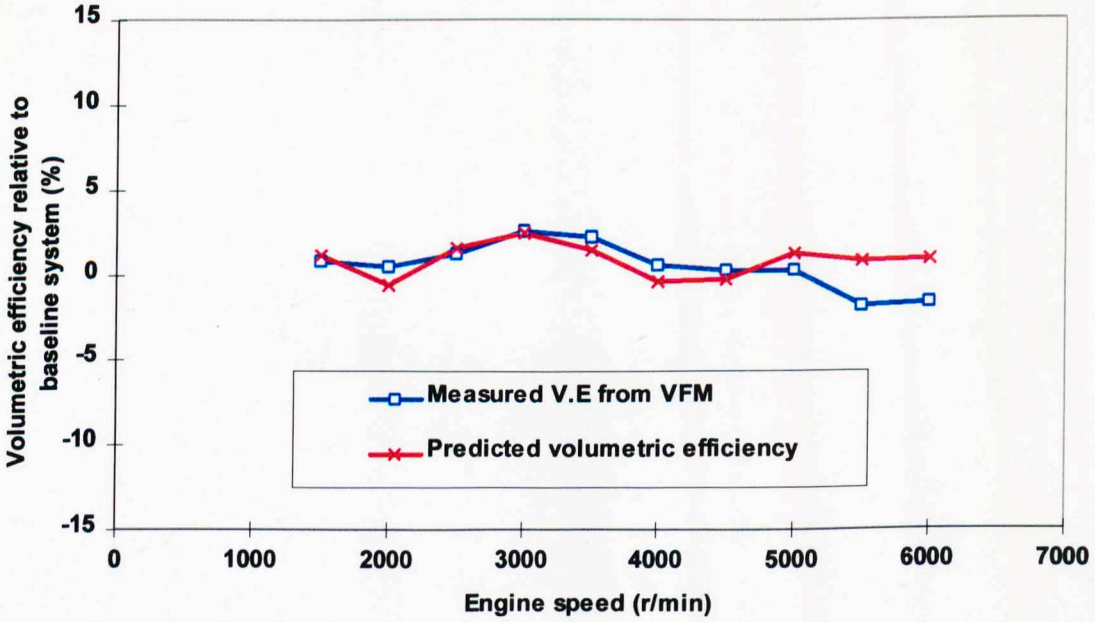

Figure 3.51 Comparisons of measured and predicted volumetric efficiency system test 8 relative to baseline system

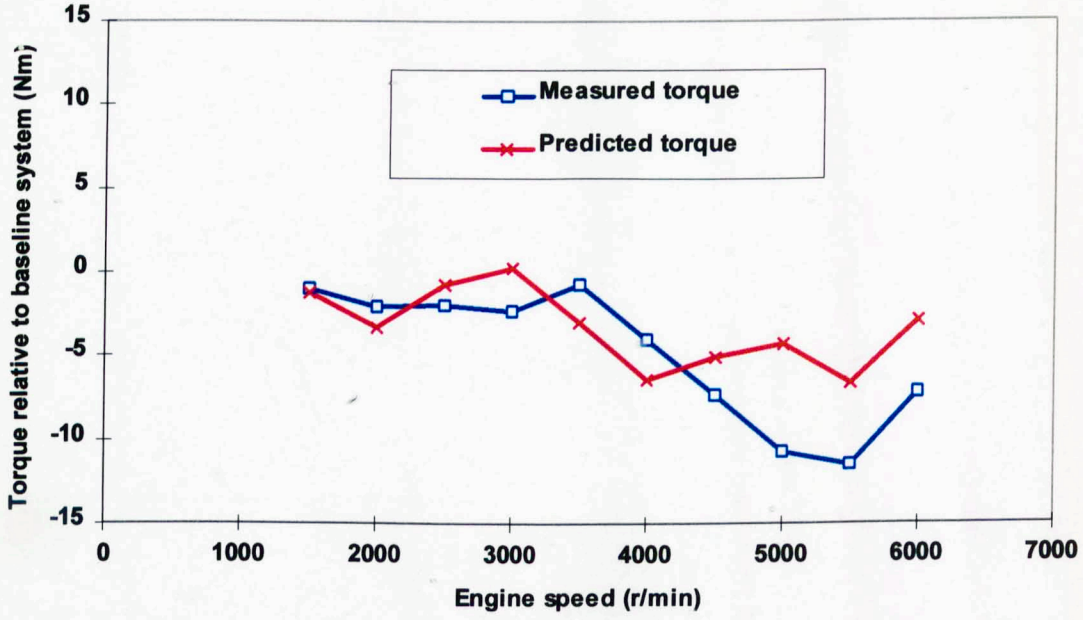

Figure 3.52 Comparisons of measured and predicted torque system test 8 relative to baseline system

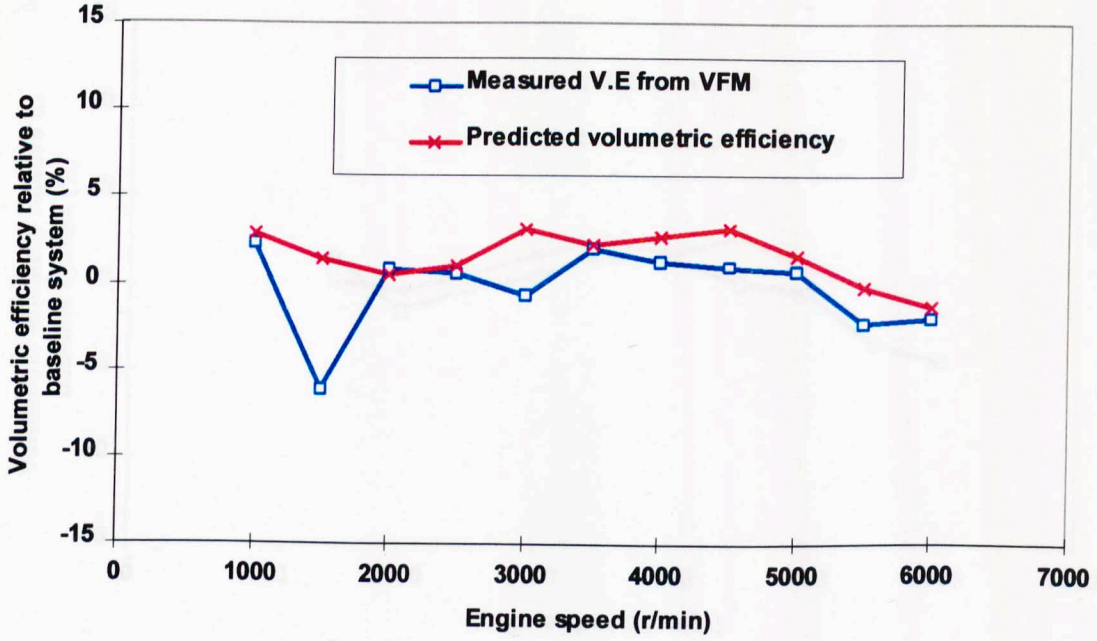

Figure 3.53 Comparisons of measured and predicted volumetric efficiency system test 9 relative to baseline system

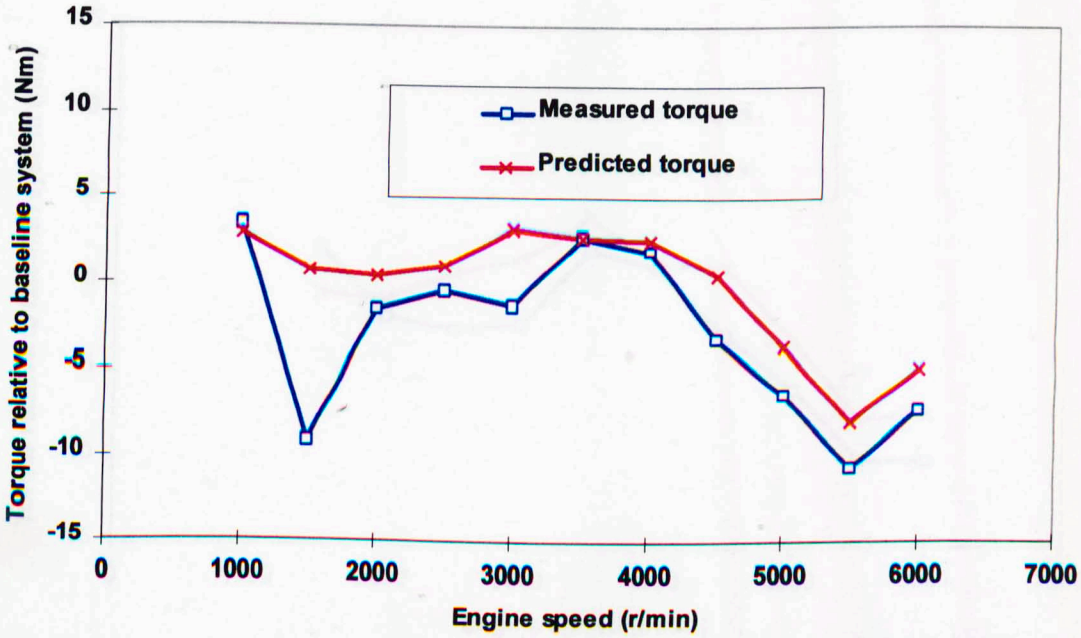

Figure 3.54 Comparisons of measured and predicted torque system test 9 relative to baseline system

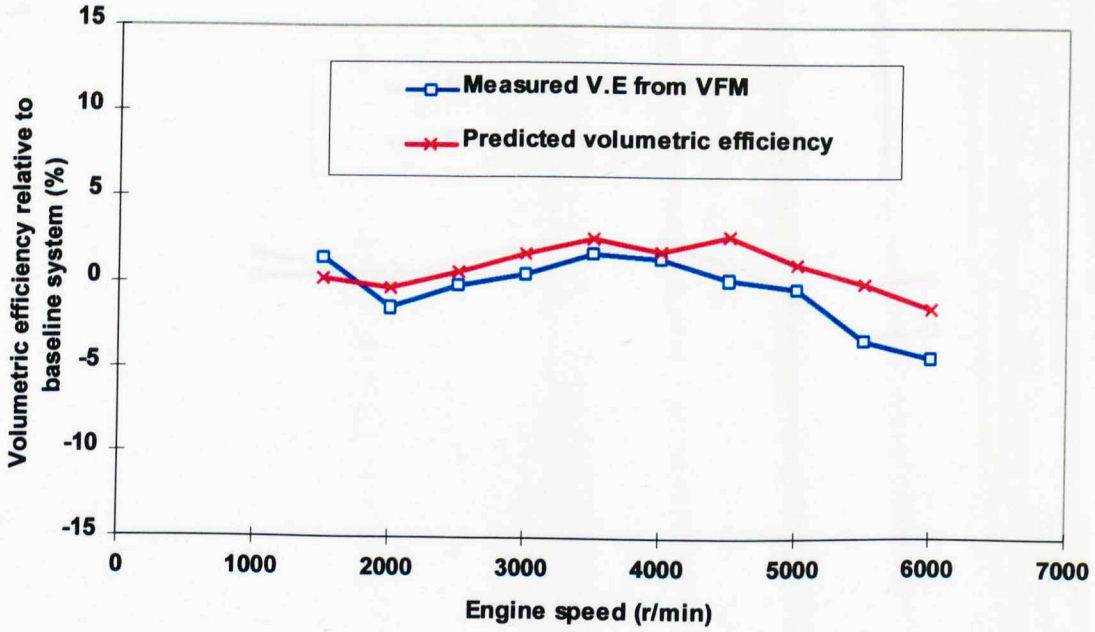

Figure 3.55 Comparisons of measured and predicted volumetric efficiency system test 10 relative to baseline system

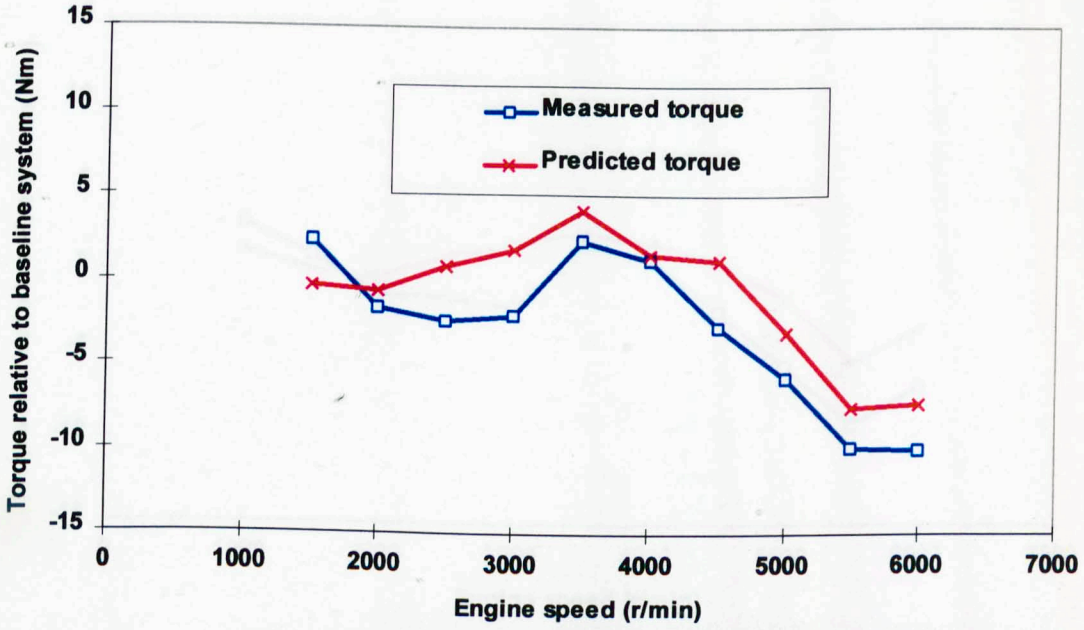

Figure 3.56 Comparisons of measured and predicted torque system test 10 relative to baseline system

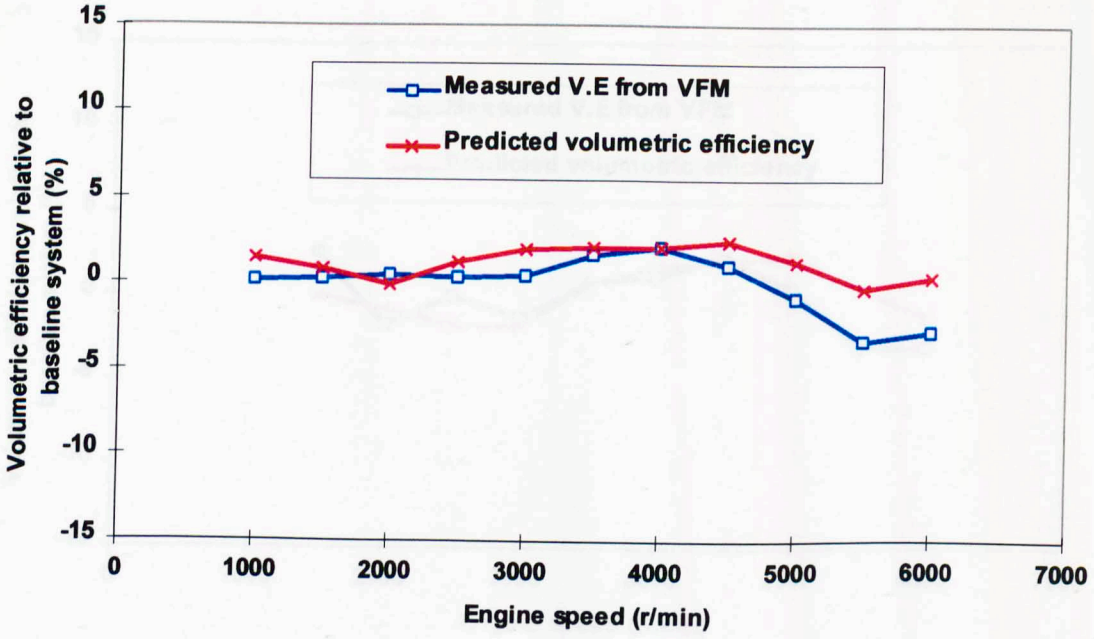

Figure 3.57 Comparisons of measured and predicted volumetric efficiency system test 11 relative to baseline system

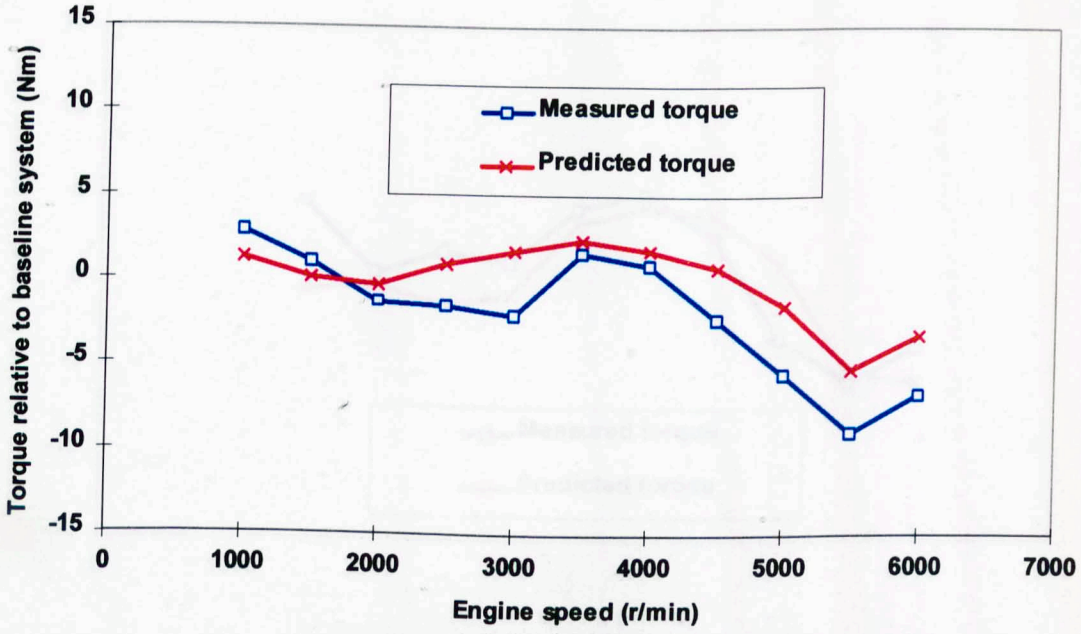

Figure 3.58 Comparisons of measured and predicted torque system test 11 relative to baseline system

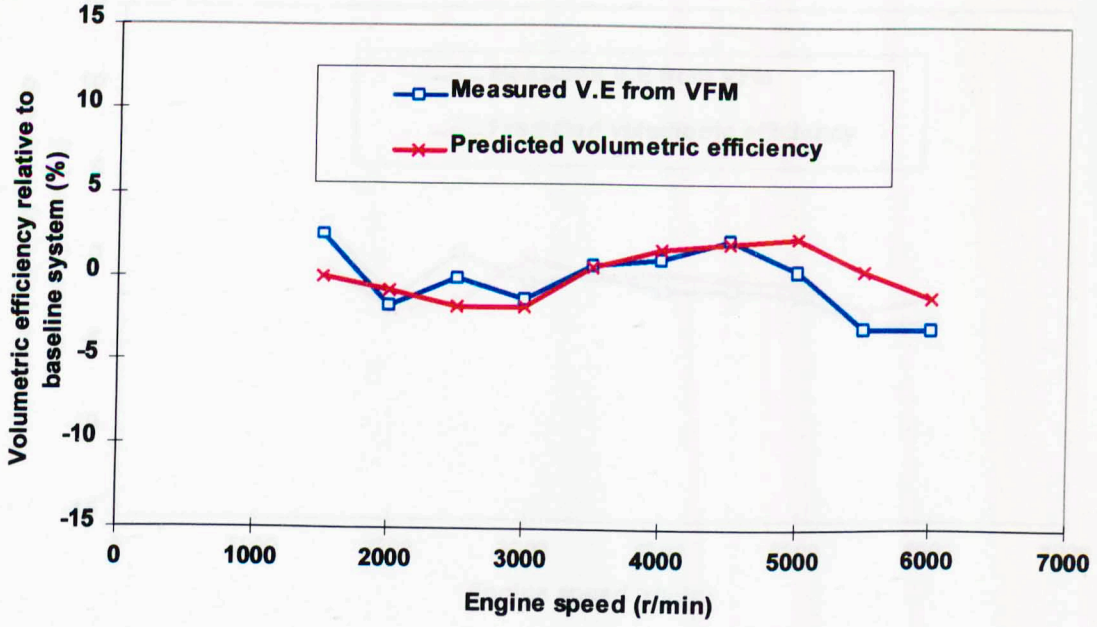

Figure 3.59 Comparisons of measured and predicted volumetric efficiency system test 12 relative to baseline system

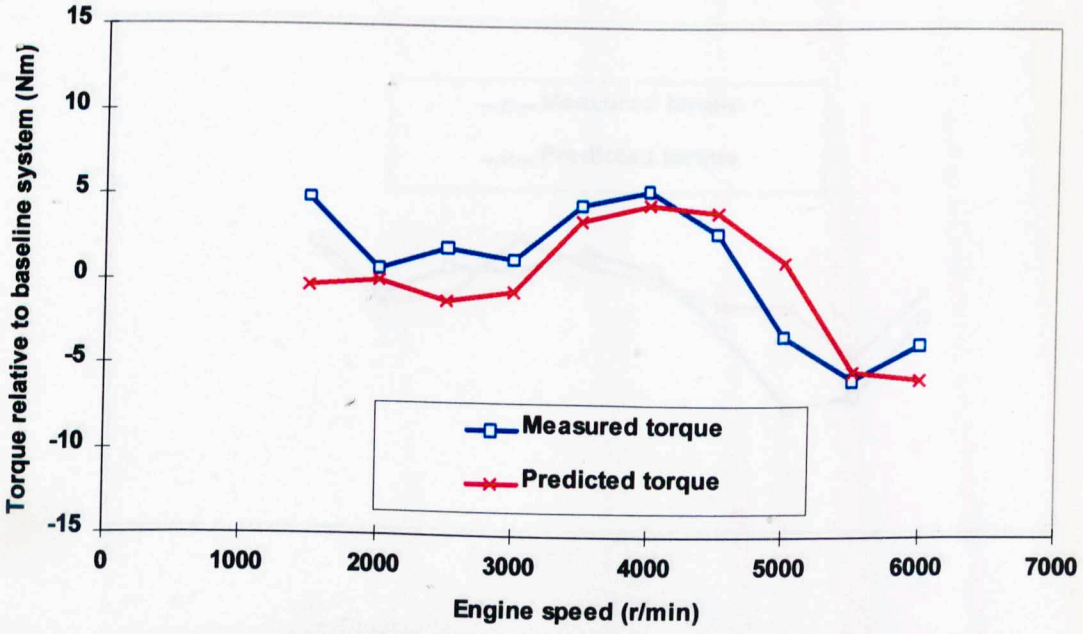

Figure 3.60 Comparisons of measured and predicted torque system test 12 relative to baseline system

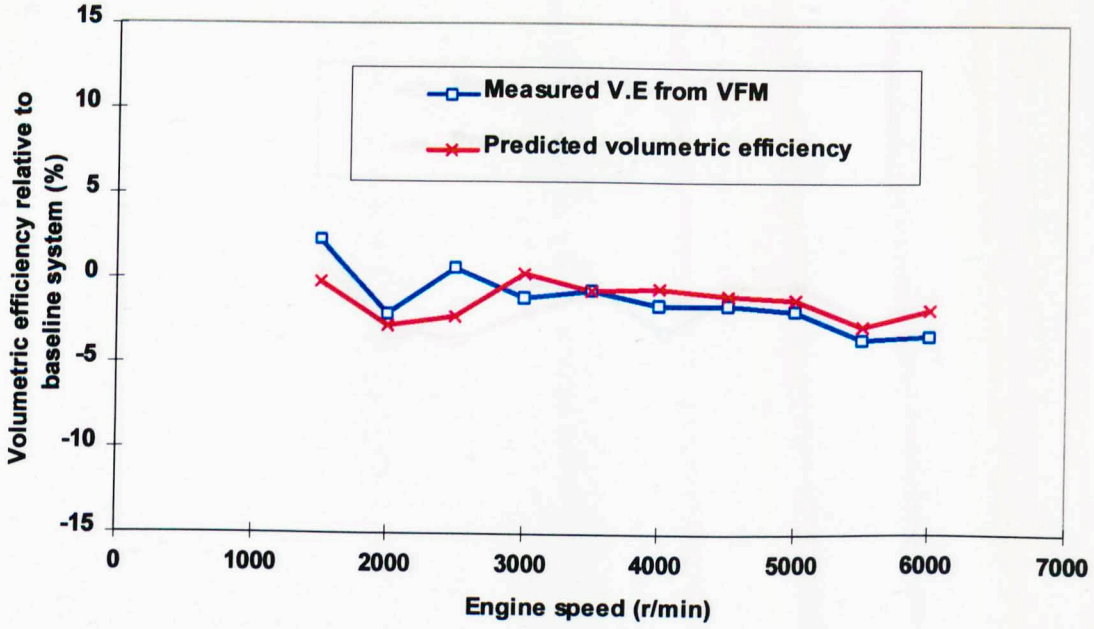

Figure 3.61 Comparisons of measured and predicted volumetric efficiency system test 13 relative to baseline system

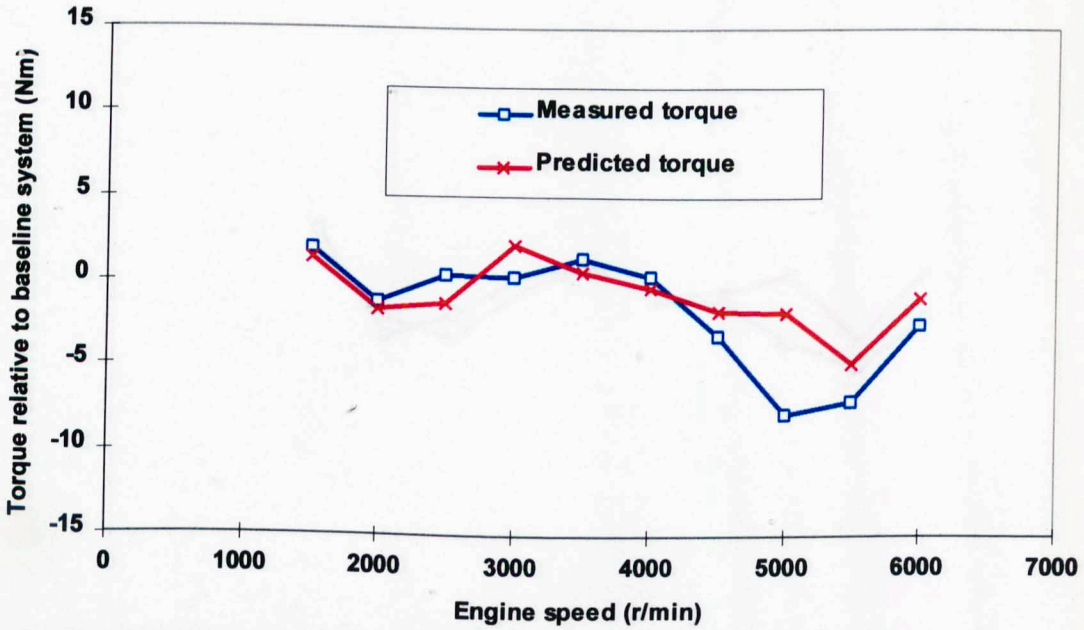

Figure 3.62 Comparisons of measured and predicted torque system test 13 relative to baseline system

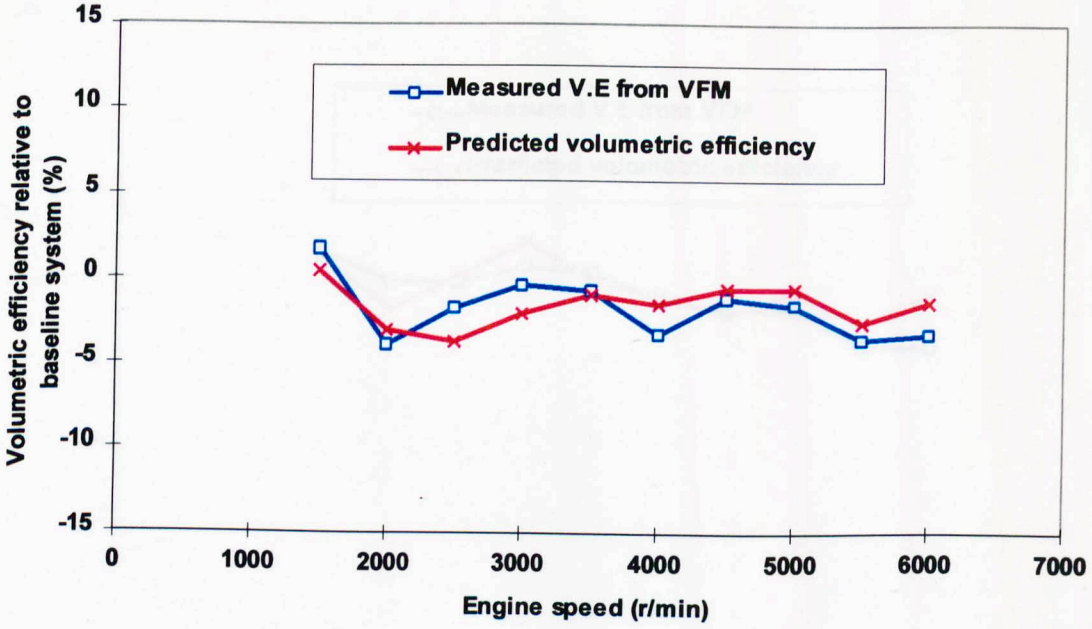

Figure 3.63 Comparisons of measured and predicted volumetric efficiency system test 14 relative to baseline system

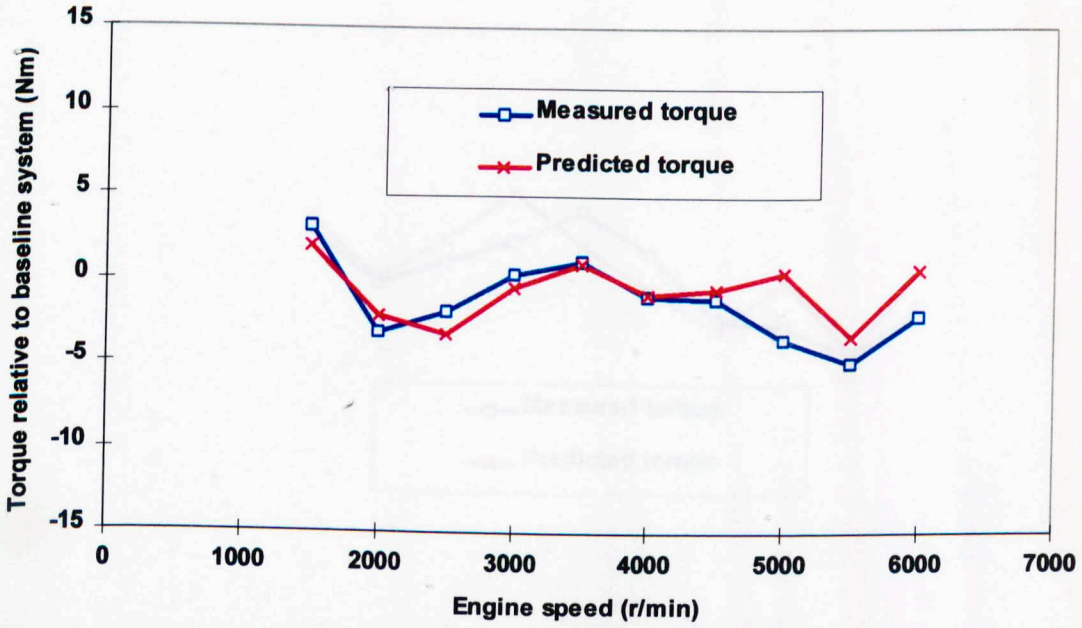

Figure 3.64 Comparisons of measured and predicted torque system test 14 relative to baseline system

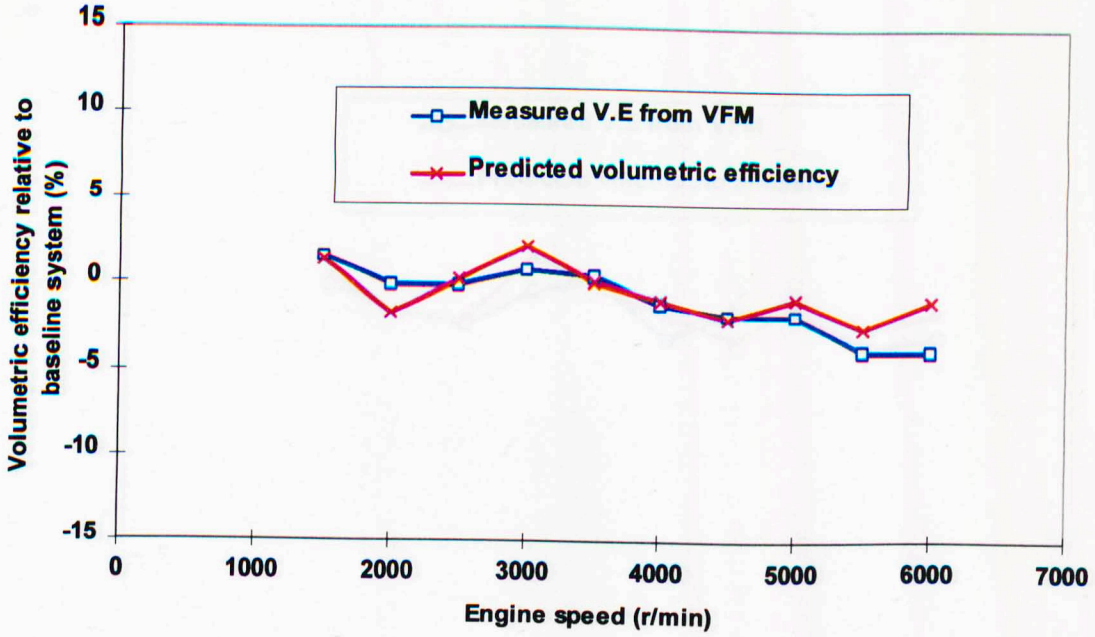

Figure 3.65 Comparisons of measured and predicted volumetric efficiency system test 15 relative to baseline system

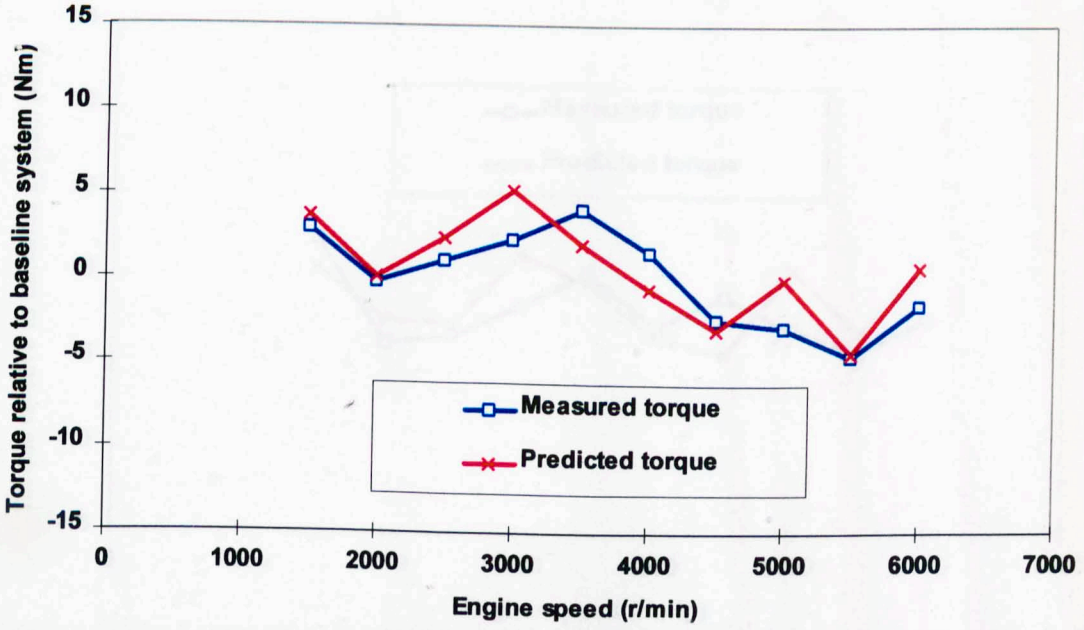

Figure 3.66 Comparisons of measured and predicted torque system test 15 relative to baseline system

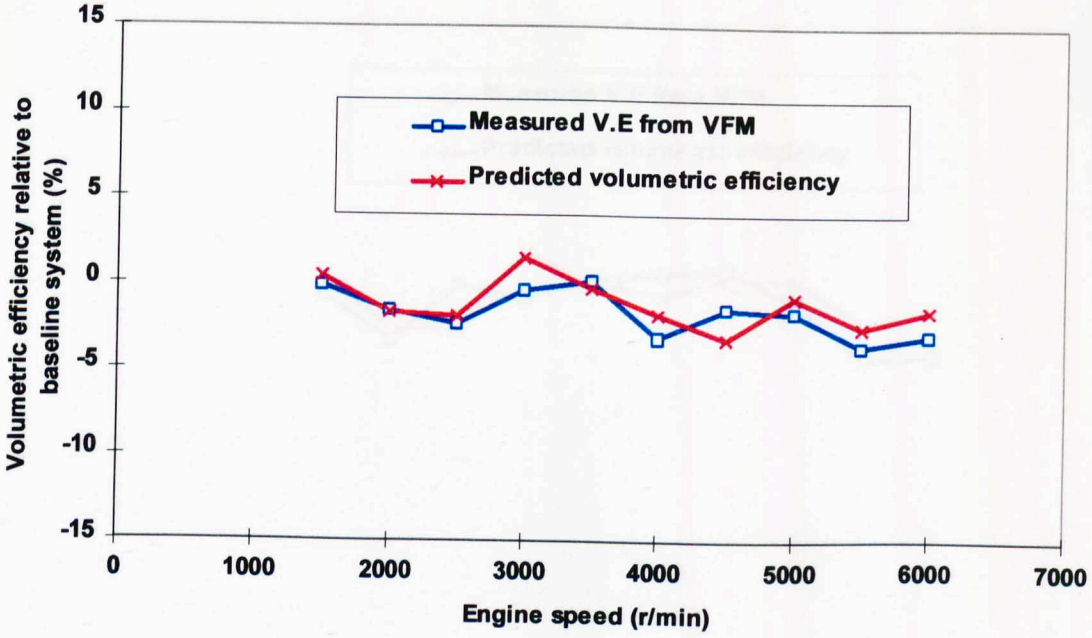

Figure 3.67 Comparisons of measured and predicted volumetric efficiency system test 16 relative to baseline system

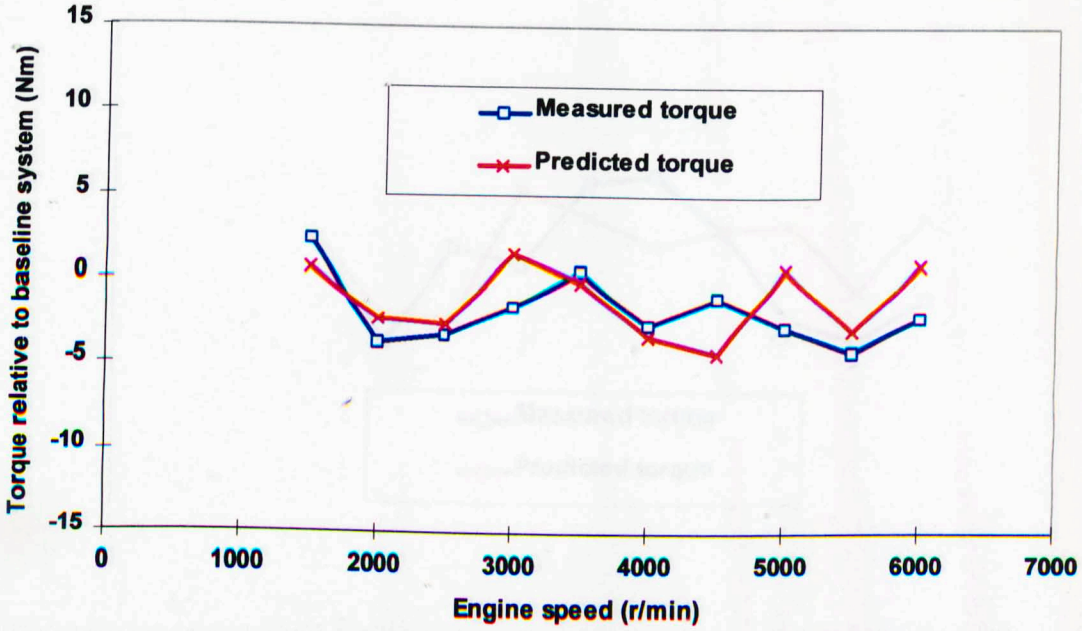

Figure 3.68 Comparisons of measured and predicted torque system test 16 relative to baseline system

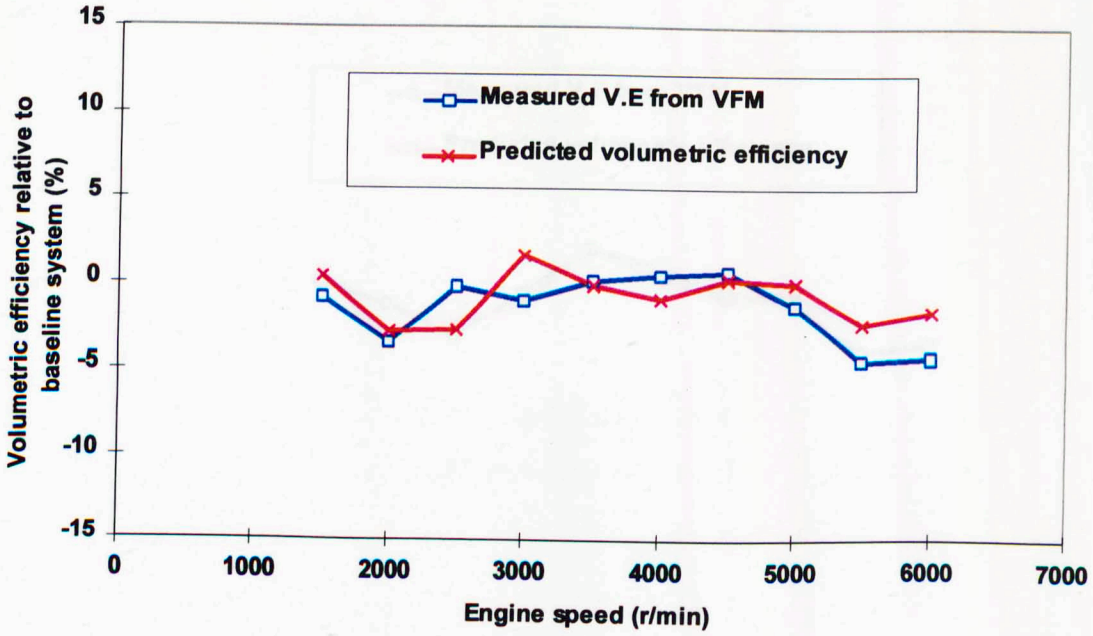

Figure 3.69 Comparisons of measured and predicted volumetric efficiency system test 17 relative to baseline system

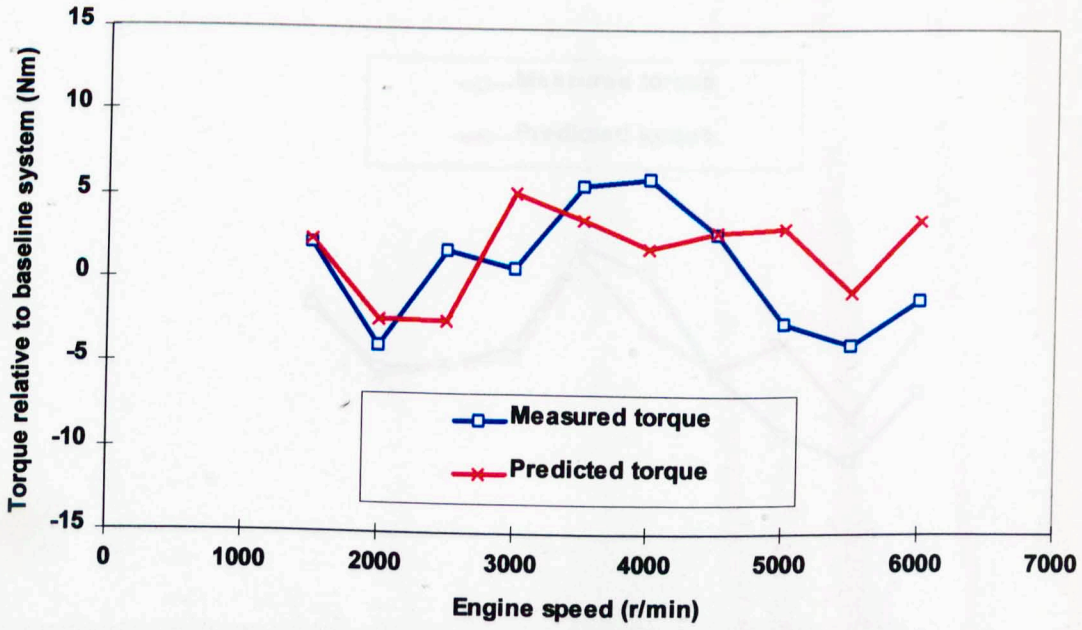

Figure 3.70 Comparisons of measured and predicted torque system test 17 relative to baseline system

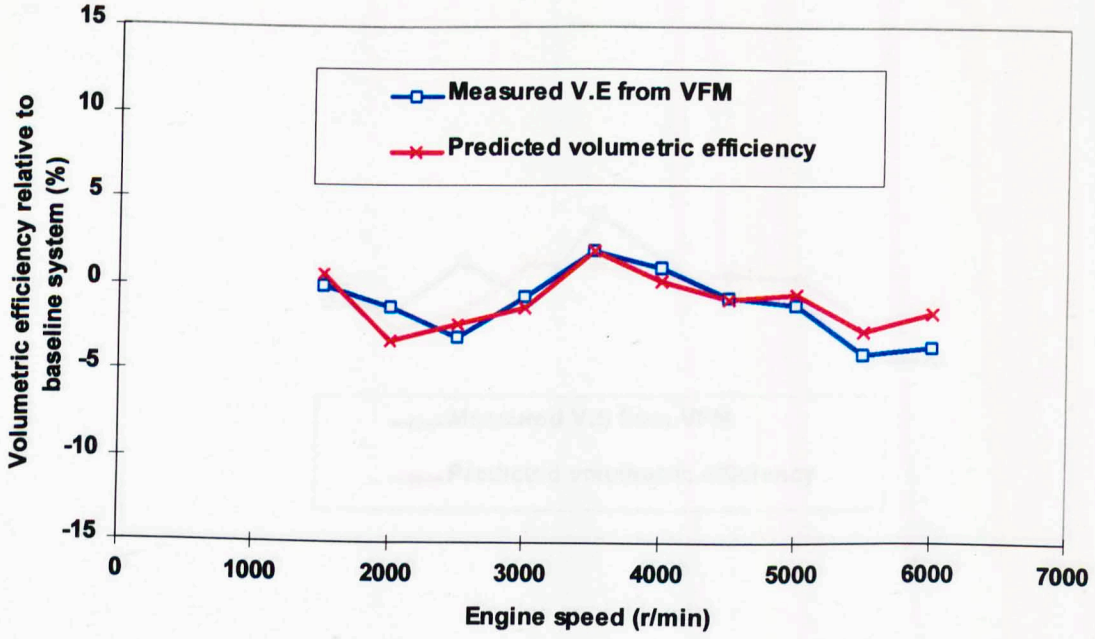

Figure 3.71 Comparisons of measured and predicted volumetric efficiency system test 18 relative to baseline system

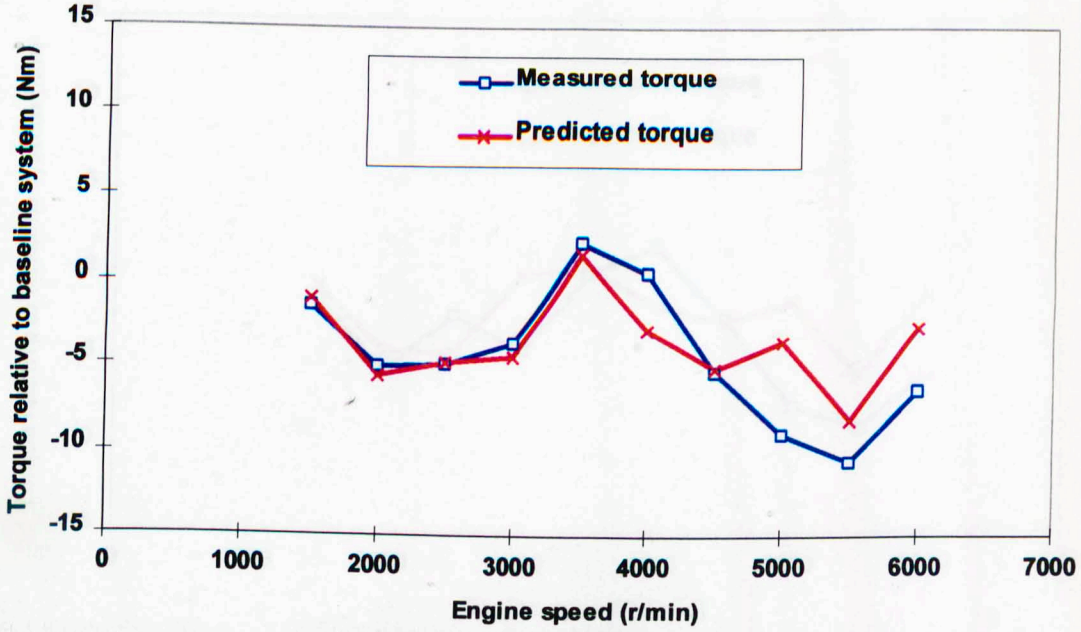

Figure 3.72 Comparisons of measured and predicted torque system test 18 relative to baseline system

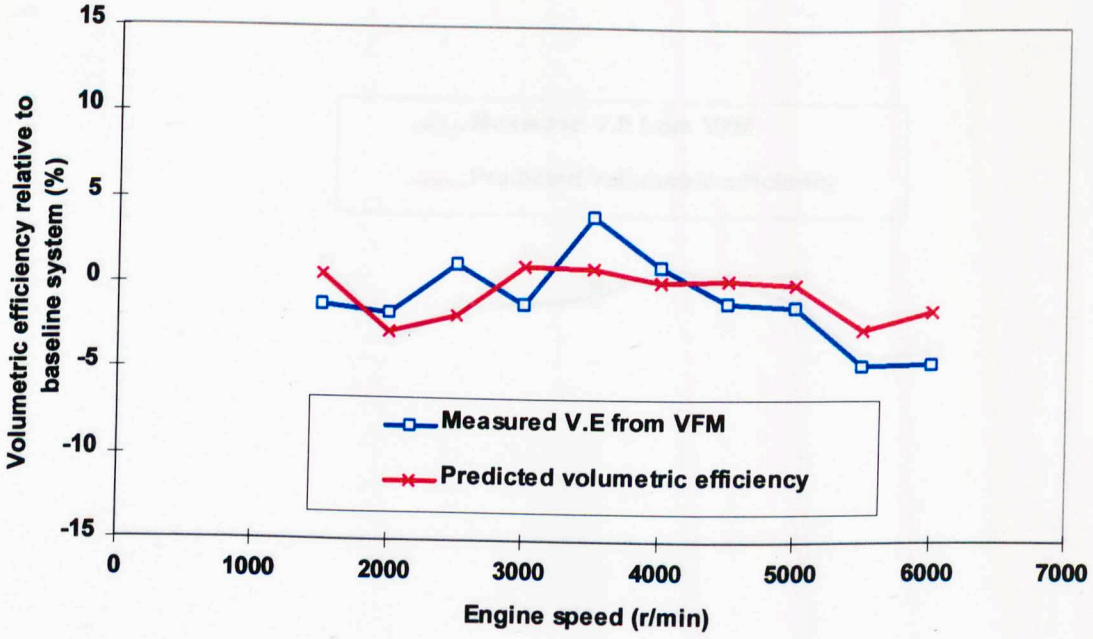

Figure 3.73 Comparisons of measured and predicted volumetric efficiency system test 19 relative to baseline system

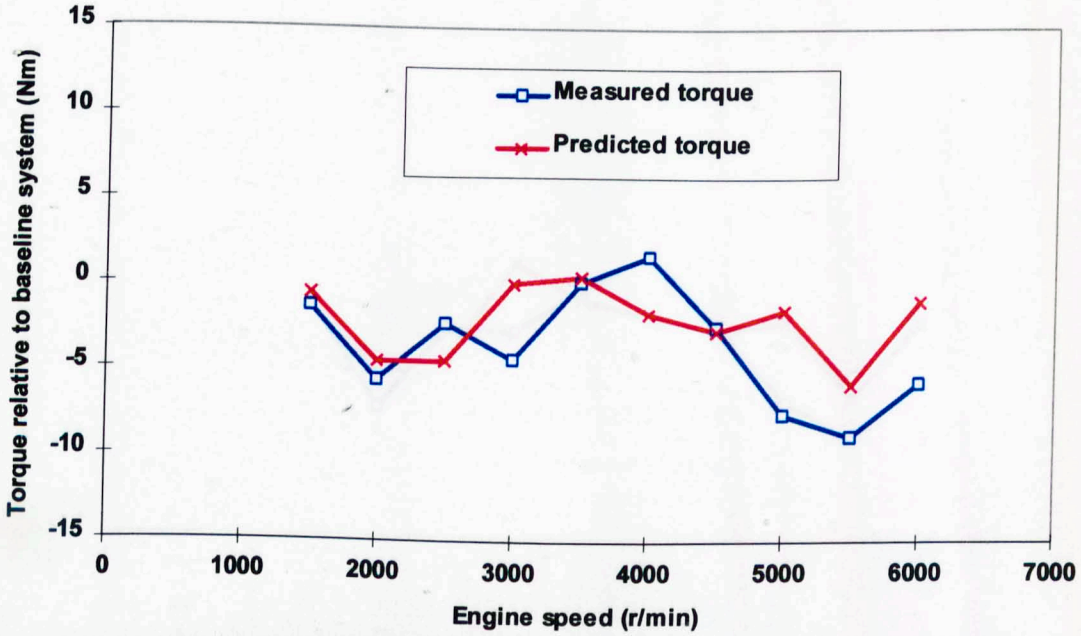

Figure 3.74 Comparisons of measured and predicted torque system test 19 relative to baseline system

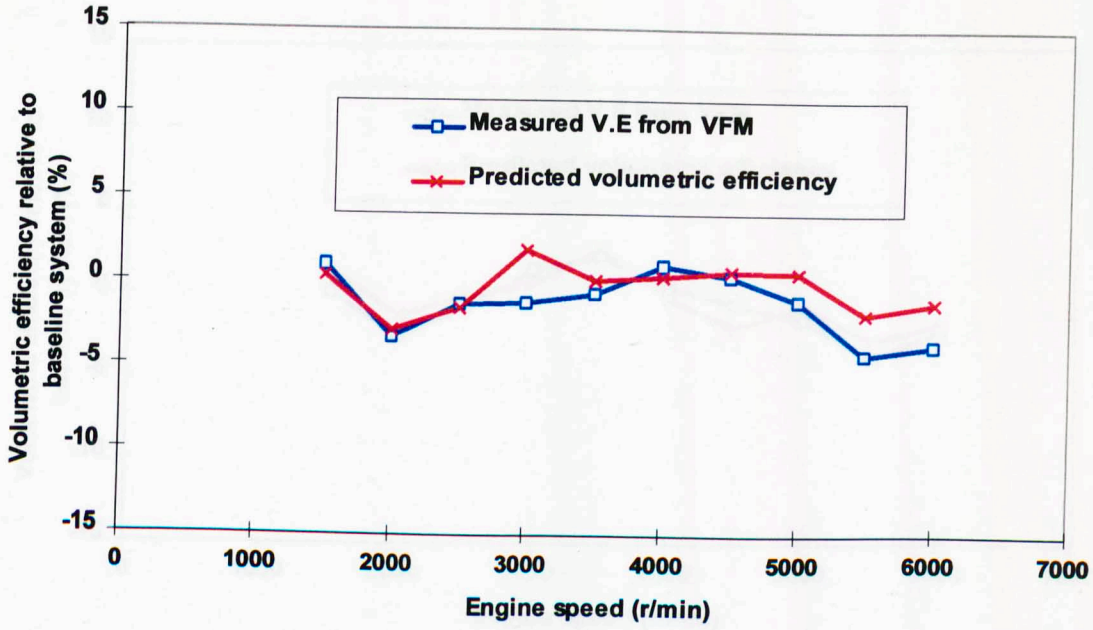

Figure 3.75 Comparisons of measured and predicted volumetric efficiency system test 20 relative to baseline system

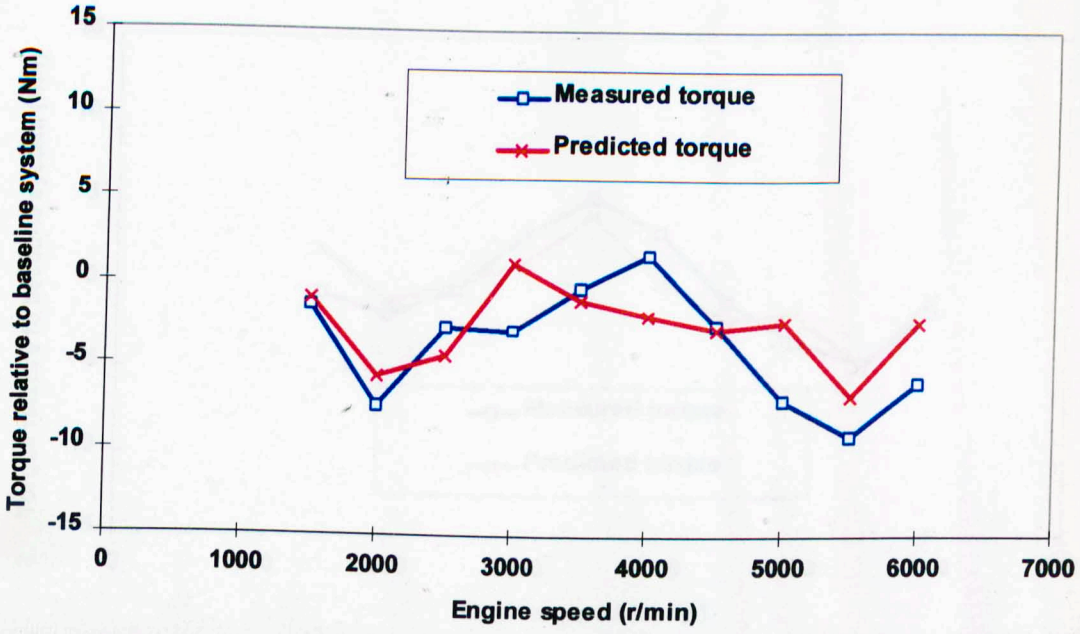

Figure 3.76 Comparisons of measured and predicted torque system test 20 relative to baseline system

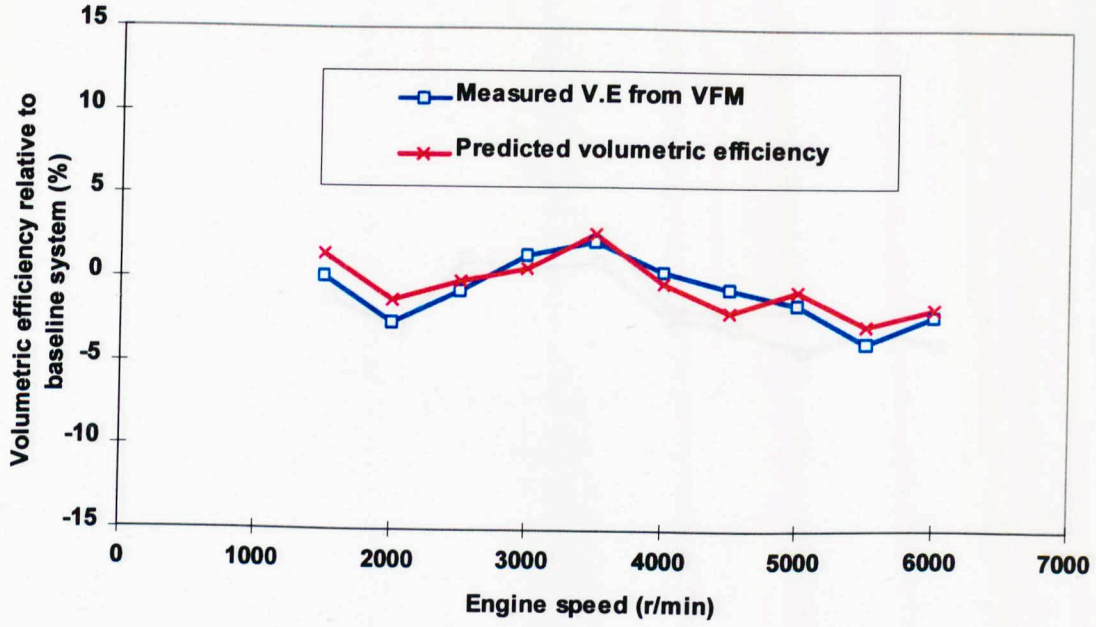

Figure 3.77 Comparisons of measured and predicted volumetric efficiency system test 21 relative to baseline system

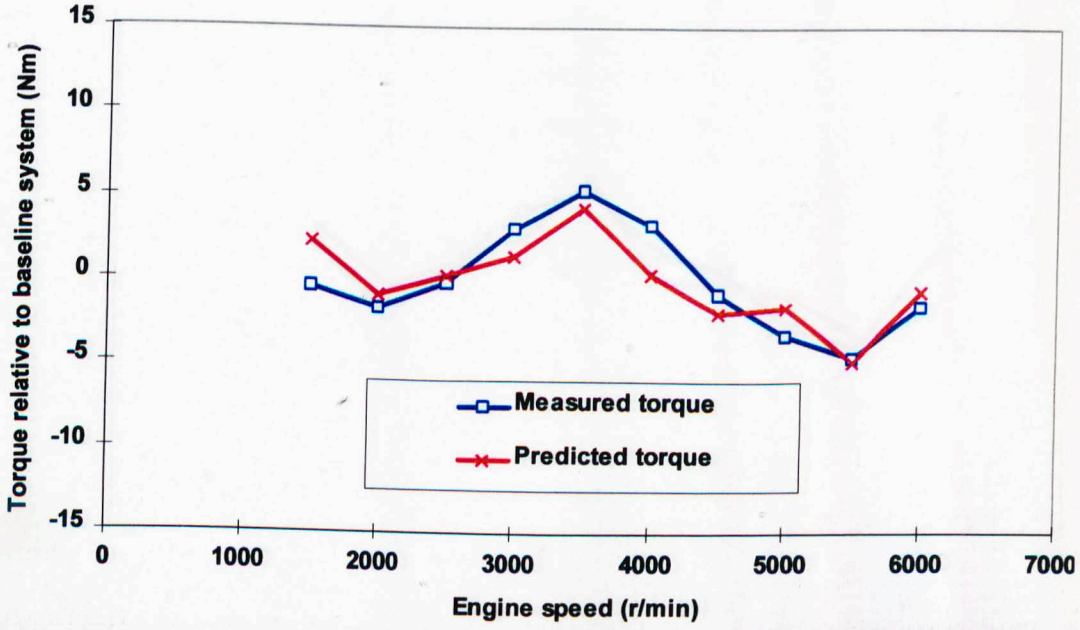

Figure 3.78 Comparisons of measured and predicted torque system test 21 relative to baseline system

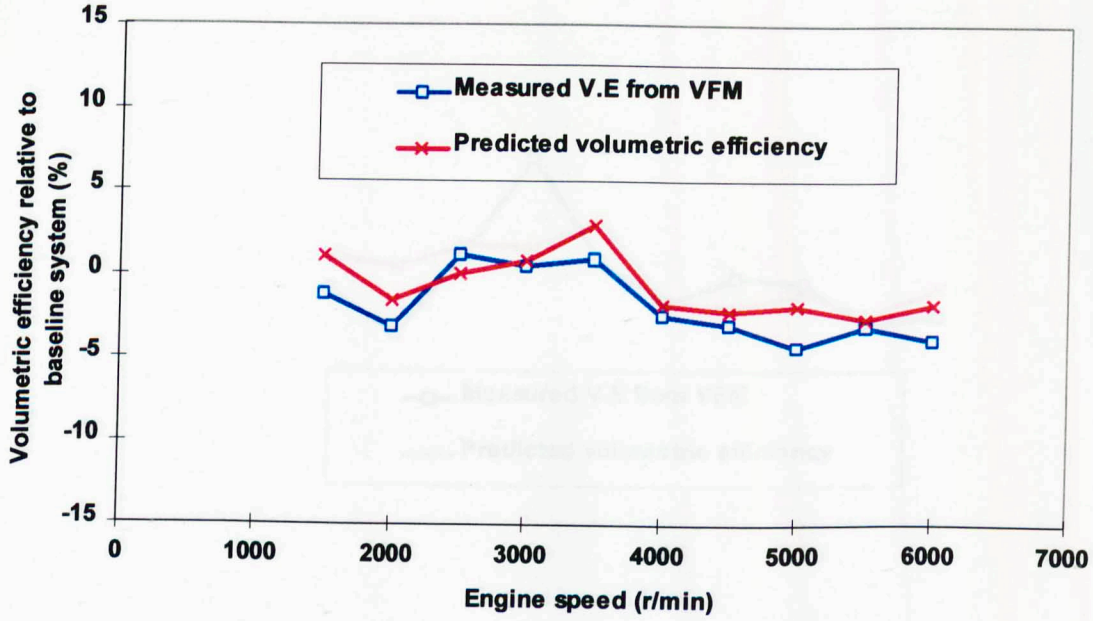

Figure 3.79 Comparisons of measured and predicted volumetric efficiency system test 22 relative to baseline system

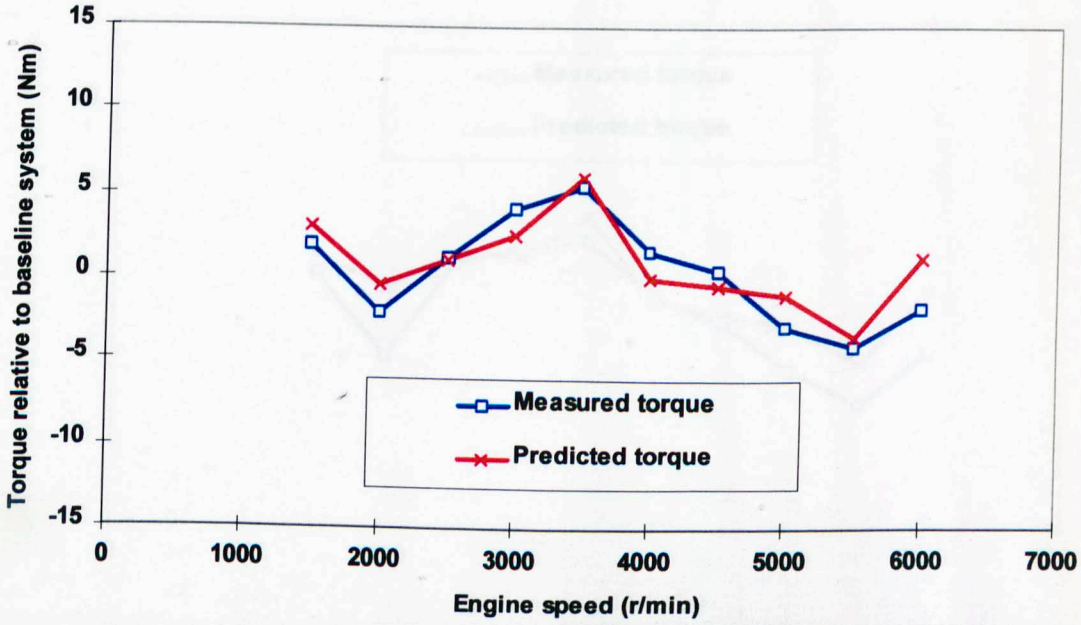

Figure 3.80 Comparisons of measured and predicted torque system test 22 relative to baseline system

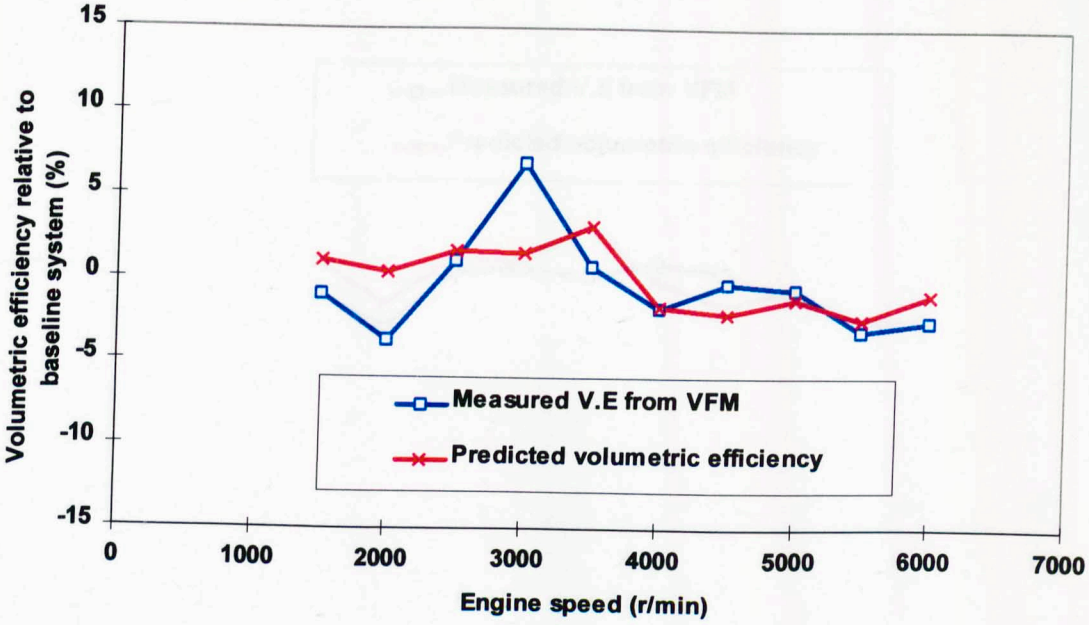

Figure 3.81 Comparisons of measured and predicted volumetric efficiency system test 23 relative to baseline system

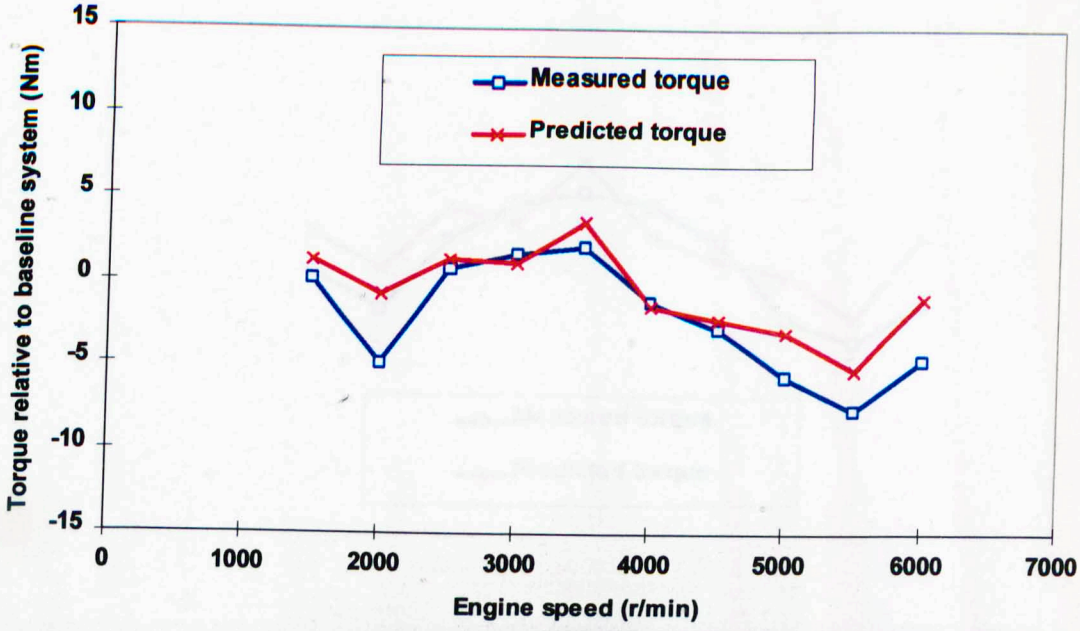

Figure 3.82 Comparisons of measured and predicted torque system test 23 relative to baseline system

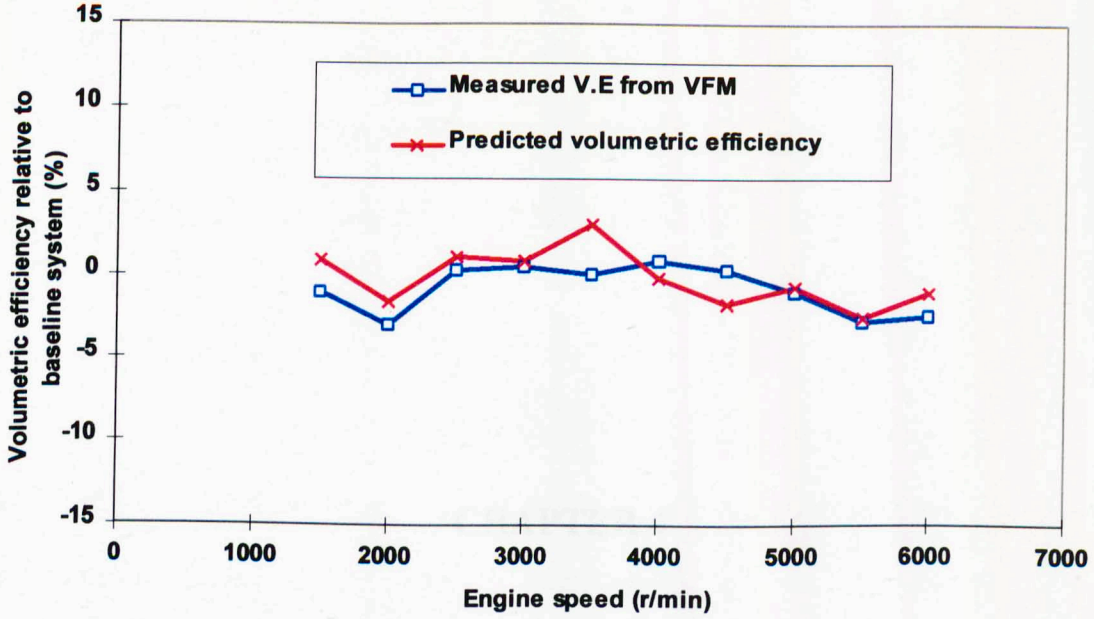

Figure 3.83 Comparisons of measured and predicted volumetric efficiency system test 24 relative to baseline system

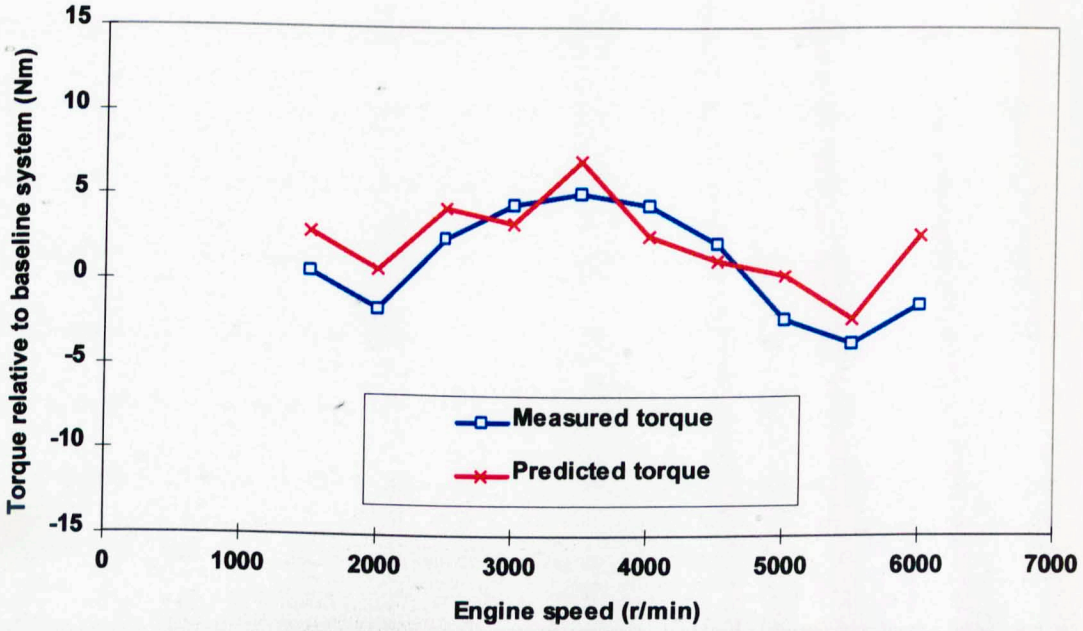

Figure 3.84 Comparisons of measured and predicted torque system test 24 relative to baseline system

CHAPTER 4

TAGUCHI STUDY OF THE EFFECT OF EXHAUST SYSTEM GEOMETRY ON ENGINE PERFORMANCE CHARACTERISTICS

CHAPTER 4

TAGUCHI STUDY OF THE EFFECT OF EXHAUST SYSTEM GEOMETRY ON ENGINE PERFORMANCE CHARACTERISTICS

4.1 INTRODUCTION

The configuration of the primary and secondary exhaust manifold pipes, and of those components located within, exercises considerable influence on the gas exchange processes, and hence the torque characteristic of an internal combustion engine. This is due to their influence on both the passage of exhaust gases and the propagation of the pressure waves generated by the sudden release of these gases from the combustion chamber into the manifold. Those exhaust system components located downstream of the secondary pipes also influence the torque characteristic to some degree. However, this has been found by others [116], and was confirmed during this phase of the study, to be primarily as a consequence of their influence on pumping losses resulting from their contribution to the overall system pressure loss and not due to any tuning effect. The design of an exhaust system that provides the optimum pressure - crank-angle history at the exhaust port during the critical periods of exhaust valve open and valve overlap necessitates a complete understanding of the influence of all the system components on the propagation of both the exhaust gases and the pressure waves.

The validated engine gas-dynamics model was used to investigate a number of these components and demonstrated how modification to their geometry influences the torque

curve. As exhaust system configurations have been modified, the simulated engine torque curves were investigated, using a commonly applied statistical analysis technique. For the engine input data utilised (in this case a 1.6 litre, 16 valve engine), it was possible to quantify the effect of each exhaust system component on the torque characteristic variation, both at individual speeds and across the entire speed range.

4.2 EXPERIMENT DESIGN

4.2.1 The Taguchi approach

To enable the likely effect of modifications to the exhaust system geometry on engine output to be predicted, an analytical method based upon the concepts advocated by Taguchi [117, 118] was utilised. Design factors considered likely to have a significant effect on the response variable (in this case torque), both individually or interacting with one another, were initially selected, along with "noise factors" (uncontrolled factors during the experiment). Levels for each factor were then set and allocated to an orthogonal array that defined the composition of each individual simulation. Once all the simulations were completed, a statistical analysis was undertaken of the results, which included factor effects both at individual speeds and across the entire speed range. This analysis indicated the contribution of each factor to the overall variation in the results for the range of levels of factors selected. Taguchi's concepts for experimental design analysis suggest that, when factors are shown to be insignificant and there is no possible confounding of them with other factors during the experiment, they can be pooled together to indicate the random experimental variation. The random experimental

variation, considered as a factor in a modelling study, is a consequence of assumptions made in the algorithm used, and results from the compromise between model accuracy and computational time and effort.

4.2.2 Exhaust system study design elements

A typical automotive exhaust system comprises a considerable number of possible design parameters. However, these simulations were part of a long-term study of exhaust system tuning effects resulting from pressure wave action. It has also been shown by others [116] that there is little influence on the exhaust port pressure profile by those components located downstream of the secondary pipes and so this phase of the study focussed on design elements from the valves to the secondary-tertiary pipe junction. Figures 4.1 and 4.2 show comparisons of predicted exhaust port pressure histories for three variations of the baseline 4:2:1 exhaust system (refer to Table 3.3 and Figure 3.12) fitted to the Rover K series engine. Each system differed only in the location of the silencer elements relative to the primary-tertiary pipe junction. It can be seen that the exhaust port pressure histories generated by each model were virtually identical. This further validated the decision to focus, for this phase of the study, on exhaust component geometry upstream of the silencer elements.

Considering only 4:2:1 configuration exhaust systems, factors initially selected for investigation were as follows:-

i. The primary pipe length;

ii. the secondary pipe length;

iii. the location of the catalytic converter within the secondary pipes;

iv. the primary pipe diameter;

v. the secondary pipe diameter;

vi. the catalyst length/diameter ratio;

vii. the catalyst free area;

viii. the interaction between the secondary pipe length and the location of the converter within; and

ix. the interaction between the primary and secondary pipe lengths.

Other factors of possible interest included:-

x. The volume and configuration of pipe junctions;

xi. the catalyst cone entry/exit angle;

xiii. the cell density of the catalyst substrate; and

xiv. the cell wall thickness within the converter.

The volume and configuration of the pipe junctions and the catalyst entry/exit cone angles were not expected to have a significant effect and predicted exhaust port pressure histories from simulations of the baseline exhaust system, whose results are shown in Figures 4.3 to 4.6, confirm this supposition. The cell density and the cell wall thickness of the catalytic converter were lumped together and considered as the catalyst free area during this study. The limitations of the catalyst model used for these simulations and its possible effect on the results, is discussed further in Chapter 6.2.3. Figure 4.7 shows the

details and dimensions of interest of those exhaust system elements considered for investigation during this study. The details of the catalyst model used and elements modified during the study are shown in Figure 4.8.

4.2.3 The design of the modelling study

Initially, a range of dimensional values over which each factor was to be varied was defined. These are shown in Table 4.1 and were selected on the basis of both typical exhaust system configurations and manufacturing constraints.

These factors were allocated to an orthogonal array in accordance with a linear diagram (shown in Figures 4.9 and 4.10). The linear diagram was itself selected on the basis of investigating possible factor interactions; in this case the possible interactions between the location of the twin catalysts within the secondary pipes and the length of the secondary pipes, and between the lengths of the primary and secondary pipes. The orthogonal array is a matrix defining the composition of each simulation undertaken during the study. The factor levels were allocated across the array so that repetition of distribution patterns did not occur between the individual columns. Using this method it was then possible to estimate the effects of those factors which have been assigned to each column in the array and eliminated the need for performing a full factorial study for those factor levels of interest. Associated with each orthogonal array are a number of predetermined linear diagrams that indicate to which column of the array the main effect factors and any interactions of interest should be allocated. The linear diagrams are derived on the basis of eliminating any possible confounding of main effects and

interaction effects. This is achieved by ensuring that the factor levels in those columns allocated to interaction effects are distributed non-orthogonally in relation to both each other and their component main factor levels.

Columns marked e1 and e2 are those that were assigned to determine random error variation and were assigned to columns 8 and 11 since there was not expected to be any interaction between the primary pipe lengths and the location of the catalyst within the secondary pipes. Any factor effects which were shown to be less than this error variation were considered due to random experimental variation and were then pooled together to provide a total random error variation for the study. This is a valid assumption for any modelling study provided both the algorithm utilised can predict sufficiently accurate results and that all potential factor effects, and any possible confounding of them, have been considered in detail during the design of the orthogonal array.

4.2.4 Method of analysis of modelling results

Simulations were made of each exhaust system configuration using 1.6 litre, 16 valve engine input data with exhaust component dimensions fixed according to the levels of each factor indicated by the orthogonal array. For each simulation the engine torque from 1000 to 6000 r/min in 500 r/min steps was predicted. A statistical analysis of variance was then made of both the predicted torque for every factor at each speed and of the complete torque curve across the entire speed range. The torque curve was analysed in terms of a signal/noise (S/N) ratio, where the noise (in this instance speed) was considered to be an uncontrollable variable which had a significant effect on the response

variable. From this analysis it was possible to quantify the effect of each design parameter on each of the response variables. The signal/noise ratio was calculated from:

$$\text{Signal/noise ratio} = -10\log_{10}\left[\frac{1}{r}\sum\frac{1}{T^2}\right] \qquad (4.1)$$

where: r = Number of torque values from which the S/N ratio was calculated

T = Torque

The S/N ratio was indicative of the magnitude of the overall mean and of the variation of the response variable about the mean across the speed range. A high value of S/N ratio is desirable indicating a high mean torque and a flatter curve, which is preferable for car drivability. Typical engine torque-speed curves tend to drop off at higher engine speeds and there was a possibility that this trend may influence the S/N ratio such that any significant torque gains at lower speeds would not be indicated. However during this study the S/N ratio was used only to compare torque curves between simulations that had the same factor varied between different levels. No single factor was identified which caused a significant change in the curve trend across the entire speed range as it was modified and therefore, during this study, a difference in the value of S/N ratio was indicative of a change in one region of the torque curve only. Hence, for this application, the use of the S/N ratio as a gauge of the effect of modifications of a parameter's geometry on torque over the entire speed range was valid.

4.3 TAGUCHI ANALYSIS RESULTS

4.3.1 Derivation of results

Table 4.2 shows the calculation of the corrected S/N ratio for each exhaust build. The mean torque value was the mean predicted torque across the range of speeds considered for one exhaust build. The standard deviation, σ, was based on the nonbiased sample population calculation, since simulations were not performed at every possible speed:

$$\sigma = \sqrt{\frac{n\sum T^2 - \left(\sum T\right)^2}{n(n-1)}} \qquad (4.2)$$

The coefficient of variability was calculated from:

$$Coefficient\ of\ variability = \frac{\sigma}{\overline{T}} \times 100 \qquad (4.3)$$

where $\overline{T}$ was the mean torque for the exhaust build considered. The S/N ratio was then calculated from equation (4.1).

Table 4.3 shows the analysis of the mean corrected S/N ratio at each level. At each level the S/N ratio mean was calculated by averaging the S/N ratio for all simulations where the factor was set at level *n*. The calculation of the overall S/N ratio was an intermediate calculation check and should be identical for all factors being considered. The standard deviation of the mean S/N ratio at each level was calculated according to equation (4.2). The sum of the squares (S.S.) was then calculated by:

$$S.S. = no.\ of\ data\ points\ being\ considered \times degrees\ of\ freedom \times \left(\sigma_{S/N\ level\ n}\right)^2 \qquad (4.4)$$

Table 4.4 shows the analysis of variance table for the S/N ratio. There are two degrees of freedom (d.o.f.) for factors being considered at three levels and interactions between two factors being considered at three levels gives four degrees of freedom. Rows e1 and e2 were used to calculate the random error variation as discussed previously. The sum of the squares was taken from Table 4.3.

The mean squared (M.S.) was calculated by:

$$M.S. = \frac{S.S.}{d.o.f} \qquad (4.5)$$

Factor effects less than the lower of the rows assigned to calculate the random error variation were pooled with these values in accordance with Taguchi's [117, 118] concepts for experimental results analysis. Thus, the pooled error S.S. was given by the sum of the designated error values. The F factor was calculated by:

$$F = \frac{M.S._i}{M.S._{pooled\ error}} \qquad (4.6)$$

The pure sum of the squares was calculated by:

$$Pure\ S.S. = S.S. - d.o.f. \times M.S._{pooled\ error} \qquad (4.7)$$

The percentage contribution to the overall S/N ratio variation was then given by:

$$\%\ contribution = \frac{pure\ S.S.}{pure\ S.S._{total\ error}} \times 100 \qquad (4.8)$$

Figure 4.11 shows comparisons of the contribution of each factor to the overall variation of the S/N ratio. For the range of levels considered, the importance of selecting the secondary pipe length to obtain the optimum S/N ratio is clear. The catalyst free area,

length/diameter ratio and location are shown to have progressively less noticeable effects. The significance of factors shown to have less than 10% contribution to S/N ratio variation is doubtful. The S/N response due to modification to the geometry of each parameter, shown in Figure 4.12, is calculated as a mean value including all simulations with the parameter in question set at level *n*.

An analysis of variance was also performed for each factor at each engine speed simulated. The contribution from each factor to the total variation in torque at each engine speed is shown in Figures 4.13 to 4.16. The method for the calculation of these values was as equations (4.1) to (4.8). The effects of modifications to the geometry of each factor on the torque curve are shown in Figures 4.17 to 4.23 and the results from each level of interaction are shown in Figures 4.24 to 4.29. These are both calculated as a mean torque including all simulations with the parameter in question set at level *n*.

4.3.2 Analysis of results

The analysis of the S/N ratio is considered first since its optimisation represents a useful improvement in engine torque across the whole speed range. Figure 4.11 quantifies the contribution of each factor to the overall variation in S/N ratio for the range of dimensions of the factors considered during the study. The secondary pipe length is shown as the most significant single factor and potentially returns the highest S/N ratio once its length is optimised from the limited range of levels considered. Figure 4.12 shows that the secondary pipe length is also highly significant at high speeds. This is validated by Figure 4.17 which shows the mean torque response due to modification of

the geometry of the secondary pipe length calculated as the mean torque of all simulations that include the secondary pipe length set at level *n*. The trend indicated shows considerable potential improvements to torque in the high-speed region as the secondary pipe lengths were progressively reduced. The catalyst free area and length/diameter ratio are shown in Figure 4.11 to be the next most significant factors that influence S/N ratio variation and Figure 4.15 shows that they both contributed relatively little to the torque variation at individual speeds across the speed range. This suggests that their dimensions should therefore be selected on the basis of the optimum value for S/N ratio only for the range of dimensions considered. Figure 4.12 shows little variation in S/N ratio for catalyst length/diameter ratios of 1-2, allowing for other design factors to be considered at the design stage with little compromise to the engine performance; the S/N ratio is however more sensitive to changes in the geometry of the catalyst free area.

Figure 4.11 shows the location of the catalytic converter to be the fourth most significant factor for S/N variation. However, since this contribution is less than 10% and Figure 4.15 shows the converter location to be highly significant at 1500 r/min and 2500-5000 r/min, the converter location should only be selected on the basis of torque curve improvement in the low to mid-speed range. The remaining exhaust system components shown in Figure 4.11 are considered to have insignificant influence on the S/N ratio variation. Table 4.4 shows that the exhaust system factors considered during this study have accounted for over 75% of the total S/N ratio variation.

The remaining exhaust system components and the effect of any modification to their geometry on the torque variation in the low, mid and high-speed ranges were then considered. Referring to Figures 4.13 to 4.16, in the low to mid-speed region the catalyst location is shown to be the most significant factor. Figure 4.19 indicates how substantial smoothing of the torque characteristic from 2000-3500 r/min is possible at the expense of peak torque and small improvements from 3500-5500 r/min result from locating the catalyst in the downstream location. There is a small loss from 6000-7000 r/min as a consequence.

The next most significant factor in the low to mid-speed region was the interaction between the primary and secondary pipe lengths as shown in Figure 4.16 from 2000-5000 r/min. Figures 4.24 to 4.26 show the mean predicted torque curves for each level of interaction of which the exhaust systems comprising of long primary and short secondary pipes are preferable for engine drivability and show a relatively smooth progression to the peak torque at 3000 r/min. For the range of factors considered in this experiment, the secondary pipe length should be selected on the basis of obtaining the optimum S/N ratio. The primary pipe length alone is shown in Figure 4.13 not to have a significant effect on torque variation at any individual speed, then the primary pipe length should be selected so as to obtain the optimum torque based on the interaction between the primary and secondary pipe lengths only. There are no further factors that are shown to have any notable effect on low to mid-speed torque.

Analysis of the mid to high-speed ranges shows that the secondary pipe diameter, as indicated in Figure 4.14, is the only remaining factor that has any significant influence on torque variation during the study. As shown in Figure 4.21, between 4500-6000 r/min, the torque is improved considerably as the secondary pipe diameter is increased with torque reduced slightly at 2500 r/min and increased slightly at 3000 r/min.

The interaction between the secondary pipe length and the location of the catalytic converter is shown in Figure 4.16 to have little effect on torque variation at individual speeds, except at 1000 and 5000 r/min where a high significance is indicated. The mean predicted torque curves for each level of interaction are shown in Figures 4.27 to 4.29 and, although showing considerable variation between the torque curve trends for each level of interaction, the variation is dominated by the location of the catalyst within the secondary pipes.

The primary pipe diameter is indicated in Figure 4.14 to have little effect on torque variation at any speed for the range of diameters considered. Figure 4.20 indicates that as the diameter is reduced, an optimum dimension is reached that gives a high torque at high speed but reduction of the diameter beyond this point causes the torque to drop off at high speeds as a consequence of restricted flow as would be expected. It is not likely that any significant improvement to either torque or S/N ratio can be made by optimising the geometry of the primary pipe diameter; it is necessary only to select a pipe bore which is just greater than the diameter that results in restricted flow at high speeds.

4.3.2 Conclusions

For the range of factors considered during this study only, the following conclusions can be drawn:

i. Of the exhaust system components investigated the following list prioritises those parameters whose geometry should be optimised to improve the S/N ratio:-

   i. The secondary pipe length;

   ii. the catalyst free area; and

   iii. the catalyst length/diameter ratio.

ii. The remaining components investigated can be subdivided into separate priority lists of components which have been shown to have the most significant contribution to the torque variation at low to medium and medium to high speeds. For the low to mid-speed region, in order of priority, the following system parameters should have their geometry optimised:-

   i. The location of the catalyst; and

   ii. the interaction between the primary and secondary pipe lengths.

Similarly for the mid to high-speed region in order of priority:-

   i. The secondary pipe diameter; and

   ii. the primary pipe diameter.

The success of a statistical analysis of this type is entirely dependent on identification of those factors, and any interactions thereof, that have a significant influence on the response variable being considered. Furthermore, only a limited range of exhaust system

configurations can be considered. If other factors such as valve events and profiles are considered, then there are also potentially more interactions to consider and the method may become impractical as a rapid method for identifying the optimum system geometry. Hence, the following chapters detail further studies of the exhaust system wave action and gas exchange process. The objective of these studies is to define an exhaust system design strategy that enables an optimum system to be defined for any engine geometry and eliminates the requirement for a parametric or statistical study of predefined systems.

Table 4.1 Table of main factors considered during the study

Factors	Levels		
	1	2	3
A. Secondary pipe length	100 mm	350 mm	600 mm
B. Primary pipe length	200 mm	350 mm	500 mm
C. Catalyst location within secondary	upstream	midpoint	downstream
D. Primary pipe diameter	35 mm	42 mm	49 mm
E. Secondary pipe diameter	35 mm	42 mm	49 mm
F. Catalyst length/diameter ratio	2	3	4
G. Catalyst free area	30%	50%	70%

Table 4.2 Analysis of S/N ratio

Exhaust build	Mean torque (Nm)	Standard deviation	Coeff of Variability (CV) %	S/N ratio	Corrected S/N ratio (-40)
1	108.92	15.37	14.111	40.423	0.4229
2	109.46	14.813	13.533	40.496	0.4958
3	109.77	14.749	13.436	40.527	0.5272
4	109.77	14.726	13.416	40.524	0.5241
5	109.92	15.201	13.829	40.521	0.5208
6	108.23	16.569	15.309	40.313	0.3131
7	110.08	14.705	13.359	40.554	0.5545
8	109.62	15.163	13.833	40.494	0.494
9	109.31	15.955	14.596	40.422	0.4215
10	110	14.532	13.211	40.553	0.5528
11	108.31	17.08	15.77	40.278	0.278
12	109.31	15.223	13.926	40.46	0.4598
13	108	16.406	15.191	40.292	0.2918
14	109.69	15.424	14.061	40.487	0.4872
15	108.69	17.226	15.848	40.286	0.2855
16	107.85	18.479	17.135	40.126	0.1265
17	110.23	15.15	13.744	40.54	0.54
18	109.15	16.577	15.187	40.378	0.3783
19	107.85	17.31	16.051	40.236	0.2356
20	109.85	15.47	14.083	40.489	0.4893
21	108.85	17.444	16.027	40.3	0.2996
22	108.62	18.228	16.782	40.2	0.1999
23	107.54	16.86	15.678	40.231	0.2309
24	108.46	17.548	16.179	40.255	0.2551
25	108	15.626	14.468	40.344	0.3443
26	108.46	15.967	14.721	40.364	0.3643
27	107.85	19.33	17.923	40.076	0.0755

	1	2	3	4	5	6	7	8	9	10	11	12	13
Level	A: Sec pipe length	B: Prim pipe length	AB	AB	C: Cat loc'n	AC	AC	e1	D: Prim pipe dia	E: Sec pipe dia	e2	F: Cat L/dia ratio	G: Cat free area
1	0.4748	0.4178			0.3613			0.3848	0.3409	0.3391	0.3695	0.4161	0.3243
2	0.3777	0.3453			0.4333			0.3504	0.4105	0.3744	0.3491	0.4050	0.3552
3	0.2771	0.3665			0.3350			0.3945	0.3783	0.4161	0.4111	0.3085	0.4502
S/N mean	0.3766	0.3766			0.3766			0.3766	0.3766	0.3766	0.3766	0.3766	0.3766
Std dev of S/N mean	0.0988	0.0372			0.0508			0.0231	0.0348	0.0385	0.0316	0.0591	0.0656
S.S.	0.1759	0.0250			0.0466			0.0096	0.0218	0.0267	0.0180	0.0630	0.0775

Figure 4.3 Analysis of mean corrected S/N ratio at each level

Table 4.4 Analysis of variance table for signal/noise ratio

Source	d.o.f.	S.S.	M.S.	Pooled	F	Pure S.S.	% contribution
A. Secondary pipe length	2	0.17594	0.08797		18.7095	0.16654	33.6187
B. Primary pipe length	2	0.02503	0.01251		2.66154	0.01562	3.15418
C. Catalytic converter location	2	0.04662	0.02331		4.95741	0.03721	7.51253
D. Primary pipe diameter	2	0.02184	0.01092		2.32291	0.01244	2.51134
E. Secondary pipe diameter	2	0.02673	0.01337		2.84289	0.01733	3.49844
F. Catalyst length/diameter ratio	2	0.06301	0.03151		6.70062	0.05361	10.8218
G. Catalyst free area	2	0.07752	0.03876		8.24393	0.06812	13.7515
AB. Interaction	4	0.00996	0.00249	yes			
AC. Interaction	4	0.02105	0.00526		1.11932	0.00224	0.45301
e1	2	0.00964	0.00482	yes			
e2	2	0.01802	0.00901	yes			
(pooled e)	8	0.03762	0.0047			0.12225	24.6785
Total	26	0.49537	0.01905			0.49537	100

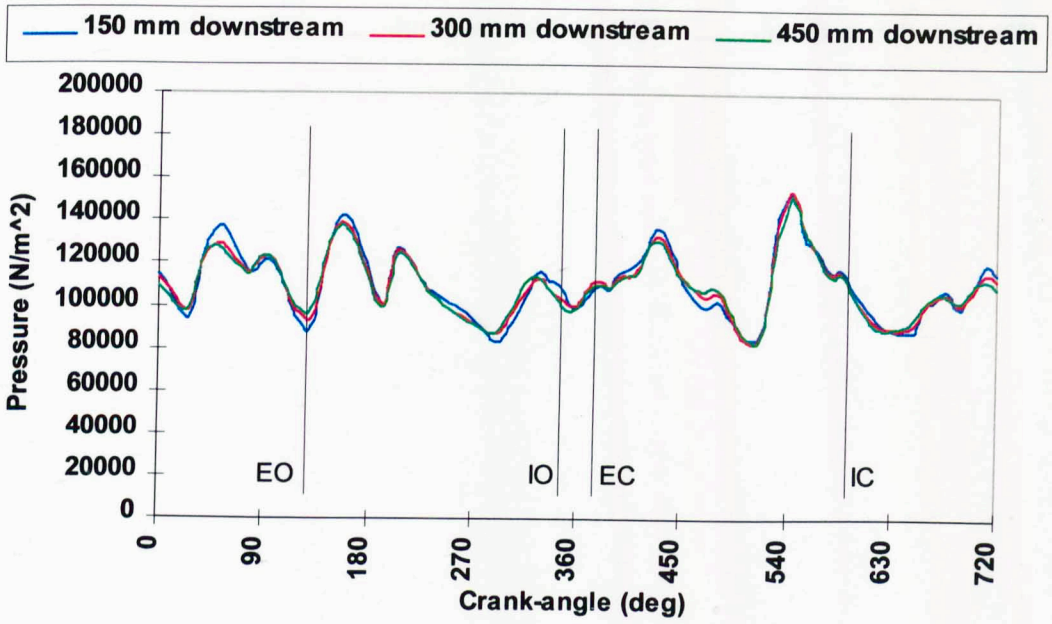

Figure 4.1 Exhaust port pressure histories of baseline exhaust system with location of the silencer box varied – 3000 r/min

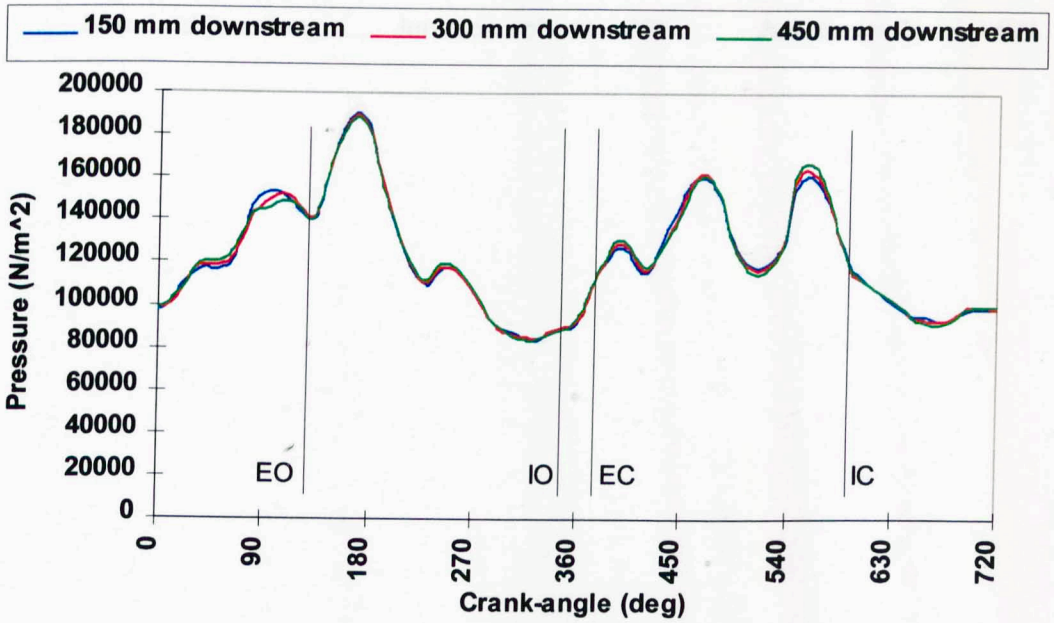

Figure 4.2 Exhaust port pressure histories of baseline exhaust system with location of the silencer box varied – 5000 r/min

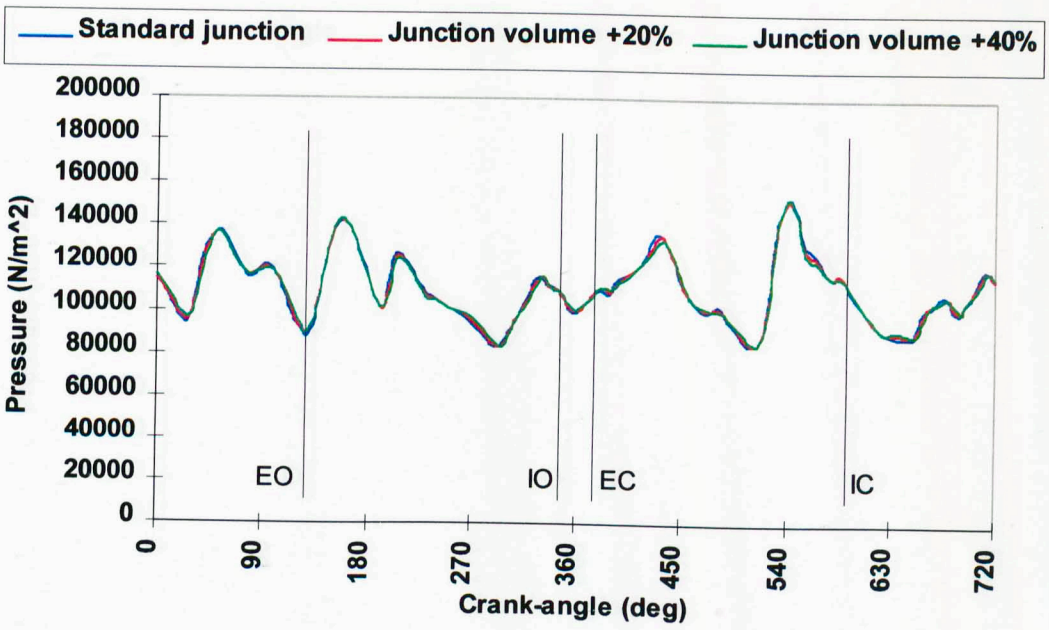

Figure 4.3 Baseline exhaust system with junction volumes varied – 3000 r/min

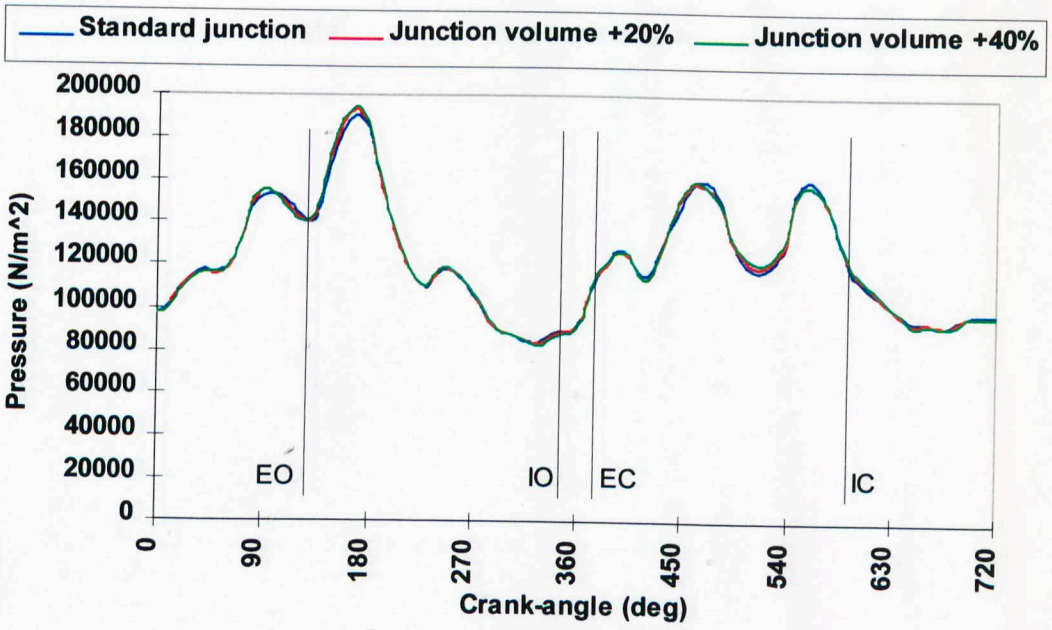

Figure 4.4 Baseline exhaust system with junction volumes varied – 5000 r/min

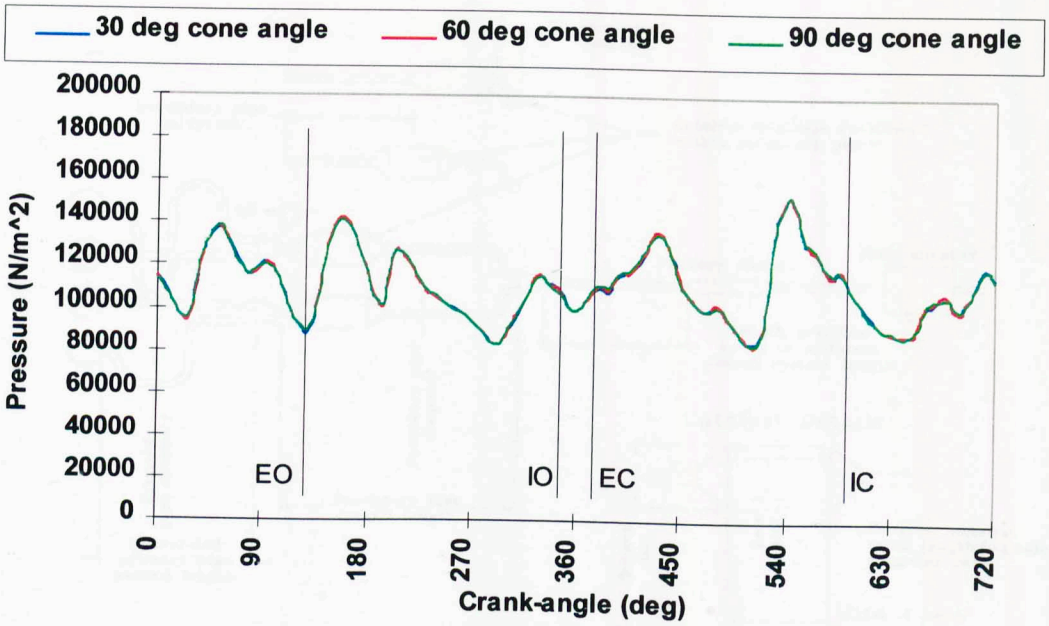

Figure 4.5 Baseline exhaust system with catalyst entry/exit cone angles varied – 3000 r/min

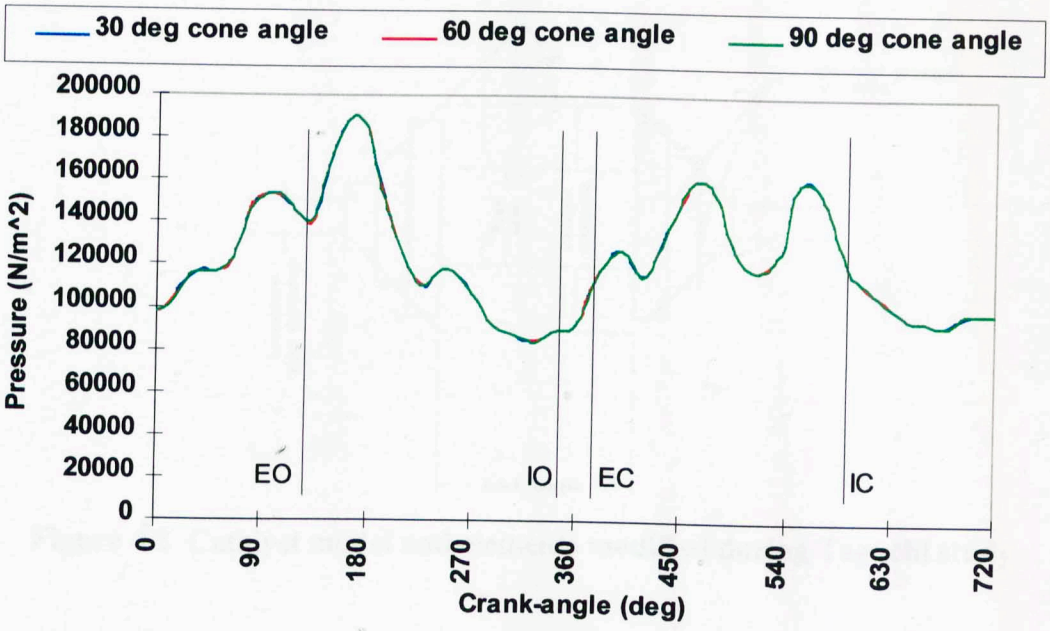

Figure 4.6 Baseline exhaust system with catalyst entry/exit cone angles varied – 5000 r/min

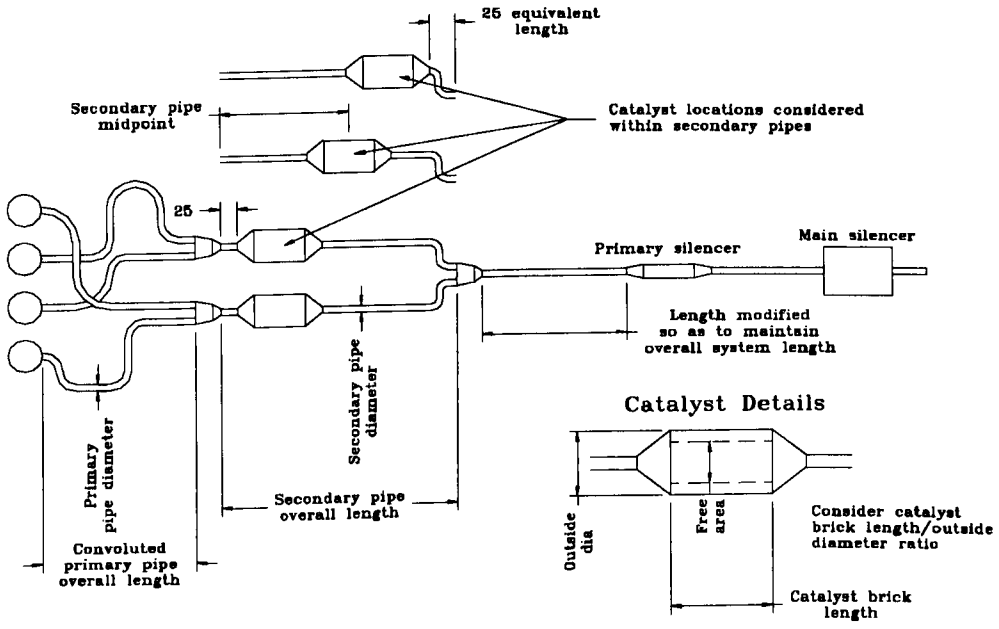

Figure 4.7 Exhaust system details and those elements modified during Taguchi study

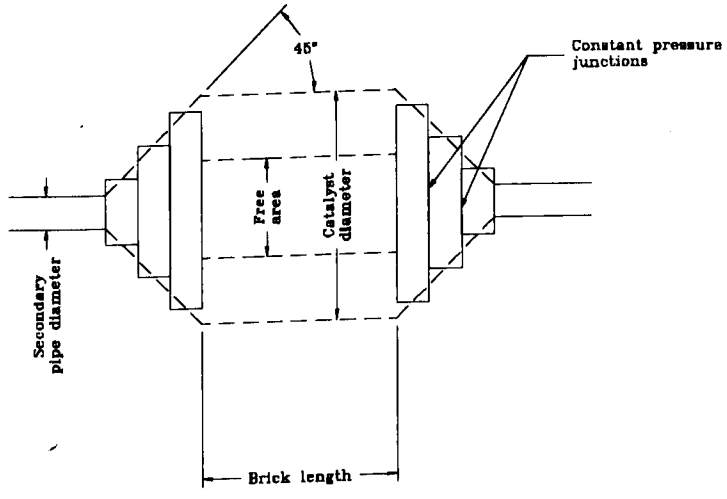

Figure 4.8 Catalyst model and elements modified during Taguchi study

	FACTORS												
	1	2	3	4	5	6	7	8	9	10	11	12	13
RUN	A	B	AB	AB	C	AC	AC	e1	D	E	e2	F	G
1	1	1	1	1	1	1	1	1	1	1	1	1	1
2	1	1	1	1	2	2	2	2	2	2	2	2	2
3	1	1	1	1	3	3	3	3	3	3	3	3	3
4	1	2	2	2	1	1	1	2	2	2	3	3	3
5	1	2	2	2	2	2	2	3	3	3	1	1	1
6	1	2	2	2	3	3	3	1	1	1	2	2	2
7	1	3	3	3	1	1	1	3	3	3	2	2	2
8	1	3	3	3	2	2	2	1	1	1	3	3	3
9	1	3	3	3	3	3	3	2	2	2	1	1	1
10	2	1	2	3	1	2	3	1	2	3	1	2	3
11	2	1	2	3	2	3	1	2	3	1	2	3	1
12	2	1	2	3	3	1	2	3	1	2	3	1	2
13	2	2	3	1	1	2	3	2	3	1	3	1	2
14	2	2	3	1	2	3	1	3	2	2	1	2	3
15	2	2	3	1	3	1	2	1	2	3	2	3	1
16	2	3	1	2	1	2	3	3	1	2	2	3	1
17	2	3	1	2	2	3	1	1	2	3	3	1	2
18	2	3	1	2	3	1	2	2	3	1	1	2	3
19	3	1	3	2	1	3	2	1	3	2	1	3	2
20	3	1	3	2	2	1	3	2	1	3	2	1	3
21	3	1	3	2	3	2	1	3	2	1	3	2	1
22	3	2	1	3	1	3	2	2	1	3	3	2	1
23	3	2	1	3	2	1	3	3	2	1	1	3	2
24	3	2	1	3	3	2	1	1	3	2	2	1	3
25	3	3	2	1	1	3	3	3	2	1	2	1	3
26	3	3	2	1	2	1	1	1	3	2	3	2	1
27	3	3	2	1	3	2	2	2	1	3	1	3	2

Figure 4.9 Allocation of factors to L_{27} orthogonal array

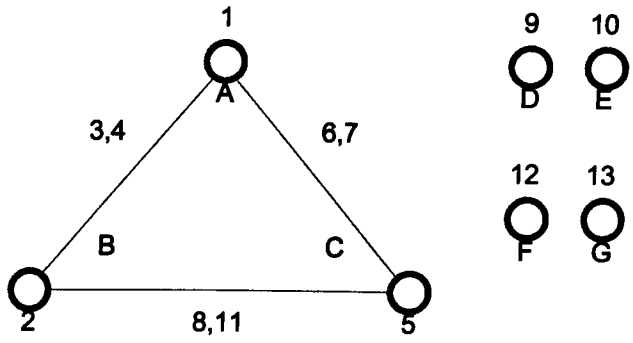

Figure 4.10 Linear diagram for L_{27} orthogonal array

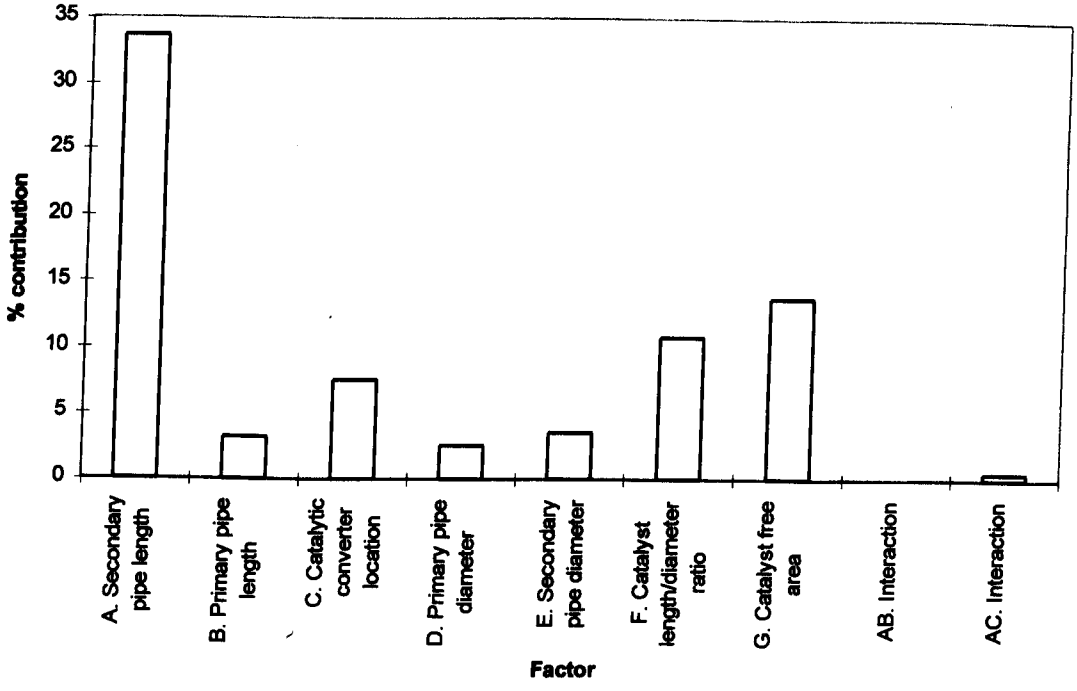

Figure 4.11 Percentage contribution of each factor to the overall variation in signal/noise ratio

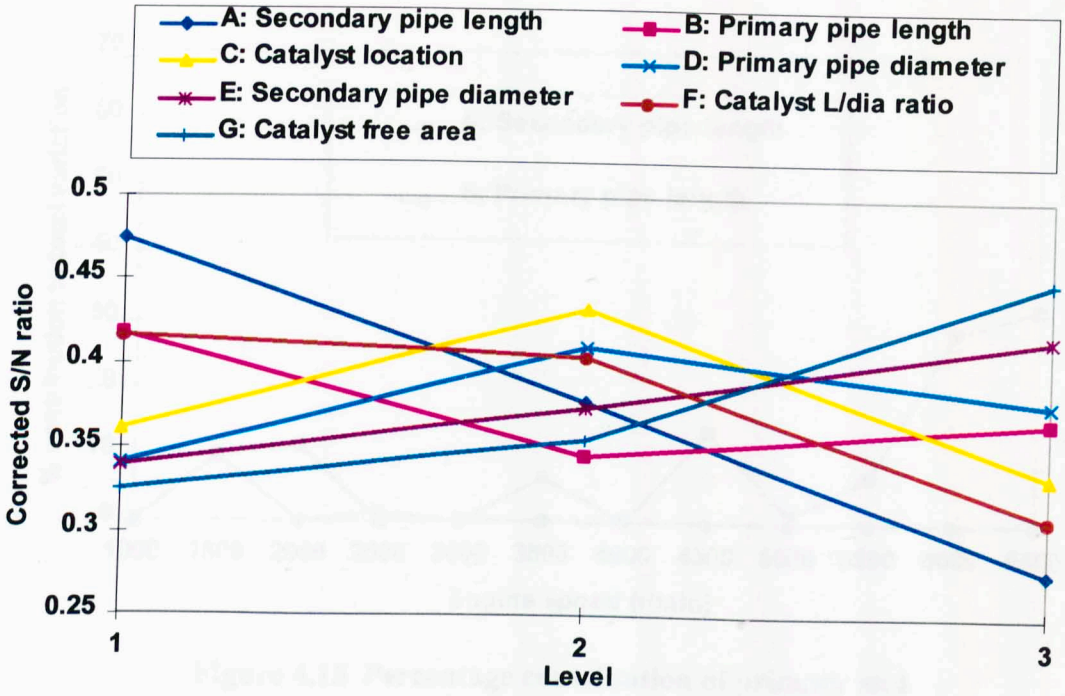

Figure 4.12 Mean S/N ratio response for each level of factors

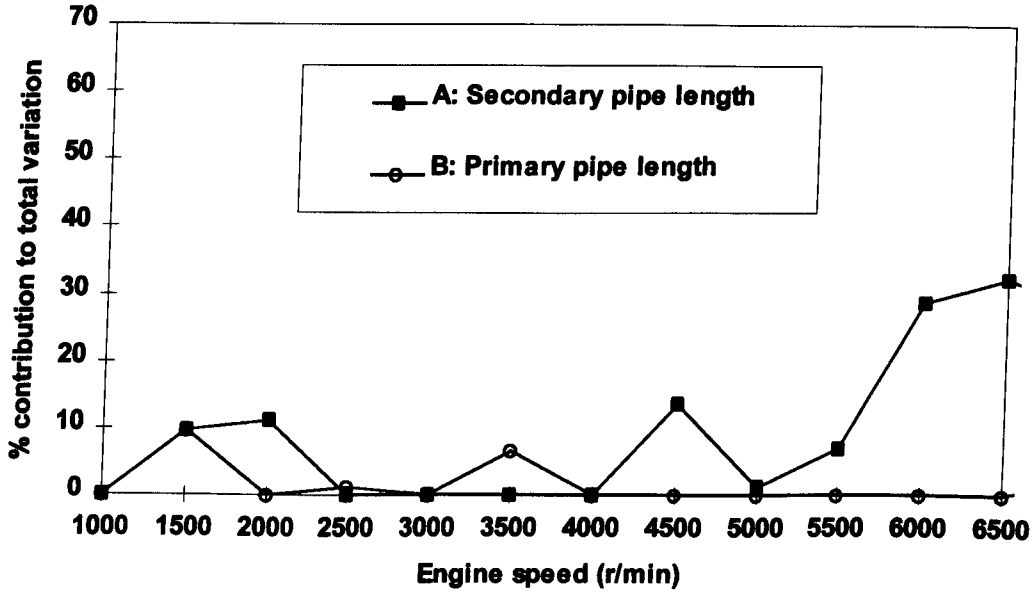

Figure 4.13 Percentage contribution of primary and secondary pipe lengths to variation in torque

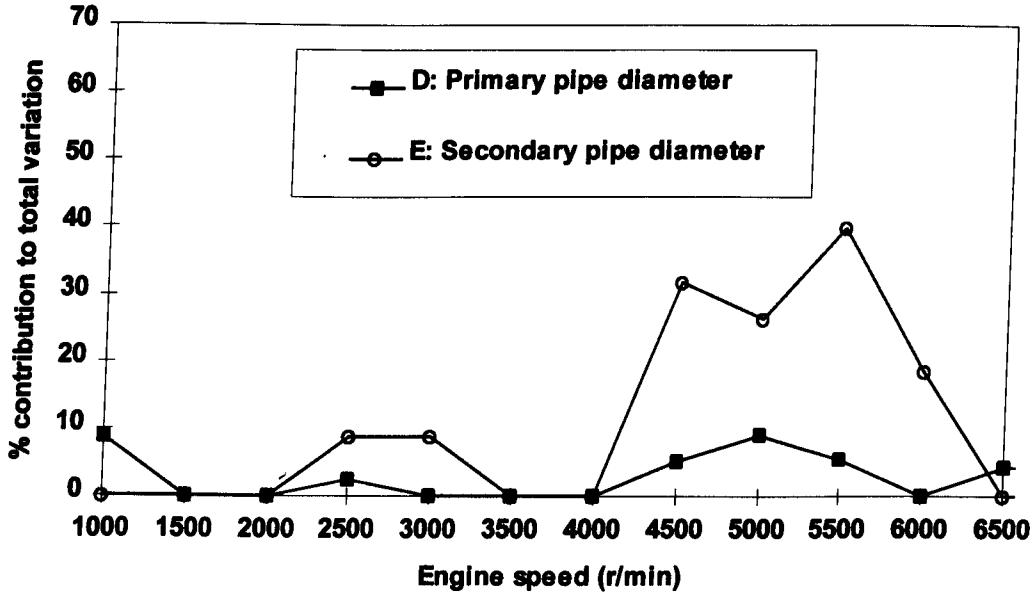

Figure 4.14 Percentage contribution of primary and secondary pipe diameters to variation in torque

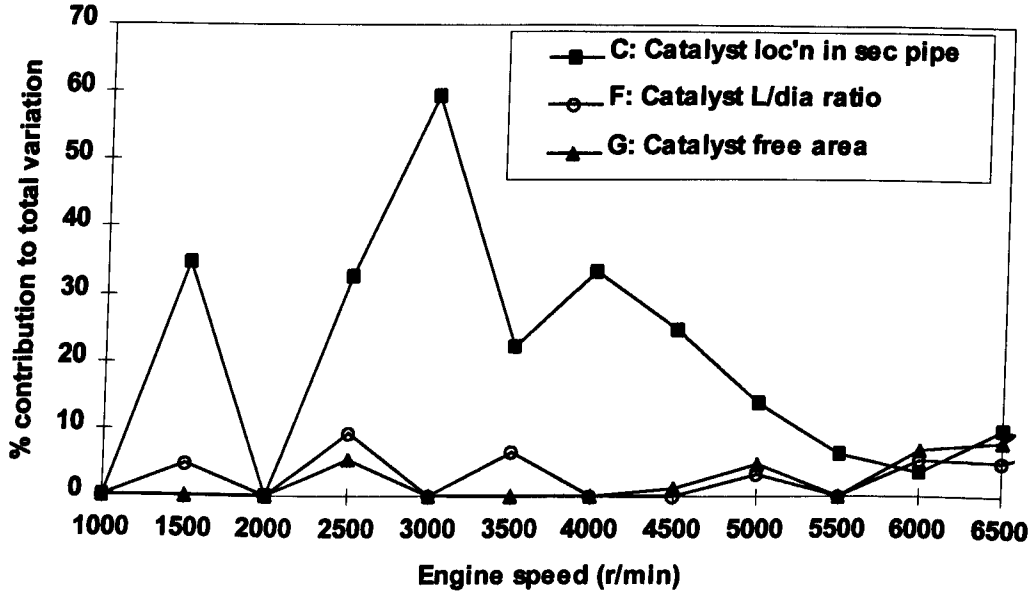

Figure 4.15 Percentage contribution of catalyst location and geometry to variation in torque

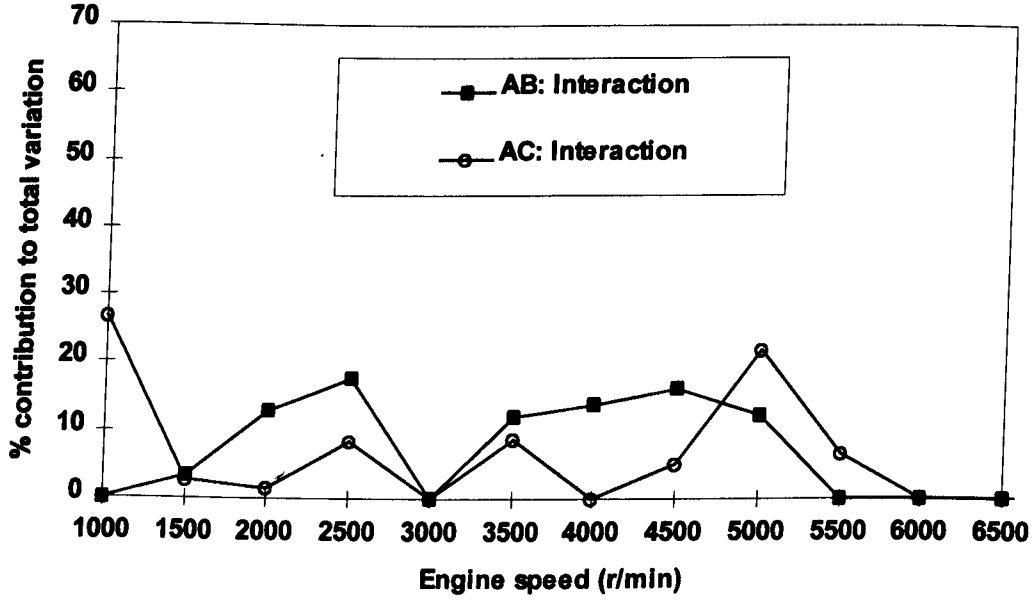

Figure 4.16 Percent contribution of interactions between AB (primary - secondary pipe length) and AC (secondary pipe length-catalyst location) to variation in torque

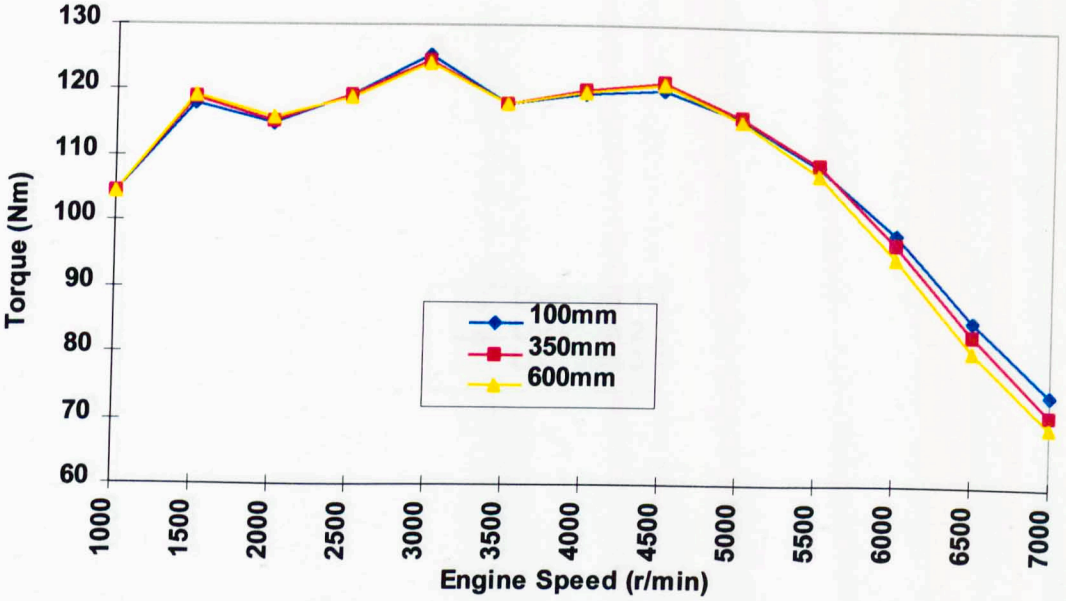

Figure 4.17 Factor A: secondary pipe length – mean effect of increase in length

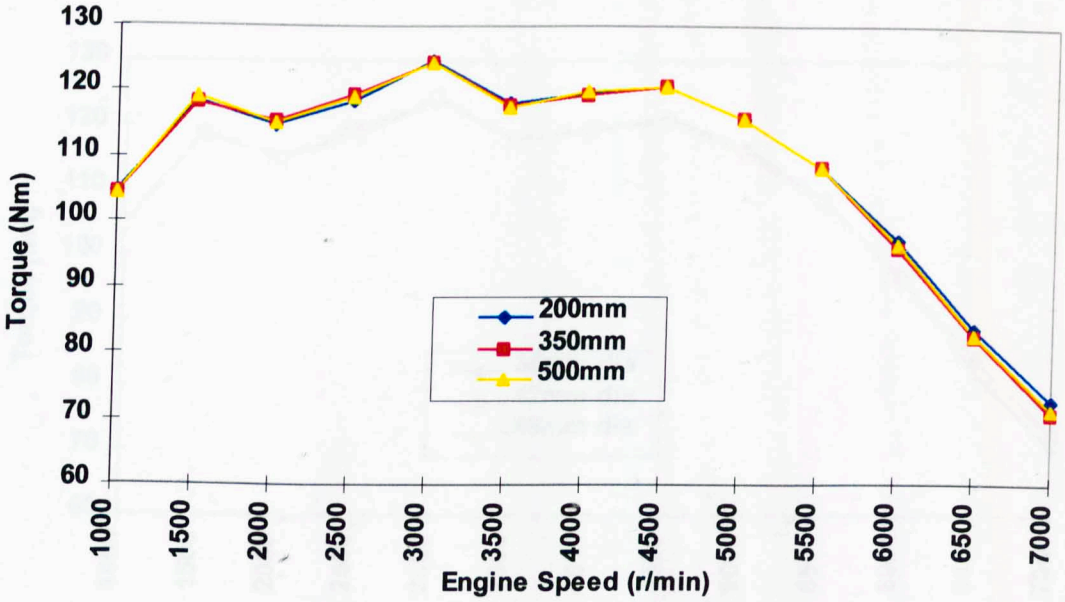

Figure 4.18 Factor B: primary pipe length – mean effect of increase in length

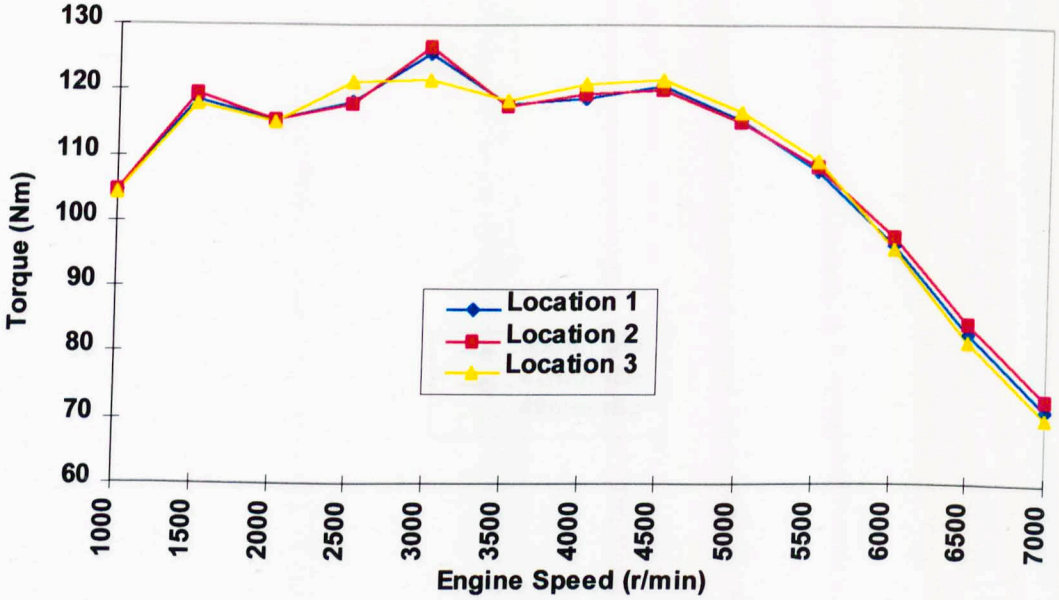

Figure 4.19 Factor C: catalyst location – mean effect of relocation

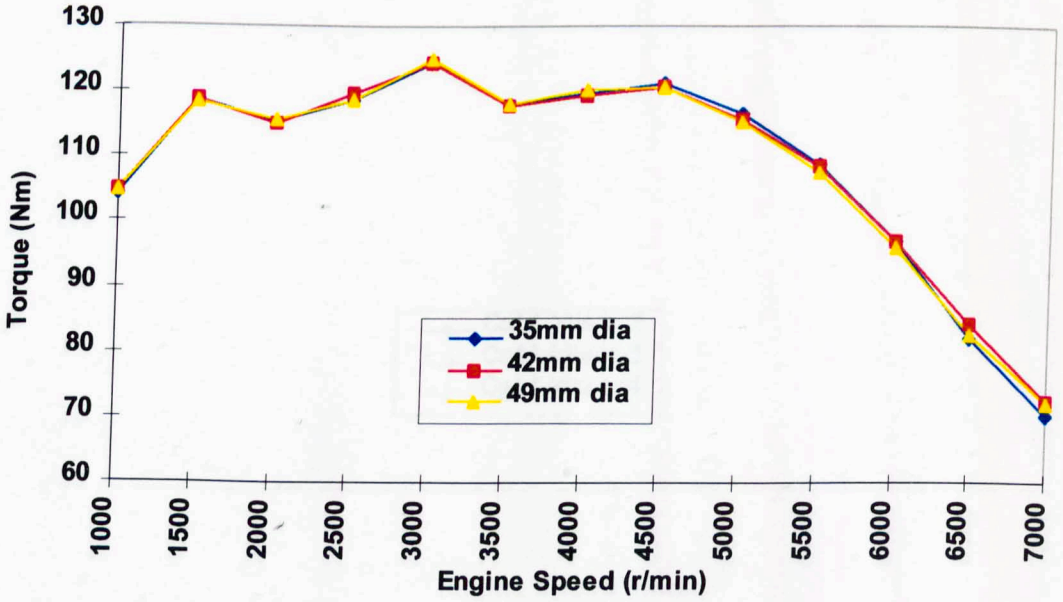

Figure 4.20 Factor D: primary pipe diameter – mean effect of increase in diameter

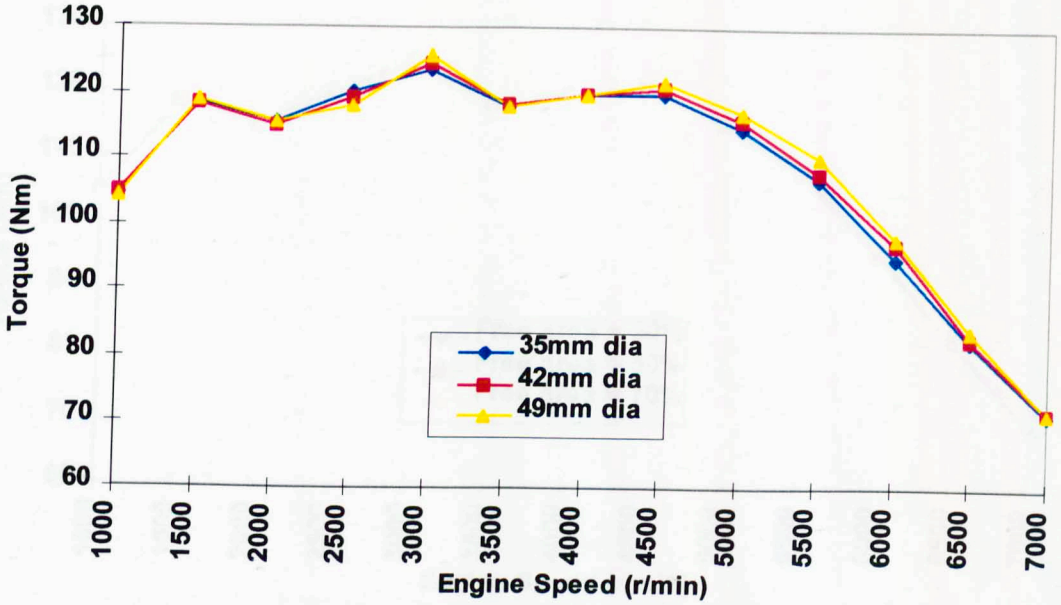

Figure 4.21 Factor E: secondary pipe diameter – mean effect of increase in diameter

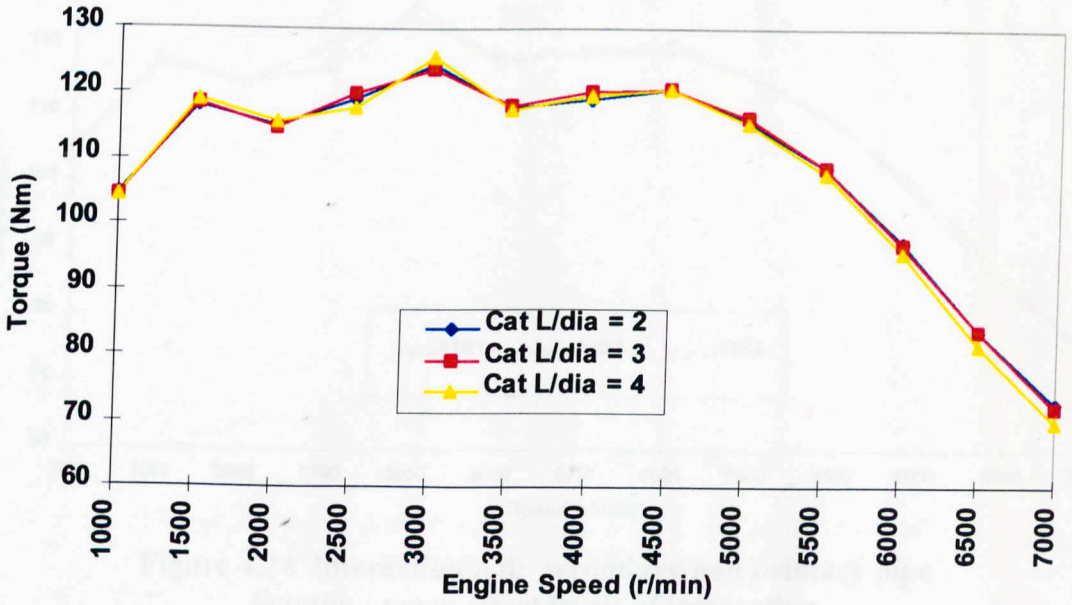

Figure 4.22 Factor F: catalyst length/diameter ratio – mean effect of increase in ratio

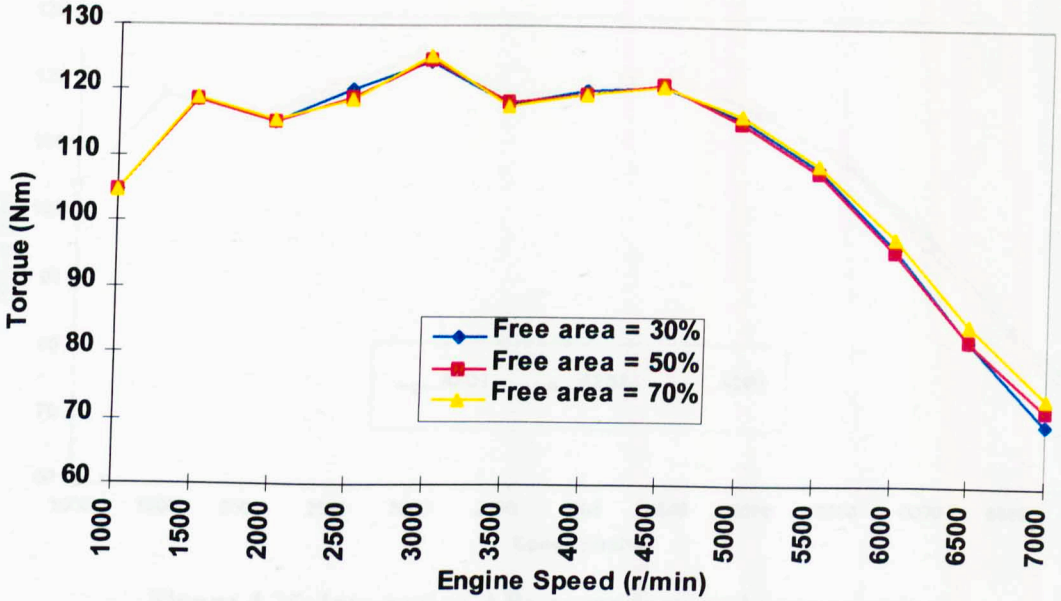

Figure 4.23 Factor G: catalyst free area – mean effect of increase in area

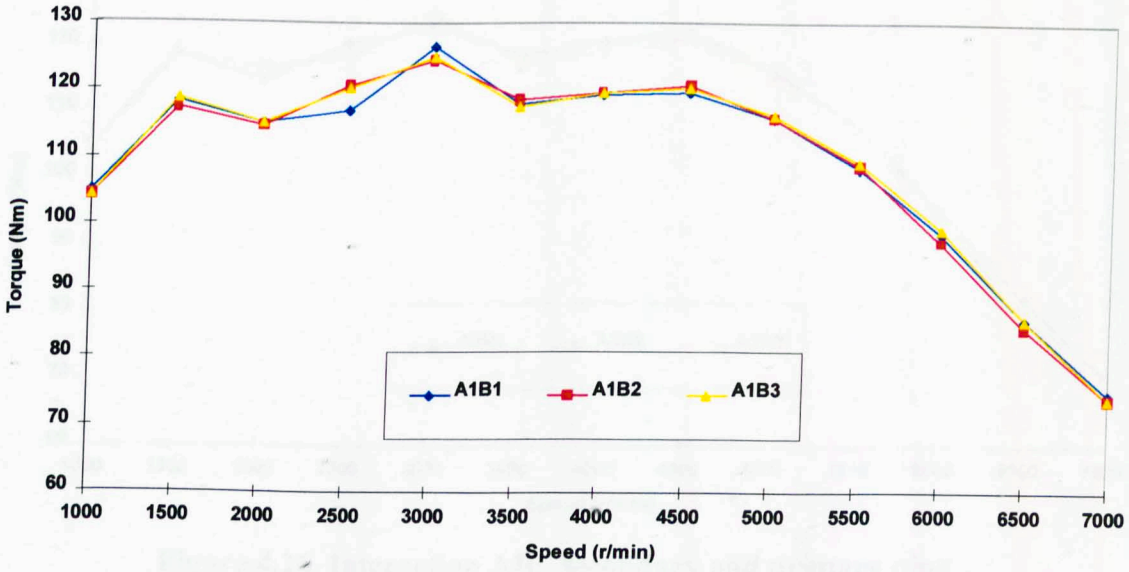

Figure 4.24 Interaction AB: secondary and primary pipe lengths – mean effect levels of interaction

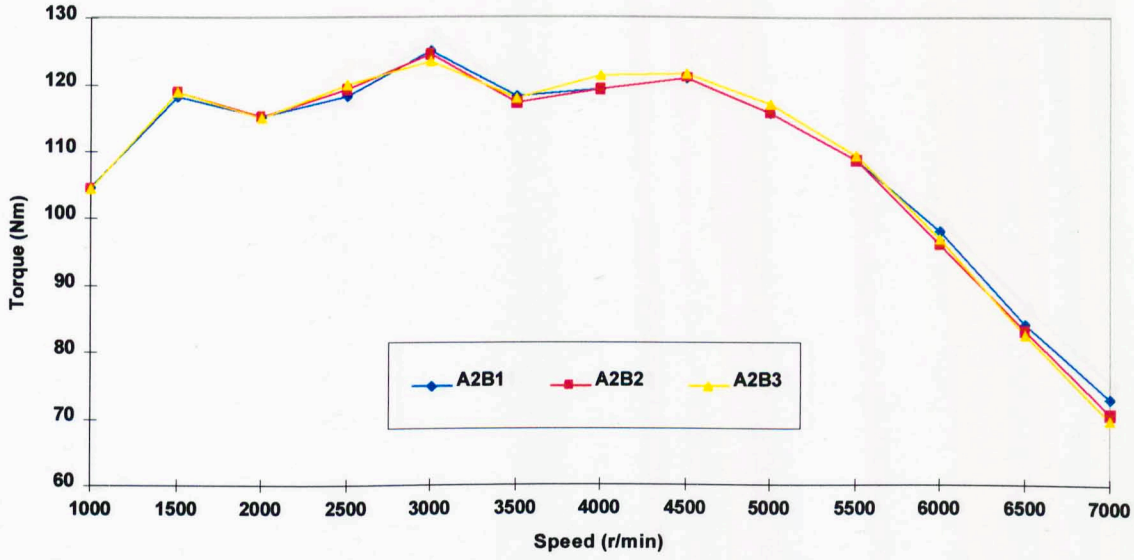

Figure 4.25 Interaction AB: secondary and primary pipe lengths – mean effect levels of interaction

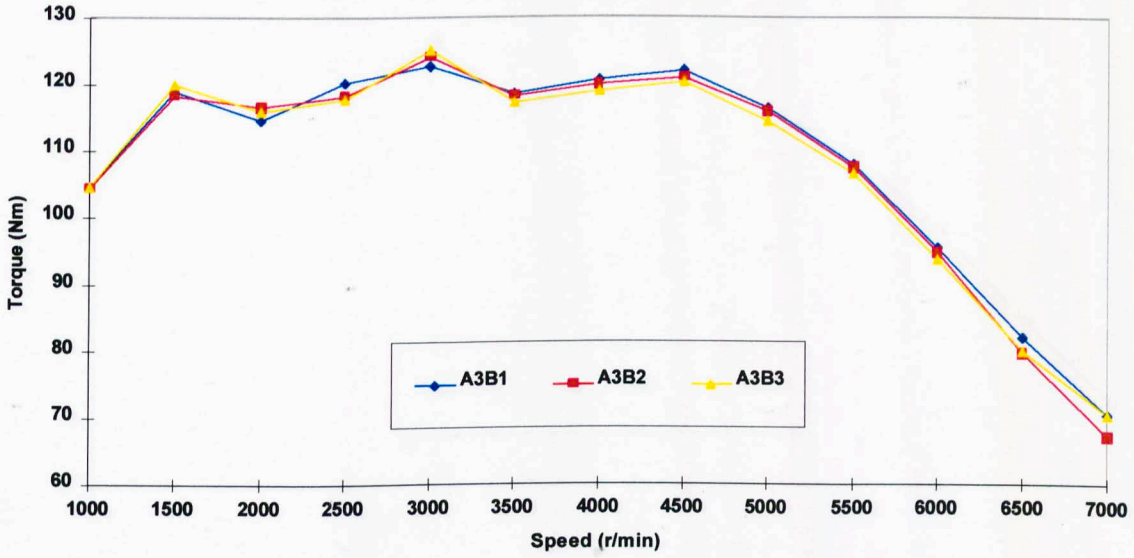

Figure 4.26 Interaction AB: secondary and primary pipe lengths – mean effect levels of interaction

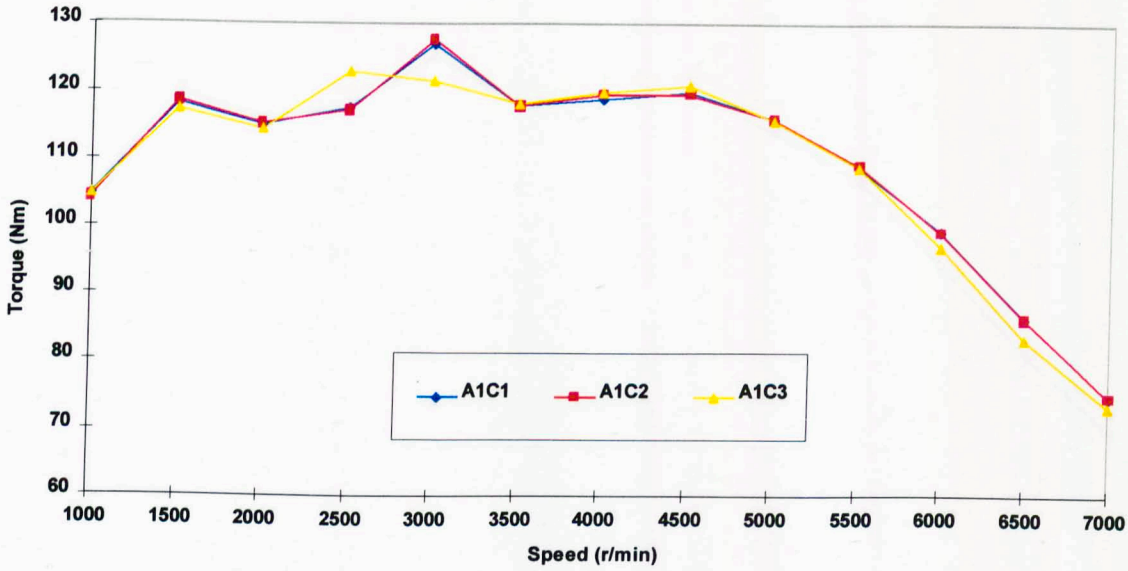

Figure 4.27 Interaction AC: secondary pipe length and catalyst location – mean effect levels of interaction

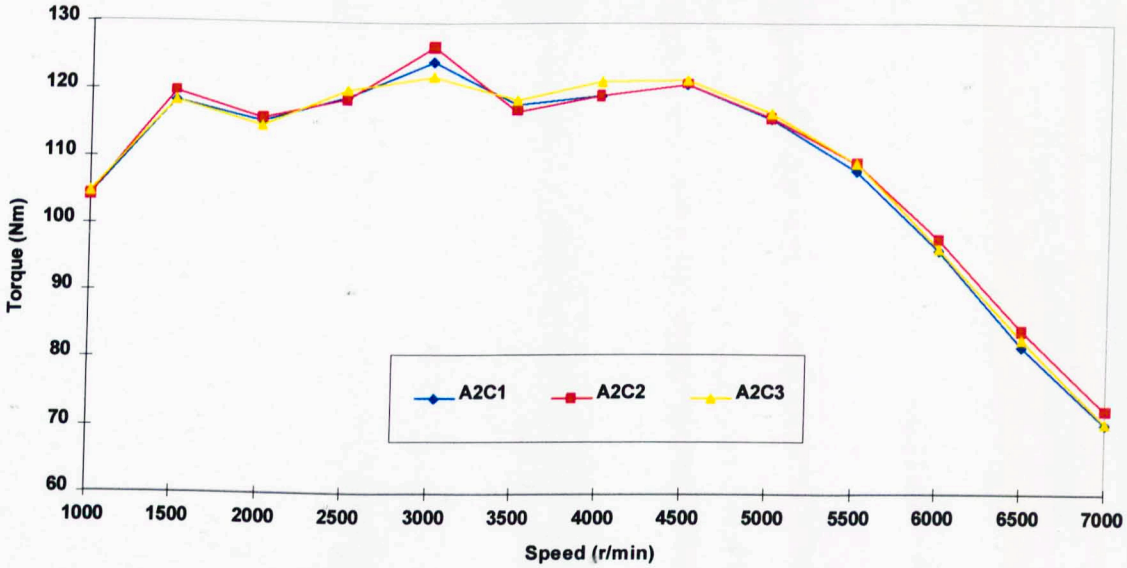

Figure 4.28 Interaction AC: secondary pipe length and catalyst location – mean effect levels of interaction

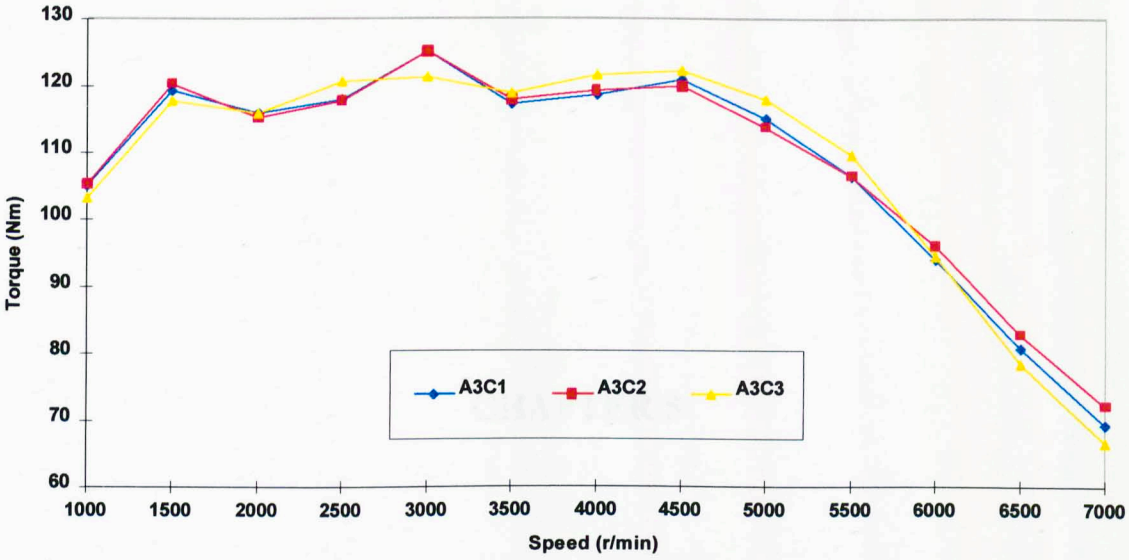

Figure 4.29 Interaction AC: secondary pipe length and catalyst location – mean effect levels of interaction

CHAPTER 5

INFLUENCE OF THE EXHAUST PORT PRESSURE HISTORY ON ENGINE BREATHING CHARACTERISTICS

CHAPTER 5

INFLUENCE OF THE EXHAUST PORT PRESSURE HISTORY ON ENGINE BREATHING CHARACTERISTICS

5.1 INTRODUCTION

The pressure history at the exhaust port, during the exhaust period of the cycle, will influence the filling and emptying of the cylinder. A high pressure differential across the exhaust valve, that is high in-cylinder pressure to low downstream exhaust valve pressure, is desirable during this period in order to assist cylinder emptying. At full load, the pressure at the exhaust port of a typical 1400 cc production SI engine can vary significantly across the driving speed range and the reader is referred to the Figures 3.18 to 3.23 for typical values. This dynamic pressure history is a result of the interaction and reflections of the high amplitude compressive pressure waves generated by each cylinder exhausting. Reverse flow can also occur if the downstream valve pressure is raised to a higher value than the in-cylinder pressure. This can result in excessive residual gases remaining in the combustion chamber at EVC, thus both reducing volumetric efficiency and influencing the subsequent combustion process. Since the phasing of this pressure history relative to the exhaust event is a function of engine speed, exhaust system geometry (ordinarily fixed) and the exhaust gas conditions, then it is not possible to generate a low pressure throughout the exhaust period at every speed. In practice a high pressure will inevitably exist at the exhaust port during some period of the exhaust process. The objective of exhaust system tuning is to select the exhaust system geometry that will give the optimum exhaust port pressure history at a given speed so as to enhance

engine breathing. Thus, it is necessary to identify the optimum achievable exhaust port pressure history.

Exhaust gas exchange processes influence two key engine operating parameters, bmep and volumetric efficiency, and these two performance indictors are related in that they generally have the same trends when they are plotted against speed for a given engine configuration. A direct relationship exists between bmep and volumetric efficiency such that an increase in the mass of induced fuel-fresh air charge, mixed in the proper proportions, will improve bmep. The relationship between mep and torque is given by:

$$mep(kPa) = \frac{2\pi n_r T(Nm)}{Vd(dm^3)} \qquad (5.1)$$

where n_r = 2 for 4 stroke engines, n_r = 1 for 2 stroke engines and Vd = displacement volume. However, it can be difficult to recognise this relationship in terms of the gas exchange processes and this is particularly the case when studying exhaust port pressure histories. A comparison of performance indicators resulting from the installation of two different exhaust systems often shows differing values of volumetric efficiency but identical values of torque. This is because the advantages gained through improved cylinder filling are offset by increased cylinder pumping losses. In comparing the exhaust port pressure histories from two such systems, it is not clear as to which period of the pressure history most influences pumping losses and which influences volumetric efficiency. Conventional theory [78, 79] has generalised that the exhaust port pressure history during the period IVO to EVC influences volumetric efficiency. However, examination of Figure 5.1 shows

predicted exhaust port pressure histories generated by models of two identical engines fitted with different exhaust systems.

System	Primary (mm)	Secondary (mm)	Tertiary (mm)
1	450 mm L × 35 mm Ø	780 mm L × 43 mm Ø	592 mm L × 47 mm Ø
2	600 mm L × 35 mm Ø	780 mm L × 43 mm Ø	592 mm L × 47 mm Ø

The models predict identical values of volumetric efficiency at a given speed but the exhaust port pressure histories, particularly during valve overlap, are clearly different. Conventional theory does not suggest why this should be the case and a question arises as to whether the volumetric efficiency is related to the mean pressure during the overlap period or to some other critical period, perhaps lying outside the overlap period. Thus, this phase of the work is intended to clearly identify the relationship between the exhaust port pressure at selected periods of the exhaust process and engine performance indicators.

5.2 CONCEPT OF STUDY

To undertake a detailed investigation of the effect of the exhaust port pressure history on engine performancé, it is necessary, for the reasons given previously, to be able to manipulate this pressure history according to user-defined requirements. This type of analysis has been undertaken previously in studies investigating the induction system and processes. Ohata and Isheda [62] fixed the pressure at the inlet port and were able to identify the critical period of the induction process from BDC to IVC in terms of its influence on cylinder filling. They used a simple model, based upon quasi-steady flow across valves into a cylinder volume, which only required the definition of the

total pressure condition upstream and downstream of each valve; pipe gas dynamics were not calculated and the exhaust port was assumed to remain at atmospheric pressure throughout the cycle. It was decided to apply a similar approach to the analysis of the exhaust port pressure history, but in this case using the fully validated engine simulation model. This more detailed model was more suited to a study of the exhaust event gas exchange process. For four-stroke engines, the relative effect of the exhaust system gas dynamics on engine performance is less than that of the intake system. Thus, the use of a more detailed model ensured that all effects were identified.

5.2.1 Manipulation of the exhaust port pressure history

The objective was be able to control the pressure at the exhaust port throughout the cycle so as to understand the effect of the pressure history on engine performance characteristics. For this phase of the study the engine cycle simulation code detailed previously in Chapter 2 was to be used. Intake system gas-dynamics, the valve models and the in-cylinder calculation were to be retained. However, at the exhaust port a user defined pressure history, that eliminated the requirement for downstream gas-dynamics calculations, was to be imposed. In terms of the organisation of the computer code, fixing the pressure at any instant has particular difficulties. At any instant in time and space, the total pressure condition is given by the superposition of all of the arriving pressure waves (see equation (A2.3.8)) travelling in both directions. Thus, referring to Figure 5.2, the total pressure condition at any instant can be composed of an infinite number of combinations of leftward and rightward moving waves. Example 1 shows a total pressure condition of p_T at time $t=\theta$, which comprises the superposition of a leftward moving, high-amplitude compressive wave

and a rightward moving rarefaction wave. In this case gas particle flow would be leftwards. Example 2 shows that the same total pressure condition is achieved through the superposition of identical amplitude leftward and rightward moving compressive waves. In this example the gas particle flow would be zero.

The engine simulation computer code used throughout this project uses the method of characteristics to solve the unsteady gas flow in the manifold systems. At the end of each time-step, the pipe calculation subroutine calculates values of the λ and β characteristics at every internal mesh and the values of the incident characteristics at the pipe ends. The valve model, detailed in Section 2.7.1, then calculates the values of the reflected characteristics, at the appropriate pipe ends, based on the values of the incident pressure characteristic, the restriction (in this case, the valve) effective free area and the in-cylinder pressure. The gas mass flow rate across the valve is then derived from the mass flow at the pipe mesh immediately adjacent to the valve. This illustrates why, when imposing a user-defined pressure condition at the exhaust port, care must be taken to ensure that the mass flow rate to and from the cylinder is also calculated correctly.

McConnell [34] organised the solutions to the pipe/volume boundary condition into a matrix format, which are accessed by the engine simulation program as required. The equations governing the various flow regimes are high order polynomial equations that are detailed in Section 2.7.1. Figure 2.6 shows the graphical solution to the various flow regimes encountered where the x-axis = $f\left(p_i,\ p_1\right)$ and the y-axis = $f\left(p_i,\ p_r,\ p_1\right)$. These are both linear functions, thus for a fixed value of k, p_1 and p_i

there is only one solution for p_r. This fact can be used to identify appropriate mass flow rates across the valve according to the pressure that the user wishes to fix at the exhaust port at any instant.

A iterative exhaust valve boundary condition subroutine was compiled that reads the total pressure that the user wishes to fix at the exhaust port at 1°CA intervals throughout the cycle. The subroutine makes extreme maximum and minimum initial guesses, at each time-step, of the incident pressure term value, p_i. The respective reflected pressure terms, p_r, are then calculated for each case based on knowledge of k and p_1. The total pressure condition for each case is then calculated, based on these first guess incident pressure terms. These calculated total pressure conditions are then compared to the pressure that the user wishes to fix at the exhaust port. If the difference falls outside pre-defined limits, then the incident pressure terms are revised and the procedure repeats until appropriate values of incident and reflected pressure terms are identified that produce the desired total pressure condition. Figure 5.3 shows a flow diagram of the calculation procedure and Appendix 3.0 lists the FORTRAN code listing of the subroutine incorporated into the main body of the code.

Such a binary iterative procedure is more suitable for this particular application compared to other methods, such as Newton-Raphson, because of the discontinuous functions that describe the solution to the sonic and subsonic flow regimes. Prior knowledge would be required of the flow regime, and hence the function, to apply such methods and this information is not available at the outset of the calculation. In addition, a different function corresponding to every value of k between 0.0 and 1.0

would have to be included explicitly in the calculation procedure. The method detailed above fails if the value of the required incident pressure term lies outside the limits of solution, $0.6 \leq \frac{2p_i - 1}{p_1} \leq 1.4$ (refer to Figure 2.6), but it is found in practice that, when imposing values of fixed pressure at the exhaust port within realistic limits, this situation rarely arises.

Pressure histories generally of the form shown in Figure 5.4 were to be imposed immediately downstream of each exhaust valve. For the greater duration of the engine cycle the pressure is fixed to some ambient pressure level. For a period of 30°CA the pressure is then either raised or lowered to a value of 160 kPa or 70 kPa, which represent compression and rarefaction waves respectively and are of amplitudes that are typically encountered in automotive exhaust systems. Simulations are performed with the pressure step indexed at 10°CA increments throughout the exhaust period. The study is intended to highlight discrete periods during the exhaust process when engine performance indicators are most sensitive to compression and rarefaction waves. Thus, an ideal achievable exhaust port pressure history can be defined.

5.2.2 Validity of calculation method

Prior to undertaking the study, the calculation method was comprehensively checked to ensure that the procedure for the calculation of the gas mass flow rate appropriate to the value of pressure imposed at the exhaust port was correct. This was checked by taking the exhaust port pressure history generated by a typical engine simulation model, shown in Figure 5.5(a). This pressure history was then used as input data and imposed at the same location in the modified model (b). The modified model requires

<10.0 mm long exhaust tracts since exhaust system gas dynamics are not calculated. If the calculation method is correct then it would be expected that, as well as having identical exhaust port pressure histories, both the modified and unmodified models would have identical valve mass flow, velocity, and in-cylinder condition histories.

Figures 5.6 to 5.17 show comparisons of key performance parameters generated by the unmodified and modified models. It can be seen that there is extremely good correlation between both sets of results. Very small differences exist between the predicted mass flow rates across the exhaust valve at 2000 and 4000 r/min (see Figures 5.7 and 5.11). These differences arise from the interpolation procedure that is required to input the unmodified model pressure data into the modified model at non-concurrent time-steps. The differences are not considered significant. They could, however, be reduced further by generating exhaust valve pressure data from the unmodified model at smaller time-steps and by further reducing the convergence criteria in the interpolation procedure (set to approx. 0.001% difference between the fixed pressure value required and the value derived from the iterated incident and reflected pressure values). Based on these results, the fixed exhaust port pressure history model was shown to be accurate and was used for the subsequent analysis.

5.3 THE EFFECT OF THE EXHAUST PORT PRESSURE HISTORY ON ENGINE BREATHING CHARACTERISTICS

Figures 5.18 and 5.19 show the effect on the torque and volumetric efficiency characteristics respectively of imposing 30°CA compressive pulses of 160 kPa absolute pressure at the exhaust ports of the validated K series model. The y-axes are

shown as relative scales to enable the effect of imposing the same pulse at different speeds to be compared directly. The relative characteristic value is given by:

Relative value = predicted value - value with pulse centred at 130°CA (5.2)

Figure 5.18 suggests that torque is sensitive to the pressure during the period following BDC to the end of valve overlap. The period from EVO to immediately after BDC corresponds to the period of peak blowdown from the cylinder, i.e. cylinder emptying results from the expansion of the burnt gases into the exhaust tract. Flow through an exhaust poppet valve has been described by the equation for compressible flow through a restriction:

$$\dot{m} = \frac{C_d A_{valve} p_{cyl}}{\sqrt{(RT_{cyl})}} \left(\frac{p_{exh}}{p_{cyl}}\right)^{1/\gamma} \left\{\frac{2\gamma}{\gamma-1}\left[1-\left(\frac{p_{exh}}{p_{cyl}}\right)^{(\gamma-1)/\gamma}\right]\right\}^{1/2} \qquad (5.3)$$

When flow through the valve becomes choked, i.e.:

$$\frac{p_{exh}}{p_{cyl}} \leq \left(\frac{2}{\gamma+1}\right)^{\frac{\gamma}{\gamma-1}} \qquad (5.4)$$

then flow through the valve is described by:

$$\dot{m} = \frac{C_d A_{valve} p_{cyl}}{\sqrt{(RT_{cyl})}} \sqrt{\gamma}\left(\frac{2}{\gamma-1}\right)^{\frac{\gamma+1}{2(\gamma-1)}} \qquad (5.5)$$

i.e. the flow through the exhaust valve is no longer a function of the downstream pressure. This offers an explanation as to why compressive waves imposed at the exhaust port prior to BDC have little or no effect on engine performance. Figure 5.18 also shows that, for the speeds 2000-6000 r/min, during the period of broad sensitivity to compressive waves there exist two clearly defined troughs. These are located at 270-280°CA and during the period immediately following IVO to TDC, with the

second trough being the greater amplitude. The first trough corresponds to approximately mid-stroke of the piston during the exhaust period. The high pressure downstream of the exhaust valve limits the flow of gases from the cylinder during this period and therefore the high in-cylinder pressure exerts a greater moment about the crankshaft axis and cylinder pumping losses are increased. The second trough also results partly from an increase in pumping losses, although losses during this period are significantly lower due to the reduced moment about the crankshaft and the lower in-cylinder pressure. The location of this second trough corresponds to the location of a single high amplitude trough in a plot of volumetric efficiency sensitivity to compressive pulses, shown in Figure 5.19. This suggests that the torque is affected more by the reduction of induced fresh air-fuel charge than by the increase in pumping losses. Figure 5.19 also shows that as the engine speed is increased, the start of the period of volumetric efficiency sensitivity to compressive waves progressively advances prior to the period of valve overlap. At 7000 r/min there is a significant step and volumetric efficiency is seen to be influenced by compressive pulses that end some 30°CA before valve overlap. The engine modelled in this case is designed for peak power at 6000-6250 r/min. At speeds above these, the valves are not designed to flow the gas mass flow rates required. Valve choking occurs and blowdown is extended beyond the period expected during usual operating speeds. This can be seen in Figure 5.18 where the pumping losses do not become apparent until 230-240°CA. At this time the first pumping loss trough begins to develop but it is not as clearly defined as at lower speeds since it merges with the second cylinder charging trough which itself starts well prior to overlap. The early starting of this second trough is a direct result of the cylinder being unable to expel the burnt gases quickly enough and so the influx of fresh charge is limited.

Figures 5.18 and 5.19 do not indicate whether the locations of these sensitivity troughs to compressive waves are related to crank-angle periods or to valve events. Figures 5.20 to 5.23 show the results of repeated fixed exhaust port pressure profiles with 260 and 280°CA exhaust and inlet valve periods. Figures 5.20 and 5.21 show that by extending the valve period to 260°CA, the sensitivity troughs remain in the same locations and are not related to the start of the overlap period; the pumping loss trough is at 270-280°CA and the cylinder charging trough at 350-360°CA. However, as the cam period is extended further, the location of the cylinder charging sensitivity trough is shifted between 10-20°CA before TDC, depending on the engine speed. This can be seen clearly in Figure 5.24 where direct comparisons are made between the different cam period engine models. As the valve overlap period is increased, torque and volumetric efficiency become increasingly sensitive to compressive waves phased during or immediately prior to valve overlap. Figure 5.22 shows one apparently spurious result at 2000 r/min; two cylinder charging troughs are indicated and the main one is located at 20°CA after TDC. At such a low operating speed it is highly unusual for an engine to utilise such an extended overlap period. By 20° after TDC the intake valve is almost 75% fully open (in terms of lift) and the exhaust valve is still 25% open. The combination of extremely poor intake system pressure wave action and an undesirable value of Δp across both the intake and exhaust valves results in high reverse flow.

Figures 5.25 to 5.30 similarly show the effect of imposing 70 kPa absolute pressure expansion pulses immediately downstream of the exhaust valve. These results mirror

those of Figures 5.18 to 5.23 in that the locations of the points of peak sensitivity are similar but the effect is reversed; the expansion pulses cause a relative improvement in performance as the Δp across the valve is increased, assisting flow from the cylinder.

Figures 5.25 to 5.30 indicate the profile of an idealised exhaust port pressure history to give optimum engine performance. A low pressure should primarily be centred on the mid-point of the overlap event to improve airflow through the engine. This will generally improve torque performance, especially when the low pressure during the overlap event follows a low pressure at mid-stroke of the piston, which will further reduce cylinder pumping losses. Figures 5.18 to 5.23 indicate that a high pressure during the period following blowdown to IVC will reduce engine performance to some degree. Therefore the exhaust system should be designed to phase incident compressive waves outside of this period. If this is not possible, then they should be phased to arrive at the exhaust port approximately 20 to 30°CA prior to the overlap event, when their effect on engine performance will be minimised. Comparisons of results for simulations with both compression and expansion pulses imposed at the exhaust port show that the relative effect of compression pulses on engine torque performance is greater than that of expansion pulses. Therefore the sources and phasing of compression waves should be considered a priority when designing an exhaust system.

5.4 SUMMARY OF RESULTS

The results from this phase of the study can be summarised as follows:

i. Torque performance has been shown to be particularly sensitive to the pressure immediately downstream of the exhaust valve at two discrete periods; the first corresponding to approximately mid-stroke of the piston and the second during the period immediately prior to IVO until TDC of the exhaust stroke, with the second period having the greater influence.

ii. Volumetric efficiency has been shown to be sensitive to the downstream exhaust valve pressure during the second period given in i. above.

iii. Volumetric efficiency is influenced by the downstream exhaust valve pressure prior to the overlap period and this is particularly evident for lower overlap periods. The start of this period of sensitivity advances as engine speed increases.

iv. Rarefaction waves arriving during any periods of sensitivity will enhance engine performance; compression waves arriving during the same periods will impair engine performance.

v. As the valve overlap period increases the relative effect of waves of the same magnitude increases.

vi. At extreme values of valve overlap the location of the cylinder charging sensitivity peak advances.

vii. The values of pressure used during this study, selected so as to be representative of typical amplitudes of compressive and expansion waves found in automotive engine exhaust manifolds, show that the relative effect of the compression waves is greater.

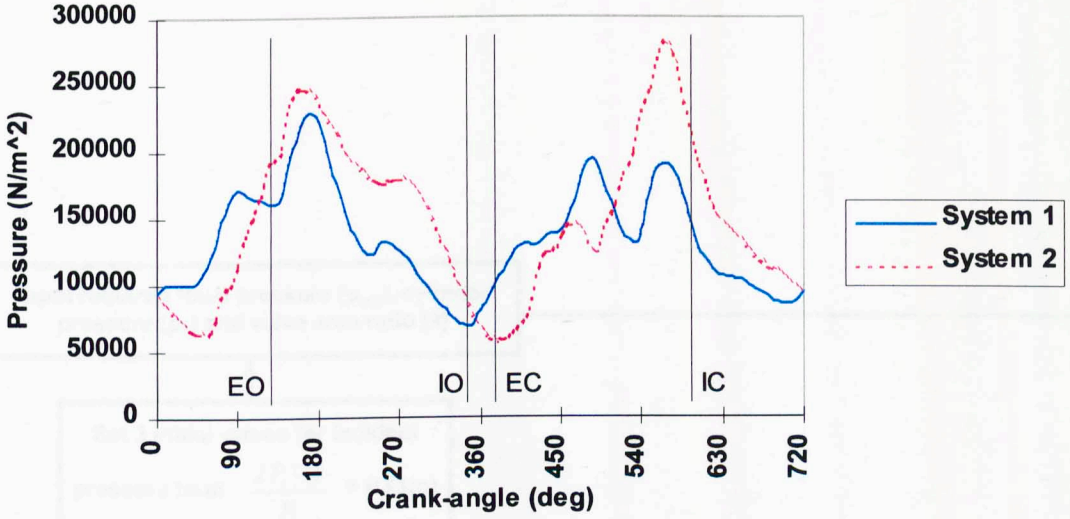

Figure 5.1 Comparison exhaust port pressure histories for different exhaust systems fitted to an engine that give identical values of volumetric efficiency

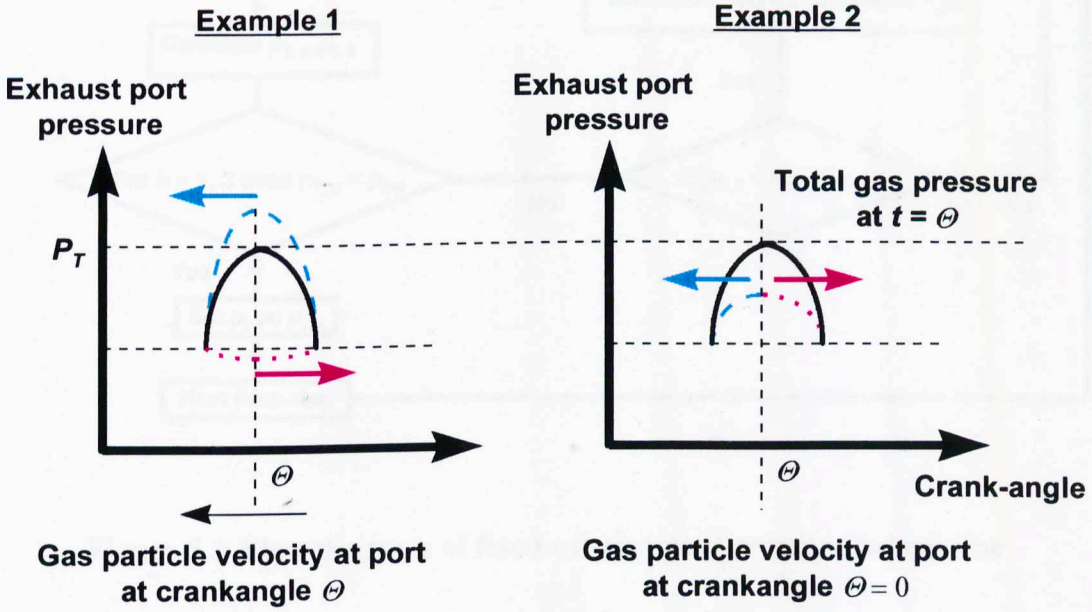

Figure 5.2 Total pressure condition calculated from incident and reflected pressure waves

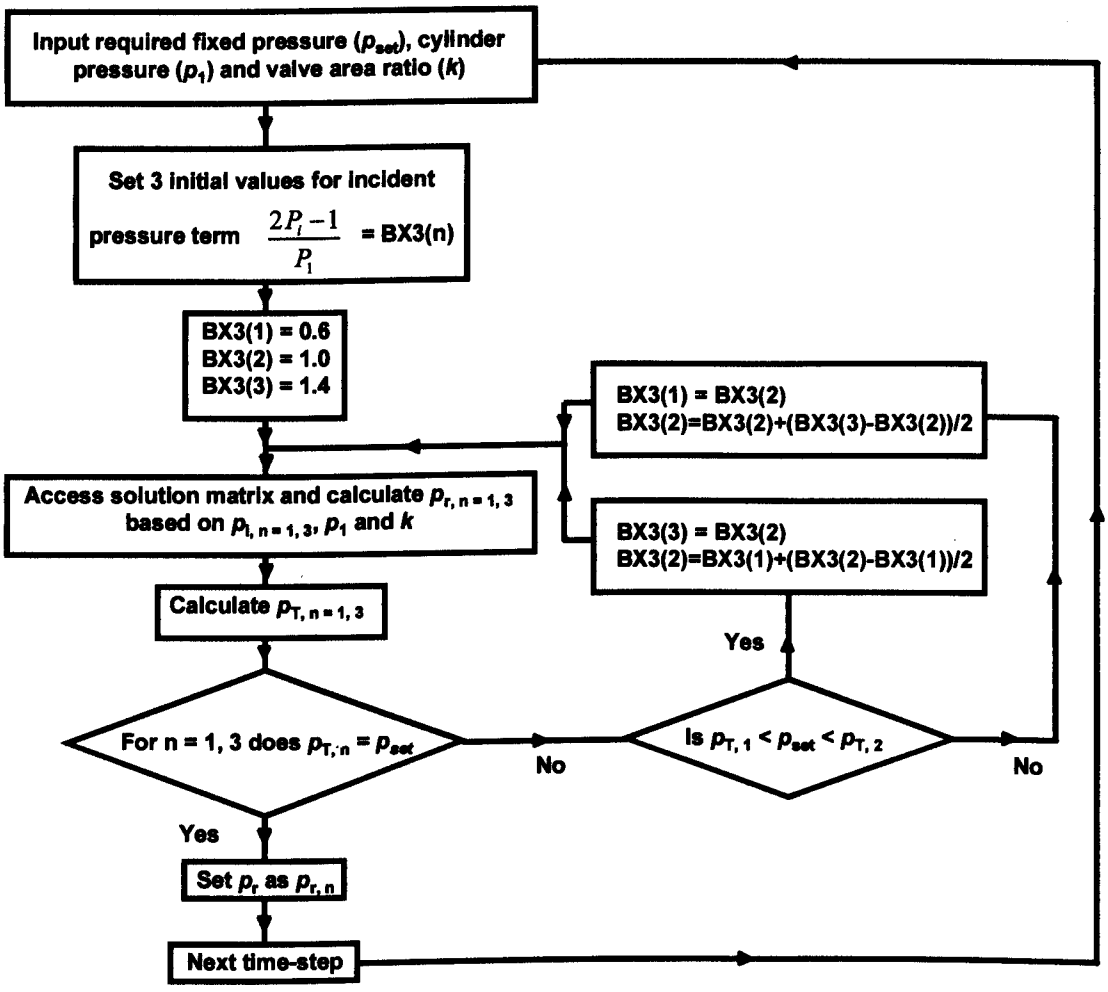

Figure 5.3 Flow diagram of fixed exhaust port pressure subroutine

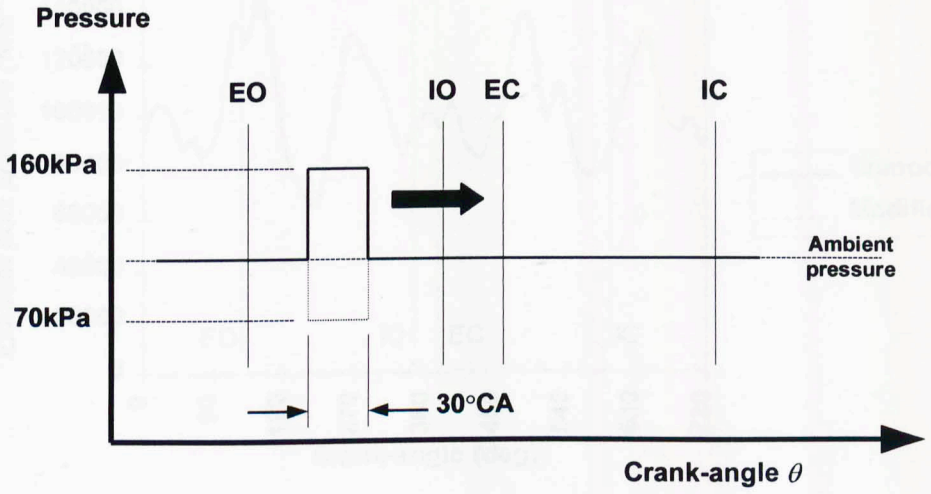

Figure 5.4 Pressure histories imposed downstream of exhaust valves

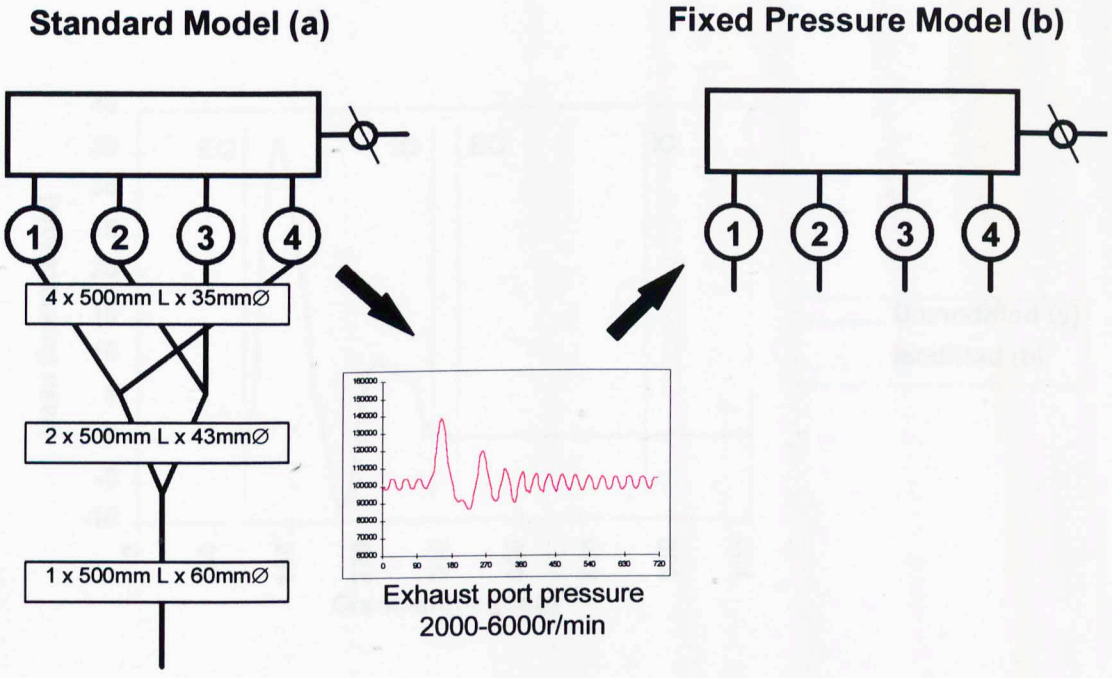

Figure 5.5 Models used for validating calculation method

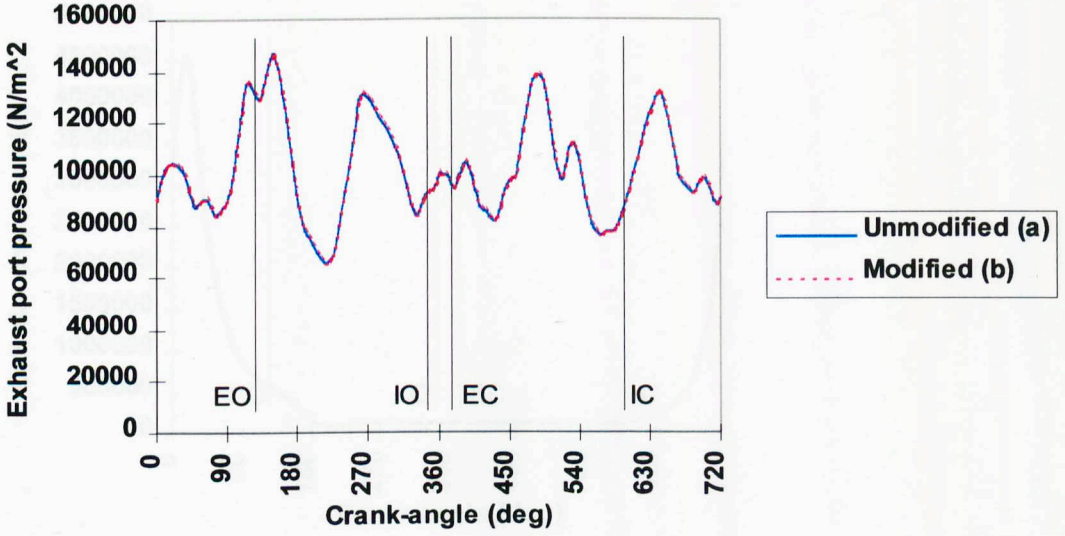

Figure 5.6 Comparison of modified and unmodified model exhaust port pressure histories at 2000 r/min

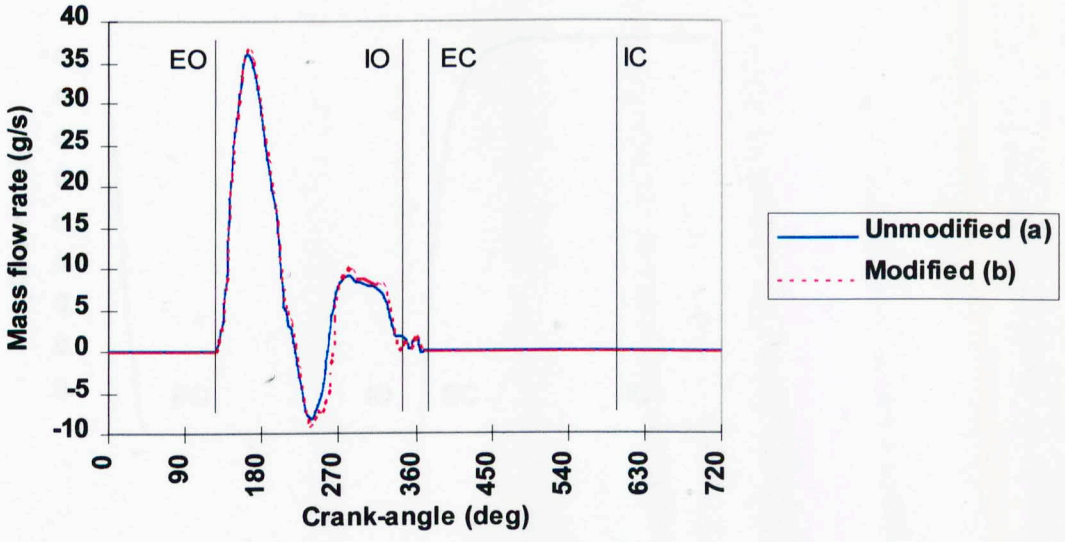

Figure 5.7 Comparison of modified and unmodified model exhaust valve mass flow histories at 2000 r/min

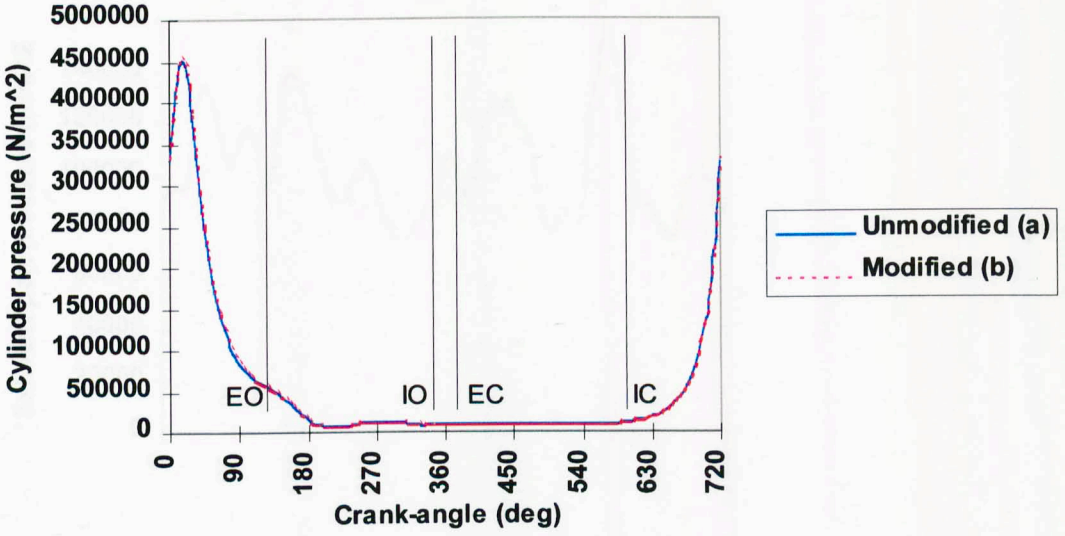

Figure 5.8 Comparison of modified and unmodified model cylinder pressure histories at 2000 r/min

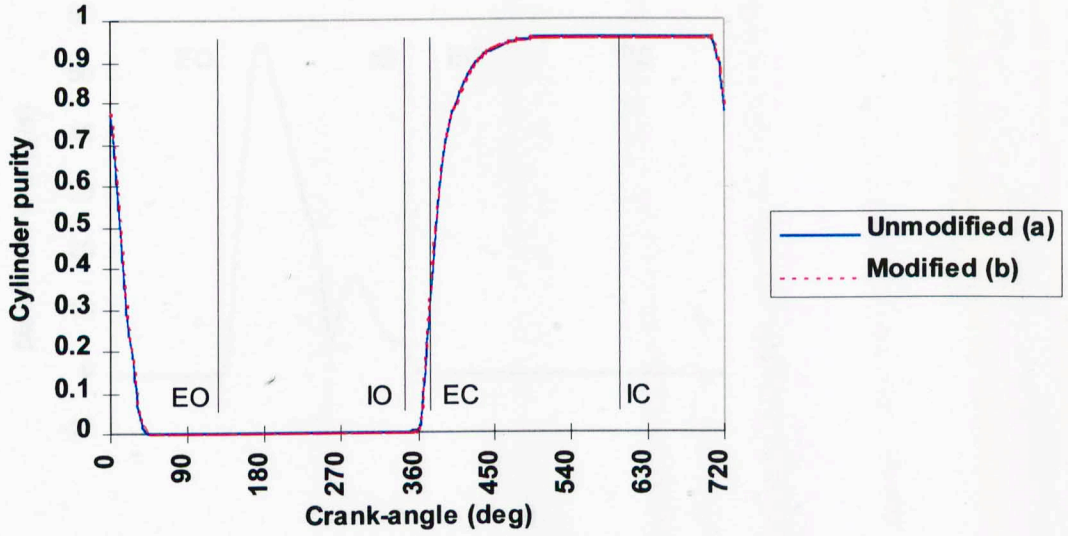

Figure 5.9 Comparison of modified and unmodified model cylinder purity histories at 2000 r/min

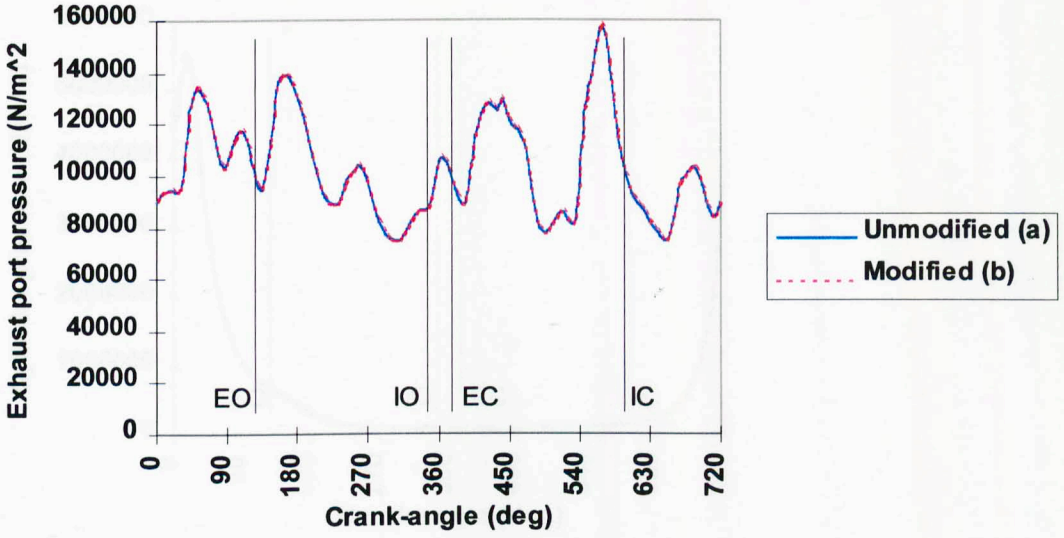

Figure 5.10 Comparison of modified and unmodified model exhaust port pressure histories at 4000 r/min

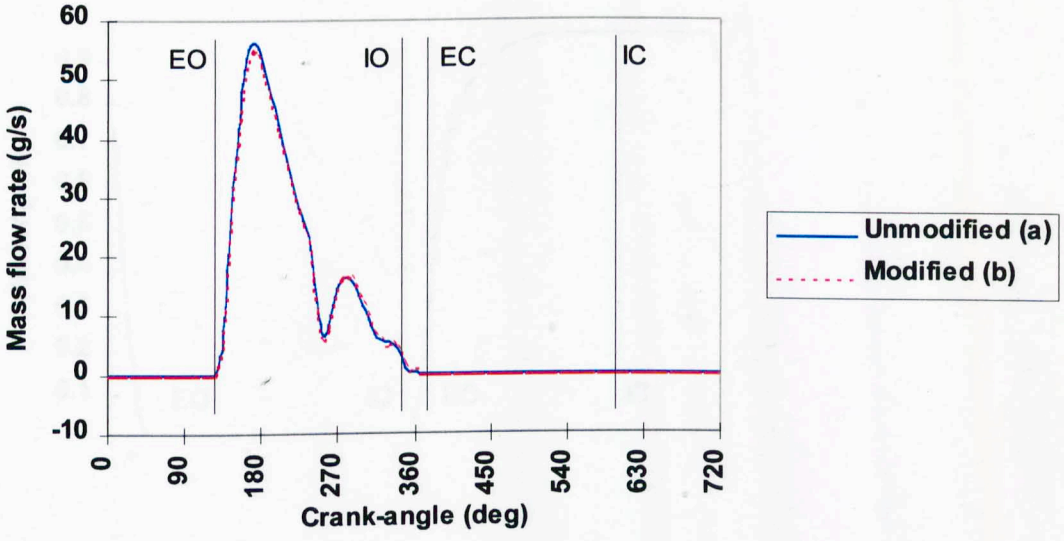

Figure 5.11 Comparison of modified and unmodified model exhaust valve mass flow histories at 4000 r/min

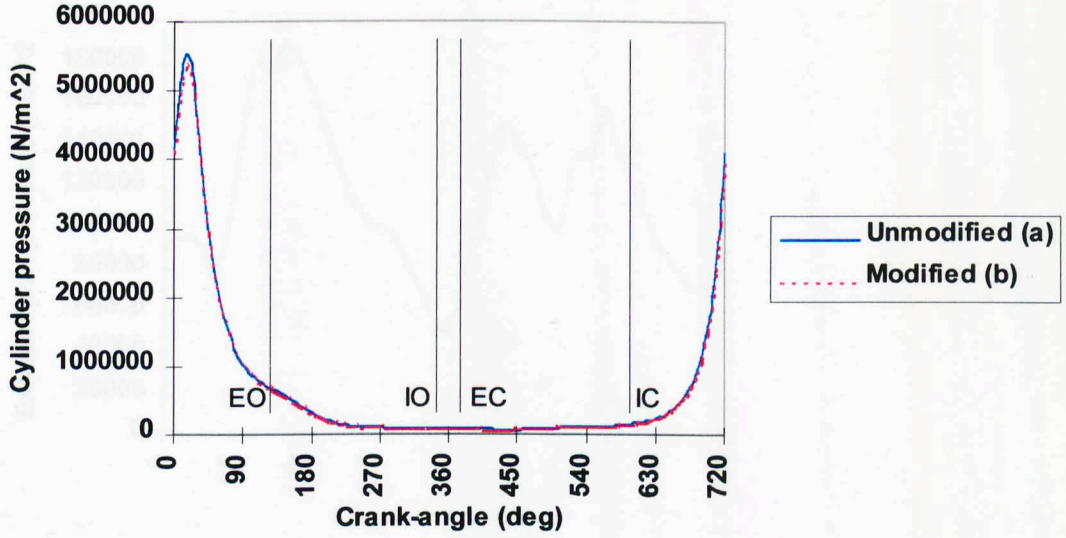

Figure 5.12 Comparison of modified and unmodified model cylinder pressure histories at 4000 r/min

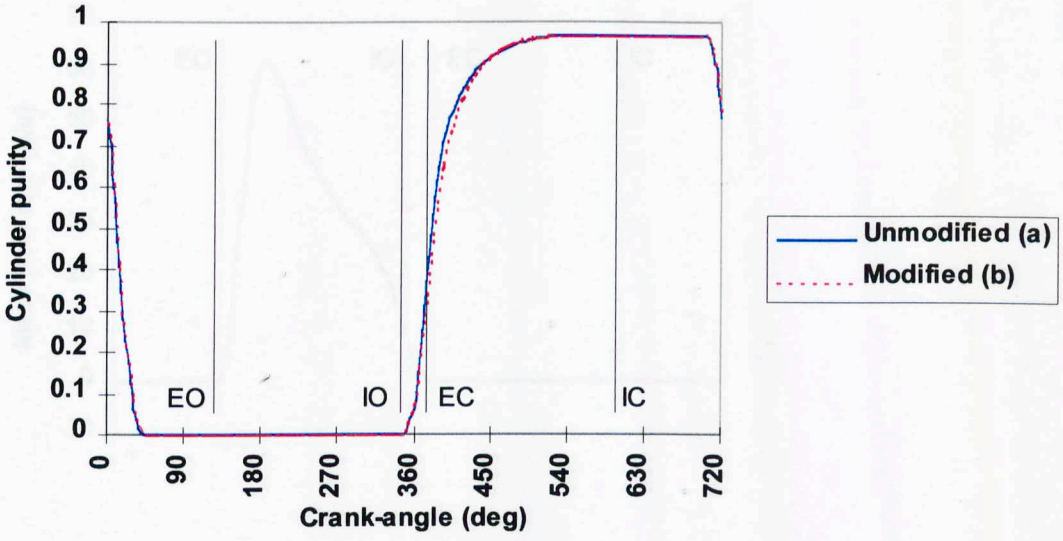

Figure 5.13 Comparison of modified and unmodified model cylinder purity histories at 4000 r/min

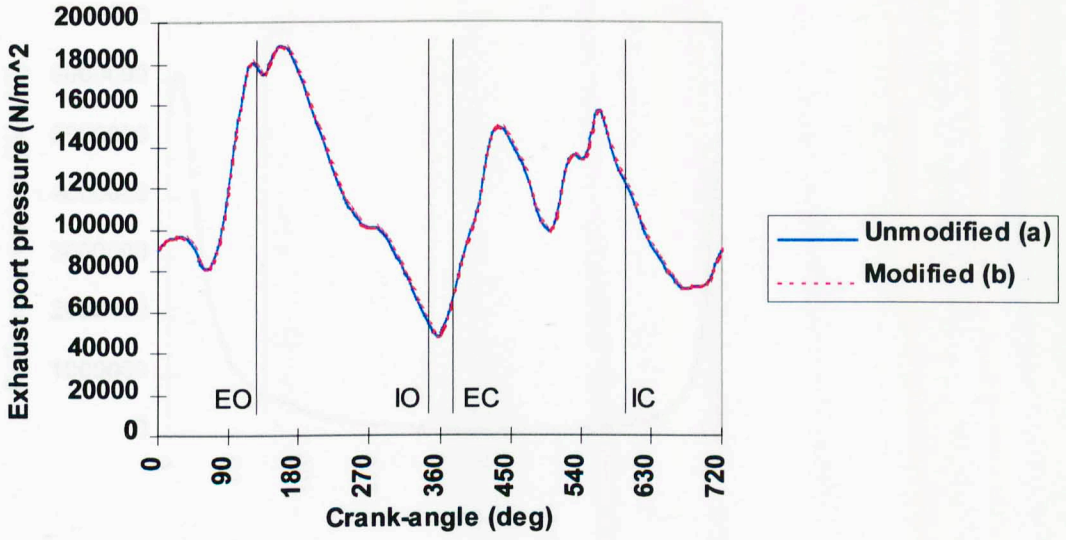

Figure 5.14 Comparison of modified and unmodified model exhaust port pressure histories at 6000 r/min

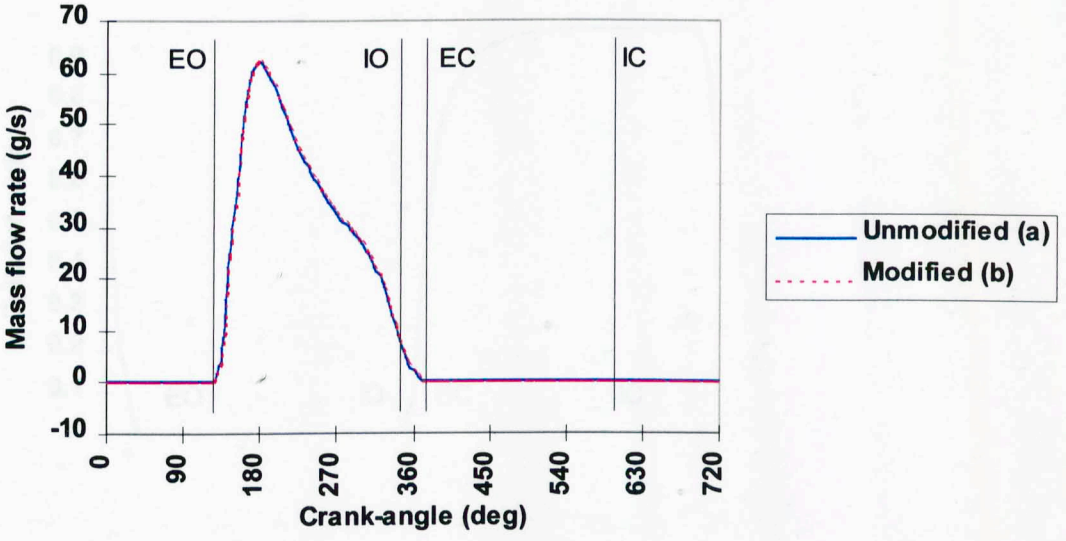

Figure 5.15 Comparison of modified and unmodified model exhaust valve mass flow histories at 6000 r/min

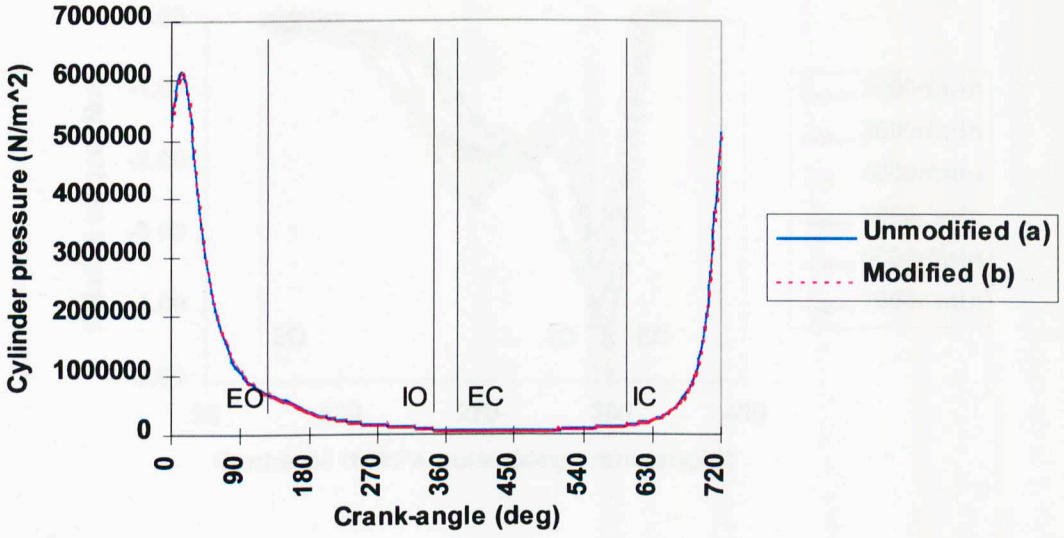

Figure 5.16 Comparison of modified and unmodified model cylinder pressure histories at 6000 r/min

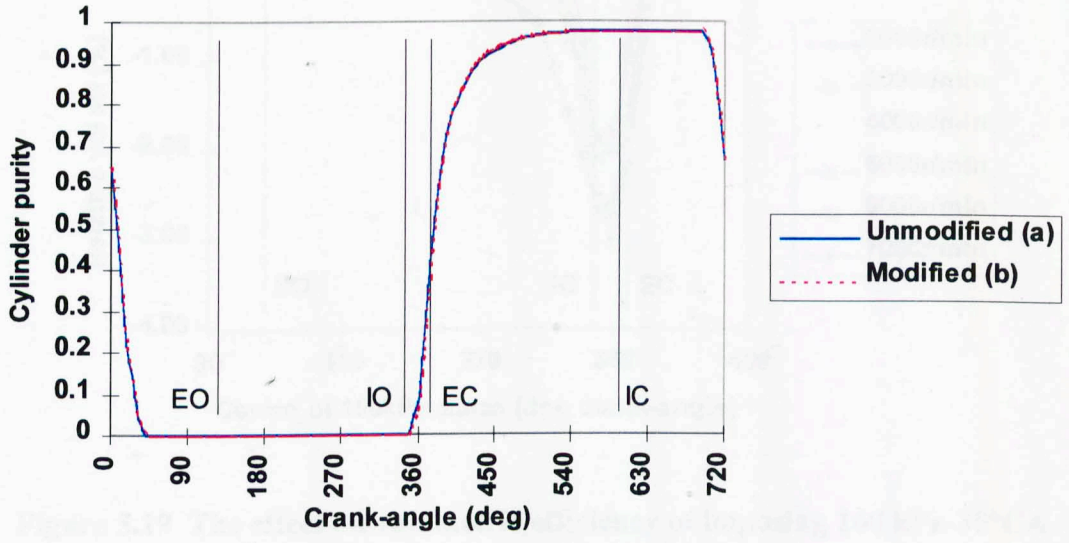

Figure 5.17 Comparison of modified and unmodified model cylinder purity histories at 6000 r/min

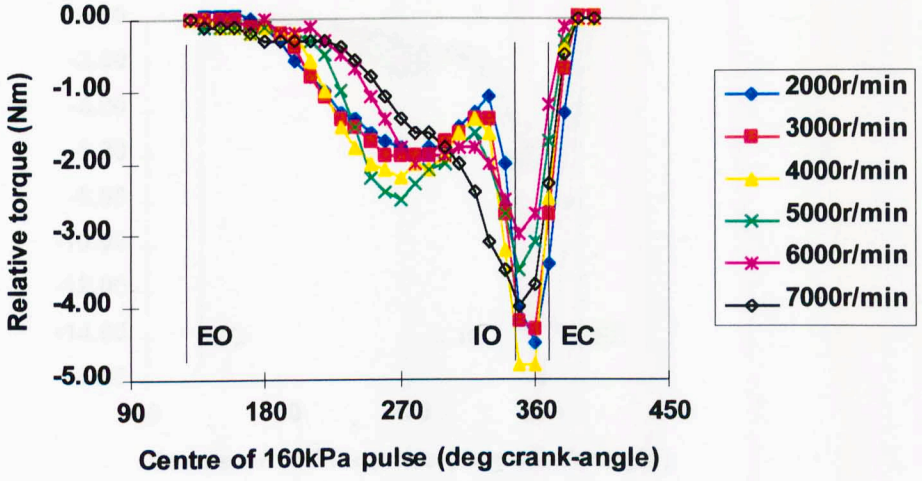

Figure 5.18 The effect on torque of imposing 160 kPa-30°CA pulse at the exhaust port of a 244° cam duration engine

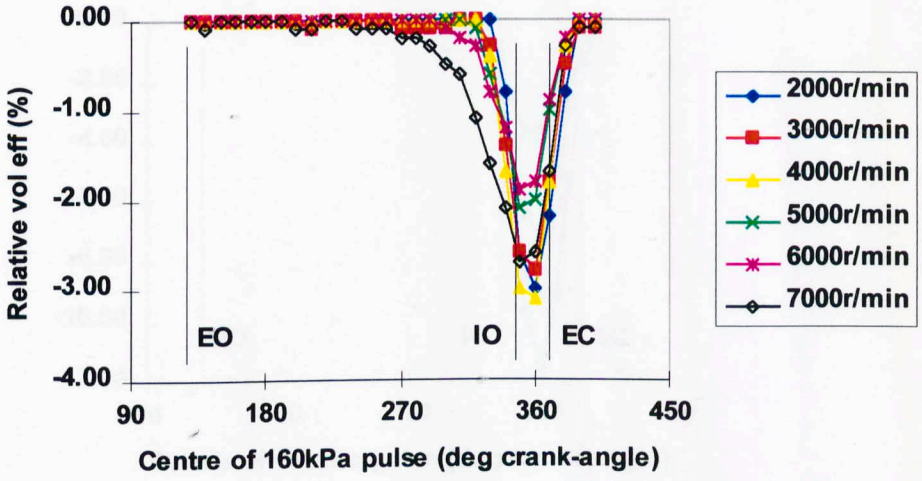

Figure 5.19 The effect on volumetric efficiency of imposing 160 kPa-30°CA pulse at the exhaust port of a 244° cam duration engine

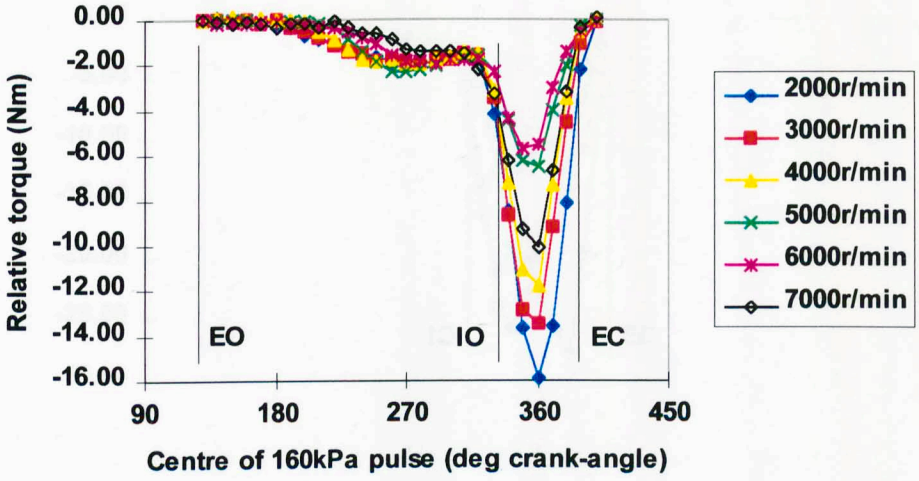

Figure 5.20 The effect on torque of imposing 160 kPa-30°CA pulse at the exhaust port of a 260° cam duration engine

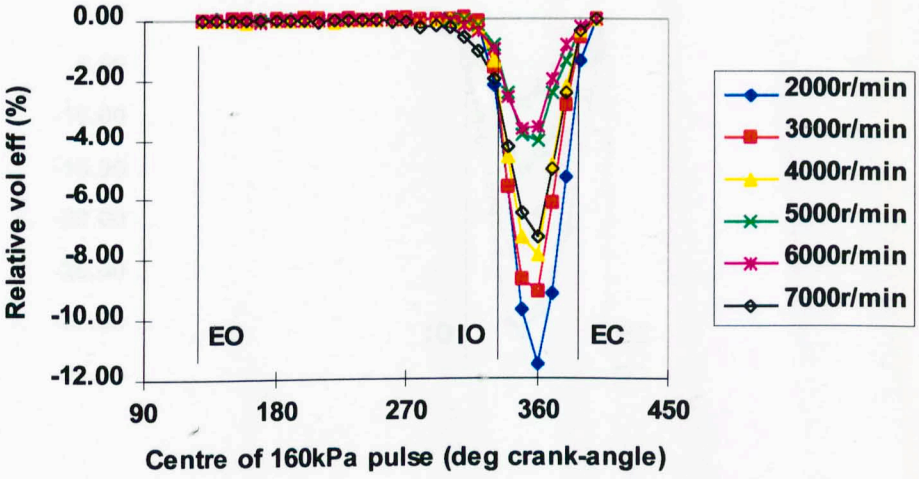

Figure 5.21 The effect on volumetric efficiency of imposing 160 kPa-30°CA pulse at the exhaust port of a 260° cam duration engine

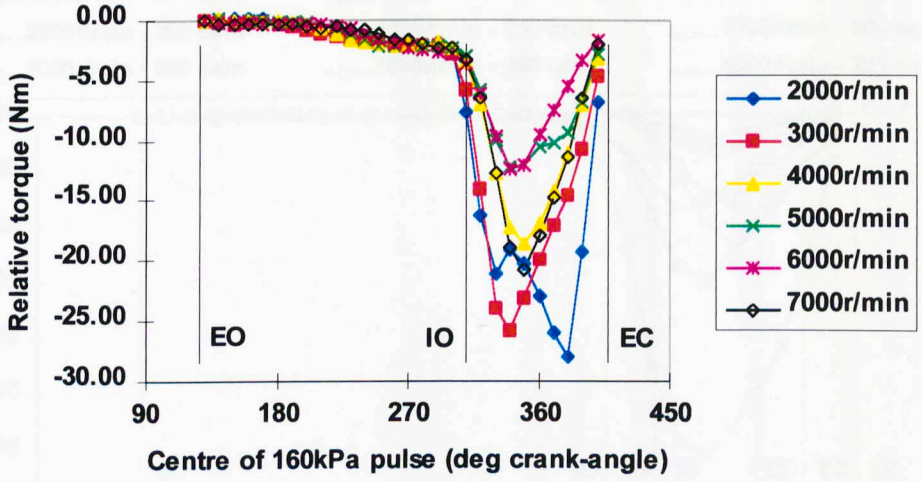

Figure 5.22 The effect on torque of imposing 160 kPa-30°CA pulse at the exhaust port of a 280° cam duration engine

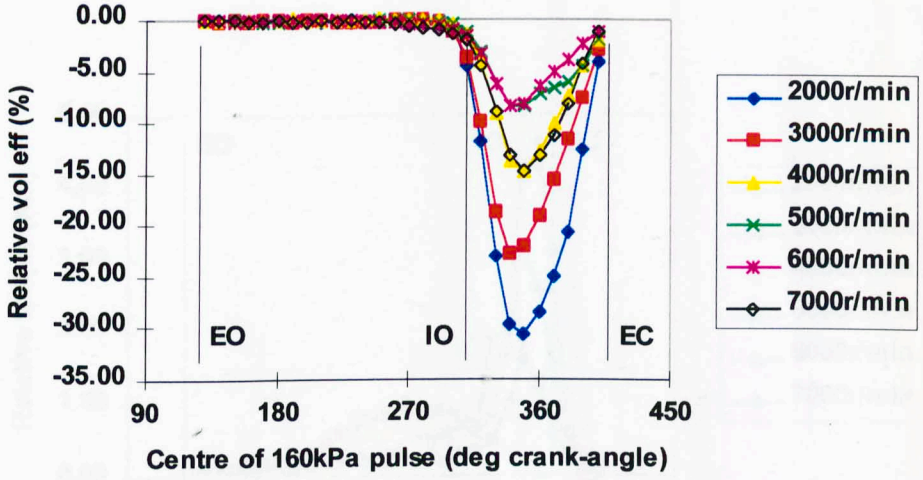

Figure 5.23 The effect on volumetric efficiency of imposing 160 kPa-30°CA pulse at the exhaust port of a 280° cam duration engine

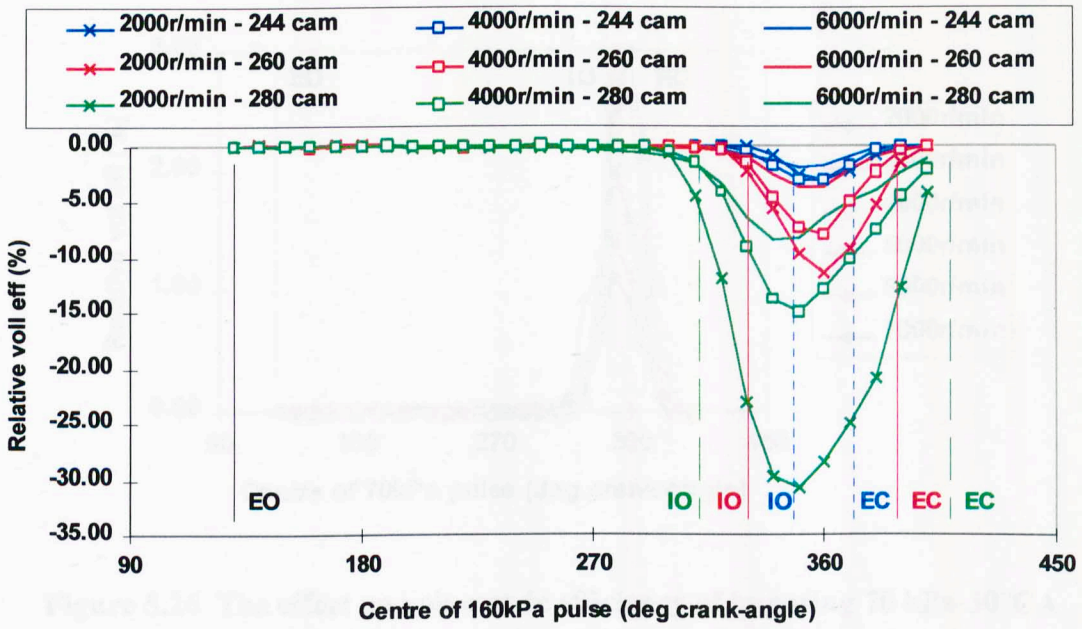

Figure 5.24 The effect on volumetric efficiency of imposing 160 kPa-30°CA pulse at the exhaust port of 244, 260 and 280°CA cam duration engines

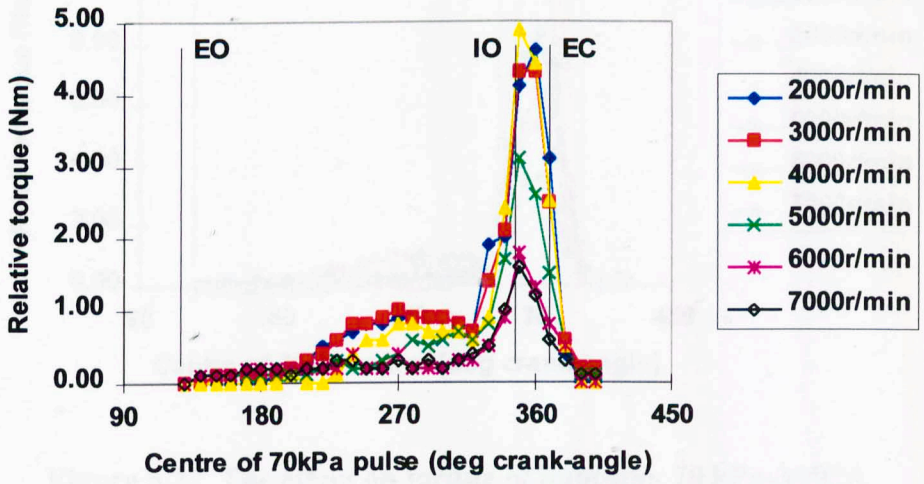

Figure 5.25 The effect on torque of imposing 70 kPa-30°CA pulse at the exhaust port of a 244°cam duration engine

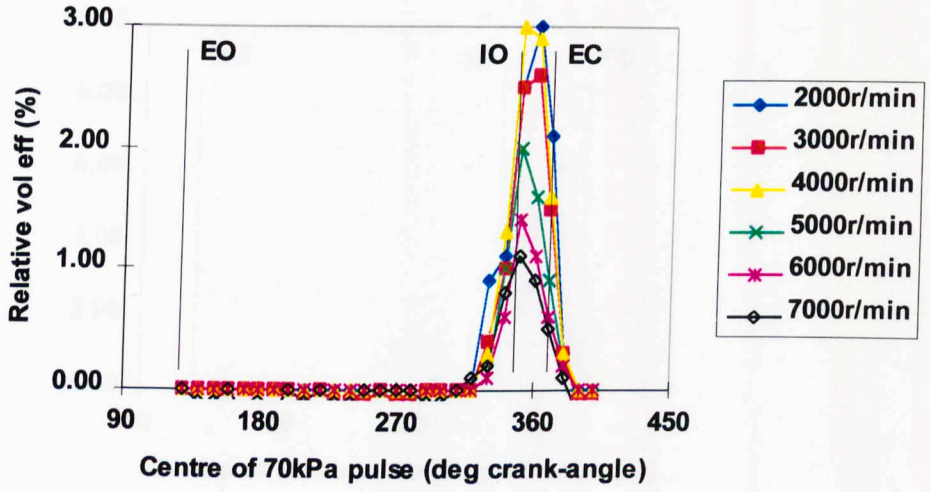

Figure 5.26 The effect on volumetric efficiency of imposing 70 kPa-30°CA pulse at the exhaust port of a 244° cam duration engine

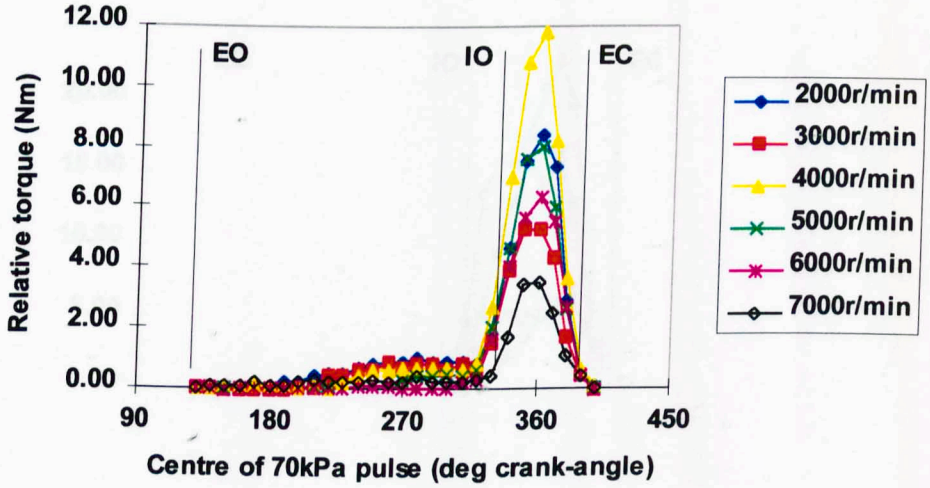

Figure 5.27 The effect on torque of imposing 70 kPa-30°CA pulse at the exhaust port of a 260° cam duration engine

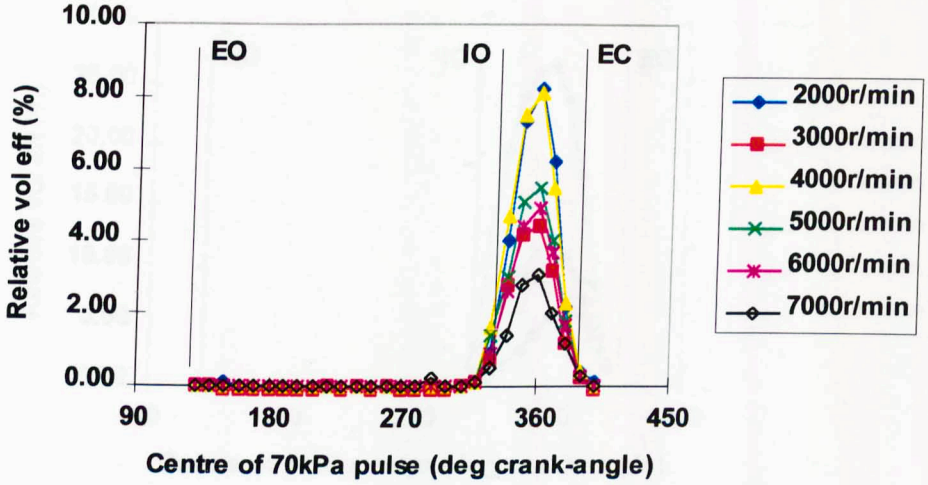

Figure 5.28 The effect on volumetric efficiency of imposing 70 kPa-30°CA pulse at the exhaust port of a 260° cam duration engine

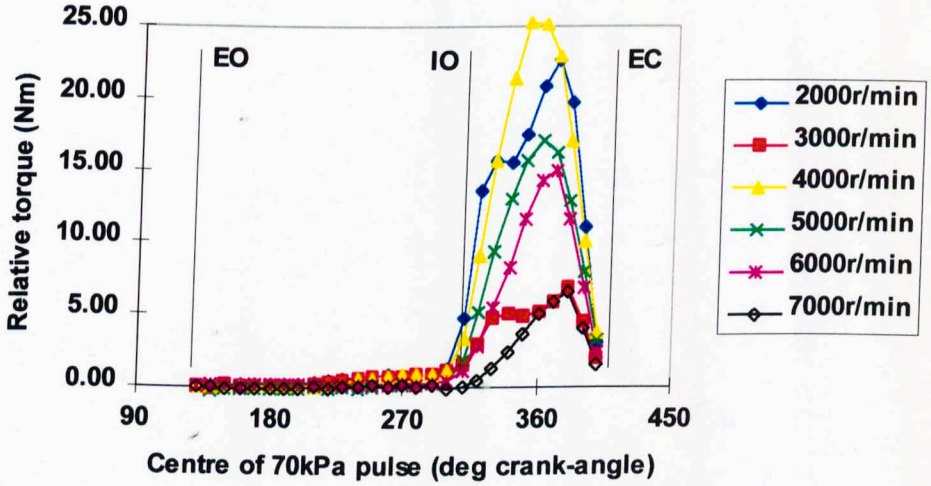

Figure 5.29 The effect on torque of imposing 70 kPa-30°CA pulse at the exhaust port of a 280° cam duration engine

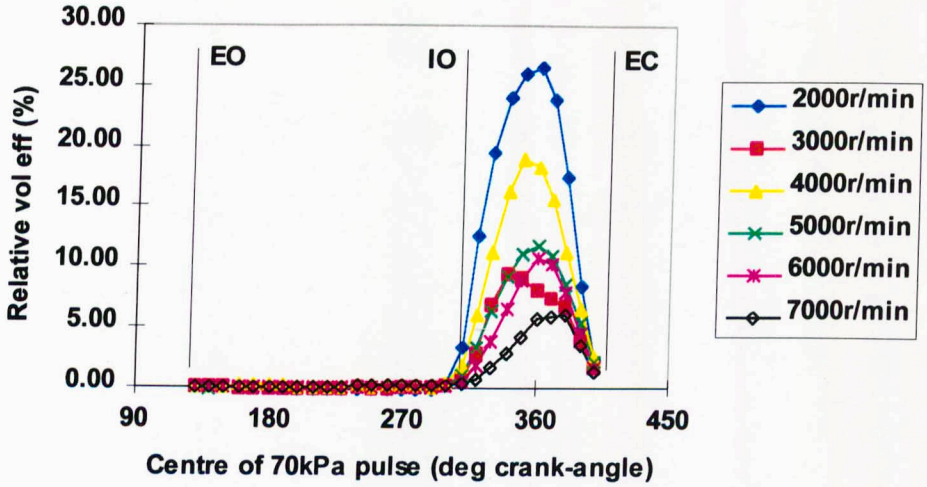

Figure 5.30 The effect on volumetric efficiency of imposing 70 kPa-30°CA pulse at the exhaust port of a 280° cam duration engine

CHAPTER 6

IDENTIFICATION OF PRINCIPAL COMPONENTS OF THE EXHAUST PORT PRESSURE HISTORY

CHAPTER 6

IDENTIFICATION OF PRINCIPAL COMPONENTS OF THE EXHAUST PORT PRESSURE HISTORY

6.1 INTRODUCTION

The dynamic pressure history at the exhaust port is the result of the superposition of pressure waves that originate from various sources throughout the exhaust system. Their phasing relative to the exhaust event and at the cylinder of interest is a function of the exhaust system geometry, the gas conditions within the exhaust system and of the exhaust events at other cylinders that are connected via the same system. The initial profiles of the waves generated by the exhaust event are a function of the in-cylinder and exhaust tract gas conditions, the exhaust tract geometry and the valve opening profile. The objective of exhaust system tuning is to optimise the pressure history at the exhaust port so as to assist cylinder scavenging and to reduce pumping losses. To design an exhaust system that generates the optimum pressure history at the exhaust port, it is necessary to understand how the dynamic pressure history is generated and from what sources its component pressure profiles originate. Having this information, the geometry of the exhaust system can be selected so as to optimise the phasing of these component pressure histories.

It has been shown previously that, as a pressure wave traverses a pipe junction, the component of the wave transmitted across the junction remains the same sign, i.e. a

compressive wave approaching a junction will cause a compressive component to traverse it. There is also a reflected component of the wave, which is of the opposite sign to the original wave, and results from the expansion of the wave into the junction. This reflected component of the wave then propagates back along the entry pipe. This action occurs at both ends of the pipe and thus, multiple pressure wave oscillations are initiated within any pipe as a result of a single pressure disturbance. The frequency of this pressure wave action within the pipe is the natural frequency of pressure wave oscillation of the pipe.

The natural frequency of oscillation of pipes has been given by equations (A2.1.32) and (A2.1.51) and these equations have been used to derive expressions for the natural frequency of oscillation of pipe networks (equation (A2.1.52). Such models do not consider the variable boundary conditions of the system which, in the case of exhaust system pipe networks, are caused by the exhaust valve events, the changing cylinder volume and the changing gas conditions within.

Chapter 5 has shown how engine performance is sensitive to the phasing of pressure waves of compression and expansion at the exhaust port. At any instant, this pressure results from the superposition of a number of incident and reflected pressure waves. The identification of the sources of these pressure waves is a prerequisite for defining the optimum exhaust system geometry. Then, knowing how waves of compression and expansion would best be phased to enhance cylinder breathing and knowing from where these individual waves originate, the designer would then have the ability to select the

dimensions of individual exhaust pipes to give the optimum pressure wave action. In order to give the exhaust system designer this information, this phase of the study investigated the following:

i. The pressure wave action within pipe networks was studied and the transmission characteristics of waves across junctions and other pipe boundary conditions typically encountered in exhaust pipe systems was demonstrated;

ii. the resonance characteristics of pipes were studied and the validity of the application of equations (A2.1.32), (A2.1.51) and (A2.1.52) to both intake and exhaust system tuning applications was investigated; and

iii. the pressure history at the exhaust port was studied in detail with the objective of identifying the principal dynamic components of the overall profile.

6.2 PRESSURE WAVE TRANSMISSION ACROSS PIPE BOUNDARIES

Although the temporal variation of pressure in manifolds is rapid, the spatial variation of the pressure is small. Even with a facility to track upstream and downstream moving pressure waves in exhaust manifolds, it is extremely difficult to differentiate separate waves because of their long wavelength relative to the geometry of the system. The leading edge of an exhaust pressure pulse that is introduced into a system, depending on the operational speed of the engine, can be approaching the exhaust exit to atmosphere before the end of the exhaust event. Thus, if plots are made of the pressure at a number of locations throughout the system at any instant, then only a shallow gradient will be observed in the pressure amplitude-distance plot along any pipe. This is illustrated in

Figures 6.1 to 6.2. Shown are plots of predicted pressure that were recorded at various locations along the length of a simple 4:1 exhaust system with 400 mm long × 35 mm diameter primary pipes and a 500 mm long × 60 mm diameter collector pipe. The simulation ran for a pre-set number of cycles to allow the pressure wave action in the manifold system to stabilise and thus the in-cylinder conditions to be correctly predicted. The simulation then ran for an additional cycle, at the beginning of which the residual pressure wave action in the exhaust system was eliminated. Thus, a compressive exhaust pressure wave was introduced into the undisturbed system by cylinder 1 emptying and the wave was allowed to propagate throughout its length without any interference from residual waves. Throughout the additional cycle, the remaining cylinders were deactivated. The figures show pressure plots at 20 mm intervals along the system limbs during the exhaust event. It is initially possible to see the compressive wave front approaching the junction but once the wave front reaches this location and the first reflection occurs, it becomes difficult to differentiate between the separate waves. Reflections occur at the open pipe end and at the closed valves of other cylinders. Even during these early stages of the exhaust event and considering only one cylinder exhausting, it becomes increasingly difficult to identify upstream and downstream moving waves and only a shallow pressure gradient is seen along each pipe length.

To assist with the investigation of the transmission characteristics of pressure waves across pipe junctions of various configurations and of various numbers of pipes, a model was compiled that allowed the introduction of user defined pressure and mass flow histories of any profile into pipe networks of any configuration. The model additionally

included the facility to track rightward and leftward moving waves and to represent anechoic pipe terminations to eliminate reflected pressure characteristics. Thus, the transmission and reflection characteristics of single pressure waves across pipe boundaries were investigated without interference from upstream and downstream reflections.

6.2.1 Pressure wave transmission across pipe junctions

Figure 6.3 shows a simple pipe network that represented a typical primary-secondary pipe junction in a 4:2:1 configuration exhaust system. The open pipe ends were modelled as anechoic terminations. Suitable pressure wave data for input into this model was generated by a model of a single-cylinder, 4-valve engine with a single exhaust pipe that opened into an anechoic termination. Thus, pressure and mass flow histories across the exhaust valve were generated that were not influenced by any tuning effects, in this case by reflections from the exhaust pipe open end. The exhaust port pressure history generated at 3000 r/min from this model was input into the pipe network model at location 1, generally as shown in Figure 6.3. The wave then traversed the junction and smaller amplitude compressive waves continued to propagate along the other pipe limbs until they were absorbed by the anechoic pipe ends. Similarly, the rarefaction wave generated as the original compressive wave traversed the junction travelled back up the entry pipe and was absorbed by the anechoic termination at the pipe entry. The simulation was repeated for a number of pipe geometries to see the effect of geometry on the reflected and transmitted pressure characteristics at the junction.

Figures 6.4 to 6.6 show comparisons of the pressure-time histories at various locations within this simple pipe network for each system geometry. It can be that as the area expansion ratio between the entry pipe and the downstream pipes increases, the magnitude of the reflected expansion wave increases. It can also be seen that the compressive component of the wave that is transmitted across the junction and continues on to location 2 is smaller in magnitude than that which continues on to location 3. Mass flow continuity across the junction is maintained. However, the pressure loss across pipes 1 and 2 is greater than that across pipes 1 and 3 since, in terms of steady flow characteristics, flow is throttled more by the acute angular relationship between pipes 1 and 2. In this instance the pressure loss manifests itself as a smaller transmitted wave component. It should be noted however that, in terms of pressure wave transmission, the difference in amplitude between the transmitted waves is relatively small. It can also be seen that, as the area expansion ratio increases, the amplitude of compressive components of the wave transmitted across the junction decreases.

6.2.2 Pressure wave transmission across open pipe ends

To investigate the pressure wave reflection characteristics of the open end boundary condition a similar model to that detailed in section 6.2.1 was compiled. As previously, typical pressure data generated during the exhaust event at 3000 r/min was input into a single pipe model that incorporated anechoic terminations at either end of the pipe. At the exit end of the pipe, the discharge coefficient (C_d) was varied so as to see the effect on the magnitude of the reflected pressure wave.

Figure 6.7 shows the magnitude of the pressure wave reflected in each instance compared to the input wave. It can be seen that as the value of C_d is progressively reduced, then the amplitude of the reflected pressure wave, which results from the expansion into atmosphere, is also reduced. Typically, the value of C_d at the exhaust open end is unlikely to be below 0.9 and so, relative to the magnitude of the arriving pressure wave, the exhaust open end can be considered to be a source of high amplitude reflections of the opposite sign. However, it should be noted that, in the case of typical automotive exhaust systems, a pressure wave will invariably traverse several different types of boundary and have its amplitude progressively reduced before it reaches the exhaust open end. The reflected pressure wave then has to traverse the same boundaries, and have its amplitude progressively reduced, before it reaches the exhaust port where it can influence cylinder breathing characteristics.

It has been demonstrated how expansion of a pressure wave into an increased volume at either a junction or an exit to atmosphere is a potential source of reflections of wave of the opposite sign. Thus, compressive waves generated during the exhaust event can themselves generate waves of rarefaction and the optimum phasing of such waves has been detailed in Chapter 5. Another potential source of reflected rarefactions from the exhaust event is the catalytic converter, which is studied in the following section.

6.2.3 Pressure wave transmission across catalytic converters

Catalytic converters introduce particular problems when considering one-dimensional modelling of engine exhaust systems. Their construction is typically a rapidly divergent

entry cone into the main body of the device. Within this body is located the catalyst monolith which physically consists of a series of narrow diameter passages, typically <2.0 mm^2 and lined with reactive elements, through which the exhaust gases are directed. An alternative construction is a pelletised monolith in which the reactive elements of the converter are impregnated into small diameter pellets, around which the exhaust gases are allowed to flow. The large surface area present within the relatively small volume of each of these converter types allows high mass transfer rates between the gas phases and the reactive bed and close to 100% pollutant conversion is possible. Immediately downstream of the monolith there is a rapidly convergent cone down to the pipe diameter within which the device is located. Thus, the converter represents the following series of boundary conditions in rapid sequence:

1. Expansion through a rapidly divergent cone into main body of the device;
2. restriction down to the monolith effective free area;
3. restricted flow through the monolith;
4. expansion back out to the main body of the device; and
5. flow through a rapidly convergent cone.

For catalytic converters to operate at their optimum pollutant conversion efficiency, high temperatures (typically >400°C) must be maintained within the device. The device is conventionally raised to a low operating temperature by heat transfer from the exhaust gasses passing through it. Then, as the exothermic catalytic reactions take place, the operating temperature of the device is raised further still. Thus, the temperature of the device is potentially higher than the temperature of the immediately adjacent pipe

network, which will influence the local acoustic velocity within the device. An additional factor to consider is the effect of the monolith on the flow characteristics of the exhaust gases in terms of the frictional losses generated by the substrate surface. Figures 6.8 and 6.9 show measured pressure data recorded immediately upstream and downstream of a catalytic converter installed in the collector pipe of a 4:2:1 exhaust system. These plots demonstrate that pressure wave action across the monolith of catalytic converters is preserved.

6.2.3.1 The effect of catalytic converter geometry

Catalytic converters are typically represented in one-dimensional gas-dynamics models as shown in Figure 6.10. Model type 1 represents the actual layout of the device and all of the principal dimensions of the device are the same except for the catalyst monolith, which is represented by a single pipe. However, errors that manifest themselves as mass flow discontinuities across the rapidly changing areas of the entry and exit cones can be observed when using catalyst models of this configuration. In the case of method-of-characteristics based gas-dynamic models the problem can arise because of the first order accuracy of the solution scheme and cumulative linear interpolation errors. Payri *et al* [119] suggested the use of type 2 models. The total equivalent volume of the actual converter is maintained in the model. A single intermediate pipe of length L_2 represents the catalyst monolith and is of the same overall length as the monolith to maintain the correct phasing of pressure waves between the entry and exit cones. The pipe diameter is initially selected to give the same overall pressure loss that the monolith would produce in steady flow. The volumes of the entry and exit parallel pipes, which represent the

entry and exit cones, are then calculated to maintain the total volume of the catalyst. As with the intermediate pipe, the overall length of the entry and exit pipes is the same as the overall length of the entry and exit cones to ensure the correct phasing of pressure waves. Model type 3 is similar to type 2 in that the total volume of the device and the individual lengths of components are maintained. It differs in that the entry and exit cones are modelled in such a way as to generate progressive reflections from an incident pressure wave. In each of these models, the additional frictional losses that would be incurred due to the high surface area are lumped as a single loss coefficient across a single pipe element. Such a simplification does not allow for the correct calculation of heat transfer across the pipe walls using conventional methods since the pipe wall surface area is less than that which exists in reality across the monolith.

A model was compiled to enable each of these catalyst models to be studied systematically. As in sections 6.2.1 and 6.2.2 exhaust port pressure data, representing that generated during a typical exhaust event at a given speed, was input into a series of catalyst models to investigate the reflected pressure characteristics. The first of these series of models is shown in Figure 6.11 and investigated the type 2 catalyst models, shown in Figure 6.10. Exhaust port pressure data generated at 3000 r/min was input into each of the model configurations shown. Each model included an anechoic termination at the exit end. The upstream moving pressure history recorded at location i. for model A represented the reflection from the expansion into the entry cone only (location ii.). The upstream moving pressure history recorded at location i. for model B represented the

reflection from the expansion into the entry cone (location ii.) and the reflection generated as the wave passed into the catalyst monolith (location iii.) and so on.

Figure 6.12 shows the comparison of these pressure histories. The effect of each of the constituent parts of this catalyst model on the overall reflected pressure wave characteristic (reflected wave – model D) is clearly shown. The single rarefaction wave reflected from the expansion into the entry cone (reflected wave – model A) was a mirror of the input wave and of reduced amplitude, as was expected. When the input wave was allowed to pass into the catalyst monolith, a small compressive wave was generated which reduced the overall amplitude of the expansion wave (reflected wave – model B). When the input wave was allowed to pass through the monolith and expand into the exit cone then another rarefaction was generated that was superposed with those waves generated upstream (reflected wave – model C) and increased the amplitude of the rarefaction. The most significant change in the reflected wave profile occurred when the input wave was allowed to pass through the exit cone. The reduction in pipe area is rapid and a large compressive reflection was generated that caused the overall reflected pressure wave to have a significant compressive component following the initial rarefaction (reflected wave – model D).

The type 3 catalyst models were similarly investigated and the series of models used to study the reflected wave characteristics are shown in Figure 6.13. As previously, the input wave was passed through a succession of catalyst elements, which allowed the effect of each of these elements on the overall reflected profile to be quantified. Figure

6.14 shows comparisons of these pressure histories, which are almost identical to those shown in Figure 6.12. Figure 6.15 shows direct comparisons of the reflected waves generated by models D and H and the reflected wave profiles are almost identical. This leads to the conclusion that, so far as pressure wave action is concerned, it is sufficient to represent entry and exit cones of catalytic converters with parallel pipes of suitable dimensions. A pressure wave passing through a rapidly diverging or converging cone behaves as though the change of cross sectional area is instantaneous.

6.2.3.2 The effect of catalytic converter temperature

In investigating the influence of catalytic converter temperature on pressure wave action, there are two effects that must be considered. The first is the effect of the temperature on the local acoustic velocity and the second is the effect of temperature discontinuities on finite pressure wave propagation.

The method-of-characteristics gas-dynamics model based on the homentropic solution calculates the spatial and temporal variation of gas conditions according to the values of λ and β at every mesh point and at each time-step. The ambient gas temperature is maintained constant throughout the system and so only pressure information can be derived from these variables. Temperature information can only be calculated by the introduction of a third parameter, A_a, which is commonly, although incorrectly, referred to as gas entropy in method-of-characteristics based calculations. A_a actually refers to the non-dimensional acoustic velocity after isentropic change of state to reference pressure p_o; the relationship between entropy and acoustic velocity is given in Appendix

A2.2. It is necessary to use the non-homentropic calculation to study the effect of the variation of gas temperature.

McGinnity [120] demonstrated the effect of temperature discontinuities on finite pressure wave propagation and some of his results are shown in Figure 6.16. Shown are a series of plots from simulations of a compressive pressure wave introduced into a 10 m long pipe within which a sudden temperature rise of 2364°C occurred half way along the pipe. The wave was introduced by the action of a poppet valve in a high-pressure cylinder opening and the plots are shown at time-steps of degrees cam-angle rotation with the poppet valve cam operating at 10000 r/min. The non-homentropic calculation was based on the modified Benson technique, outlined in Section 2.6.2. As the compressive wave reached the temperature discontinuity at approximately 800 degrees cam angle, the leading edge of the wave was seen to accelerate and the amplitude of the wave reduce. As the original wave continued to traverse the temperature discontinuity, it was seen that a reflected rarefaction was generated which then travelled upstream.

These results showed that high temperature discontinuities can generate reflected waves as well as influence the propagation velocities of transmitted waves because of the rapid change in gas density. However, in this example, the temperature discontinuity was extremely large and extended over 5 m of pipe. In the case of catalytic converters in exhaust systems, the temperature discontinuity will extend typically for a maximum of 500 mm and the temperature discontinuity will certainly be significantly less than 2364°C, depending on the operational characteristics of the engine.

For a catalytic converter to reduce the NO, CO and HC emissions most efficiently, it is necessary for it to have reached its optimum operational temperature and for the engine to be operating with an air/fuel ratio at, or close to, stoichiometric. Within this narrow bandwidth of air/fuel ratio operation a gas temperature rise occurs across the converter monolith due to the increase in catalytic activity. This study has focussed particularly on the pressure wave action in exhaust systems at WOT conditions, since it is at these conditions that high amplitude pressure waves are generated and engine breathing characteristics can be significantly influenced. At this condition, engine management systems will switch to a mode of operation to give an enriched air/fuel ratio, typically in the range of 12-12.5:1, to give maximum power. At the high temperatures following combustion, oxygen can still be present in the cylinder charge due to dissociation and so additional fuel can be added to increase power. However, mixture enriching decreases combustion efficiency, so reducing fuel conversion efficiency and significantly reducing catalytic converter activity. Thus, at steady-state WOT conditions, the exhaust gas temperature rise across the catalytic converter will be relatively small, if indeed there is any temperature rise at all.

Figure 6.17 shows an example of experimental results of thermocouple recorded temperatures at the entry and exit cones of a catalytic converter located 100 mm downstream of the collector junction in a 4:1 configuration exhaust system. In this example the engine was operating at WOT. Throughout the speed range the measured temperature at the catalyst exit was lower than that of the entry. It should be noted that these measured temperatures were not strictly those of the exhaust gases since no account

was taken of convection or radiation heat effects. Nevertheless the results were indicative of trends of speed related gas temperature across the catalyst. The minor peak in temperature at 3000 r/min corresponded to a tuned speed for this particular engine configuration; combustion temperatures and pressures were higher due to the increase in air-fuel mass induced and so the exhaust gas temperature was correspondingly increased.

The correlation between measured experimental and predicted exhaust port pressure histories, shown in Figures 3.19 to 3.23, was good. The homentropic model was used for these comparisons and there were not any significant features of the measured wave profile that the model did not capture although wave amplitudes were slightly over predicted. This model was unable to predict reflections at temperature discontinuities since the whole flow field was assumed to have fixed reference values of temperature and pressure. The results indicate that, during these operating conditions, there were no significant reflections occurring at the pipe-catalyst interface due to temperature discontinuities.

In considering the effect of catalyst temperature on the local acoustic velocity, the period, in terms of degrees crank-angle θ, for a pressure wave to traverse a pipe of length L m is given by:

$$\theta = \frac{6NL}{a} \qquad (6.1)$$

To cause significant changes to the phasing of pressure waves traversing the pipe, a large change to the local acoustic velocity would be required. Since the change to the local acoustic velocity is given by $\sqrt{\gamma RT}_2 - \sqrt{\gamma RT}_1$, then extremely high temperature

variations would be necessary. Any resultant phasing differences would be more apparent over longer lengths of pipes, but, in this case of relatively short catalyst lengths, the differences are minimal.

6.3 PRESSURE WAVE OSCILLATION IN PIPES

In considering the pressure wave action in pipe networks, it has been demonstrated in Sections 6.2.1 to 6.2.3 how reflections generated at various pipe boundaries propagate in the opposite direction to that of the original pressure disturbance, with a sign dependant on the type of boundary encountered. Similarly, reflections are generated at the opposite end of the pipe with the disturbing pressure, in this case, being the reflection first generated at the other end of the pipe. This pressure wave oscillation will continue within the pipe until such time as the reflections are attenuated and there is no other disturbing pressure wave incident in the pipe.

A model was compiled to investigate this pressure wave oscillation phenomena to see how long such oscillations continued for when they were initiated by a single disturbing pressure pulse. The model used is illustrated in Figure 6.18 and represented the geometry of a typical dual exhaust tract and primary manifold runner. A short duration pressure wave, initiated at location i., was allowed to propagate to the junction (iii.) where the partial transmission of the wave across the junction occurred. The reflected component of the wave and that transmitted component that travelled along the adjacent exhaust tract were absorbed by the anechoic boundaries at the pipe ends (i. and ii.). The component of

the wave that propagated along the primary runner reached the pipe end and then expanded into a volume that represented the expansion into a typical junction volume (iv.). The transmitted component of the wave was absorbed and the reflected component of the wave was allowed to propagate back towards the junction at the exhaust tract-primary runner (iii.). Thus, pressure-time histories recorded at location iii. were a result of the superposition of reflections from the primary runner ends only, i.e. such a plot indicated the natural frequency characteristics of the pipe geometry.

Figures 6.19 and 6.20 show the pressure-time histories generated by each model, recorded at location iii., each for a short duration input pulse of approximately 250 kPa. Figure 6.19 shows that as the diameter of the primary runner was increased the magnitude of the reflected pressure wave was reduced. However, the phasing of the reflected waves remained unchanged. Figure 6.20 shows that as the length of the primary runner was increased, the time taken for the reflected pressure wave to return was correspondingly increased; when the pipe length was doubled, the period of pressure wave oscillation doubles. Of greater interest, however, is that both figures show how quickly the pressure wave action in a single pipe will decay when not disturbed by additional wave action. This result has particular significance when considering the sources of pressure waves in exhaust systems and the effect of waves of different magnitudes, which has been outlined in Chapter 5. The results suggest that it may only be necessary to consider the first reflection from any pipe boundary since the subsequent reflections have been shown to be of such small magnitude that their relative effect on cylinder scavenging and pumping losses can be considered negligible.

Equations based on linear acoustic models have been applied to describe the characteristics of pressure wave oscillation in pipe systems. The solution to equation (A2.1.51), shown in Appendix A2.1, gives the natural frequency of a single pipe. Models 1 to 5, shown in Figure 6.18, contain air at approximately 850°K, which gives a local acoustic velocity of approximately 575 m/s. The natural frequency of pressure wave resonance of these models, given by equation (A2.1.51), for each pipe configuration is:

Model	Pipe length (m)	Resonance half period (ms) from $\cos\left(\frac{\omega}{a}l\right)=0$
1 – 3	0.4	1.391
4	0.6	2.087
5	0.8	2.783

These values correspond very well with the half periods indicated in Figures 6.19 and 6.20 although the correlation is not exact since there is some change to the wave profile as the wave traverses the pipe. The natural frequency of oscillation of a complex pipe system, such as a 4:1 configuration manifold, has been given by the solution to equation (A2.1.52) [107]:

$$\frac{F^2}{f_1 a_5}\cot\left(\frac{\omega}{a_5}L\right)-\frac{\omega V}{{a_5}^2 f_1}-\frac{4f_1}{a_1}\tan\left(\frac{\omega}{a_1}l\right)=0 \qquad (6.2)$$

Considering a simple 4:1 configuration exhaust manifold with 360 mm long, 35 mm diameter primary pipes and a 500 mm long, 43 mm diameter collector pipe, the predicted pressure-time history at the exhaust port generated by this system at 3000 r/min is shown in Figure 6.21. Taking the average exhaust gas temperature as ≈620°K, $\gamma = 1.35$ and a gas constant of ≈270 $^{J}/_{kgK}$, the average acoustic velocity is 475 m/s. The solution for the

natural frequency ω of equation (6.2) applied to this system is ≈613 rad/s, which, in terms of period of degrees crank-angle rotation for an engine operating at this speed, is:

$$Crank-angle\ period\ =\ \frac{2\pi}{613}\times\frac{3000}{60}\times 360\ =\ 184.5^{\circ}CA$$

This calculated natural period of pressure wave oscillation does not correspond with that calculated by the method of characteristics, shown in Figure 6.21. The period of oscillation is over predicted by 15-20°CA. Such models do not consider the transient boundary conditions that are a feature of the actual conditions within practical exhaust systems or the characteristics of finite pressure wave propagation such as wave attenuation.

6.4 IDENTIFICATION OF THE PRINCIPAL PRESSURE COMPONENTS OF THE EXHAUST PORT PRESSURE HISTORY

To design an exhaust system to generate the optimum pressure wave action at the exhaust port at a given operating speed, it is necessary to identify the component pressure waves that, when superposed, will result in this overall pressure profile. Thus, by identifying the sources of the compressive and expansive waveforms and further identifying the factors that influence the phasing and amplitude of the arriving waveforms, the basis of an exhaust system design methodology can be defined.

This phase of the study used a series of theoretical simulation models to trace individual reflected and transmitted waves throughout typical exhaust system configurations. Using

this method it was possible to generate pressure histories which comprised of a number of principal wave components. These generated pressure histories were shown to represent the key features of predicted pressure histories at the exhaust port for any configuration of exhaust system.

6.4.1 Theoretical wave tracking models

A series of models was compiled that allowed pipe networks, representing various exhaust system configurations, to be defined. Reference gas conditions in these networks were set to those that would exist within the corresponding exhaust system at the given operating speed. The mass flow history from a single exhaust event was input into the system and the resulting pressure wave was allowed to propagate throughout the system. To track the single reflected wave from a given boundary condition, the wave component continuing downstream was absorbed by an anechoic boundary. Any wave oscillations that would normally occur within upstream pipes were eliminated by resetting the λ and β characteristics to give ambient pressure and temperature conditions at the meshes adjacent to the pipe boundaries at the end of every time-step. By this method, the progress of single waves, which resulted from a single reflection at a pipe boundary, could be tracked throughout an exhaust pipe network. The models appropriate to individual exhaust system configurations are shown in detail in the following sections.

6.4.1.1 4:1 configuration system

Figure 6.22 shows the series of models used to investigate the phasing of single waves throughout a simple 4:1 configuration exhaust manifold. Initial input data for the first of

these models (model A) was generated by a model of an engine cylinder exhausting into an anechoic boundary at a given speed, which gave pressure and mass flow data across the exhaust valve that was not influenced by exhaust tuning effects. This pure pressure-mass flow data was input into model A at location (1). The resultant pressure wave was allowed to traverse the junction at location (5) at which point a reflected wave was generated. The reflected wave then propagated back to location (1) where the wave was absorbed by an anechoic boundary. The upstream moving pressure data at location (1) was recorded and represented a single pure reflection from the junction during an exhaust event. The compressive components of the wave that continued on to locations (2), (3), (4) and (6) were absorbed by anechoic boundaries. The pressure data at these locations was retained as input data for subsequent simulations.

Model B was used to obtain a correctly phased pure reflection from the open end of the exhaust system. Pressure data retained from model A immediately downstream of location (5) was input into model B at the same location. The wave reached the open end of the system at location (6) where a reflected wave was generated. The reflected wave then traversed the junction and continued on to locations (1) to (4) where the wave was absorbed by anechoic boundaries. When the reflected wave traverses the junction, it would normally be expected that another reflected wave would be generated that travels back to location (6). To eliminate any interference between such reflections and the wave profile of interest, the model allowed the junction subroutine to be completed normally. Thus, incident and reflected λ and β characteristics were calculated at all the adjacent pipe meshes as normal. The appropriate reflected characteristics in the pipes of

interest were then reset to 1.0 at the end of each time-step. Therefore, the pressure data recorded at location (1) represented a pure reflection from the open end of the system that resulted from the cylinder exhausting during a single cycle.

Model C was used to obtain a correctly phased pure reflection from the pipe-valve boundaries at cylinders 2 to 4. In this model it was assumed that all of these valves were closed and so the pipe boundaries were represented as closed ends. In reality, depending on the lengths of the primary pipes, the local acoustic velocity of the gas within and the cam timing, it is possible that when the exhaust pulse generated by the cylinder of interest first arrives at the adjacent cylinders, one or more of the exhaust valves may be partially open. In the case of an engine with a 1342 firing order, cylinder 3 may be just starting to exhaust or cylinder 2 may be just finishing exhausting. For practical lengths of primary pipes and for conventional exhaust cam timing, only one cylinder is likely to be exhausting at the instant of the exhaust pulse arriving and the exhaust valves will only be partially open. Thus, it is reasonable to assume that the component of an exhaust pulse arriving from cylinder 1 at such a cylinder will behave in a similar fashion to the components of the wave that arrive at cylinders with the exhaust valves closed.

Pressure data retained from model A at locations (2) to (4) was input into model C at the same locations. Reflections were generated at the pipe closed ends. The resultant waves traversed the junction and continued on to locations (1) and (6) where they were absorbed by the anechoic boundaries. Internal reflections, within those primary pipes where pressure data was input, were suppressed so as to eliminate pipe resonance by the method

used for model B. The pressure data recorded at location (1) represented a pure reflection from the exhaust valves of adjacent cylinders that resulted from the cylinder of interest exhausting during a single cycle.

Since, all of the primary pipe lengths in this model were the same and the gases within were at similar conditions, the reflections from the valves at the adjacent cylinders arrived at location (1) at the same time, thus augmenting each other and increasing the amplitude of the overall pressure profile. The same was true for that component of the wave reflection that continued on to location (6) and so potentially another high amplitude reflection was generated at the open end of the system. Model D was used to obtain this reflection. Pressure data retained from model C immediately downstream of location (5) was input into model D at the same location. Pressure data was recorded at location (1) and internal reflections, within the collector pipe where pressure data was input, were suppressed as previously.

Using this method it was possible to build a composite diagram of pressure data at the exhaust port of the cylinder of interest and this data is shown in Figures 6.23 and 6.24. Each pressure history represents a single pure reflection from a given boundary condition and results from a single exhaust event during an engine cycle at a given speed. Single pressure pulses arriving from other cylinders as a result of their separate exhaust events were represented by taking the recorded pressure history at location (2) in model A and phasing this data accordingly. Similarly, reflections from the system open ends, due to the other cylinders exhausting, were also generated at ±180°CA intervals.

Figures 6.25 and 6.26 show comparisons between the superposition of these pressure histories and the predicted pressure histories generated by the unmodified model. These figures show good correlation between the pressure profiles. Some minor phasing and amplitude errors are evident but the principal features of the exhaust port pressure profile generated by the unmodified model have been captured by this method of single wave superposition. The differences between the two profiles are discussed in more detail in Section 6.4.2.

6.4.1.2 4:2:1 configuration system

Figure 6.27 shows some of the series of models that were used to investigate the phasing of single waves throughout a simple 4:2:1 configuration exhaust manifold. The models were more complex than those required to investigate 4:1 exhaust systems since there were a greater number of boundary conditions to consider and hence a greater number of sources of potential reflections.

Model A isolated the single reflected wave from the primary-secondary junction (location (5)) and generated a pressure profile at location (4) that, when phased ±360°CA, was used to represent arriving exhaust pulses from cylinder 4. Model B isolated the single reflected wave from the secondary-tertiary junction (location (7)) and generated pressure profiles at locations (2) and (3) that, when phased ±180°CA, were used to represent arriving exhaust pulses from cylinders 2 and 3. This model was also required to suppress reflections within the secondary pipe lengths to prevent interference with the pressure waves of interest. Models C and D isolated reflections from the valves at adjacent

cylinders that were considered to be closed for the purposes of this study. Additional models, based on the same principles of wave isolation, generate single reflections from the open end of the system and from waves that traverse the junctions at locations (5) and (7) and then generate a reflection at the junction at location (6).

Figures 6.28 and 6.29 show composite diagrams of pressure data at the exhaust port of the cylinder of interest at 3000 and 6000 r/min. Each pressure history represents a single pure reflection from a given boundary condition and results from a single exhaust event during an engine cycle at a given speed. Single pressure pulses arriving from other cylinders as a result of their separate exhaust events were represented by phasing recorded pressure data appropriately as previously described.

Figures 6.30 and 6.31 show comparisons between the superposition of these pressure histories and the predicted pressure histories generated by the unmodified model. The figures show good correlation between the pressure profiles and indicate that all major contributors to the full profile have been accounted for.

6.4.1.3 4:2:1 configuration system with secondary pipe catalysts

An identical series of models to those of 4:2:1 configuration exhaust systems was compiled with additional models to isolate the reflections generated at entry and exit cones of the catalysts.

Figures 6.32 and 6.33 show composite diagrams of pressure data at the exhaust port of the cylinder of interest at 3000 and 6000 r/min. Figures 6.34 and 6.35 show comparisons between the superposition of these pressure histories and the predicted pressure histories generated by the unmodified model. The figures show good correlation between the pressure profiles and again indicate that all major contributors to the full profile have been accounted for.

6.4.2 Sources of error between theoretical and full gas-dynamics models

Figures 6.25, 6.26, 6.30, 6.31, 6.33 and 6.34 show some differences between the superposed pressure histories and those pressure histories generated by the full gas-dynamics models of the equivalent systems. There are a number of sources of these differences.

The pressure histories generated by the method outlined in the previous sections tracked waves as they progressed through undisturbed pipe systems. In reality there would exist in the pipes some residual wave action from previous cycles and waves generated during exhaust events at other cylinders. This of course is the purpose of the method of characteristics; to calculate unsteady wave action and the progress of individual waves as they propagate through a non-uniform flow field. The effect on a wave as it propagates through such a field is to modify the propagation velocity of elements of the wave profile according to the local conditions. Thus, both the profile of the wave and its phasing is modified as it progresses through the pipe network. The simplified anechoic models do not allow for this effect on the wave action and the wave progresses through the pipe

network with a velocity according to its pressure relative to the uniform ambient conditions. The difference between the propagation velocities of the simplified anechoic and conventional gas-dynamics models accounts for some of the phasing discrepancies and the absence of any residual wave action accounts for some of the amplitude differences.

The pipe junction model used throughout this study was that detailed by Bingham [111]. This model requires the definition of pipes at junctions as either suppliers (pipe *s*) or collectors (pipe *c*). The convention, in the case of exhaust systems, is to define downstream pipes as collectors. The junction model proceeds by comparing the velocities in the upstream pipes to find the pipe with the highest flow velocity (pipe *l*) and it is assumed that this is the main flow through the junction at that instant. The pressure loss across the junction is then given by:

$$p_l - p_c = C_l\left(\rho_c u_c^{\,2}\right)_{previous\ \ time\ \ step} \qquad (6.3)$$

where C_l is an experimentally derived loss coefficient and is a function of the angle between pipes *l* and *c*. In cases where reverse flow across the junction occurs or flow in all pipes is towards the junction, then a constant pressure junction model is used (see Section 2.7.2.1). The theoretical model for the tracking of single waves, used for this phase of the study, suppressed resonant wave action in individual pipes and so the wave of interest traversed junctions within a uniform flow field. Thus, in the case of a compressive wave traversing a junction in a downstream moving direction, then, according to the calculation procedure (detailed in Section 2.7.2.2), the resultant pressures at all adjacent pipe meshes upstream of the junction would be deemed equal.

The pressure at the adjacent pipe mesh downstream of the junction would then be calculated according to equation (6.3). This will always be the case with the simplified anechoic model. If such a wave was approaching a junction in the same direction when using the full gas-dynamics model, then it is possible for other waves to be approaching the same junction through the collector pipe. In such a case, where flow in all pipes is towards the junction, the calculation procedure will then revert to the constant pressure junction model. Thus, differences may occur between the calculated reflected and transmitted components of waves across junctions.

The correlation between the exhaust port pressure histories of the theoretical model for tracking single waves and the full gas-dynamics model is generally very good. Although some amplitude differences are evident, the locations of individual peaks and troughs on the wave profiles correspond well. Using this method, the principal sources of the individual waves that create the overall exhaust port pressure profile have been identified. It has been shown that the superposition of the primary pipe wave action and the first reflections from pipe boundaries downstream of the primary pipe can well represent the exhaust port pressure profile. Design guidelines can now be developed that consider the sources of significant compression and rarefaction waves and the pipe geometry required to phase these waves in accordance with the guidelines indicated in Chapter 5.

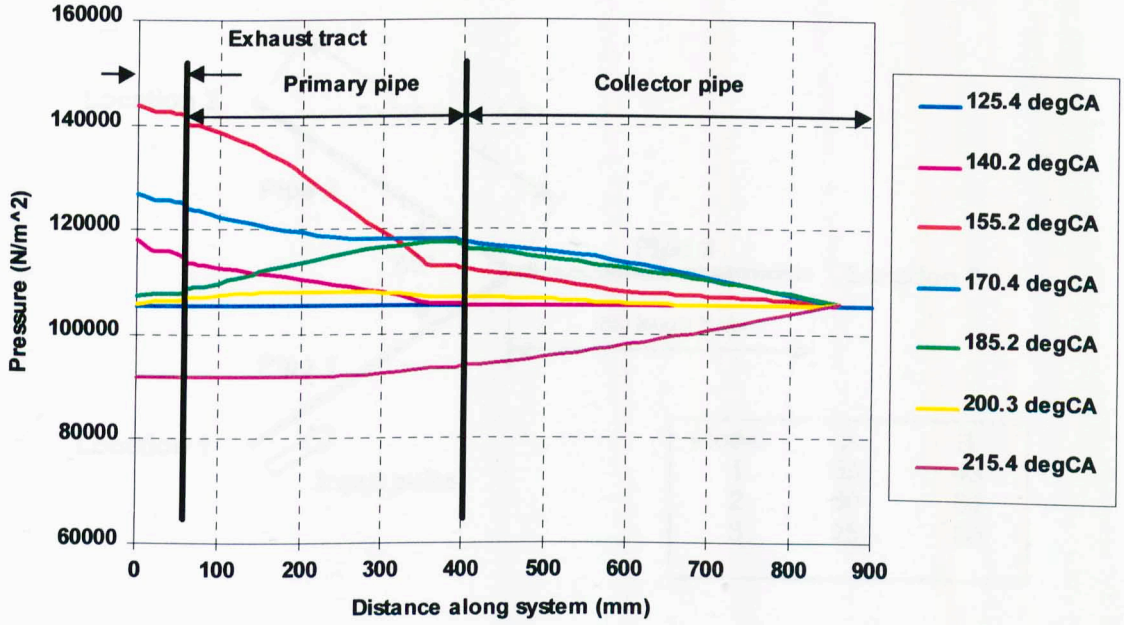

Figure 6.1 Pressure-distance plot in 4:1 configuration exhaust for single exhaust event

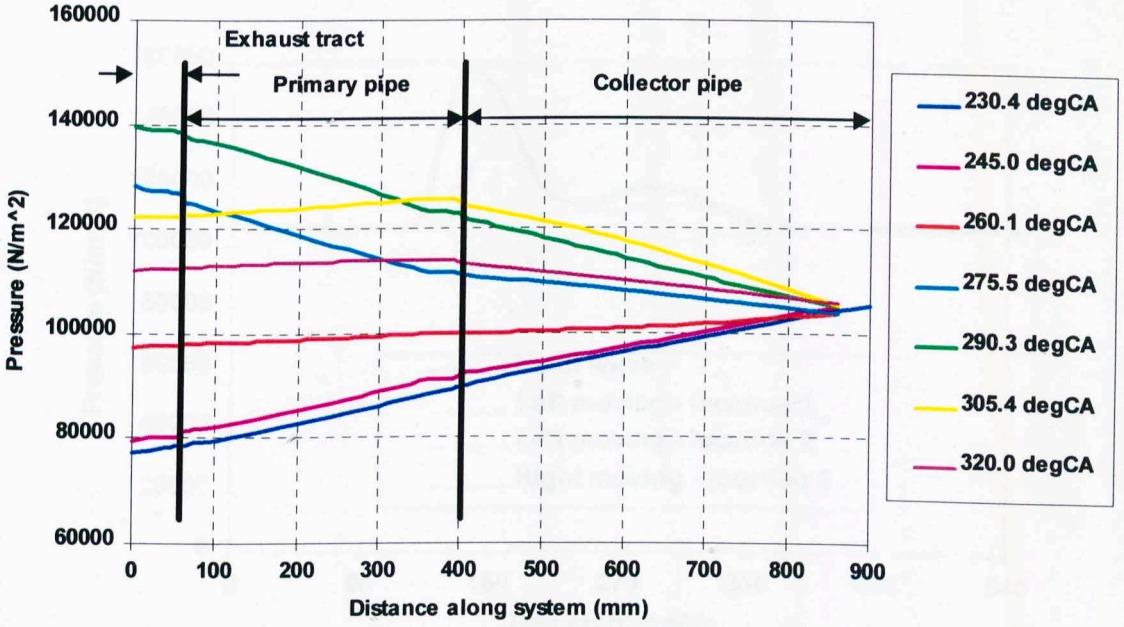

Figure 6.2 Pressure-distance plot in 4:1 configuration exhaust for single exhaust event

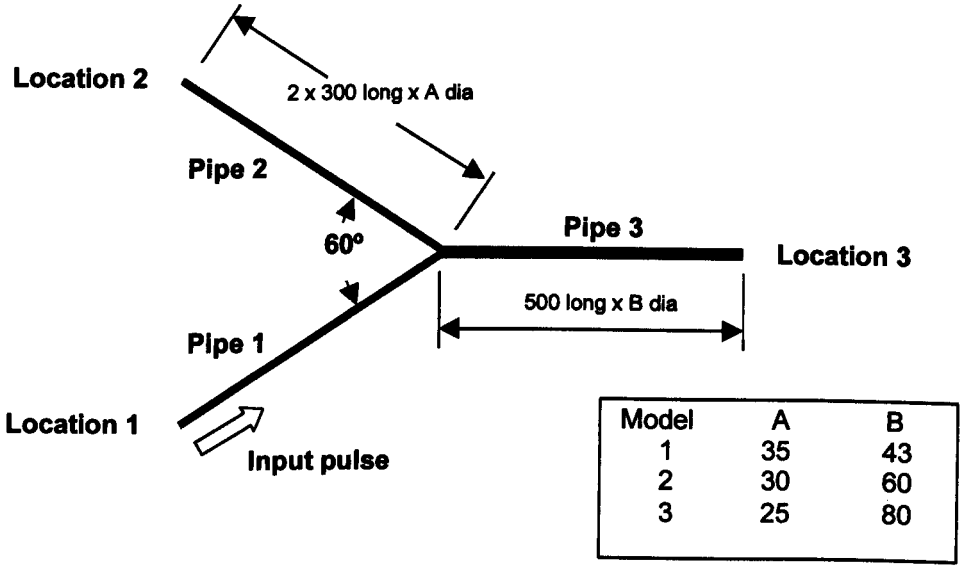

Model	A	B
1	35	43
2	30	60
3	25	80

Figure 6.3 Primary-secondary pipe junction configuration

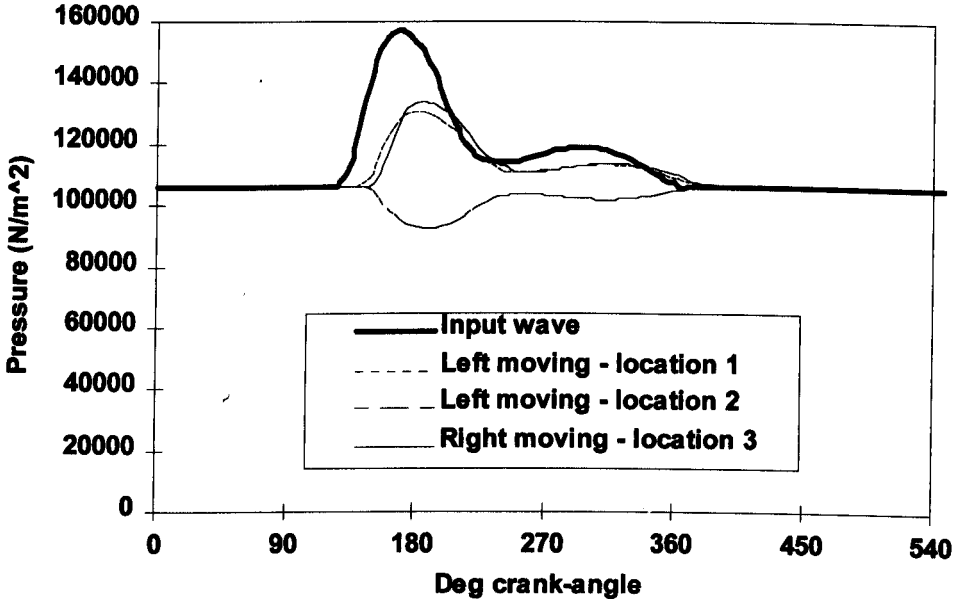

Figure 6.4 Predicted pressure histories – model 1

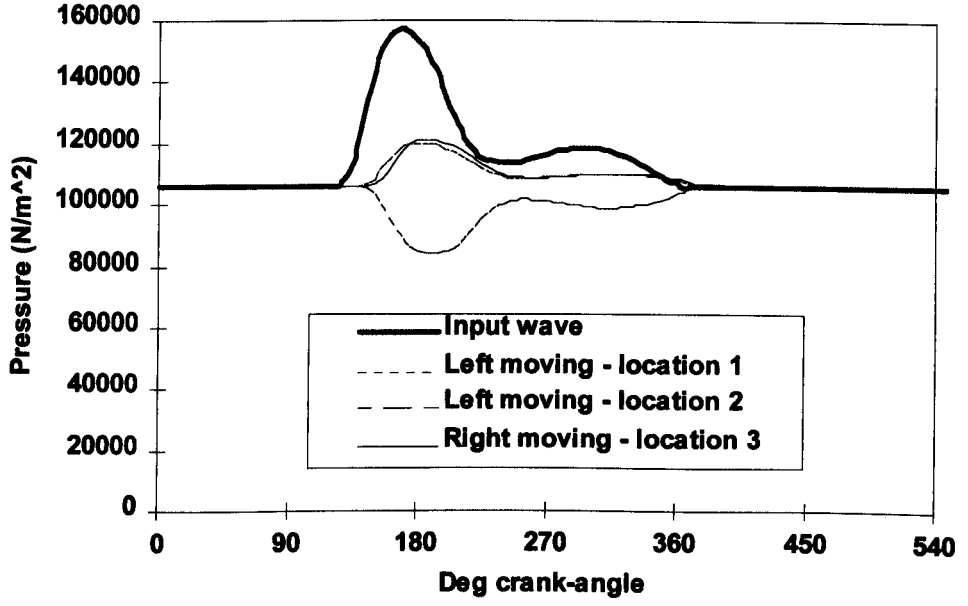

Figure 6.5 Predicted pressure histories – model 2

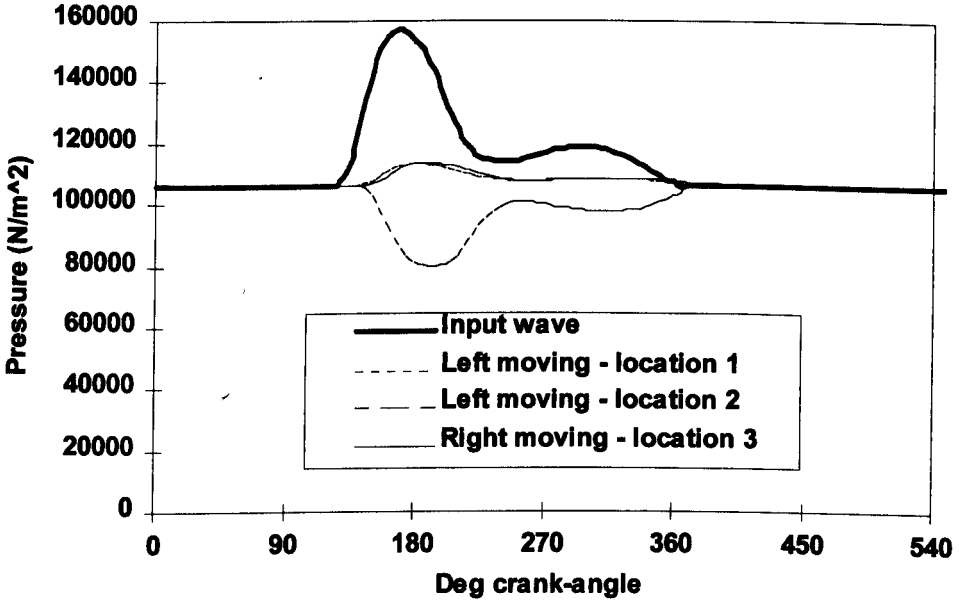

Figure 6.6 Predicted pressure histories – model 3

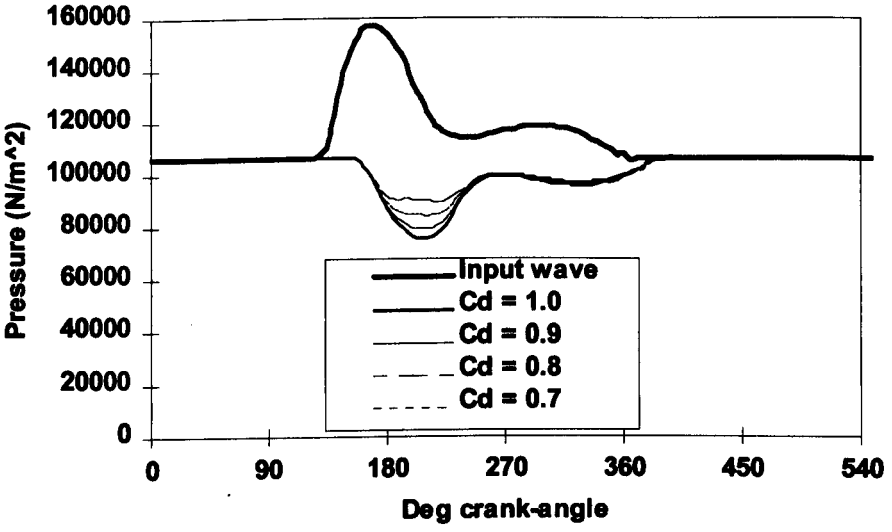

Figure 6.7 The effect of variation of C_d at exhaust open end on reflected wave characteristics

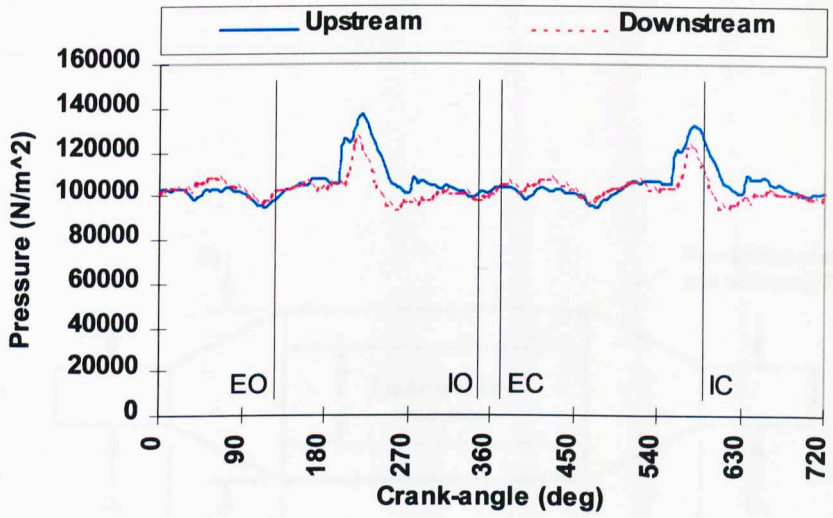

Figure 6.8 Upstream and downstream catalyst pressure – 4:2:1 system at 3000 r/min

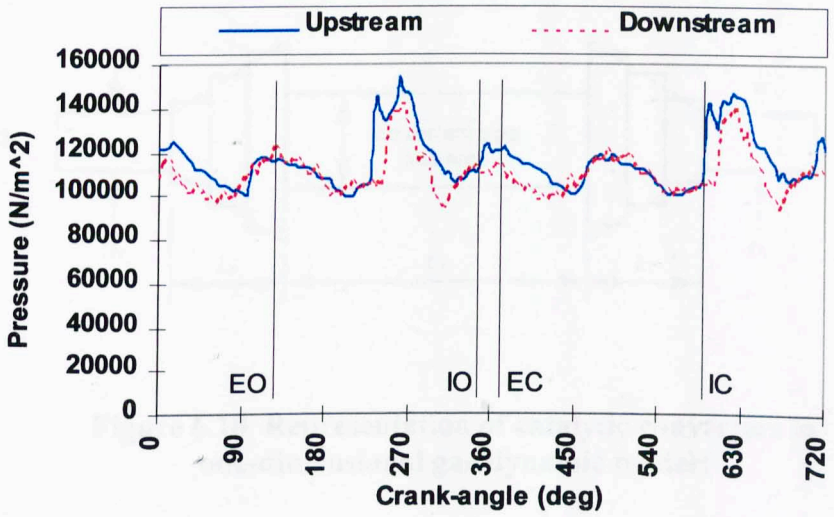

Figure 6.9 Upstream and downstream catalyst pressure – 4:2:1 system at 5000 r/min

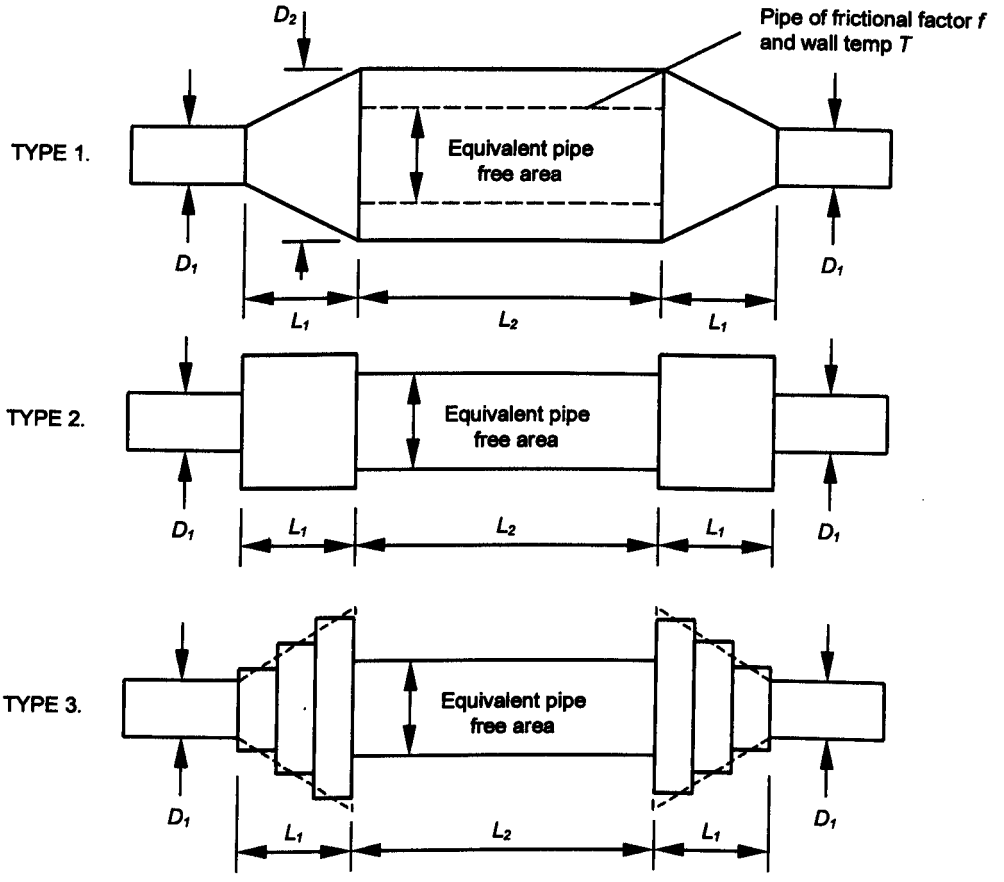

Figure 6.10 Representation of catalytic converters in one-dimensional gas-dynamic models

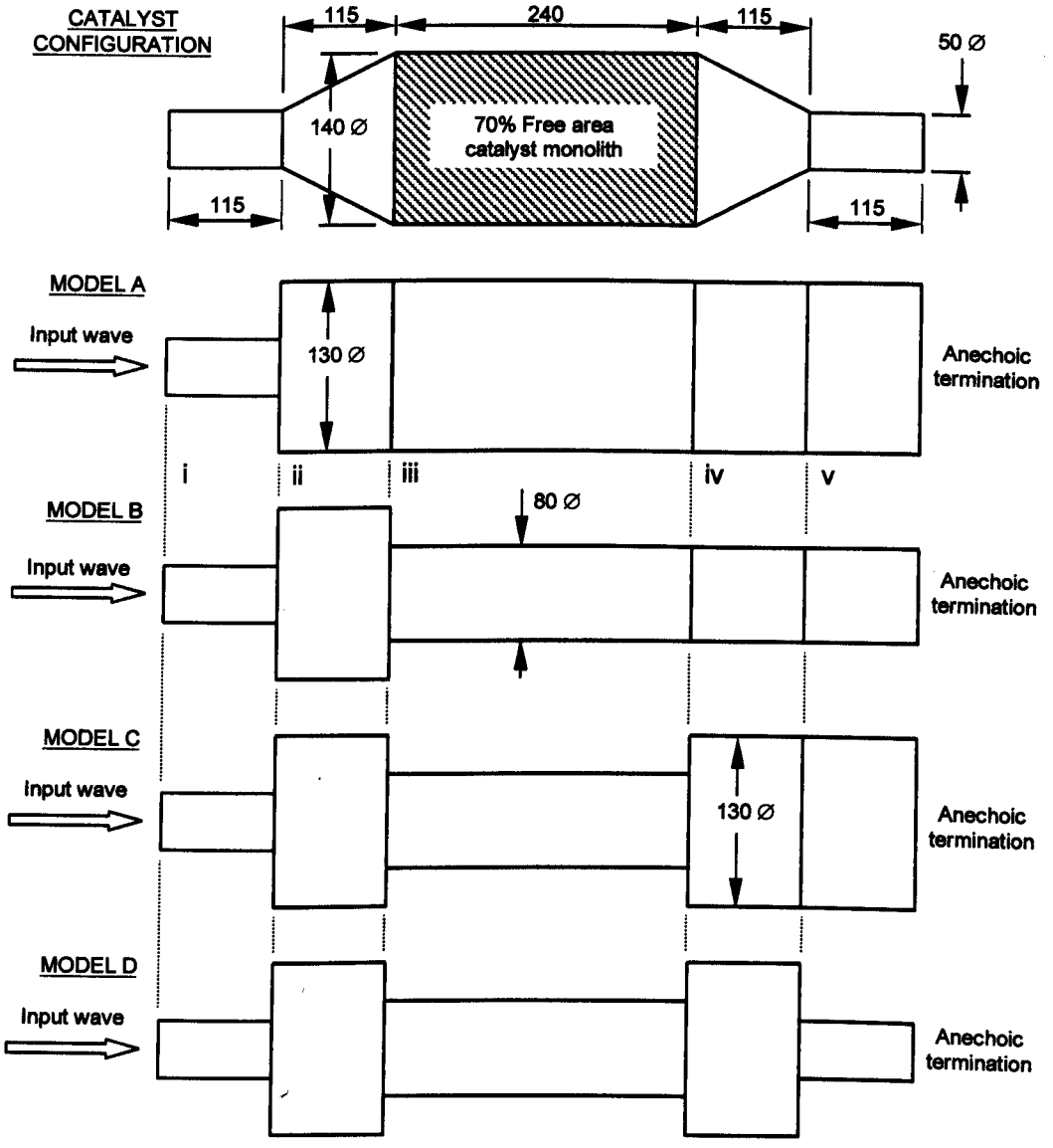

Figure 6.11 Models to investigate the reflected pressure characteristics of type 2 catalytic converter models

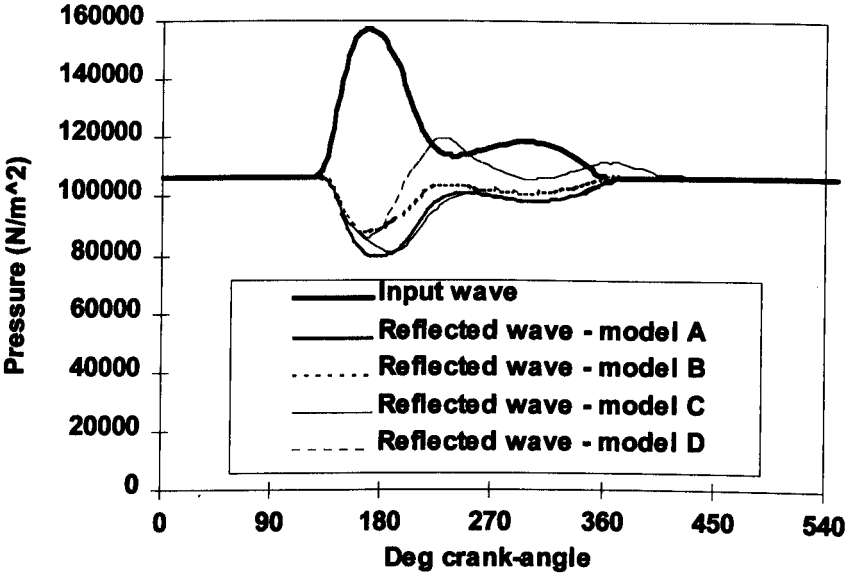

Figure 6.12 Pressure wave reflections from model A – D

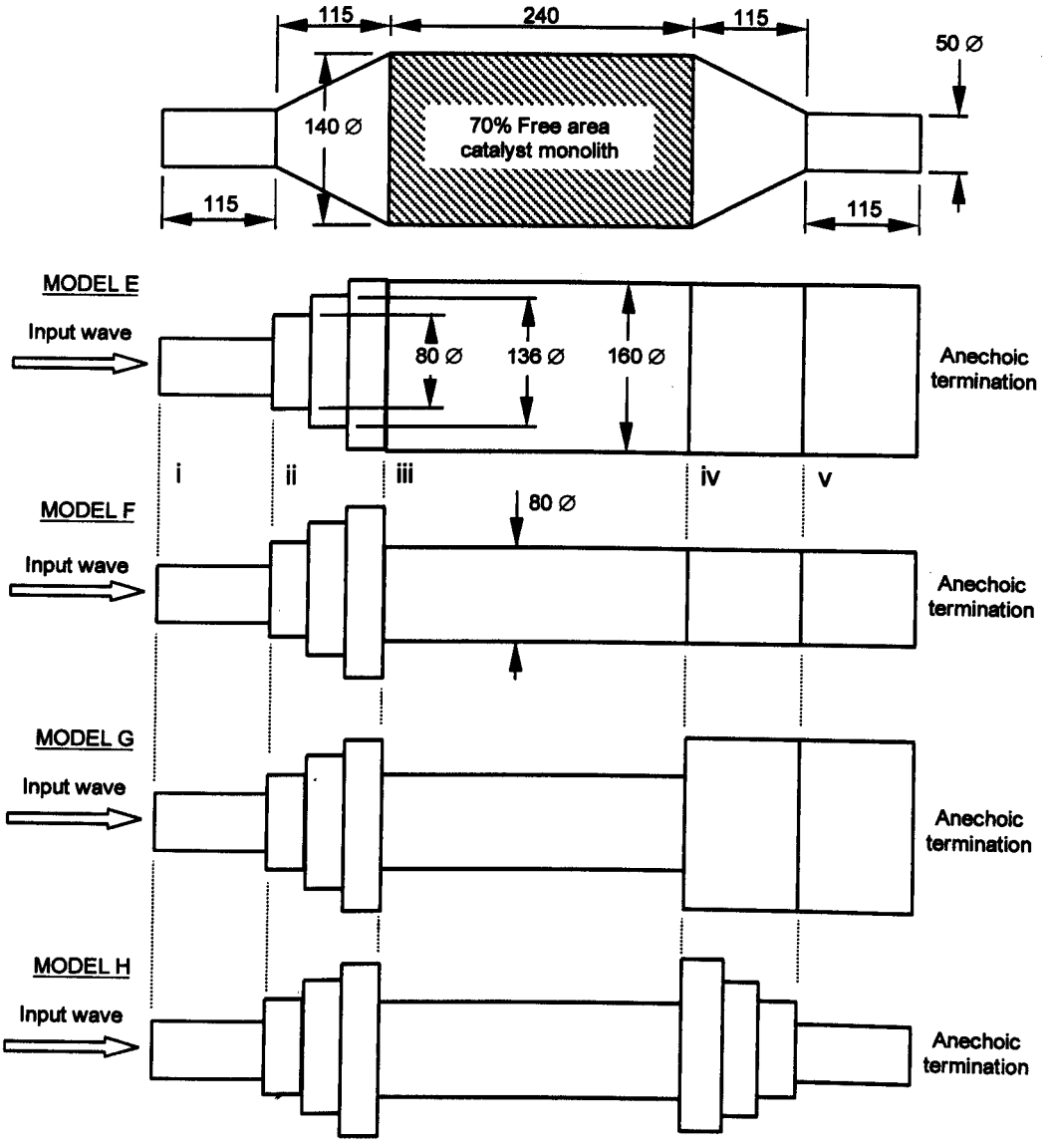

Figure 6.13 Models to investigate the reflected pressure characteristics of type 3 catalytic converter models

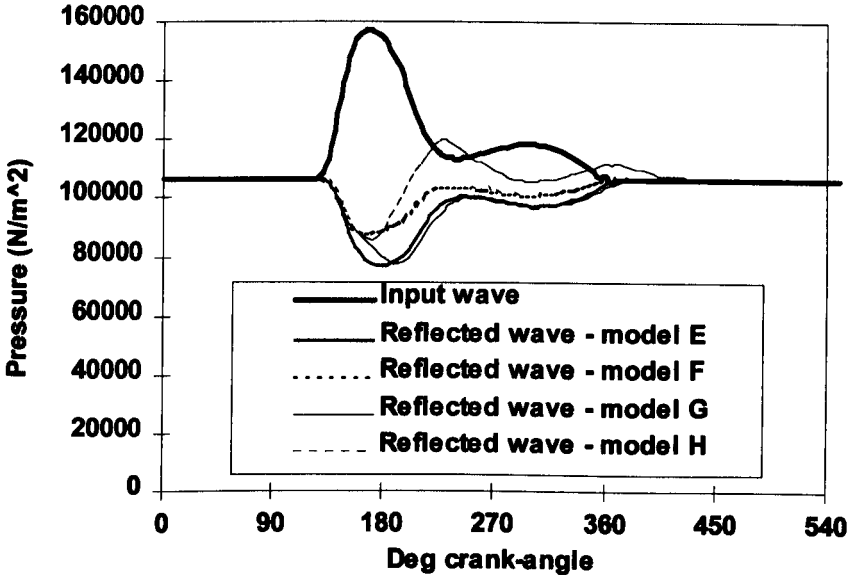

Figure 6.14 Pressure wave reflections from model E – F

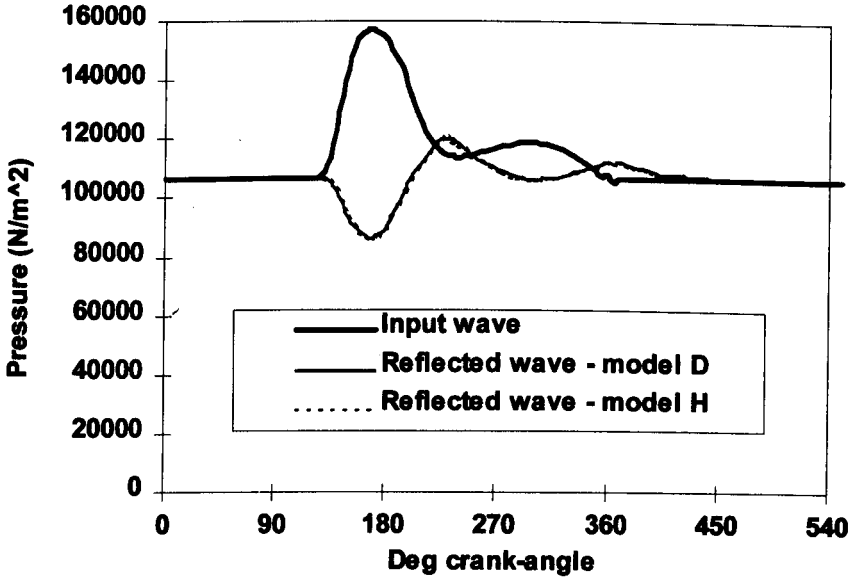

Figure 6.15 Comparison of reflected waves from models D and H

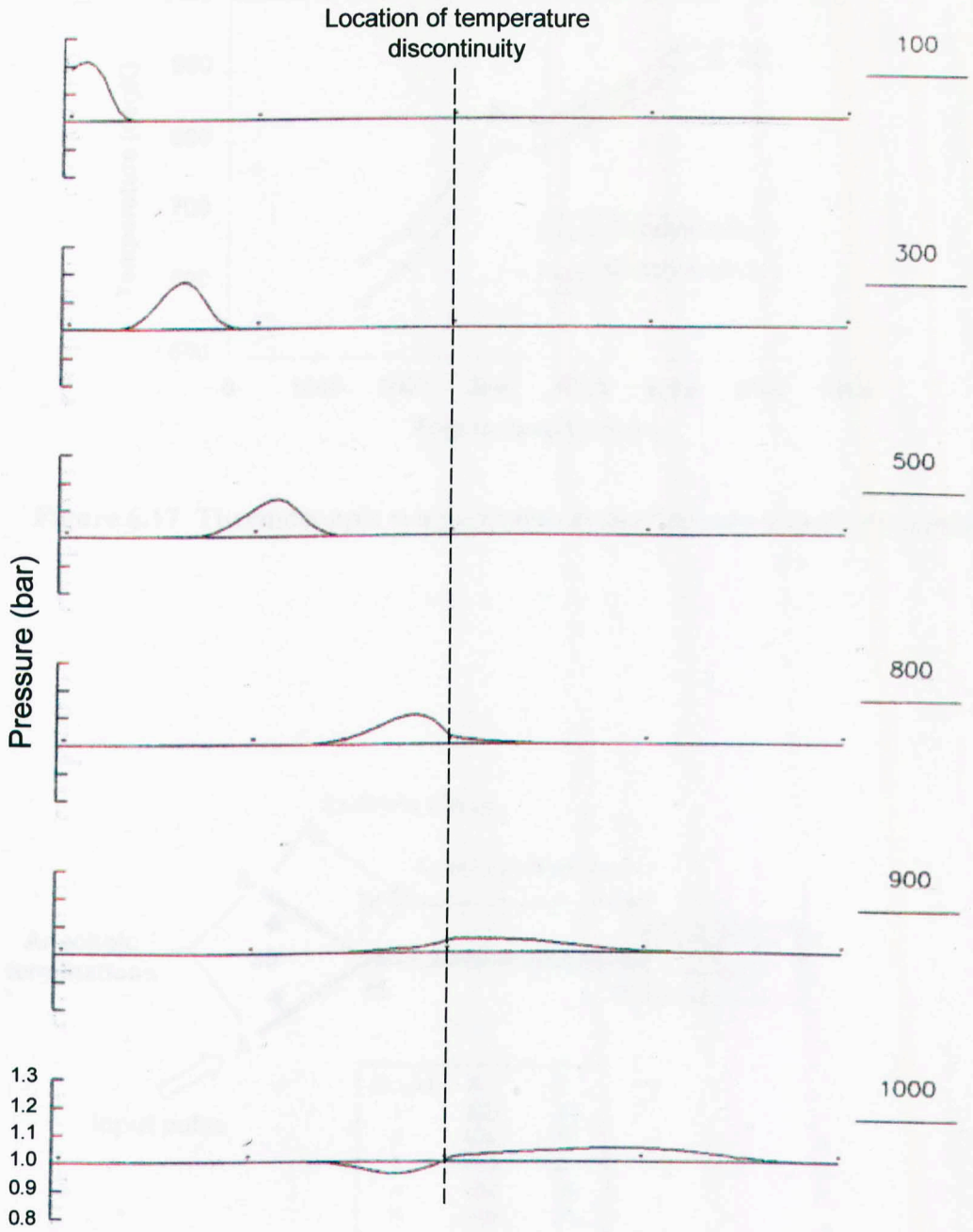

Figure 6.16 The effect of temperature discontinuity on pressure wave [120]

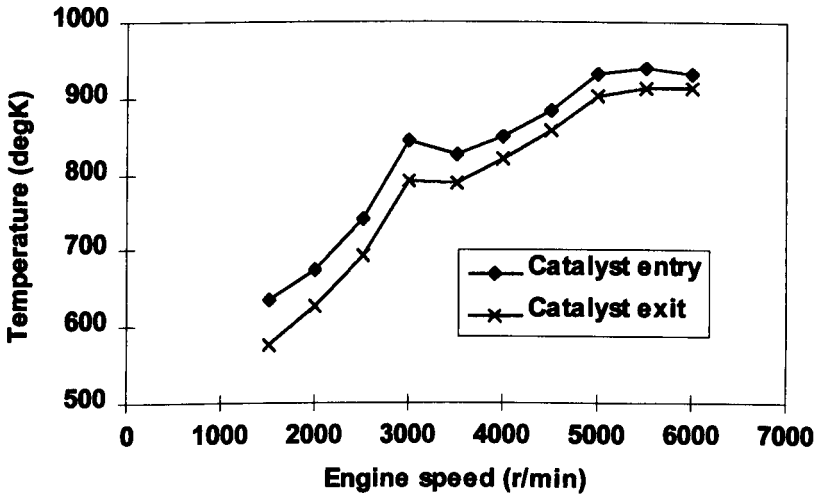

Figure 6.17 Thermocouple temperatures at catalyst entry and exit cones

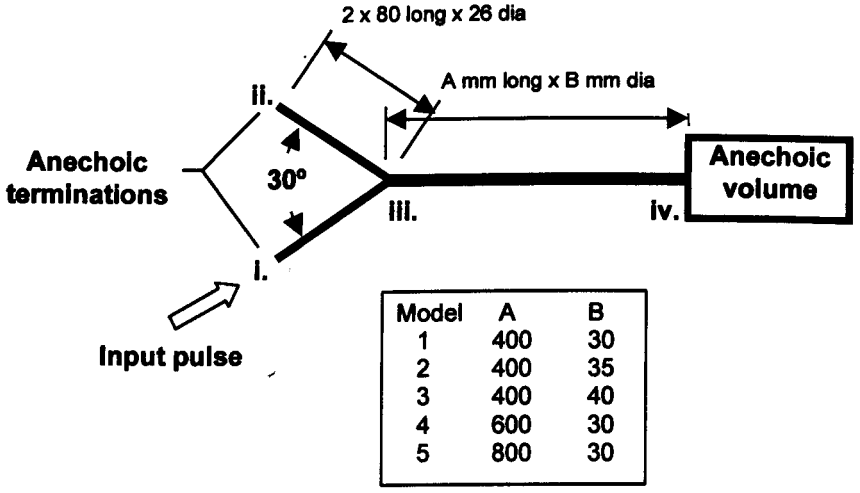

Model	A	B
1	400	30
2	400	35
3	400	40
4	600	30
5	800	30

Figure 6.18 Models for the study of resonance characteristics of pipes

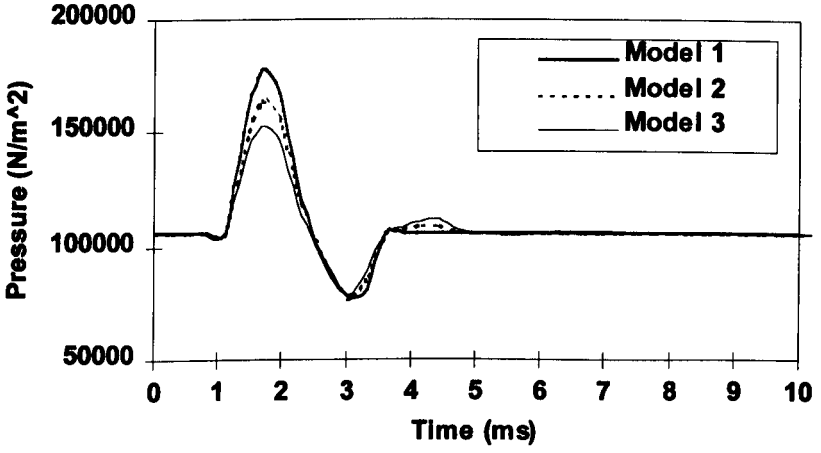

Figure 6.19 Pressure-time histories recorded at location iii.

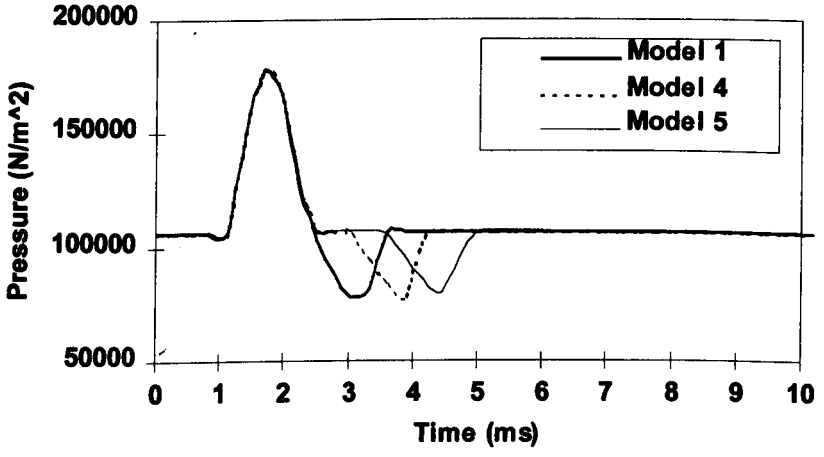

Figure 6.20 Pressure-time histories recorded at location iii.

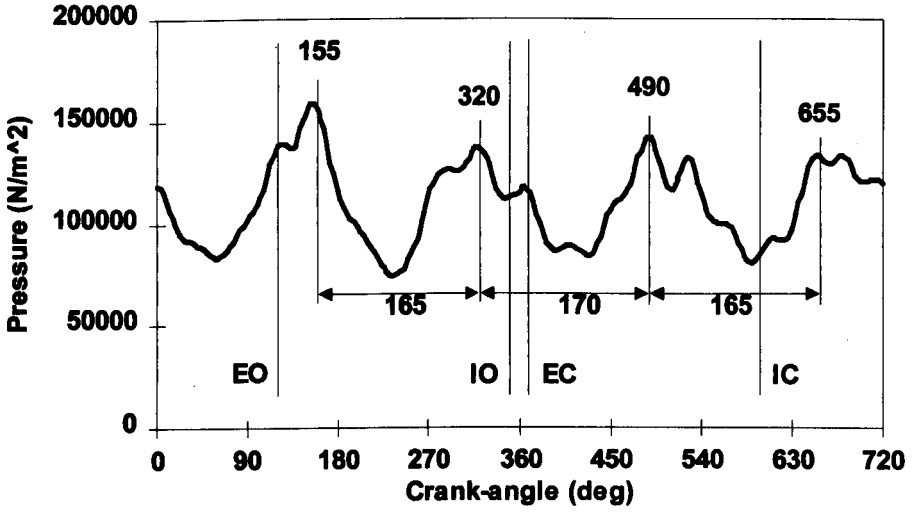

Figure 6.21 4:1 configuration system exhaust port pressure-time history at 3000 r/min

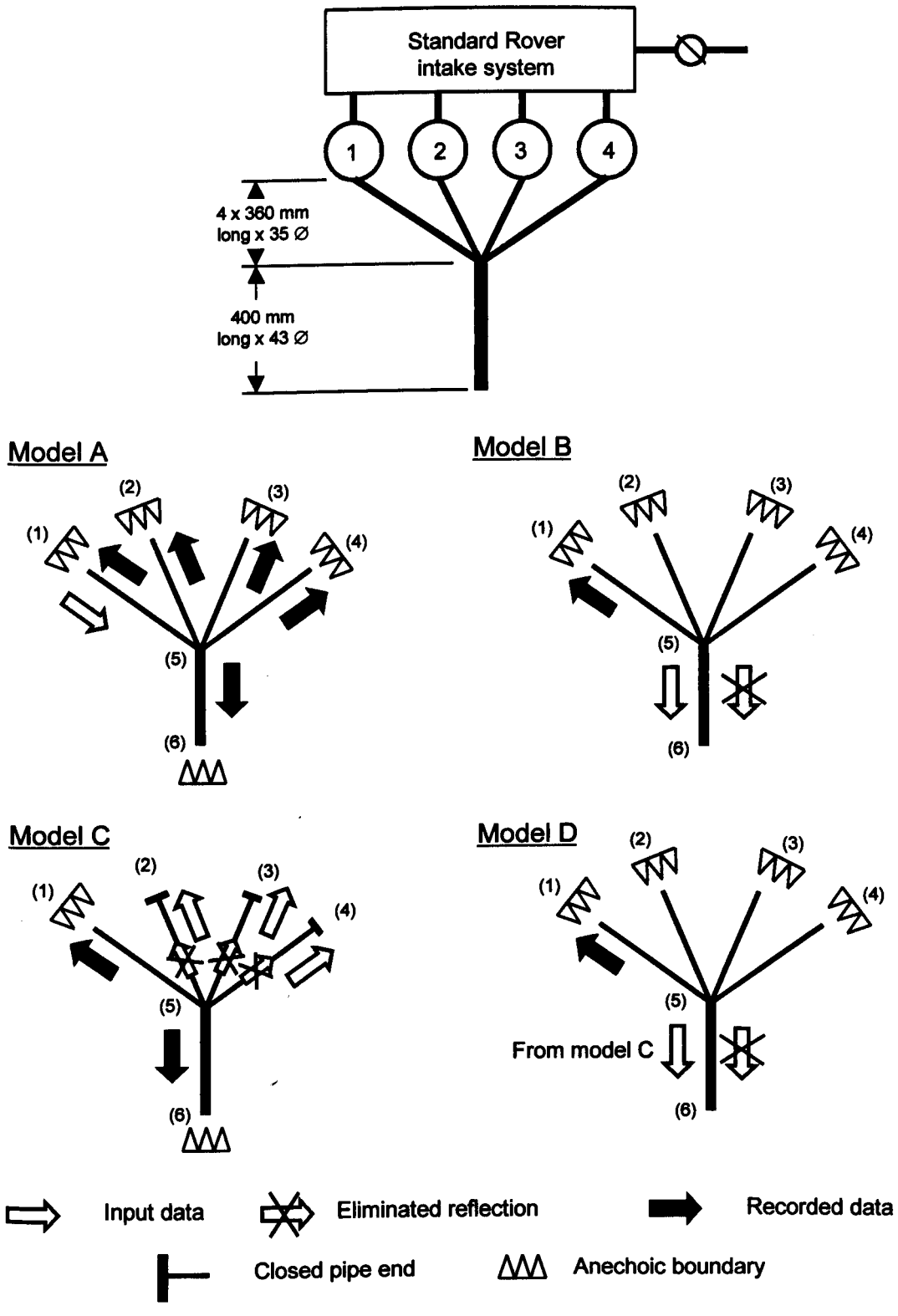

Figure 6.22 Models used to isolate single reflections in 4:1 exhaust systems

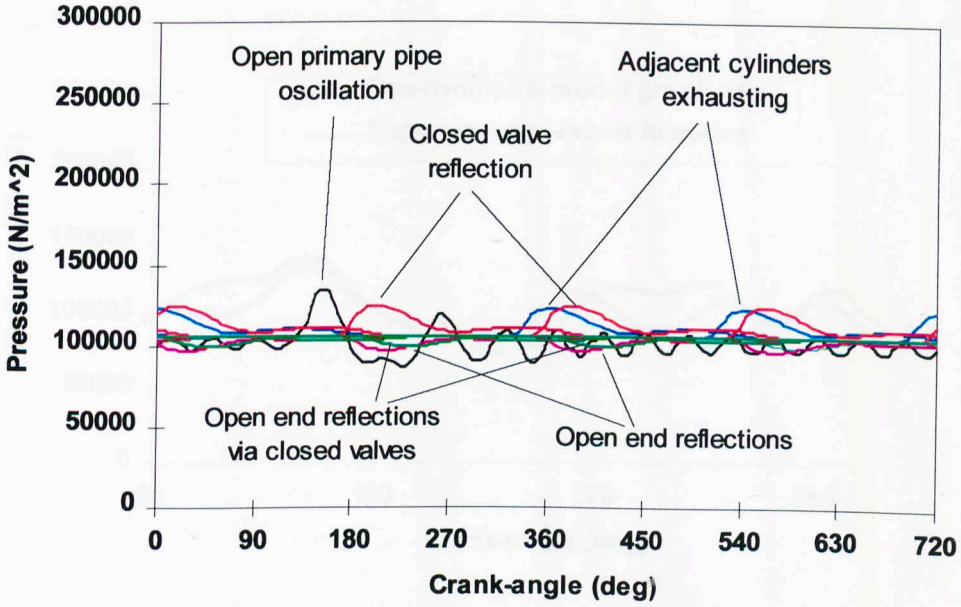

Figure 6.23 Single reflection pressure data from 4:1 configuration exhaust system at 3000 r/min

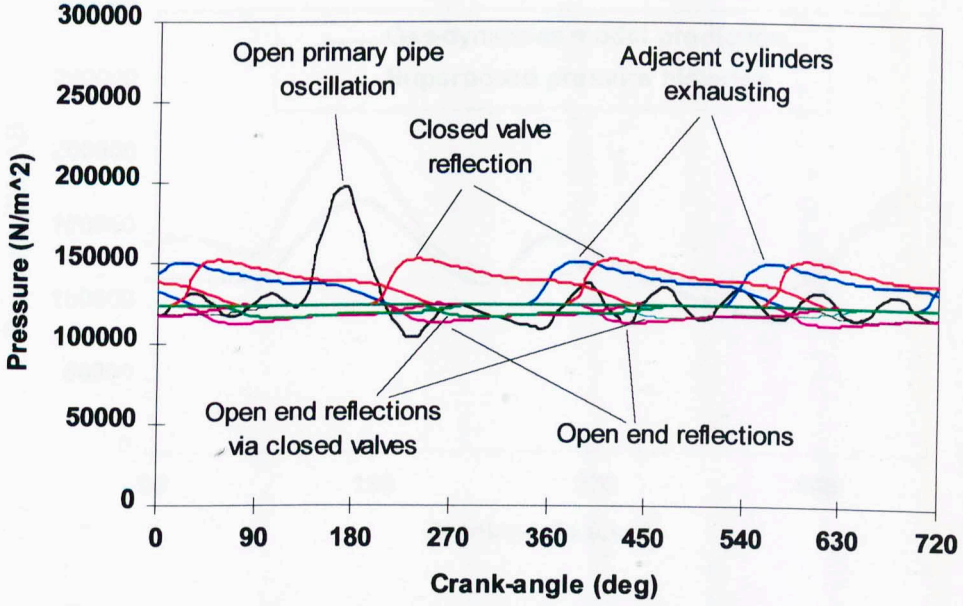

Figure 6.24 Single reflection pressure data from 4:1 configuration exhaust system at 6000 r/min

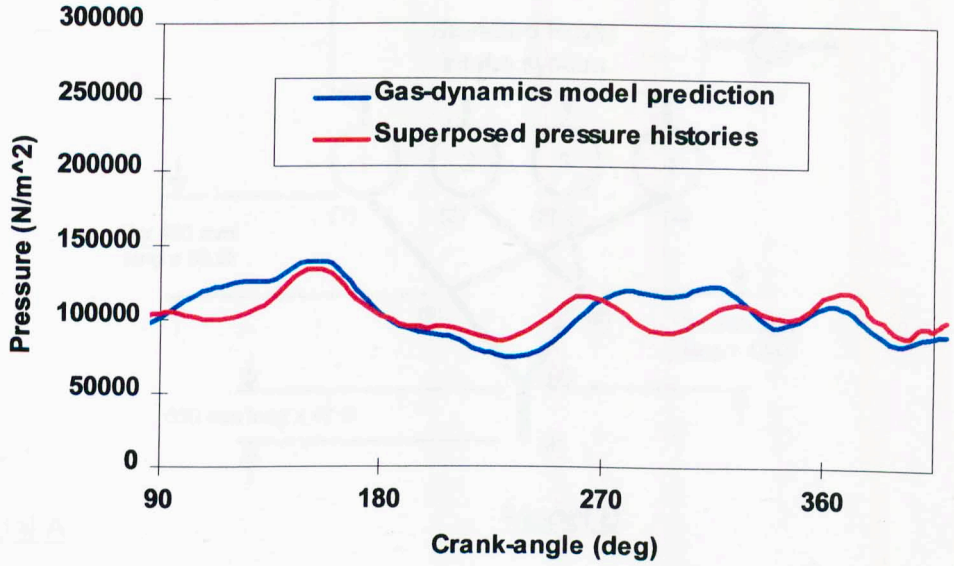

Figure 6.25 Comparison of superposed single reflections and predicted exhaust port pressure histories for 4:1 configuration exhaust system at 3000 r/min

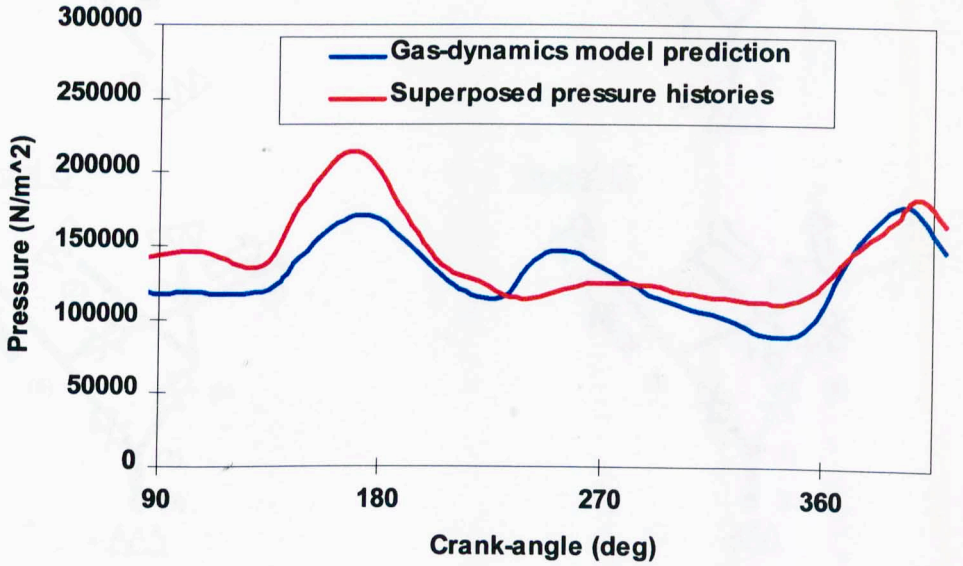

Figure 6.26 Comparison of superposed single reflections and predicted exhaust port pressure histories for 4:1 configuration exhaust system at 6000 r/min

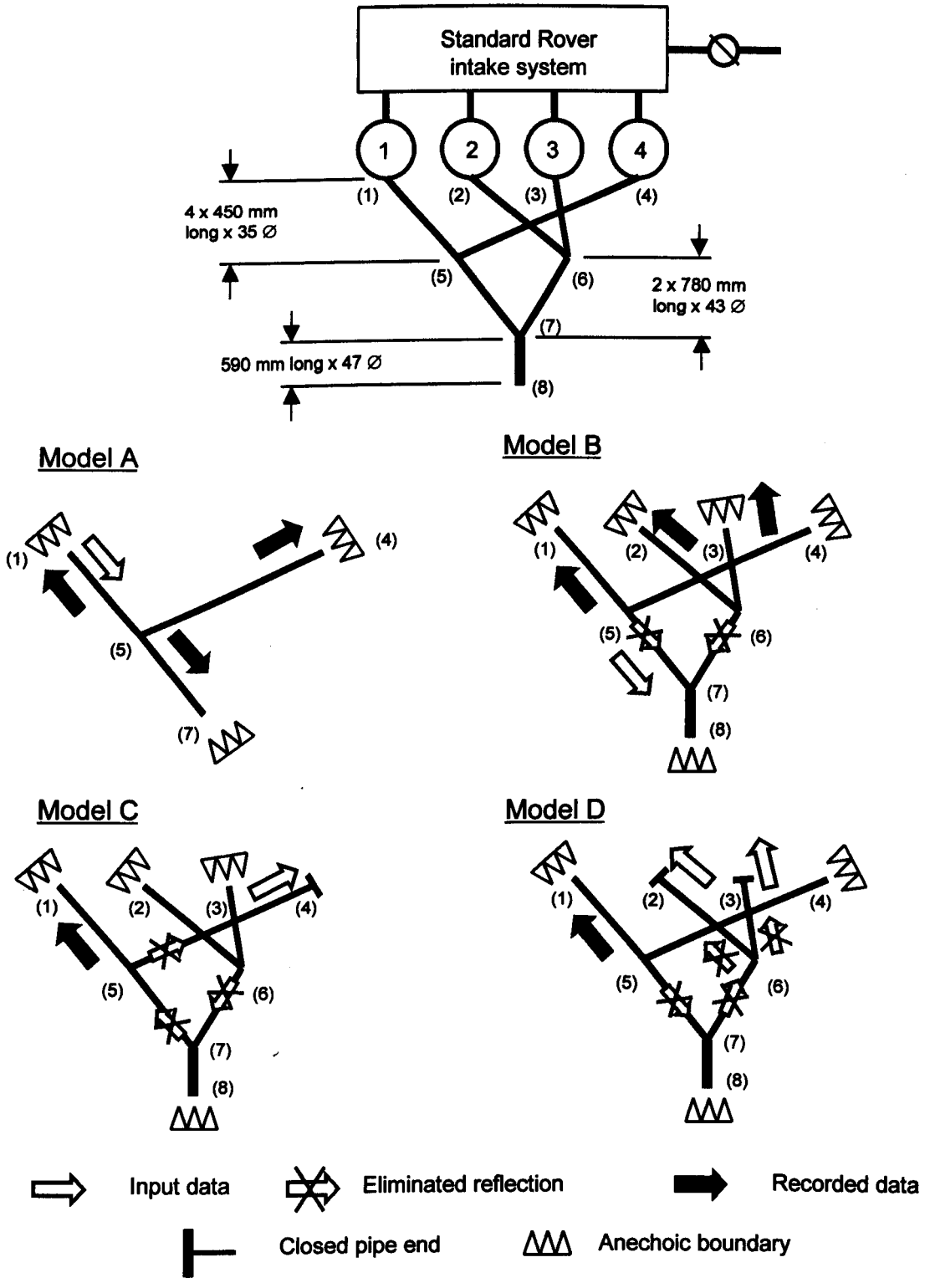

Figure 6.27 Models used to isolate single reflections in 4:2:1 exhaust systems

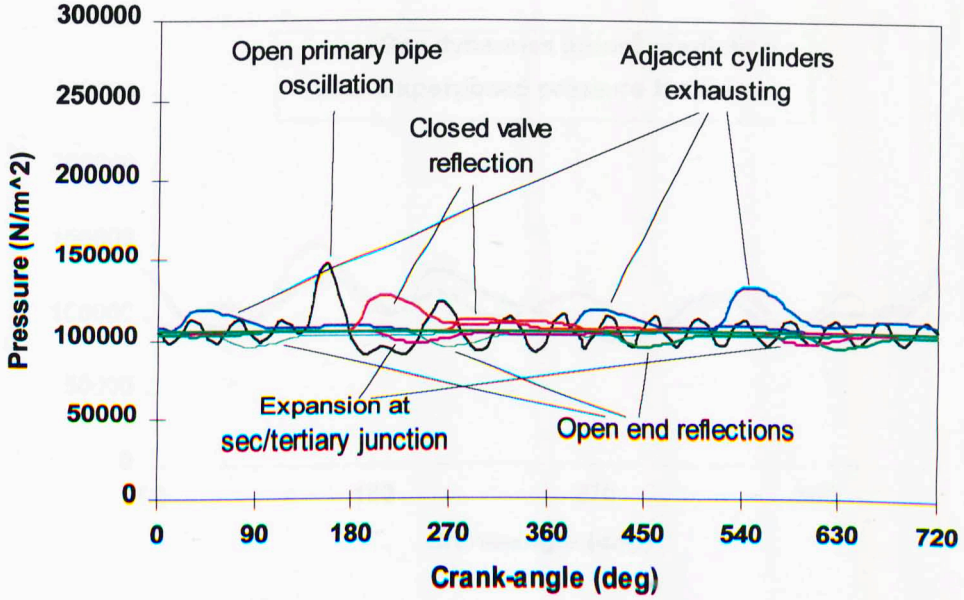

Figure 6.28 Single reflection pressure data from 4:2:1 configuration exhaust system at 3000 r/min

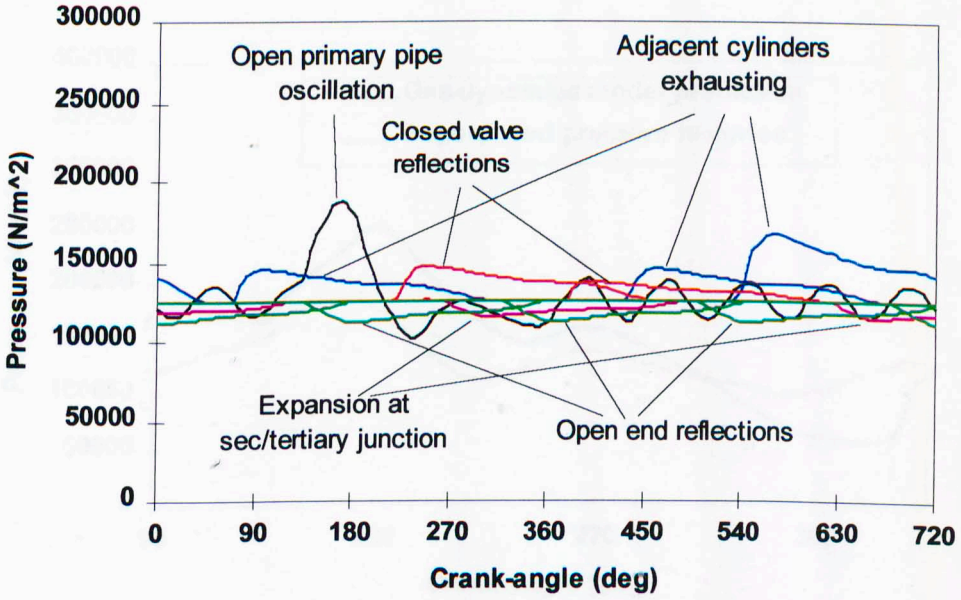

Figure 6.29 Single reflection pressure data from 4:2:1 configuration exhaust system at 6000 r/min

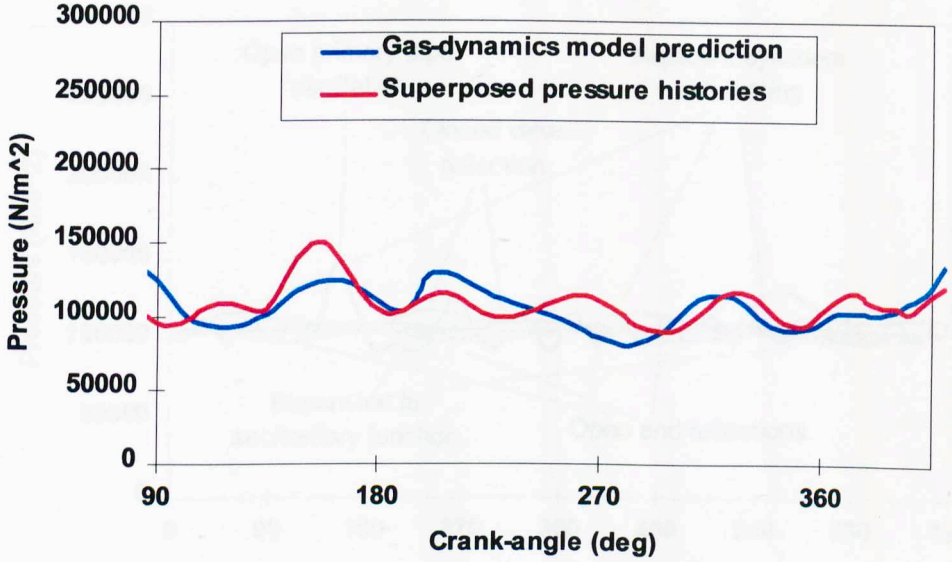

Figure 6.30 Comparison of superposed single reflections and predicted exhaust port pressure histories for 4:2:1 configuration exhaust system at 3000 r/min

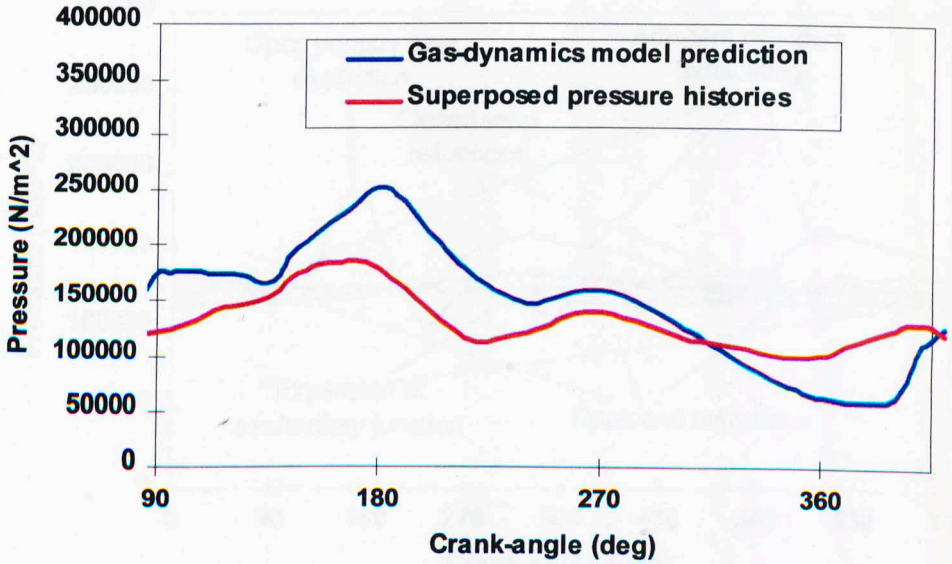

Figure 6.31 Comparison of superposed single reflections and predicted exhaust port pressure histories for 4:2:1 configuration exhaust system at 6000 r/min

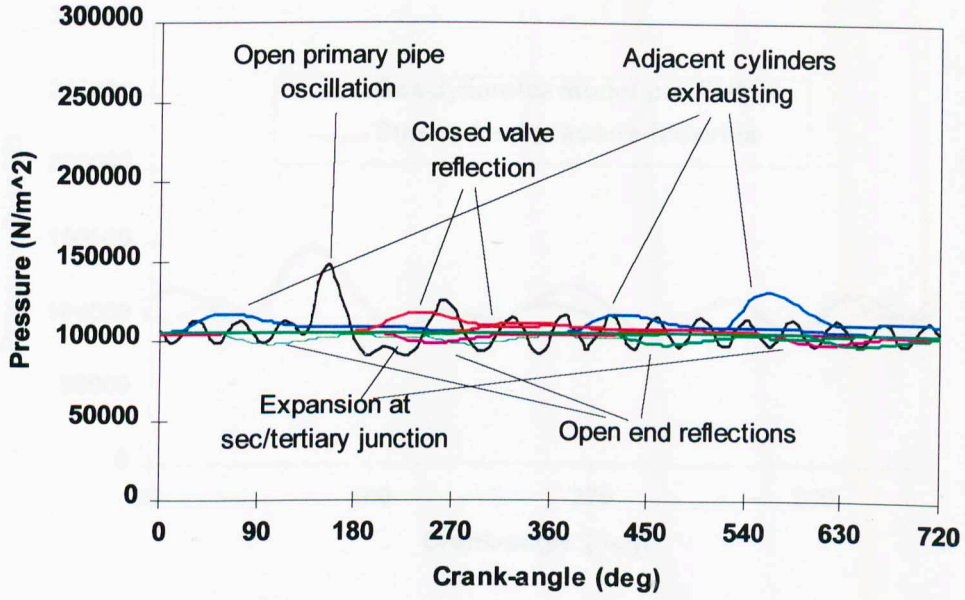

Figure 6.32 Single reflection pressure data from 4:2:1 configuration exhaust system with secondary pipe catalysts at 3000 r/min

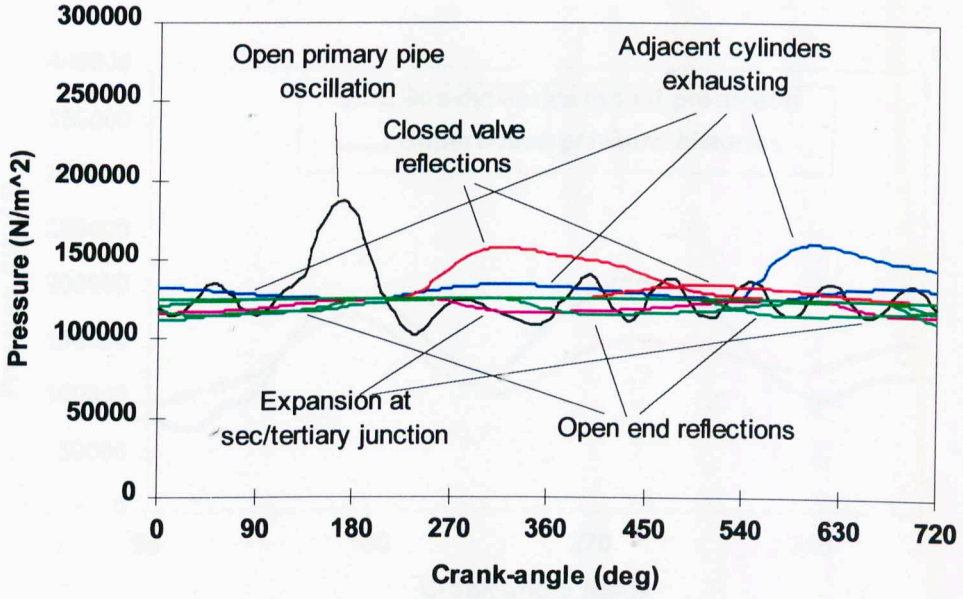

Figure 6.33 Single reflection pressure data from 4:2:1 configuration exhaust system with secondary pipe catalysts at 6000 r/min

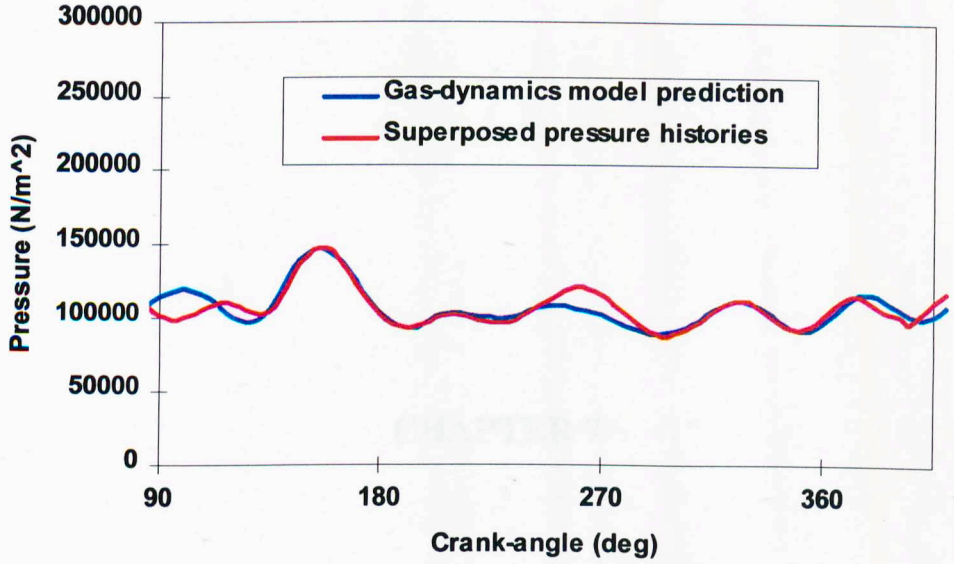

Figure 6.34 Comparison of superposed single reflections and predicted exhaust port pressure histories for 4:2:1 configuration exhaust system with secondary pipe catalysts at 3000 r/min

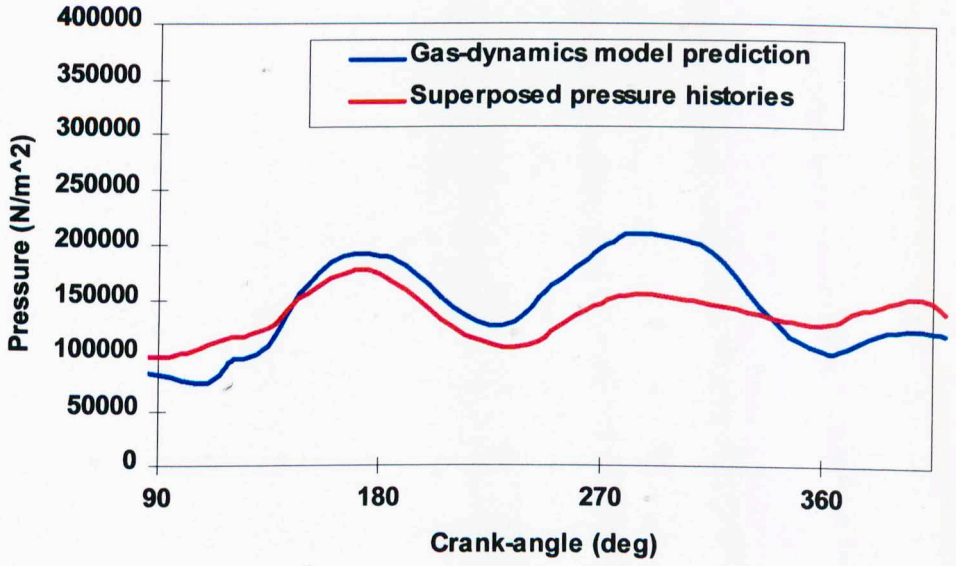

Figure 6.35 Comparison of superposed single relocations and predicted exhaust port pressure histories for 4:2:1 configuration exhaust system with secondary pipe catalysts at 6000 r/min

CHAPTER 7

EXHAUST SYSTEM DESIGN BASED ON OPTIMISATION OF GAS-DYNAMICS PROCESSES

CHAPTER 7

EXHAUST SYSTEM DESIGN BASED ON OPTIMISATION OF GAS-DYNAMICS PROCESSES

7.1 INTRODUCTION

The results detailed in previous chapters have indicated the importance of the pressure wave action within the exhaust system on the cylinder gas exchange processes. Periods during the exhaust event were identified where cylinder charging and pumping loss characteristics were shown to be sensitive to compression and expansion waves. It was also shown that the pressure history at the exhaust port could be well represented by the superposition of key reflections from sources downstream of the exhaust valve and of the pressure profile generated during the current cycle by the cylinder exhausting. Based on these results, this chapter details the development of design guidelines for exhaust system configuration that gave optimum phasing of pressure waves at the exhaust port. The application of the guidelines eliminated the necessity for full gas-dynamics simulation until the final stage of the design process. The effectiveness of the guidelines was demonstrated by using them to design a system to boost the low-speed torque characteristic of the Rover K series engine that was used during the experimental phase of the project. The effectiveness of the guidelines was demonstrated with both simulation and experimental data.

7.2 PIPE DIAMETER SELECTION

Figures 6.4 to 6.6 indicated how the pipe diameter affected the amplitude of pressure waves. A reduction in the pipe diameter increased the amplitude of a pressure wave whilst an increase in diameter decreased its amplitude. It follows that, in order to increase the effectiveness, in terms of cylinder scavenging, of rarefaction waves arriving at the exhaust valve, the diameter of the exhaust tract at this location should be as small as possible. However, this will also increase the effectiveness of compressive waves arriving during this period and a reduction in the pipe diameter will cause cylinder scavenging to be reduced.

Figures 6.23, 6.24, 6.28 and 6.29 indicated that there can be considerable overlap of the periods during which reflected compression and rarefaction waves reside at the exhaust port. An ideal exhaust system will, by the selection of pipe lengths that govern the phasing of pressure waves, separate the arrival times of these different waves at a given engine operating speed. However, the reality is that it is impossible to separate entirely the phasing of these waves and some degree of overlap will always exist. Thus, any benefits to cylinder scavenging from defining the exhaust tract diameter on the basis of increasing the effectiveness of rarefaction waves are likely to be offset to some degree by the reduction in Δp across the exhaust valve resulting from the arrival of compression waves.

The effect of the pipe diameter on pipe flow must also be considered. If the exhaust tract diameter were to be selected to increase the amplitude of arriving rarefaction waves at a given speed then, at higher operating speeds, the reduced diameter may throttle flow from the cylinder, increasing pumping losses.

Since a typical automotive engine is expected to have a wide range of operational speeds, and drivability across this speed range is a key design issue, pipe diameters must be selected primarily on the basis of their being of sufficient free area to flow the exhaust gases at WOT at maximum operational speed. This speed, generally corresponding to the peak power speed, will have already been defined by the engine manufacturers and the exhaust and intake valves will have been designed for the airflow rates required at this condition.

7.2.1 Exhaust tract diameter

Considering the diameter of the exhaust tract first, plots can be generated of exhaust tract diameter against exhaust gas mass flow rate. A single cylinder engine with four valves was modelled with separate exhaust tracts 100 mm long, each exiting into an anechoic boundary. The configuration of the engine corresponded to the configuration of a single cylinder of the K series engine considered throughout the course of the project. The anechoic boundaries were necessary to eliminate tuning effects caused by reflections at the open ends of each of the exhaust tracts. The configuration of this model is shown in Figure 7.1. A simulation was run at 6500 r/min (approximately 250 r/min faster than the peak power speed of the K series engine) with progressively increasing diameters of

exhaust tract. To ensure that the single cylinder engine model had a similar volumetric efficiency characteristic to a given cylinder of the four cylinder engine at the same speed, the intake port pressure history from the four cylinder simulation was imposed at the intake valve of the single cylinder model using the method for imposing user-defined pressure histories detailed in Section 6.2.1. In this way, appropriate exhaust gas mass flow characteristics were maintained.

Figure 7.2 shows the results from these simulations. As the diameter of the exhaust tract was progressively increased from 10 to 30 mm, the exhaust valve mass flow rate increased. Small diameters, such as those <15 mm diameter, were of insufficient free area to flow the gas flow rates required and flow losses were excessive. At the point where $\frac{d\dot{m}}{d\varnothing} \rightarrow 0$, between 20 and 30 mm diameter, any further increase in exhaust tract diameter did not produce significant increases in exhaust gas mass flow rate.

For this particular engine configuration the optimum pipe diameter was shown to lie within the range 20 to 22 mm. An exhaust tract diameter of 22 mm was selected. This was to allow for subsequent improvements to cylinder air consumption once the final optimum exhaust system was identified.

7.2.2 Primary pipe diameter

Figure 7.3 shows the configuration of the model used to identify the optimum primary pipe diameter. A single cylinder was modelled, generally as in case of the exhaust tract model. The two short length exhaust tracts converged into a single primary runner. The

diameter of the exhaust tracts was fixed at 22 mm diameter, as identified by the previous model. The length of the exhaust tracts (10 mm) was considerably shorter than that which would exist in a production engine. This was done to eliminate, as far as possible, the effect of gas-dynamics within the exhaust tracts on the cylinder gas-exchange process. Similarly, the primary pipe exited into an anechoic boundary to eliminate tuning effects resulting from the usual expansion at the open end of the pipe.

Figure 7.4 show results from a series of simulations with the primary pipe diameter progressively increased. It can be seen that as the diameter was increased from 10 to 35 mm, the exhaust valve mass flow rate progressively increased. As was the case with the exhaust tract, the small diameters of primary pipe were unable to flow the gas mass flow rates required. Between 33 and 35 mm diameter, any further increase in exhaust tract diameter did not produce significant increases in exhaust gas mass flow rate. It was in this range that the optimum primary pipe diameter for this particular engine configuration was located. A primary pipe diameter of 35 mm was selected to allow for any subsequent improvements to engine air consumption once the final optimum system was identified. Any further increase in pipe diameter after 35 mm caused an apparent drop in mass flow rate. It is believed that this was due to the increase in static pressure as the gas velocity was reduced further. The same increase in static pressure as the pipe diameter was increased from 10 to 35 mm was offset by the reduced flow losses in the primary pipe.

7.2.3 Secondary pipe diameter

Figure 7.5 shows the model that was compiled for the selection of the secondary pipe diameter. Two cylinders were modelled, firing at 360°CA intervals, with four short exhaust tracts converging into a single collector pipe, which represented the secondary pipe. The exhaust tracts were kept to a minimum length and the common secondary pipe exited into an anechoic boundary to minimise tuning effects.

Figure 7.6 shows plots of the results from these simulations. It can be seen that the region where $\frac{d\dot{m}}{d\varnothing} \rightarrow 0$ was not as clearly defined as in the previous cases. Since the cylinders were exhausting at 360°CA intervals and the exhaust period, for this particular engine, was 244°CA there was no overlap of each exhaust pulse in the secondary pipe. This may lead one to the incorrect assumption that the secondary pipe would therefore have been of similar size to the primary pipe since there would be no interference between successive exhaust pulses. However, there would be less time for the local gas to cool between each successive exhaust pulse of a two-cylinder engine compared with that of a single-cylinder engine. Thus, a fresh pulse, phased 360°CA after the previous pulse, would propagate into a region of higher temperature and pressure than would be the case if it were phased 720°CA after the previous pulse. This effectively reduces the Δp across each gas element and flow through the pipe is decreased. The effect manifests itself as an increase in back-pressure at the exhaust valve.

In the example shown the secondary pipe diameter was selected as 43 mm.

7.2.4 Collector pipe diameter

Figures 7.7 and 7.8 show the model used for the selection of the collector pipe diameter and the results from the simulations respectively. As in the case of the secondary pipe, the dimension of the optimum diameter is not as clearly defined as the cases of the exhaust tract and primary pipe diameters. However, a general trend can be observed although the variation in flowrate is extremely small.

7.3 OPTIMUM PHASING OF PRESSURE WAVES AT THE EXHAUST PORT

Chapter 5 identified specific periods during the exhaust event when engine performance characteristics were most sensitive to compression and expansion pressure waves. Chapter 6 showed that the pressure history at the exhaust port comprised the superposition of specific incident and reflected pressure waves. Based on these results, mathematical criteria were defined that, when satisfied, gave the optimum phasing of pressure waves at the exhaust port.

7.3.1 Expansion waves

Figures 5.25 to 5.30 indicated that there were two periods during the exhaust event when the arrival of an expansion wave at the exhaust valve had a significant effect on cylinder charging and pumping losses. The figures showed that an expansion wave arriving at approximately mid-stroke of the piston decreased cylinder pumping losses by the greatest amount. An expansion wave that arrived phased with the mid-point of the overlap event caused volumetric efficiency to be increased by the greatest amount. It was concluded

that ideally the arrival time of all expansion waves at the exhaust valve should be phased during the period following blowdown to IVC; within this period they were best phased with the mid-piston stroke or centred on the overlap event.

Figure 7.9 shows the exhaust port pressure history that was generated by a single-cylinder engine model exhausting into an open-ended pipe system from 2000 to 7000 r/min. The exhaust system ended in an anechoic termination. The exhaust event in each case is shown to have two distinct phases in terms of the pressure wave released into the exhaust system. The earlier of these is a high-pressure blowdown phase generated by the expansion of the burnt gases into the exhaust system and this is followed by a lower amplitude phase generated by the piston pumping the remaining burnt gases from the cylinder. Figure 7.10 shows a single plot, generated by the same model, at 3500 r/min and defines the start of the blowdown phase as θ_1, the end of the blowdown phase as θ_2, the end of the piston pumping phase as θ_{2*} and the peak pressure during blowdown as θ_{peak}.

Consider the compression wave shown in Figure 7.10 being introduced into a primary runner. From equation (1.7), the crank-angle timing of the wavefront of the rarefaction generated at the first downstream junction (or expansion into atmosphere) to arrive back at the exhaust valve can be given by:

$$\theta_{CA} = \theta_1 + \frac{12NL_p}{a_p} \qquad (7.1)$$

Similarly, the crank-angle timing of the arrival of the trailing edge of the rarefaction at the exhaust valve can be given by:

$$\theta_{CA} = \theta_{2*} + \frac{12NL_p}{a_p} \qquad (7.2)$$

Figures 5.25 to 5.30 indicated the crank-angle periods during which the arrival of an expansion wave can significantly increase torque and volumetric efficiency. Figure 7.11 identifies these periods as θ_{Te1} to θ_{Te2} and θ_{VEe1} to θ_{VEe2} for torque and volumetric efficiency respectively. Considering the arrival of a single rarefaction wave generated at a downstream expansion then ideally, for optimum torque:

$$\theta_{Te1} \leq \theta_1 + \frac{12NL_p}{a_p} \quad \text{and} \quad \theta_{Te2} \geq \theta_{2*} + \frac{12NL_p}{a_p} \qquad (7.3)$$

and for optimum volumetric efficiency:

$$\theta_{VEe1} \leq \theta_1 + \frac{12NL_p}{a_p} \quad \text{and} \quad \theta_{VEe2} \geq \theta_{2*} + \frac{12NL_p}{a_p} \qquad (7.4)$$

7.3.2 Compression waves

High amplitude compression waves arriving at the exhaust port are generated by adjacent cylinders exhausting or by the compression wave generated during the current cycle being reflected at closed or nearly closed pipe ends. Figures 5.18 to 5.24 indicated that there were two periods during the exhaust event when the arrival of a compression wave at the exhaust valve will have a significant effect on cylinder charging and pumping losses. A compression wave that arrived at approximately mid-stroke of the piston increased cylinder pumping losses by the greatest amount. A compression wave that

arrived phased with the mid-point of the overlap event caused volumetric efficiency to be decreased by the greatest amount.

Ideally, compression waves arriving at the exhaust port should be phased to arrive either during the blowdown event or following IVC. Compression waves unavoidably arriving during the exhaust event should preferably have the peak pressure phased at approximately 20°CA before IVO to minimise their effect on engine performance. Figure 7.12 identifies the periods of torque and volumetric efficiency sensitivity to compression waves as θ_{Tc1} to θ_{Tc2} and θ_{VEc1} to θ_{VEc2} respectively.

Considering adjacent cylinders as sources of compressive pressure waves then a pair of inequalities can be defined that consider the phasing of the exhaust pulse generated by cylinder 3 on cylinder 1 (assuming a firing order of 1342) in a 4 into 1 system. In this case cylinder 3 fires 180°CA after cylinder 1. Therefore, with reference to Figure 7.13, to achieve optimum torque one of the following inequalities should be satisfied:

$$\theta_{Tc1} \geq \theta_{2^*} + \frac{12NL_p}{a_p} + 180 \qquad \text{or} \qquad \theta_{Tc2} \leq \theta_1 + \frac{12NL_p}{a_p} + 180 \qquad (7.5)$$

These expressions can be written in a more general form to consider the arrival of compressive pulses from all adjacent cylinders:

$$\theta_{Tc1} \geq \theta_{2^*} + \frac{12NL_p}{a_p} \pm 180n \qquad \text{or} \qquad \theta_{Tc2} \leq \theta_1 + \frac{12NL_p}{a_p} \pm 180n \qquad (7.6)$$

where n is an integer ≥ 0.

Similarly for optimum volumetric efficiency:

$$\theta_{VEc1} \geq \theta_{2^*} + \frac{12NL_p}{a_p} \pm 180n \quad \text{or} \quad \theta_{VEc2} \leq \theta_1 + \frac{12NL_p}{a_p} \pm 180n \qquad (7.7)$$

7.3.3 Four-cylinder exhaust system configurations

Conventional four-cylinder engine exhaust configurations fall into one of the following categories:

i. 4 into 1 systems;

ii. 4 into 2 into 1 systems with emissions and silencer devices located in the tertiary pipe; and

iii. 4 into 2 into 1 systems with additional emissions devices located within the secondary pipes.

Knowing that the exhaust port pressure history comprises the superposed profiles of the primary pipe wave action and specific reflections from downstream of the primary pipe, tuning criteria can be defined. Chapter 6 identified the principal sources of the downstream reflections for each of the system configurations listed. By expanding expressions (7.3) to (7.7) to include each of these sources for each of the systems, a series of inequalities were defined. When satisfied, these inequalities indicated bandwidths of pipe geometry within which lengths should be selected to generate an optimum pressure history at the exhaust port. The pipe optimum lengths were then defined exactly using a modified acoustic model to identify quickly the varying period of oscillation during the exhaust event in the primary pipes only. The following sections detail these design criteria.

7.3.3.1 4:1 configuration system

Figure 7.14 shows the principal sources of reflections in 4:1 configuration exhaust systems. Considering the compressive waves generated by adjacent cylinders exhausting, for optimum torque by minimising pumping losses:

$$\theta_{Tc1} \geq \theta_{2*} + \frac{12NL_p}{a_p} \pm 180n \quad \text{or} \quad \theta_{Tc2} \leq \theta_1 + \frac{12NL_p}{a_p} \pm 180n \qquad (7.8)$$

and for optimum volumetric efficiency:

$$\theta_{VEc1} \geq \theta_{2*} + \frac{12NL_p}{a_p} \pm 180n \quad \text{or} \quad \theta_{VEc2} \leq \theta_1 + \frac{12NL_p}{a_p} \pm 180n \qquad (7.9)$$

where n is an integer ≥ 0.

For the compressive reflection generated at closed or partially open exhaust valves, for optimum torque:

$$\theta_{Tc1} \geq \theta_{2*} + \frac{24NL_p}{a_p} \quad \text{or} \quad \theta_{Tc2} \leq \theta_1 + \frac{24NL_p}{a_p} \qquad (7.10)$$

and for optimum volumetric efficiency:

$$\theta_{VEc1} \geq \theta_{2*} + \frac{24NL_p}{a_p} \quad \text{or} \quad \theta_{VEc2} \leq \theta_1 + \frac{24NL_p}{a_p} \qquad (7.11)$$

Considering the expansion wave generated at the open end of the exhaust system (or by the expansion into a silencer or emissions device), then for optimum torque:

$$\theta_{Te1} \leq \theta_1 + 12N\left(\frac{L_p}{a_p} + \frac{L_c}{a_c}\right) \pm 180n \quad \text{and} \quad \theta_{Te2} \geq \theta_{2*} + 12N\left(\frac{L_p}{a_p} + \frac{L_c}{a_c}\right) \pm 180n \qquad (7.12)$$

and for optimum volumetric efficiency:

$$\theta_{VEe1} \leq \theta_1 + 12N\left(\frac{L_p}{a_p} + \frac{L_c}{a_c}\right) \pm 180n \quad \text{and} \quad \theta_{VEe2} \geq \theta_{2*} + 12N\left(\frac{L_p}{a_p} + \frac{L_c}{a_c}\right) \pm 180n \quad (7.13)$$

where n is an integer ≥ 0.

The inequalities represented in (7.13) are idealised and cannot be satisfied in normal circumstances since $(\theta_{2*} - \theta_1) > (\theta_{VEe2} - \theta_{VEe1})$. Therefore, since it is the high-pressure phase of the exhaust event that potentially has the greater effect and referring to Figure 7.10, expression (7.13) can be rewritten:

$$\theta_{VEe1} \leq \theta_1 + 12N\left(\frac{L_p}{a_p} + \frac{L_c}{a_c}\right) \pm 180n \quad \text{and} \quad \theta_{VEe2} \geq \theta_2 + 12N\left(\frac{L_p}{a_p} + \frac{L_c}{a_c}\right) \pm 180n \quad (7.14)$$

If, at the given engine operating conditions: $(\theta_2 - \theta_1) > (\theta_{VEe2} - \theta_{VEe1})$, then the following should be satisfied in order to phase the highest amplitude rarefaction during the period when it will have the greatest effect:

$$\frac{(\theta_{IVO} + \theta_{EVC})}{2} \approx \theta_{peak} + 12N\left(\frac{L_p}{a_p} + \frac{L_c}{a_c}\right) \pm 180n \quad (7.15)$$

Equation (7.15) can only be satisfied for one value of n and it would be usual to consider only the rarefaction generated during the current cycle or during the cycles at ±180°CA, otherwise pipe lengths will become excessively long.

By initially satisfying inequalities that include primary pipe length terms only, as opposed to collector pipe length terms, broad bandwidths of primary pipe dimensions will initially be identified within which a length should ideally be selected. It was previously demonstrated that the pressure history at the exhaust port comprised the superposed profiles of the primary pipe wave action and specific reflections from downstream of the primary pipe. The inequality groups (7.8) to (7.15) consider each of the principal reflections from downstream of the primary pipe. A primary pipe length should then be selected that lies within the identified bandwidths and that generates a suitably low-amplitude pressure trough centred on the valve overlap event and/or coincides with the mid-point of the piston stroke.

7.3.3.1.1 Primary pipe length selection with modified acoustic theory models

In order to identify a suitable selection of primary pipe length, a single-cylinder gas-dynamics model can be compiled to investigate the exhaust port pressure history generated by a selection of appropriate primary pipe lengths. However, since this requires the assembly of dedicated models of some complexity, other methods of investigating this dynamic phenomenon were investigated.

Figure 7.15 shows the pressure history generated by a typical single-cylinder engine at 3000 r/min with a 400 mm long open pipe exhaust system. To phase the low-pressure troughs favourably, the geometry of the primary pipe, and particularly its length, must be modified in order to change its resonance characteristics during the exhaust event. Various simplified methods have been proposed previously to assist with the rapid

identification of the optimum primary pipe geometry. Distributed parameter acoustic models have been used with some success when applied to intake system design [62, 106]. The manipulation of the general wave equation into a pipe transfer matrix (see appendix A2.1) enables expressions to be derived for multiple pipe networks. It has been suggested that the solutions of these equations give the natural frequencies of pressure wave oscillation of exhaust pipe networks of given dimensions. Similarly, the application of the Helmholtz model (1.8) has been used to identify the period of pressure wave oscillation of simple manifold systems during the intake and exhaust events.

Figure 7.15 shows that, in this example, there are a number of oscillations during the exhaust event and the period changes with each oscillation. This is principally due to the changing cylinder volume and valve area boundary condition and to the large variation of the acoustic velocity during the exhaust event.

Although the Helmholtz model does consider the cylinder volume as the equivalent spring in a spring-mass system, it does not consider the variation of the cylinder volume during the valve event. Its usual form of application with some fixed volume term will not hold and it will return a constant period. However, referring to Figure 7.15, equation (1.8) can be applied between any two successive pressure peaks where the volume term is given by:

$$V = \frac{V_{\theta_1} + V_{\theta_2}}{2} + V_{cl} \quad (7.16)$$

and where θ_1 and θ_2 are the locations of successive peaks in degCA.

Thus, incorporating an expression for cylinder volume into equation (1.8) and writing in terms of degCA gives:

$$0=\theta_1-\theta_2+\frac{12N\pi}{a}\left(\frac{A_p}{L_p}\right)^{-\frac{1}{2}}\times$$

$$\left(\frac{V_{\theta_1}}{2}+\frac{1}{2}\left[\left\{\left(\tfrac{S}{2}+L_R\right)-\left[\left(\tfrac{S}{2}\cos\theta_2\right)+\sqrt{L_R{}^2-\left(\tfrac{S}{2}\sin\theta_2\right)^2}\right]\right\}A_c+V_{cl}\right]\right)^{\frac{1}{2}} \qquad (7.17)$$

If the location of the first pressure peak is known, then equation (7.17) can be solved iteratively for θ_2 to give the location of the second peak (see Appendix A4.0 and A5.0).

A model was compiled that required basic cylinder and primary pipe geometry as input data. Assuming that the location of the first pressure peak corresponded approximately with the location of the peak pressure during the blowdown phase of the exhaust event, then the model calculated the phasing of the second pressure peak (θ_2). θ_2 was then set to θ_1 and the location of the third peak was then calculated. This continued until the exhaust valve closed at which time the calculation ceased. The calculation is valid only for the period following blowdown to EVC. Outside of this period, the primary pipe wave action is decoupled from the cylinder volume by either sonic flow through the exhaust valve during blowdown or because the exhaust valve is closed.

Figures 7.16 to 7.18 show examples of the location of oscillation peaks calculated using this method. It should be noted that this method does not calculate the relative amplitude of these peaks, but they have been shifted on the y-axis to enable comparisons with the

full gas-dynamics simulation to be made. This approach provides an extremely rapid method of identifying the basic gas-dynamic characteristics of any open primary exhaust system.

7.3.3.2 4:2:1 configuration system

4:2:1 configuration exhaust systems have a greater number of potential sources of reflections and propagation paths back to the exhaust valve than do 4:1 systems. Figure 7.19 shows the principal sources of these reflections. Considering the compressive wave generated by cylinder 4 exhausting and arriving at cylinder 1 via the primary pipes, then for optimum torque by minimising pumping losses:

$$\theta_{Tc1} \geq \theta_{2^*} + \frac{12NL_p}{a_p} \pm 360n \quad \text{or} \quad \theta_{Tc2} \leq \theta_1 + \frac{12NL_p}{a_p} \pm 360n \qquad (7.18)$$

and for optimum volumetric efficiency:

$$\theta_{VEc1} \geq \theta_{2^*} + \frac{12NL_p}{a_p} \pm 360n \quad \text{or} \quad \theta_{VEc2} \leq \theta_1 + \frac{12NL_p}{a_p} \pm 360n \qquad (7.19)$$

where n is an integer ≥ 0.

For the compressive waves generated by cylinders 2 and 3 arriving at cylinder 1 via the primary and secondary pipes, then for optimum torque:

$$\theta_{Tc1} \geq \theta_{2^*} + 12N\left(\frac{L_p}{a_p} + \frac{L_s}{a_s}\right) \pm 180n \quad \text{or} \quad \theta_{Tc2} \leq \theta_1 + 12N\left(\frac{L_p}{a_p} + \frac{L_s}{a_s}\right) \pm 180n \qquad (7.20)$$

and for optimum volumetric efficiency:

$$\theta_{VEc1} \geq \theta_{2^*} + 12N\left(\frac{L_p}{a_p} + \frac{L_s}{a_s}\right) \pm 180n \quad \text{or} \quad \theta_{VEc2} \leq \theta_1 + 12N\left(\frac{L_p}{a_p} + \frac{L_s}{a_s}\right) \pm 180n \qquad (7.21)$$

where n =1, 3, etc.

For the compressive wave generated by cylinder 1 and reflected at the closed valve of cylinder 4 via the primary pipes, for optimum torque:

$$\theta_{Tc1} \geq \theta_{2^*} + \left(\frac{24NL_p}{a_p} \right) \quad \text{or} \quad \theta_{Tc2} \leq \theta_1 + \left(\frac{24NL_p}{a_p} \right) \tag{7.22}$$

and for optimum volumetric efficiency:

$$\theta_{VEc1} \geq \theta_{2^*} + \left(\frac{24NL_p}{a_p} \right) \quad \text{or} \quad \theta_{VEc2} \leq \theta_1 + \left(\frac{24NL_p}{a_p} \right) \tag{7.23}$$

For the compressive wave generated by cylinder 1 and reflected at the closed valves of cylinder 2 and 3 via the primary and secondary pipes, for optimum torque:

$$\theta_{Tc1} \geq \theta_{2^*} + 24N\left(\frac{L_p}{a_p} + \frac{L_s}{a_s} \right) \quad \text{or} \quad \theta_{Tc2} \leq \theta_1 + 24N\left(\frac{L_p}{a_p} + \frac{L_s}{a_s} \right) \tag{7.24}$$

and for optimum volumetric efficiency:

$$\theta_{VEc1} \geq \theta_{2^*} + 24N\left(\frac{L_p}{a_p} + \frac{L_s}{a_s} \right) \quad \text{or} \quad \theta_{VEc2} \leq \theta_1 + 24N\left(\frac{L_p}{a_p} + \frac{L_s}{a_s} \right) \tag{7.25}$$

Considering the expansion wave generated at the junction of the secondary and tertiary pipe junction, then for optimum torque:

$$\theta_{Te1} \leq \theta_1 + 12N\left(\frac{L_p}{a_p} + \frac{L_s}{a_s} \right) \pm 360n \quad \text{and} \quad \theta_{Te2} \geq \theta_2 + 12N\left(\frac{L_p}{a_p} + \frac{L_s}{a_s} \right) \pm 360n \tag{7.26}$$

and for optimum volumetric efficiency:

$$\theta_{VEe1} \leq \theta_1 + 12N\left(\frac{L_p}{a_p} + \frac{L_s}{a_s}\right) \pm 360n \quad \text{and} \quad \theta_{VEe2} \geq \theta_2 + 12N\left(\frac{L_p}{a_p} + \frac{L_s}{a_s}\right) \pm 360n \quad (7.27)$$

or alternatively:

$$\frac{(\theta_{IVO} + \theta_{EVC})}{2} \approx \theta_{peak} + 12N\left(\frac{L_p}{a_p} + \frac{L_s}{a_s}\right) \pm 360n \quad (7.28)$$

where n is an integer ≥ 0.

Considering the expansion wave generated at the open end of the system, then for optimum torque:

$$\theta_{Te1} \leq \theta_1 + 12N\left(\frac{L_p}{a_p} + \frac{L_s}{a_s} + \frac{L_c}{a_c}\right) \pm 180n \text{ and } \theta_{Te2} \geq \theta_2 + 12N\left(\frac{L_p}{a_p} + \frac{L_s}{a_s} + \frac{L_c}{a_c}\right) \pm 180n \quad (7.29)$$

and for optimum volumetric efficiency:

$$\theta_{VEe1} \leq \theta_1 + 12N\left(\frac{L_p}{a_p} + \frac{L_s}{a_s} + \frac{L_c}{a_c}\right) \pm 180n \text{ and } \theta_{VEe2} \geq \theta_2 + 12N\left(\frac{L_p}{a_p} + \frac{L_s}{a_s} + \frac{L_c}{a_c}\right) \pm 180n \quad (7.30)$$

or alternatively:

$$\frac{(\theta_{IVO} + \theta_{EVC})}{2} \approx \theta_{peak} + 12N\left(\frac{L_p}{a_p} + \frac{L_s}{a_s} + \frac{L_c}{a_c}\right) \pm 180n \quad (7.31)$$

where n is an integer ≥ 0.

As pressure waves propagate through duct junctions and duct lengths their amplitude will be progressively reduced and their effectiveness in terms of tuning will be correspondingly reduced. Thus, when considering the inequalities presented, priority should be given to the sources of reflections located upstream in the system, since

reflections generated at these locations have the greatest potential effect on engine breathing characteristics.

7.3.3.3 4:2:1 configuration system with secondary pipe catalysts

4:2:1 systems that incorporate emissions devices within the secondary pipe lengths behave in a similar way to those that do not. However, such systems also generate additional reflections as incident pressure waves propagate through the catalyst.

Figures 6.11 to 6.14 demonstrated how the catalytic converter will generate an expansion wave rapidly followed by a compression wave as an incident compression wave passed through the device. These waves were generated at the catalyst entry and exit cones. Although reflections were also generated at the entry and exit of the reactive monolith, their effect on the overall profile was relatively insignificant. Thus, inequalities (7.18) to (7.28) should be satisfied for 4:2:1 configuration systems with secondary pipe catalysts and additionally the following inequalities should also be satisfied:

For the expansion wave generated at the secondary catalyst entry, then for optimum torque:

$$\theta_{Te1} \leq \theta_1 + 12N\left(\frac{L_p}{a_p} + \frac{L_{cat}}{a_{cat}}\right) \pm 360n \text{ and } \theta_{Te2} \geq \theta_2 + 12N\left(\frac{L_p}{a_p} + \frac{L_{cat}}{a_{cat}}\right) \pm 360n \quad (7.32)$$

where n is an integer ≥ 0 and where subscript *cat* refers to the conditions and geometry of the pipe run from the primary-secondary pipe junction to the secondary catalyst entry.

For optimum volumetric efficiency:

$$\theta_{VEe1} \leq \theta_1 + 12N\left(\frac{L_p}{a_p} + \frac{L_{cat}}{a_{cat}}\right) \pm 360n \text{ and } \theta_{VEe2} \geq \theta_2 + 12N\left(\frac{L_p}{a_p} + \frac{L_{cat}}{a_{cat}}\right) \pm 360n \qquad (7.33)$$

or alternatively:

$$\frac{(\theta_{IVO} + \theta_{EVC})}{2} \approx \theta_{peak} + 12N\left(\frac{L_p}{a_p} + \frac{L_{cat}}{a_{cat}}\right) \pm 360n \qquad (7.34)$$

It follows that if inequality (7.34) is satisfied, the compressive wave that is generated at exit of the secondary pipe catalyst will be phased towards the end of, or immediately following, the overlap event, i.e. outside the period of sensitivity to compressive waves.

7.4 OPTIMUM SYSTEM DESIGN

7.4.1 Design target

The design guidelines detailed in Sections 7.2 and 7.3 were applied to design a system to boost the mid-range torque of the Rover K series engine used throughout the course of this project (see Chapter 3). The geometry of the baseline modular exhaust system replicated that of the production system, which undoubtedly would have had considerable time spent on its design. One of the principal design targets for the production system was peak power performance and so it was not expected that significant improvements could be made in the high-speed performance range; thus, it was decided to focus on mid-range torque to demonstrate the effectiveness of the design guidelines.

The production system was a 4:2:1 configuration system (see Figure 3.11) with the catalytic converter located under the floor of the vehicle. A consequence of satisfying current emissions legislation is that catalytic converters are often located as far upstream in the exhaust system as possible. Close-coupled catalytic converters inevitably increase the pressure drop across the system as the gas that passes into the converter is hotter. Assuming quasi-steady flow and applying the perfect gas law ($p/\rho = RT$) and mass flow continuity at the catalyst monolith entry, then an increase in temperature causes an increase in pressure or a decrease in density (or both). To maintain mass flow continuity across the monolith, the flow velocity increases and flow losses correspondingly increase. A close-coupled catalytic converter is also likely to experience an increased pressure drop across the device compared to one located downstream because of the practical design difficulties in ensuring good flow distribution across the monolith face. Primary pipes are often directed straight onto the monolith face and therefore the flow "sees" a reduced effective free area; a device located further downstream will usually have an entry cone design that allows improved flow development across the monolith face. For these reasons it was decided to design an optimum system without a close-coupled catalytic converter so that direct comparisons could be made between the optimum system and baseline system in terms of gas dynamics performance only.

7.4.2 Primary pipe diameter selection

The selection procedure detailed in Section 7.2 was demonstrated using the engine configuration being considered in this case. The application of this selection procedure

gave the following pipe diameters applicable to 4:1 and 4:2:1 configuration systems as required:

Primary pipe	35 mm diameter
Secondary pipe	43 mm diameter
Tertiary pipe	50 mm diameter

Table 7.1 Pipe diameters

7.4.3 Primary pipe length selection – 4:1 systems

The system was to be designed to give improved torque performance between 3000 and 4000 r/min. For this engine configuration at WOT at 3500 r/min, a mean acoustic velocity of 485 m/s in the primary pipes was assumed (from $\gamma \approx 1.35$ and $T_{mean} \approx 605°K$).

Referring to Figure 7.10 then the start and end of the blowdown phase of the exhaust event, the end of the piston pumping phase and the location of the peak blowdown pressure at 3500 r/min were defined as:

θ_1	≈140°CA
θ_2	≈250°CA
θ_{2*}	≈370°CA
θ_{peak}	≈175°CA

Table 7.2 Exhaust phase definitions

Referring to the crank-angle period definitions shown in Figures 7.11 and 7.12, then for optimum torque and volumetric efficiency performance, the periods of peak sensitivity to compression and expansion waves were defined as:

$\theta_{VEc1}, \theta_{VEe1}$	≈330°CA
$\theta_{VEc2}, \theta_{VEe2}$	≈390°CA
$\theta_{Tc1}, \theta_{Te1}$	≈180°CA
$\theta_{Tc2}, \theta_{Te2}$	≈390°CA

Table 7.3 Sensitivity period definitions

Considering the compressive pulse arriving from the cylinders firing ±180°CA, inequality (7.8) was applied, thus:

$$180 \geq 370 + \frac{12 \times 3500 \times L_p}{485} \pm 180 \quad \text{or} \quad 390 \leq 140 + \frac{12 \times 3500 \times L_p}{485} \pm 180 \qquad (7.35)$$

For the cylinder exhausting at -180°CA, then –0.11 m ≥ L_p, or L_p ≥ 4.96 m. Negative values were not considered and a primary pipe length of 4.96 m was not practical.

The negative indicated pipe length arises with 4:1 systems when considering the previously firing cylinder because there is an overlap of the valve events. The upper pipe length is excessive because inequality pair (7.8) completely separates the exhaust event with arrival of the leading edge of an incident compression wave.

For practical 4:1 systems, some interference from the previously firing cylinder is inevitable. Since an improvement in volumetric efficiency potentially gave a greater improvement in torque than by the reduction of pumping losses alone, then in this case inequality pair (7.9) was applied, considering only the high pressure component of the exhaust event. Thus:

$$330 \geq 250 + \frac{12 \times 3500 \times L_p}{485} - 180 \quad \text{or} \quad 390 \leq 140 + \frac{12 \times 3500 \times L_p}{485} - 180 \qquad (7.36)$$

which for the cylinder firing -180°CA gave 3.0 m $\geq L_p$, or $L_p \geq 4.97$ m.

For the cylinder firing +180°CA, then the application the same inequality pair gave:

$$330 \geq 250 + \frac{12 \times 3500 \times L_p}{485} + 180 \quad \text{or} \quad 390 \leq 140 + \frac{12 \times 3500 \times L_p}{485} + 180 \qquad (7.37)$$

which gave –1.15 m $\geq L_p$, or $L_p \geq 0.80$ m.

The application of these inequality pairs to adjacent firing cylinders gave:

Cylinder firing order	$L_p \leq$	$L_p \geq$
-360°CA	5.08	7.04
-180°CA	3.00	4.97
+180°CA	-1.15	0.80
+360°CA	-3.23	-1.27

Table 7.4 Primary pipe length bandwidths to eliminate interference from other cylinders exhausting

Next the reflected compressive pulse generated at the closed valves of the adjacent cylinders was considered; the application of inequality pair (7.11) gave:

$$330 \geq 370 + \frac{24 \times 3500 \times L_p}{485} \quad \text{or} \quad 390 \leq 140 + \frac{24 \times 3500 \times L_p}{485} \qquad (7.38)$$

which gave –0.231 m $\geq L_p$, or $L_p \geq 1.44$ m.

Having identified initial bandwidths within which primary pipe lengths should ideally be selected, a specific primary pipe length was identified that generated the optimum

primary pipe wave action. The dimensions given in Table 7.4 and the results given by inequality pair (7.38) indicated that the optimum pipe lengths to avoid all interference from compressive pulses arriving from downstream of the primary pipes lay within the range 1.44 m $\leq L_p \leq$ 3.0 m. However, these pipe lengths were excessive and it was not possible to identify a primary pipe length that generated an optimum high frequency wave action. Since the primary pipe wave action has the greater influence on engine breathing characteristics than the reflections generated at the closed valves, so the pipe range initially considered was based on those values indicated in Table 7.4 only i.e. 0.8 m $\leq L_p \leq$ 3.0 m.

Using the modified Helmholtz model and confirming the results with engine cycle simulation, it was found that a primary pipe length of 850 mm generated the optimum pressure history exhaust port. This is shown in shown in Figure 7.20 where it can be seen that during the overlap period a low pressure condition was generated

7.4.4 Collector pipe length selection – 4:1 systems

Having selected a primary pipe length of 850 mm, the collector pipe length was selected based on the solution of equation (7.15). A mean acoustic velocity in the collector pipe of 440 m/s was assumed, thus:

$$\frac{(348+372)}{2} \approx 175+12\times 3500\times\left(\frac{0.85}{485}+\frac{L_c}{440}\right)\pm 180n \quad (7.39)$$

where n is an integer ≥ 0.

The solutions for the collector pipe length represented a single reflection at the first expansion encountered in the collector pipe, each generated by a separate cylinder exhausting.

Cylinder firing order	n	L_c (m)
-360°CA	-2	4.94
-180°CA	-1	3.05
current cycle	0	1.17
+180°CA	1	-0.72
+360°CA	2	-2.60

Table 7.5 Optimum collector pipe lengths

Negative values of pipe length were ignored and a collector pipe length of 1.17 m was selected. The geometry of the optimum 4:1 configuration system identified is shown in Table 7.6.

Pipe	Length (mm)	Diameter (mm)
Primary	850	35
Collector	1.17	50

Table 7.6 Optimum collector pipe lengths

7.4.5 Primary pipe length selection – 4:2:1 systems

To define the optimum 4:2:1 configuration system, the inequality pair (7.18) were considered for the cylinders firing ±360°CA:

$$180 \geq 370 + \frac{12 \times 3500 \times L_p}{485} \pm 360 \quad \text{or} \quad 390 \leq 140 + \frac{12 \times 3500 \times L_p}{485} \pm 360 \qquad (7.40)$$

For the cylinder firing at -360°CA, then 7.04 m ≤ L_p, or L_p ≤ 1.96 m. For the cylinder firing at +360°CA, then –1.27 m ≤ L_p, or L_p ≤ -6.35 m. These results demonstrated that

4:2:1 systems effectively eliminate pressure wave interference between the adjacent firing cylinders that are connected via the primary pipes only.

As in the case of the 4:1 system, the primary pipe resonance was considered next. A pipe length of 850 mm was similarly selected since it generated a powerful rarefaction at the exhaust valve during the overlap event and fell well within the range of pipe lengths identified by inequality pair (7.40).

7.4.6 Secondary pipe length selection – 4:2:1 systems

Having defined the primary pipe length the secondary pipe length was defined on the basis of optimising the phasing of the rarefaction generated at the secondary-tertiary pipe junction and minimising interference from the cylinders firing at ±180°CA.

Assuming a mean local acoustic velocity in the secondary pipes of 440 m/s, the optimum secondary pipe length for the optimum phasing of the rarefaction generated at the secondary-tertiary pipe junction was given by the application of equation (7.28), thus:

$$\frac{(348+372)}{2} \approx 175+12\times 3500\times\left(\frac{0.85}{485}+\frac{L_s}{440}\right)\pm 360n \quad (7.41)$$

which gave solutions of L_s = -2.6, 1.15 and 4.93 m.

The optimum secondary pipe length to eliminate interference from the cylinders firing ±180°CA and considering the high pressure phase of the exhaust event only was calculated by the application of inequality pair (7.21), thus:

$$330 \geq 250 + 12 \times 3500 \left(\frac{0.85}{485} + \frac{L_s}{440} \right) \pm 180n \qquad \text{or}$$

$$390 \leq 140 + 12 \times 3500 \left(\frac{0.85}{485} + \frac{L_s}{440} \right) \pm 180n \qquad (7.42)$$

For the cylinder firing at +180°CA, this gave –0.03 m ≤ L_p, or $L_p \leq$ -1.82 m; for the cylinder firing at -180°CA, this gave 3.73 m ≤ L_p, or $L_p \leq$ 1.95 m. Hence, from (7.41), the secondary pipe length was fixed at 1150 mm.

7.4.7 Tertiary pipe length selection – 4:2:1 systems

The optimum tertiary pipe length was based on the solution of (7.31) and an assumed mean local acoustic velocity in the tertiary pipe of 430 m/s, thus:

$$\frac{(348+372)}{2} \approx 175 + 12 \times 3500 \times \left(\frac{0.85}{485} + \frac{1.15}{440} + \frac{L_c}{430} \right) \pm 180n \quad (7.43)$$

which gave positive solutions of L_c of 0.02, 1.85 and 3.70 m. However, modification of the length of the tertiary pipe does not significantly change the exhaust port pressure history since the incident pressure waves arriving from the open end of the system traverse a large number of junctions and pipes. This can be seen in Figures 6.28 and 6.29 where the arriving rarefactions are shown to be relatively low in amplitude. In this case, because of the practicalities of installing a test system in the test cell area, a tertiary pipe length of 490 mm was selected

7.4.8 Performance characteristics of the optimum and baseline systems

The following systems were compared with full gas-dynamics engine cycle simulations:

1. Baseline: 450 mm long × 35 Ø primary
   780 mm long × 43 Ø secondary
   592 mm long × 47 Ø tertiary

2. Optimum 4:1: 850 mm long × 35 Ø primary
   1170 mm long × 50 Ø collector

3. Optimum 4:2:1: 850 mm long × 35 Ø primary
   1150 mm long × 43 Ø secondary
   490 mm long × 50 Ø tertiary

The comparison of these systems is shown in Figures 7.21 and 7.22. The 4:2:1 system shows significant improvements in torque and volumetric efficiency between 3000 and 4000 r/min relative to the baseline system. From 4000 to 5500 r/min there is a drop in performance but at 6000 r/min the engine performance is similar to the baseline system. A study of the exhaust port pressure histories at 3500 and 5000 r/min, shown in Figures 7.23 to 7.24 respectively, indicate why this is the case. At 3500 r/min a powerful expansion from the start to the mid-point of the overlap event assists with cylinder charging. The long primary pipe length selected facilitates this. Long pipe lengths, as well as having a lower natural frequency of pressure wave oscillation, are also generally able to generate more powerful pressure troughs during the exhaust event. This is because at any given time during the event, the total pressure at the exhaust valve will comprise of the superposition of a fewer number of reflected and incident waves than in the case of short pipe length. Each of these waves will have been reflected at the pipe boundary a fewer number of times and hence their amplitude will not have been reduced to the same degree. The total pressure condition is therefore the superposition of a fewer number of alternate high and low pressure, high amplitude waves.

Figure 7.23 shows the 4:1 system also generates a low pressure during the overlap event at 3500 r/min and this improves volumetric efficiency above that of the baseline system, as seen in Figure 7.22. However, immediately prior to the overlap event a high pressure exists and therefore the resulting increase in cylinder pumping work reduces torque relative to the 4:2:1 system.

At 5000 r/min the exhaust port pressure history, generated by both the 4:1 and 4:2:1 systems, is not conducive to improved engine breathing. High pressure conditions exist during the overlap event and flow from the cylinder is restricted. The benefits of the low pressure generated during the period of pumping loss sensitivity by the 4:1 system are outweighed by the reduction in volumetric efficiency.

The predicted results indicated that the 4:2:1 system gave the best improvement in performance at the required engine speeds. The predicted results were then validated experimentally by back to back performance testing of the baseline and optimum 4:2:1 systems. The results of these tests are shown in Figure 7.25 and 7.26 and show excellent correlation between measured and predicted results. These results are evidence of the validity of the design méthodology detailed.

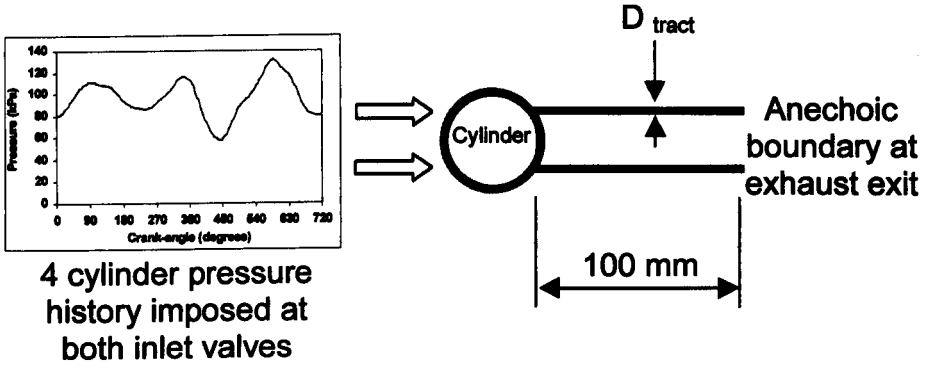

Figure 7.1 Model for selection of exhaust tract diameter

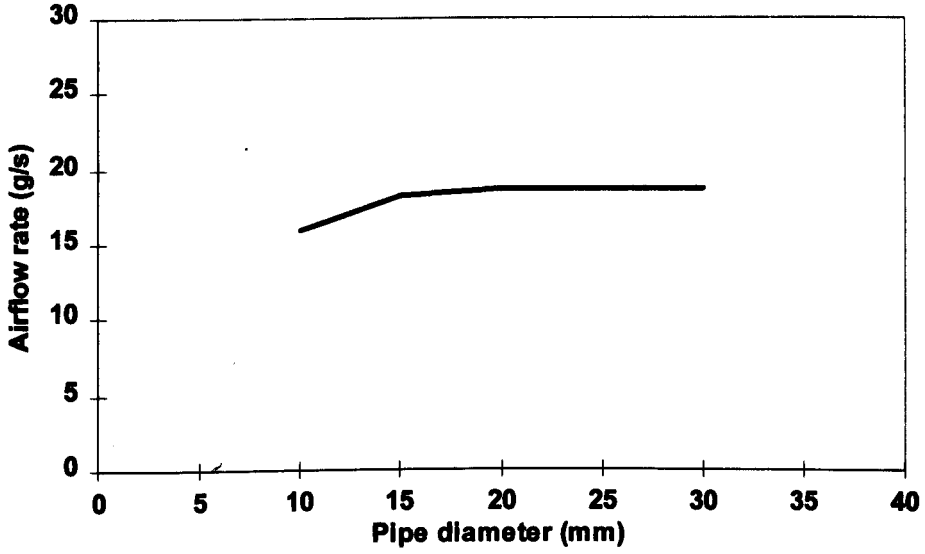

Figure 7.2 Variation of exhaust valve mass flow rate with increase of exhaust tract diameter

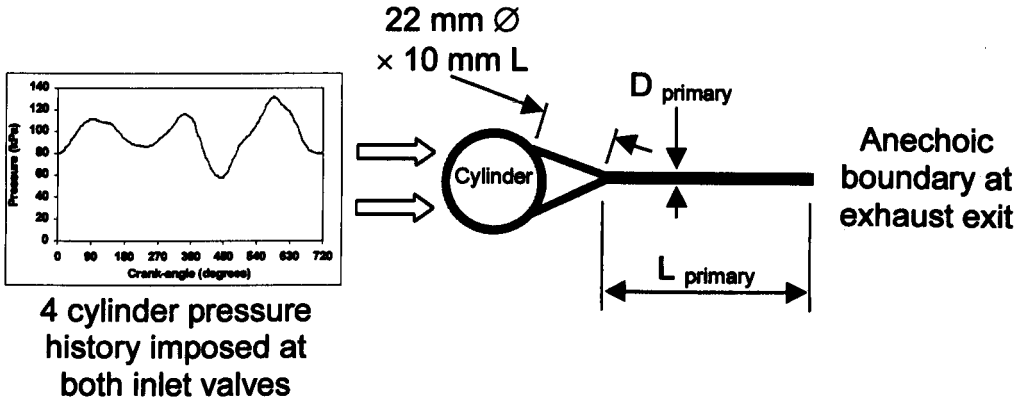

Figure 7.3 Model for selection of primary pipe diameter

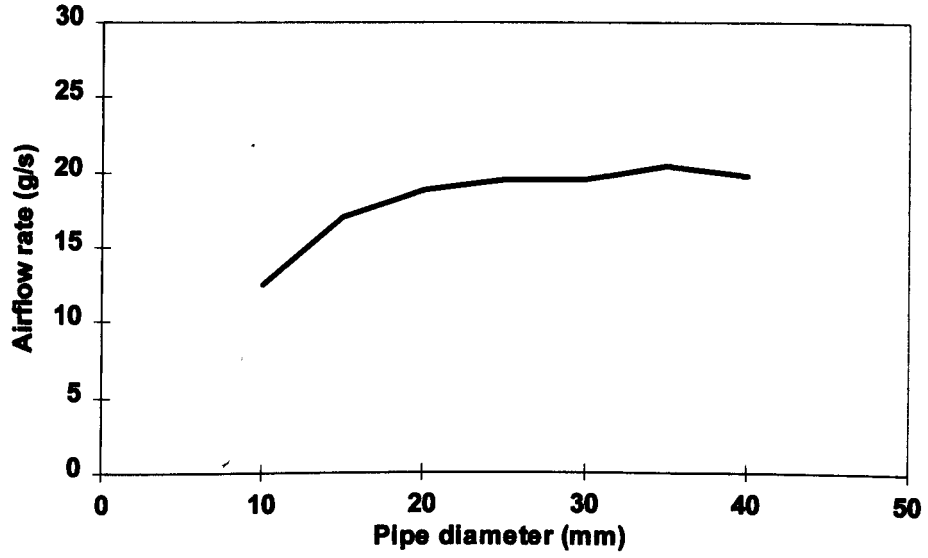

Figure 7.4 Variation of exhaust valve mass flow rate with increase of primary pipe diameter

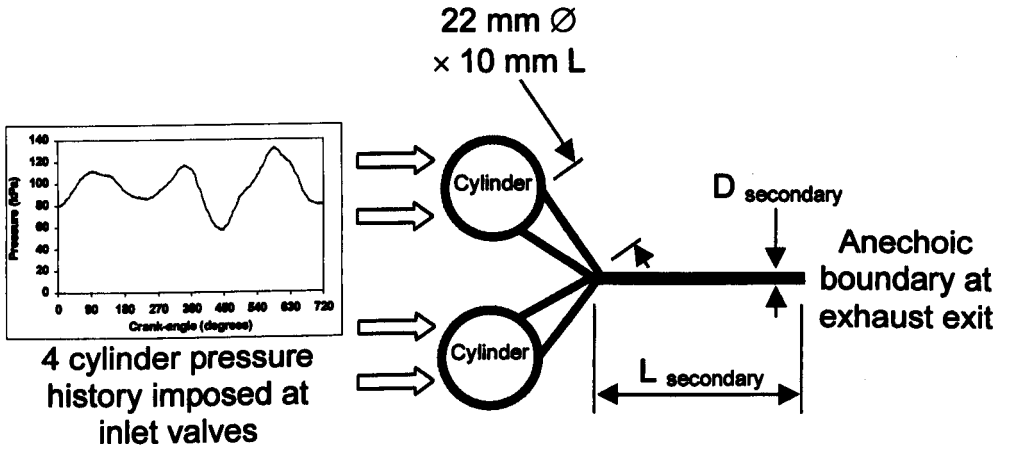

Figure 7.5 Model for selection of secondary pipe diameter

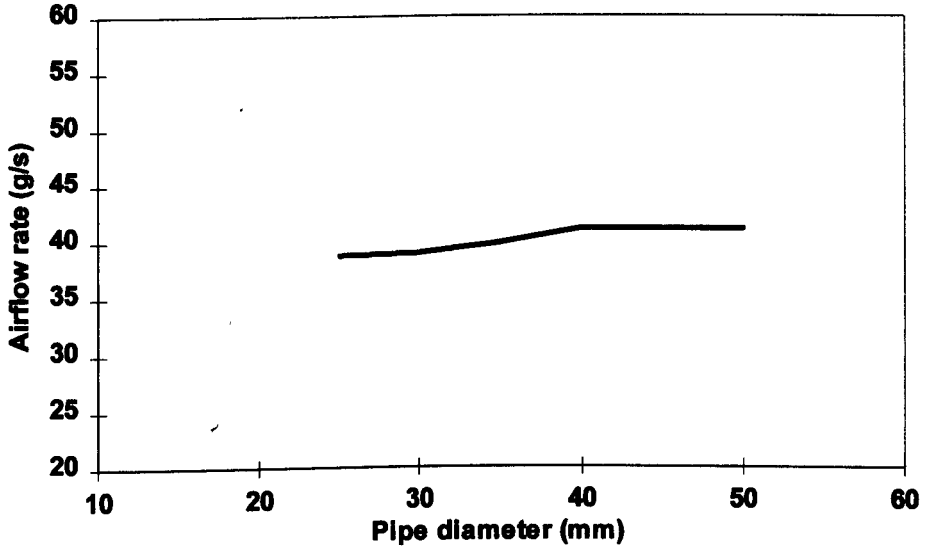

Figure 7.6 Variation of exhaust valve mass flow rate with increase of secondary pipe diameter

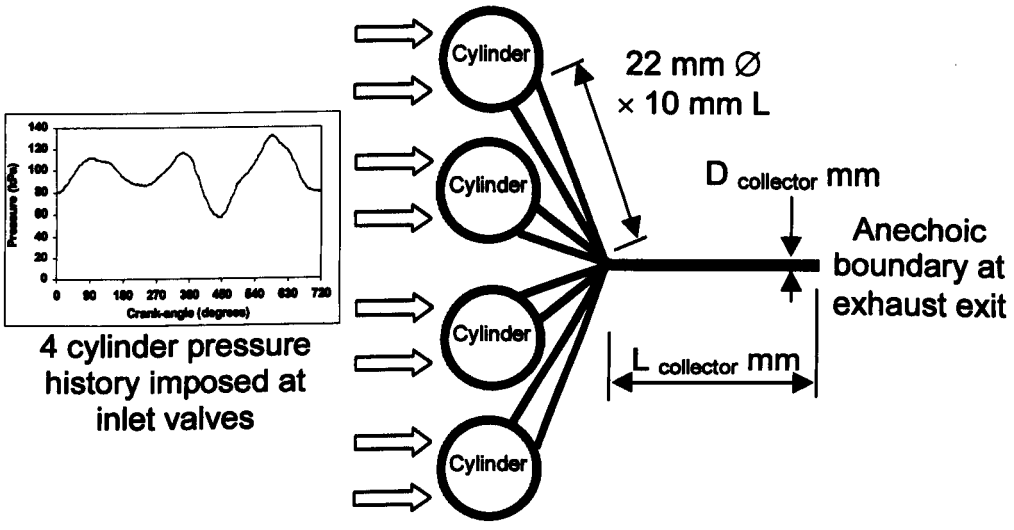

Figure 7.7 Model for selection of collector pipe diameter

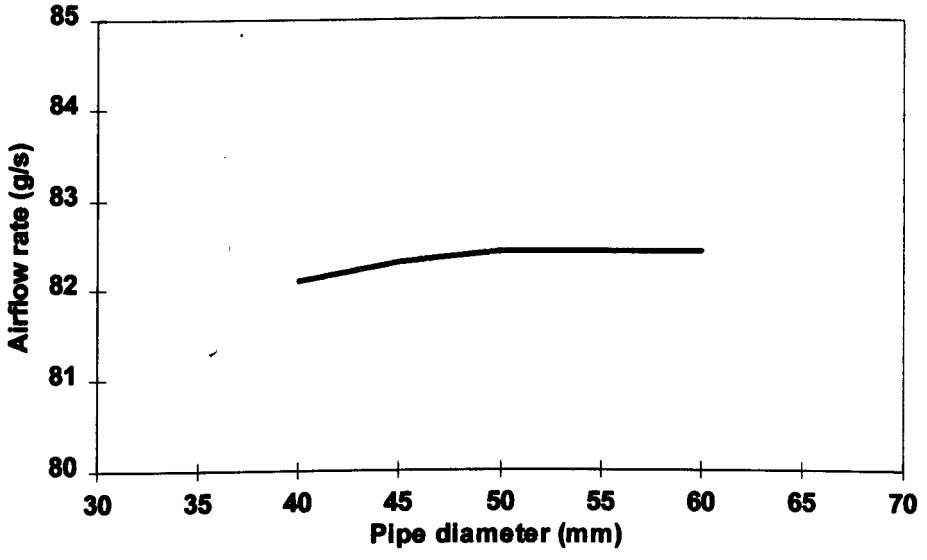

Figure 7.8 Variation of exhaust valve mass flow rate with increase of collector pipe diameter

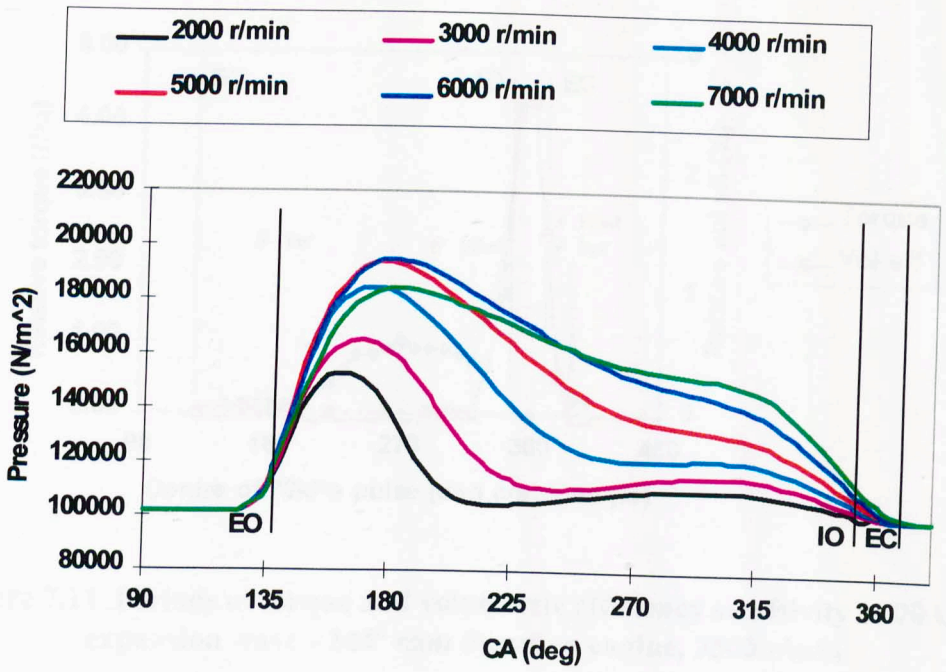

Figure 7.9 Exhaust port pressure history – single cylinder engine into anechoic termination exhaust

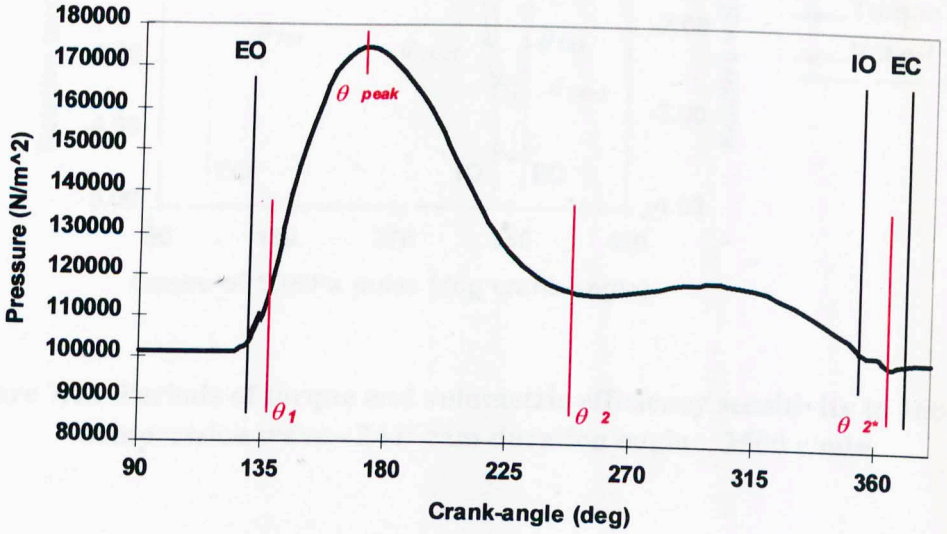

Figure 7.10 Exhaust port pressure history – single cylinder engine into anechoic exhaust at 3500 r/min

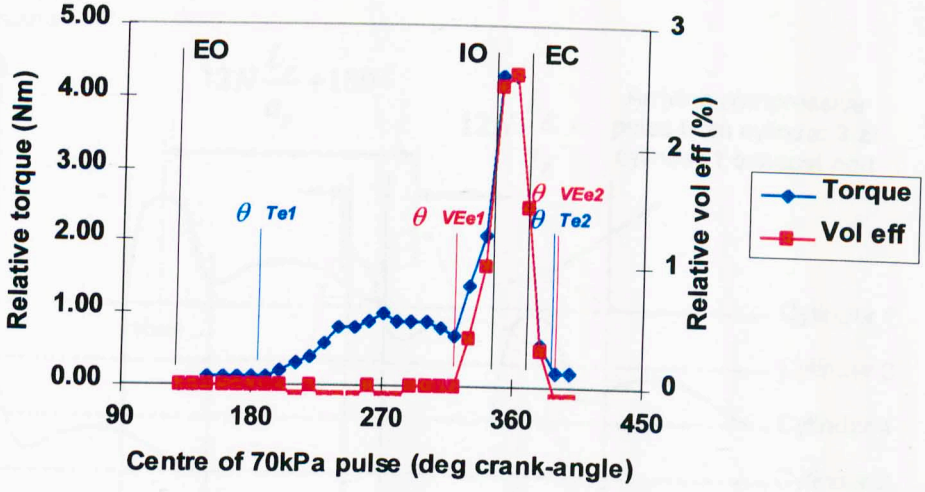

Figure 7.11 Periods of torque and volumetric efficiency sensitivity to 70 kPa expansion wave - 244° cam duration engine, 3500 r/min

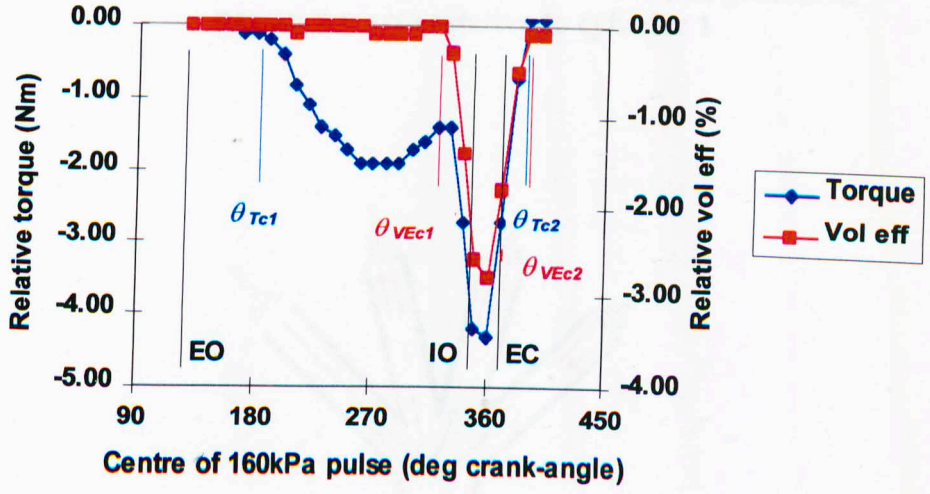

Figure 7.12 Periods of torque and volumetric efficiency sensitivity to 160 kPa compression wave - 244° cam duration engine, 3500 r/min

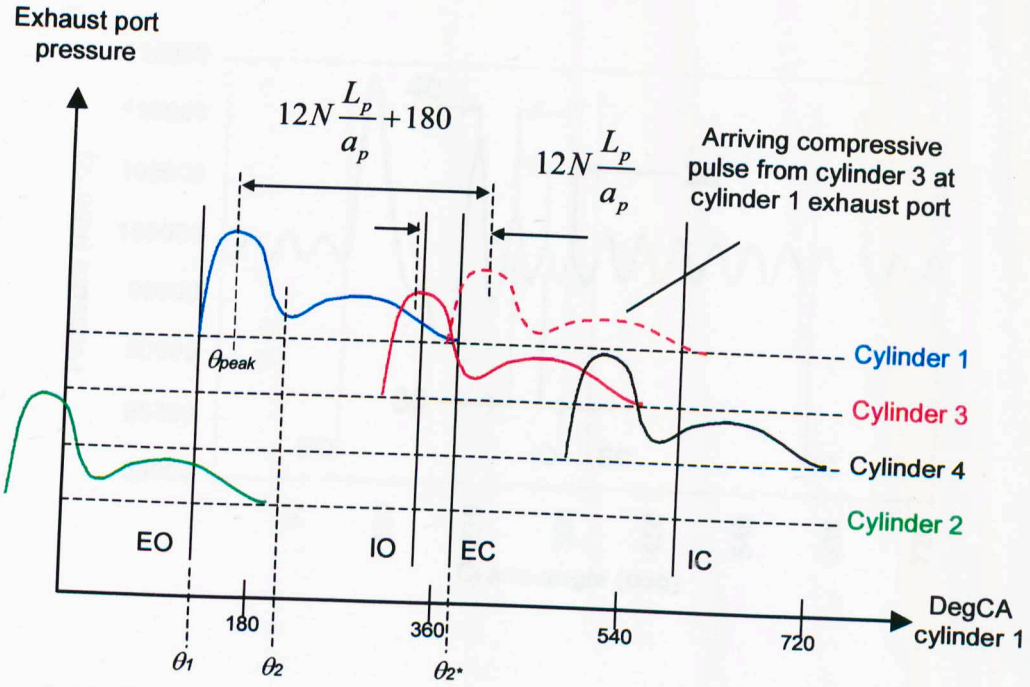

Figure 7.13 The phasing of exhaust events and generated pressure waves relative to cylinder 1

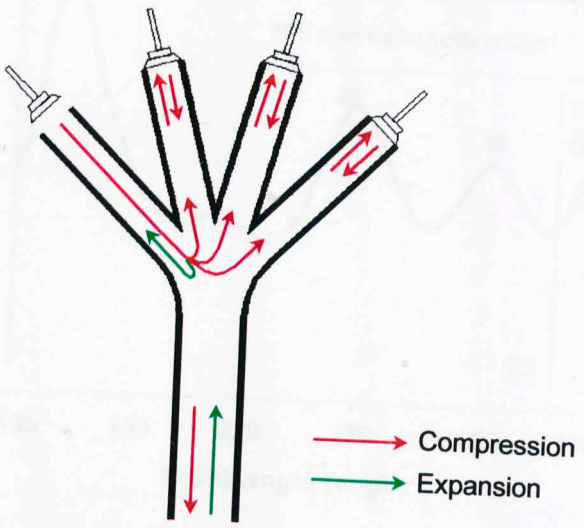

Figure 7.14 The sources of principal reflections in 4:1 configuration exhaust manifolds

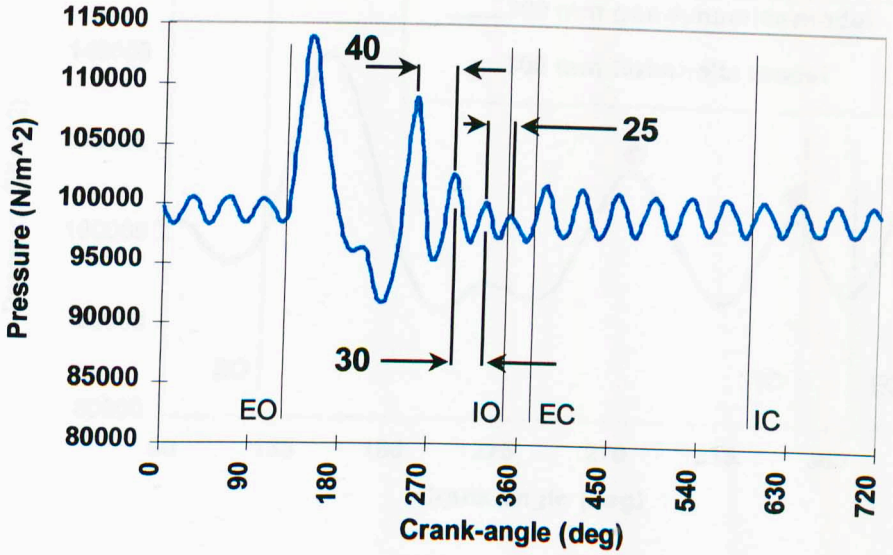

Figure 7.15 The exhaust port pressure history generated by a single-cylinder engine with a 400 mm long open primary pipe at 3000 r/min

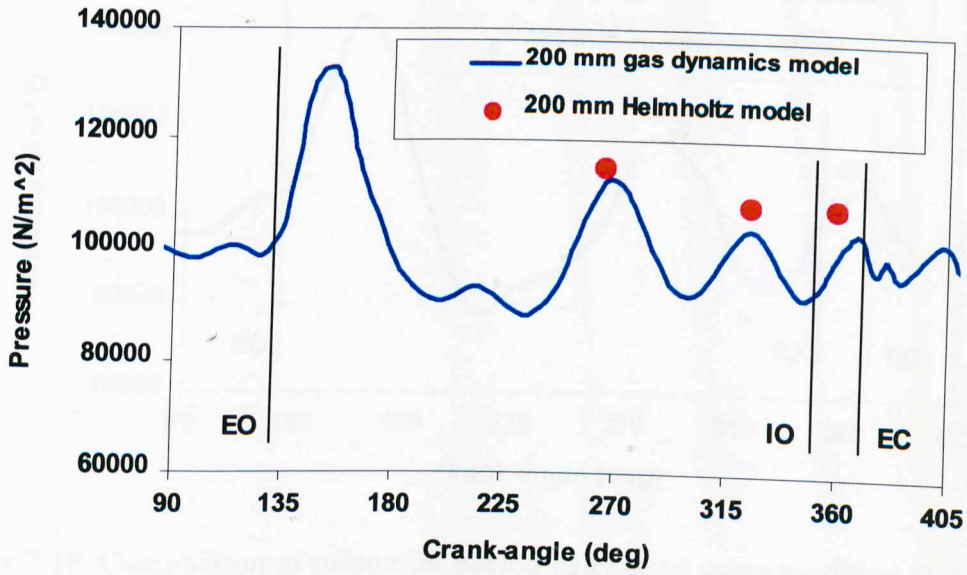

Figure 7.16 Comparison of resonance period calculated using modified Helmholtz model and gas-dynamics simulation – 200 mm open primary pipe

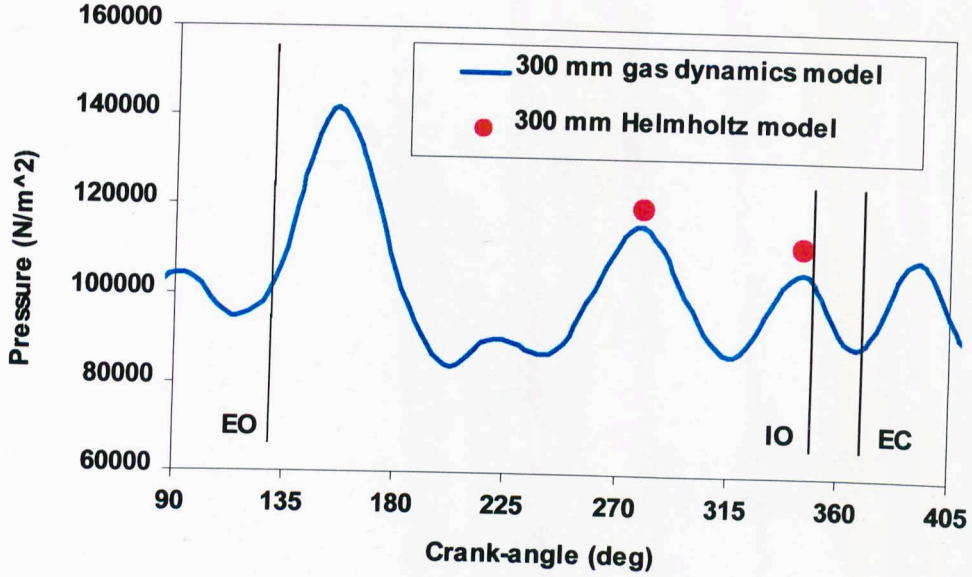

Figure 7.17 Comparison of resonance period calculated using modified Helmholtz model and gas-dynamics simulation – 300 mm open primary pipe

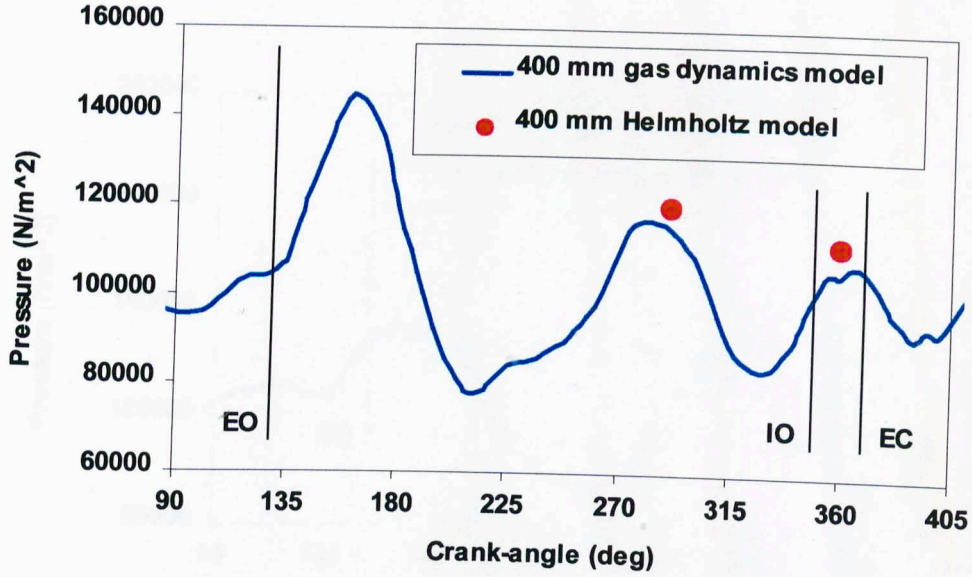

Figure 7.18 Comparison of resonance period calculated using modified Helmholtz model and gas-dynamics simulation – 400 mm open primary pipe

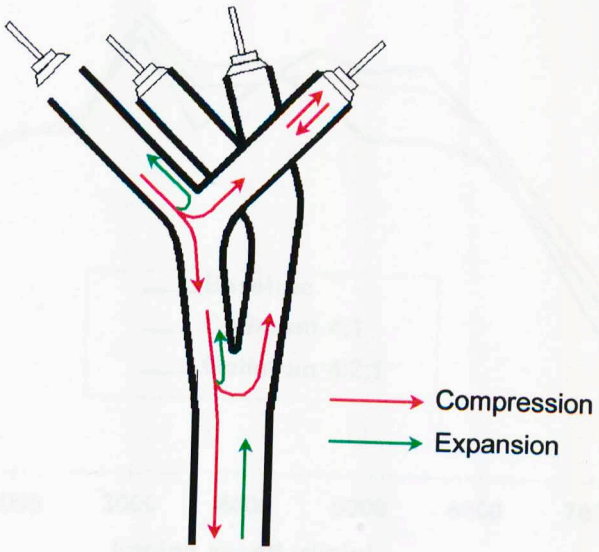

Figure 7.19 The sources of principal reflections in 4:2:1 configuration exhaust manifolds

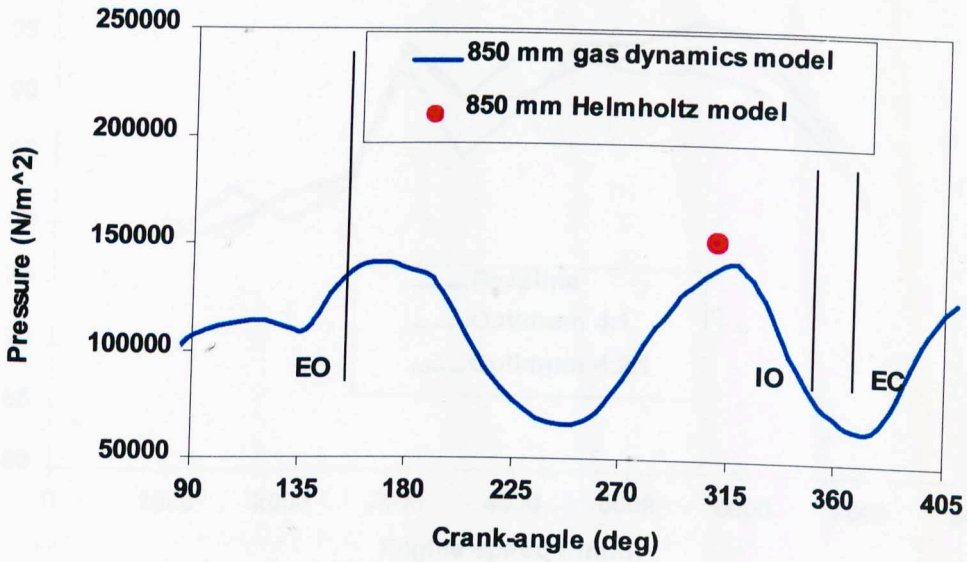

Figure 7.20 Exhaust port pressure history generated by 850 mm long open ended primary pipe – gas dynamics simulation and modified Helmholtz model

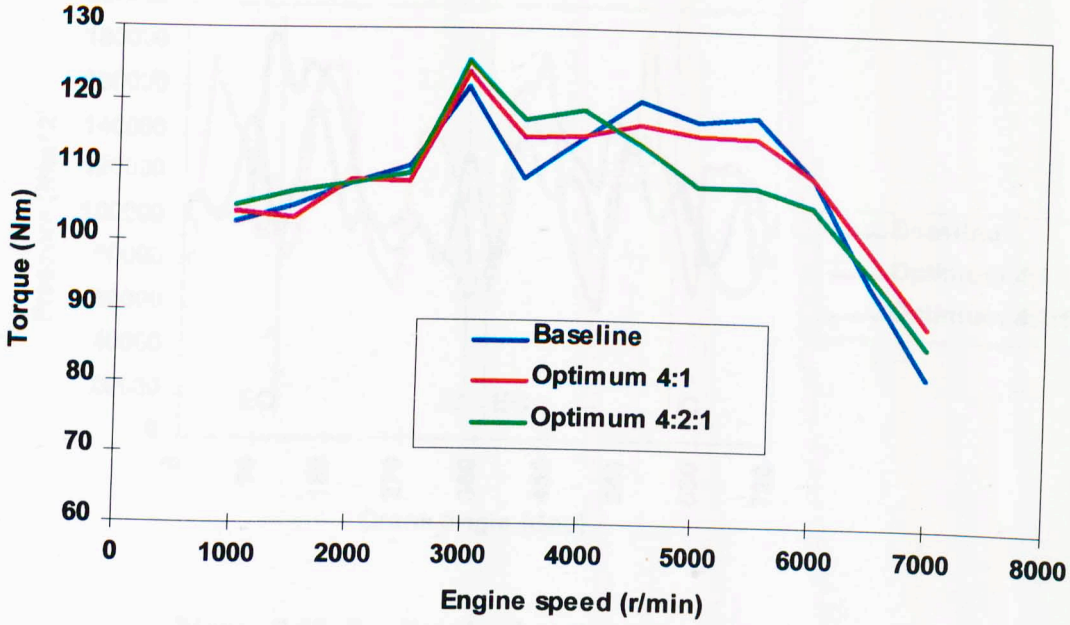

Figure 7.21 Predicted torque performance of baseline and optimum systems

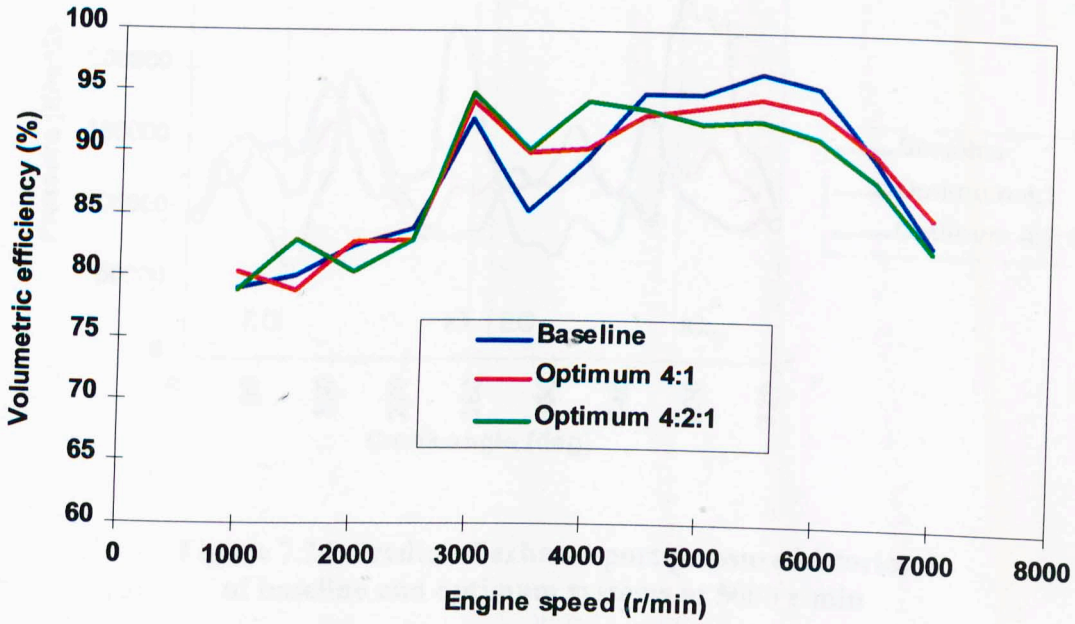

Figure 7.22 Predicted volumetric efficiency performance of baseline and optimum systems

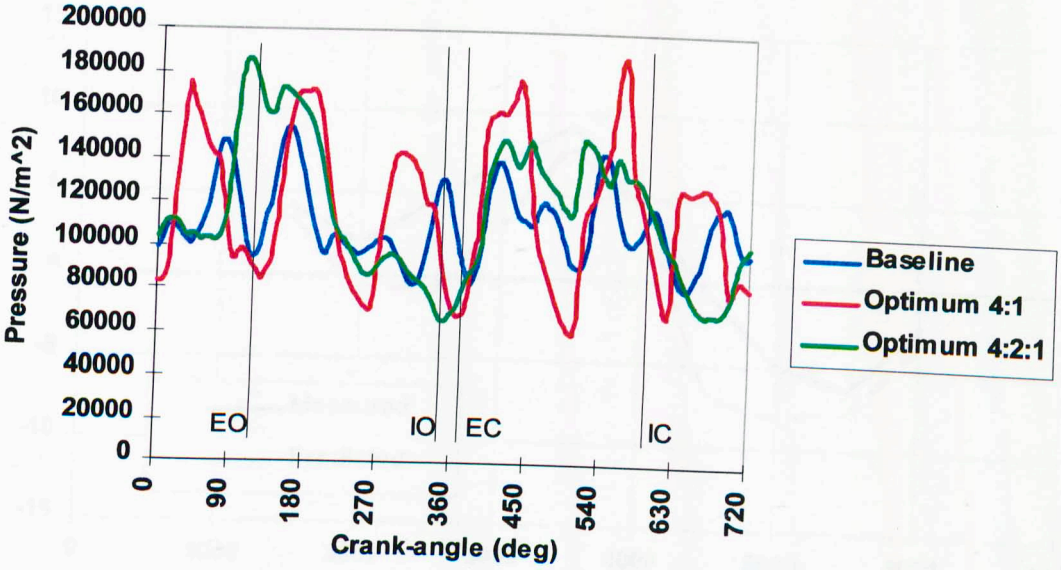

Figure 7.23 Predicted exhaust port pressure histories of baseline and optimum systems at 3500 r/min

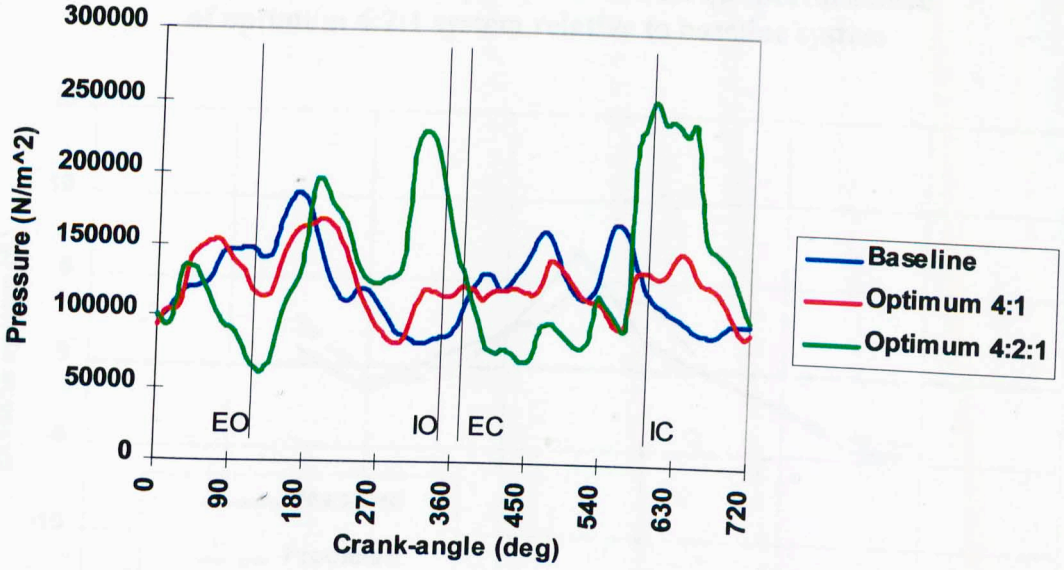

Figure 7.24 Predicted exhaust port pressure histories of baseline and optimum systems at 5000 r/min

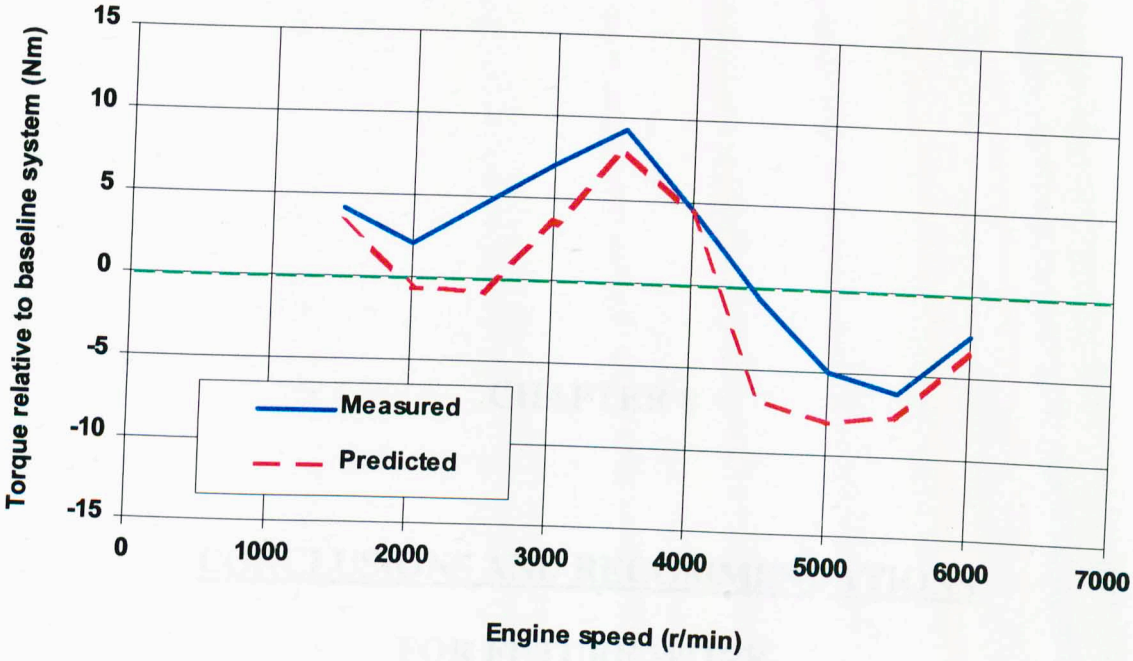

Figure 7.25 Measured and predicted torque performance of optimum 4:2:1 system relative to baseline system

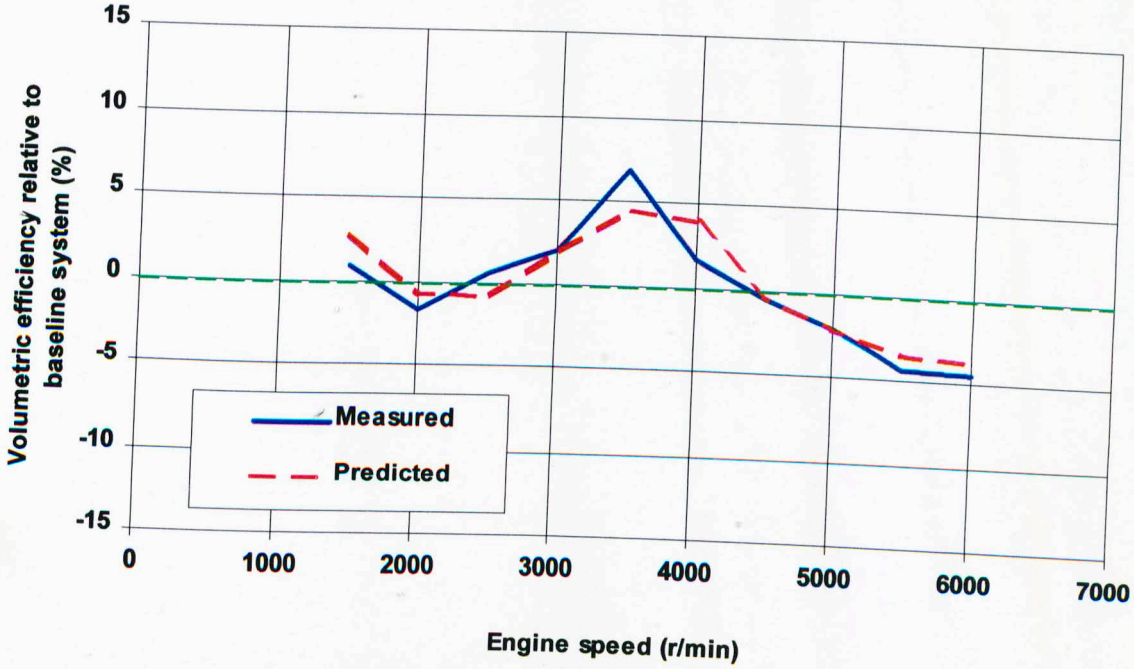

Figure 7.26 Measured and predicted volumetric efficiency performance of optimum 4:2:1 system relative to baseline system

CHAPTER 8

CONCLUSIONS AND RECOMMENDATIONS FOR FUTURE WORK

CHAPTER 8

CONCLUSIONS AND RECOMMENDATIONS FOR FUTURE WORK

8.1 GENERAL

The following conclusions have been drawn from this study:

1. Cylinder breathing characteristics are influenced by the dynamic pressure action in the exhaust system; the action is initiated by cylinder exhaust events. The pressure wave action that occurs in the hot end of the system, that is the manifold network including and upstream of the main catalyst, has the greater influence on mass flow characteristics across the exhaust valve. This is because the amplitude of the reflected pressure waves generated at these locations are of higher amplitude than those generated further downstream. Components located downstream in the exhaust system influence engine performance characteristics principally by their contribution to the overall system back pressure.

2. The mass flow characteristics across the exhaust valve are influenced by the pressure immediately downstream of the exhaust valve during the period following blowdown until IVC. During this period there are two discrete periods during which the pressure downstream of the valve has a significant effect. The first period is approximately centred on the mid-stroke of the piston and the second period is centred on the mid-point of the valve overlap event. Pressure waves arriving during the second period have a greater potential effect on engine breathing than those arriving during the first period.

A low pressure downstream of the exhaust valve during mid-stroke of the piston reduces engine pumping losses, increases torque and decreases BSFC. A low pressure during the overlap event decreases engine pumping losses a small amount and increases air consumption. The opposite effect results in both cases when the pressure is increased. The engine pumping losses are influenced most by the pressure downstream of the valve at approximately mid-stoke of the piston because at this time, the piston exerts the greatest turning moment about the crankshaft axis.

Pressure waves arriving during the second period, that is centred on the mid-point of the valve overlap event, modify the Δp across the exhaust valve and affect mass flow from the cylinder; this in turn modifies the Δp across the inlet valve and affects the quantity of fresh charge induced into the cylinder. Compression waves arriving during this period decrease airflow through the cylinder; expansion waves arriving during this period increase the airflow through the cylinder. As the overlap period is extended, then the potential effect of pressure waves arriving during the overlap event is significantly increased. Engine performance has been shown to be most sensitive to the pressure downstream of the exhaust valve at the mid-point of the overlap event.

Pressure waves arriving at the exhaust port immediately prior to the overlap event can influence the quantity of fresh charge induced into the cylinder. This is because, in the case of an incident compression wave, the cylinder pressure remains high during the period when the wave is resident at the exhaust port. After this period, the cylinder pressure drops but, because an increased burnt

charge mass still resides in the cylinder, the pressure remains higher than the case of there being no incident compression wave at the exhaust port prior to overlap. Thus, the quantity of fresh charge induced into the cylinder during the early stages of valve overlap is reduced.

3. The pressure-time history at the exhaust port of a four-cylinder engine is generated by the interacting wave action that is initiated by the exhaust event of each cylinder. The phasing of this wave action is a function of the exhaust events, the valve lift profiles, the geometry of the exhaust system and the gas conditions within. The exhaust port pressure history generated by any configuration of exhaust system can be well represented by the superposition of the primary pipe pressure wave action, incident reflections from key pipe boundaries and incident compression pulses originating from exhaust events occurring at adjacent cylinders.

4. When the phasing of incident compression waves at the exhaust port is such that the pressure waves do not significantly influence the cylinder gas exchange process and the phasing of incident expansion waves assists the gas exchange process, the exhaust is said to be tuned. At a given engine operating condition, a tuned exhaust system can be identified by considering the sources of each of the pressure waves in turn and defining the pipe geometry associated with the propagation path of the wave to phase the wave appropriately. A rapid design procedure, based on this methodology, has been proposed. The effectiveness of the procedure has been demonstrated with both predictive methods and with experimental results.

5. A key factor in the development of the design methodology is the identification of the resonance characteristics of the primary pipes, specifically the changing phasing of the pressure wave oscillations at the exhaust valve during the exhaust event. A method has been developed, based on an existing acoustic model, that rapidly identifies these characteristics and includes the effect of the changing cylinder volume during the exhaust process.

8.2 RECOMMENDATIONS FOR FUTURE WORK

The following recommendations are suggested for future work:

1. The effect of the configuration of manifold junctions on engine performance characteristics should be studied in detail. The junction in a practical 4:1 configuration exhaust system should ideally be designed to minimise the pressure wave interaction between adjacent cylinders, effectively minimising the detrimental effect of incident exhaust pulses from other cylinders. However, the secondary/tertiary junction in 4:2:1 configuration exhaust systems should be designed to generate as high an amplitude expansion pulse as possible to incident downstream moving compression waves. The detail design of each junction is a compromise between the overall pressure loss generated across the junction, i.e. its contribution to the overall system back pressure, and the tuning effect of the junction design. Practical manufacturing feasibility must be considered also. Production junction designs require pipe ends to be formed at the junction and this can create changes in cross section in the pipe bores adjacent to the junction. It is possible to design a junction that minimises the pressure wave interaction between the pipes upstream of the collector but the design may increase back

pressure unacceptably. A study should be undertaken to get a complete understanding of the effect of exhaust junction geometry on engine performance characteristics.

2. Work should be undertaken to expand the design guidelines to include other engine configurations. Each engine configuration presents particular challenges in terms of the application of the guidelines. For instance an in-line, 6 cylinder engine has an increased overlap of the exhaust event between adjacent cylinders and therefore some of the assumptions that were made in the development of the four-cylinder engine guidelines may not be applicable in this instance. Similarly, a V6 configuration engine, depending on the inclination angle of each cylinder bank, may have an uneven phasing of exhaust events. The use of a symmetrical exhaust system, in this instance, would generate different cyclic boundary conditions at each cylinder and hence both performance and emissions will be affected.

3. Variable geometry exhaust systems for four-stroke engines for performance improvement have had only limited application in production engines. Variable geometry intake systems are a mature technology and have demonstrated significant benefits to engine performance characteristics. The use of a similar methodology on the exhaust manifold, in terms of eliminating or facilitating pressure wave interaction between cylinders, offers the potential for similar benefits, although of reduced magnitude. The design guidelines developed in this work are applicable only to a predefined target speed and a variable geometry exhaust system would allow their application over a wider speed range.

Developments in materials, lubrication and sealing technology make this a practical production proposition.

4. The design methodology developed in this work has considered only naturally aspirated engines. Dynamic wave action is generated in turbocharged engine exhausts by the same processes, but improved engine performance results from harnessing the wave action to best effect at the turbine entry rather than at the exhaust port. Optimum wave action at the turbine entry can be achieved in part by detail design of manifold junctions to retain as much energy in the transmitted component of a downstream moving compression wave as possible. A study should be undertaken with the objective of developing design guidelines for turbocharged engine exhaust systems.

5. Studies should be made of the influence of emissions control devices such as particulate filters and lean NO_x exhaust gas heat exchangers on pressure wave action in exhaust systems. Particulate traps are increasingly becoming standard fitment on new compression ignition engines, particularly large capacity engines. Devices such as lean NO_x heat exchangers have been proposed to control exhaust gas temperature within a limited temperature window for optimum NO_x reduction in GDI engines. Each of these devices will influence pressure wave action in the exhaust system and their location and geometry should ideally be selected, not only for emissions performance, but also to utilise pressure wave action to best effect.

APPENDICES

A1.0 REFERENCES

1. Euro III, 2000 and Euro IV, 2005 emissions standards.

2. US passenger car and light duty trucks, LEV and ULEV, 2001-2006 emissions standards.

3. LAGRANGE, L.J. Miscellanea Taurinensia, t, II, 11, 1760

4. POISSON, S.D. "Memoire sur la theorie du son". Journ. de l'Ecole Polytechn., vol. 7, p 319, 1808

5. STOKES, Sir G.G. "On a difficulty in the theory of sound". Phil. mag., Vol. 23, p 349, 1848.

6. EARNSHAW, S. "On the mathematical theory of sound". Phil. Trans. Roy. Soc. (London), vol. A150, p 133, 1860.

7. RIEMANN, B. "Uber die fortpflanzungebener Luftwellen von endlicher Schwingungswiete". Goth. Abh., vol 8 (Math.), p 43, 1858-59.

8. CAPETTI, A. "Contributo allo studio del flusso nei cilindri dei motori veloci". Ingegneria 2, p 206, 1923.

9. MUCKLOW, G.F. "Exhaust pipe effects in a single cylinder four-stroke engine". Proc. I. Mech. E., vol. 143, p 109, (1940).

10. JENNY, E. "The utilisation of exhaust-gas energy in the supercharging of the four-stroke diesel engine". Brown Boveri Review, vol. 37, p 433, 1950.

11. JENNY, E. "Unidimensional transient flow with consideration of friction, heat transfer and change of section". Brown Boveri Review, vol. 37, 1950.

12. De HALLER, P. "The application of a graphic method to some dynamic problems in gasses". Sulzer Tech. Review, No. 1, p 6, 1945.

13. BANNISTER, F.K. and MUCKLOW, G.F. "Wave action following the sudden release of compressed gas from a cylinder". Proc. I. Mech. E., vol. 159, p 269, (1948).

14. WALLACE, F.J. and STUART-MITCHELL, R.W. "Wave action following the sudden release of air through an engine port system". Proc. I. Mech. E., vol. 1B, p 343, (1953).

15. WALLACE, F.J. and NASIF, M.H. "Airflow in a naturally aspirated two-stroke engine". Proc. I. Mech. E., vol. 168, p 515 (1954).

16. WALLACE, F.J. "Wave action in the diffusers of pipe systems". Engineering, 22 Oct., 1954.

17. MUCKLOW, G.F. WILSON, A.J. "Wave action in gases: attenuation and reflection of and compressive waves propagated in pipes". Proc. I. Mech. E., vol. 169, p 69, (1955)

18. WALLACE, F.J. and BOXER, G. "Wave action in diffusers for exhaust pipe systems with special reference to the scavenging of two-stroke engines". Proc I. Mech. E., vol. 170, no. 39, p 1131 (1956)

19. BENSON, R.S., GARG, R.D. and WOOLATT, D. "A numerical solution of unsteady flow problems". Int. Journ. Mech. Sci., vol. 6, p 117, 1964.

20. BENSON, R.S. and WHITEHOUSE, N.D. "Internal combustion engines". Vols. 1 and 2, Pergammon Press, Oxford, 1979.

21. BENSON, R.S., Ed: HORLOCK, J.H., WINTERBONE, D.E. The thermodynamics and gas dynamics of internal combustion engines". Vols. 1 and 2, Clarendon Press, Oxford, 1982.

22. BENSON, R.S., GARG, R.D. and WOODS, W.A. "Unsteady flow in pipes with gradual or sudden area changes". Proc. I. Mech. E., vol 178, pt. 3I (iii), p 1, (1963-4).

23. BENSON, R.S. "Numerical solution of one-dimensional non-steady flow with supersonic and subsonic flows and heat transfer". Int. Journ. Mech. Sci., vol. 14, p 635, (1972).

24. BENSON, R.S., ANNAND, W.J.D., and BARUAH, P.C. "A simulation model including intake and exhaust systems for a single cylinder four-stroke cycle spark ignition engine". Int. J. Mech. Sci., vol. 17, p 97, (1975).

25. BENSON, R.S. and BARUAH, P.C. "Performance and emission predictions for a multi-cylinder spark ignition engine". Proc. I. Mech. E., vol. 191, p 339, (1977)

26. BENSON, R.S. "A comprehensive digital computer program to simulate a compression ignition engine including intake and exhaust systems". SAE paper no. 710173.

27. BENSON, R.S., and GALLOWAY, K. "An experimental and analytical investigation of the gas exchange process in a multi-cylinder pressure charged two-stroke engine". Proc. I. Mech. E., vol. 183, pt. 1, no. 14, p 253, (1968-69).

28. BLAIR, G.P. and GOULBURN, J.R. "The pressure-time history in the exhaust system for multi-cylinder automobile engines". SAE paper no. 670477.

29. BLAIR, G.P. and GOULBURN, J.R "An unsteady flow analysis of exhaust systems for multi-cylinder automobile engines". SAE paper no. 690469.

30. BLAIR, G.P. and JOHNSTON, M.B. "Unsteady flow effects in exhaust systems of naturally aspirated, crankcase compression, two-cycle internal combustion engines". SAE paper no. 680594.

31. BLAIR, G.P. and ARBUCKLE, J.A. "Unsteady flow in the induction system of a reciprocating internal combustion engine". SAE paper no. 700443.

32. BLAIR, G.P. and CAHOON, W.L. "A more complete analysis of unsteady gas flow through a high-specific-output two-cycle engine". SAE paper no. 720156.

33. CAHOON, W.L. "Unsteady gas flow through a naturally aspirated two-stroke internal combustion engine". Ph.D. thesis, Dept. Mech. Eng., The Queen's University of Belfast, Nov., 1971.

34. McCONNELL, J.H. "Unsteady gas flow through naturally aspirated four-stroke internal combustion engines". Ph.D. thesis, Dept. Mech. Eng., The Queen's University of Belfast, March, 1974.

35. BLAIR, G.P. and SPECHKO, J.A. "Sound pressure levels generated by internal combustion engine exhaust systems". SAE paper no. 720155.

36. BLAIR, G.P. and COATES, S.W. "Noise produced by unsteady exhaust efflux from an internal combustion engine". SAE paper no. 730160.

37. COATES, S.W. and BLAIR, G.P. "Further studies of noise characteristics of internal combustion engine exhaust systems". SAE paper no. 740713.

38. BENSON, R.S. WOOLATT, D. and WOODS, W.A. "Unsteady flow in simple branch systems". Proc. I. Mech. E., vol. 178, pt. 3I(iii), no. 10, p 21, (1963-64).

39. BENSON, R.S. and WOOLATT, D "Compressible flow loss coefficients at bends and T-junctions". The Engineer, p 153, 28 Jan. 1966.

40. BINGHAM, J.F. "Unsteady gas flow in the manifolds of multi-cylinder automotive engines". Ph.D. thesis, Dept. Mech. Eng., The Queen's University of Belfast, October, 1983.

41. DECKKER, B.E.L. and MALE, D.H. "Unsteady flow in a branched duct". Proc. I. Mech. E., vol. 182, pt. 3H, no. 10, p 104, (1967-68)

42. DECKKER, B.E.L. and MALE, D.H. "Fluid dynamic aspects of unsteady flow in branched ducts". Proc. I. Mech. E., vol. 182, pt. 3H, no. 18, p 167, (1967-68).

43. MALE, D.H., CHELSOM, R.A. and DECKKER, B.E.L. "Behaviour of rarefaction waves at the junction of a branched duct". Proc. I. Mech. E., vol. 184, pt. 3G(1), no. 18, p 1, (1969-70).

44. BENSON, R.S., BARUAH, P.C. and SIERENS, R. "Steady and non-steady flow in a simple carburettor". Proc. I. Mech. E., vol. 188 53/74, p 537, (1974).

45. WOODS, W.A. and GOH, G.K. "Compressible flow through a butterfly throttle valve in a pipe". Proc. I. Mech. E., vol. 193, p 237, (1979).

46. BAJEMA, D.L., and GATECLIFF, G.W. "Prediction and measurement of fluid flow in single cylinder engine carburettors". SAE paper no. 780285.

47. LEDGER, J.D. "A finite difference approach for solving the gas-dynamics in an engine exhaust". Journ. Mech. Eng. Sci., vol. 17, no. 3, p 125, 1975.

48. RICHTMYER, R.D. and MORTON, K.W. "Difference methods for initial value problems". 2nd ed., 1967, Interscience Publishers.

49. MacLAREN, J.F.T., TRAMSCHEK, A.B., SANJINES, A. and PASTRANA, O.F. "A comparison of numerical solutions of the unsteady flow equations applied to reciprocating compressor systems". Journ. Mech. Eng. Sci., vol. 17, no. 5, p 271 1975.

50. MacLAREN, J.F.T., TRAMSCHEK, A.B. and PASTRANA, O.F. "Research note: An alternative scheme to solve the equations for unsteady gas flow". Journ. Mech. Eng. Sci., vol. 18, no. 3, p 161, 1976.

51. TAKIZAWA, M., UNO, T., OUE, T. and YURA, T. "A study of gas exchange process simulation of an automotive multi-cylinder internal combustion engine". SAE paper no. 820410.

52. CHAPMAN, M. "FRAM - non-linear damping algorithms for the continuity equation". Journ. Comp. Phys., vol. 44, p 84-103, 1981.

53. CHAPMAN, M., NOVAK, J.M.. and STEIN, R.A. "Numerical modelling of inlet and exhaust flows in multi-cylinder internal combustion engines." Proc. of winter annual meeting of ASME, Phoenix, Arizona, Nov. 14-19, 1982.

54. MOREL, T., FLEMMING, M.F., and LaPOINT, L.A. "Characterization of manifold dynamics in Chrysler 2.2 SI engine by measurement and simulation". SAE paper no. 900679.

55. SATO, K. and KIDO, K.. "The simulation of the gas exchange process in a small two-stroke cycle engine". (1st report, theoretical treatment). JSME, vol. 26, no. 217, p 1178, (1983).

56. SATO, K. and NAKANO, M. "The simulation of the gas exchange process in a small two-stroke cycle engine". (2nd report, comparison between experimental and theoretical treatments). JSME, vol. 26, no. 217, p 1188, (1983).

57. BULATY, T. and NIESSNER, H. "Calculation of 1-D unsteady flows in pipe systems of IC engines". ASME Journ. Fluids Eng., vol. 107, p 407, (1985).

58. CORBERÁN, J.M and GASCÓN, L. "New method to calculate unsteady 1-D compressible flow in pipes with variable cross section. Application to the calculation of the flow in intake and exhaust pipes of I.C. engines". ICE, vol. 23, Engine Modelling, p 77-87, ASME, 1995.

59. LUI, J.P., SCHORN, N., SCHERNUS, C. and PENG, L. "Comparison studies on the method-of-characteristics and finite difference methods for one dimensional gas flow through IC engine manifold". SAE paper no. 960078

60. PEARSON, R.J. and WINTERBONE, D.E. "Calculation of one-dimensional unsteady flow in internal combustion engines - how long should it take?". I. Mech. E., C499/012, 1996

61. MUNJAL, M.L. "The acoustics of ducts and mufflers". John Wiley and Sons, 1987.

62. OHATA, A and ISHIDA, Y. "Dynamic inlet pressure and volumetric efficiency of four cycle four cylinder engine". SAE paper no. 820407.

63. MATSUMOTA, I. and OHATA, A. "Variable induction systems to improve volumetric efficiency at low and/or medium engine speeds". SAE paper no. 860100.

64. PEARSON, R.J and WINTERBONE, D.E. "A rapid synthesis technique for intake manifold design". Int. Journ. of Vehicle Design, vol. 10, no. 6, 1989.

65. BENAJES, J., REYES, E., GALINDO, J., and PEIDRO, J. "Predesign model for intake manifolds in internal combustion engine". SAE paper no. 970055.

66. BENAJES, J., REYES, E., BERMUDEZ, V. and SERRANO, J.R. "Predesign criteria for exhaust manifolds in IC automotive engines". SAE paper no. 980783.

67. CHAPMAN, M. "Two dimensional numerical solution of inlet manifold flow in a four cylinder internal combustion engine". SAE paper no. 790244.

68. TOSA, Y., SHIMODA, K., and OIKAWA, H. "Calculation of two-dimensional unsteady flows in inlet pipe systems and its application for V-8 resonant intake system". ASME Int. Symp. On Flows in Internal Comb. Eng. III, p 63-70, 1985.

69. DIMITRIADIS, C., LESCHZINER, M.A., WINTERBONE, D.E., ALEXANDER, G.I. and SIERENS, R. "Computation of three-dimensional flow in manifold type junctions". ASME Int. Symp. On Flows in Internal Comb. Eng. III, p 57-62, 1985.

70. AMSDEN, A.A., BUTLER, T.D., O'ROURKE, P.J. and RAMSHAW, J.D. "KIVA - a comprehensive model for 2-D and 3-D engine simulations". SAE paper no. 850554.

71. "WAVE v3.5 engine simulation software user manual". Ricardo Software, November, 1999.

72. JONES, A. "Noise characteristics and exhaust process gas dynamics of a small 2-stroke engine". Ph.D. thesis, Dept. of Mech. Eng., The University of Adelaide, 1978.

73. KONG, H. and WOODS, R.L. "Tuning of intake manifold of an internal combustion engine using fluid transmission line dynamics". SAE paper no. 920685.

74. MARGOLIS, D. "Modelling of two-stroke internal combustion engine dynamics using the bond graph technique". SAE paper no. 750860.

75. BLAIR, G.P. "An alternative method for the prediction of unsteady gas flow through the internal combustion engine". SAE paper no. 911850.

76. BLAIR, G.P. "Correlation of an alternative method for the prediction of engine performance data with measured data". SAE paper no. 930501.

77. BAXENDALE, A.J. "The role of computational fluid dynamics in exhaust system design and development". SAE paper no. 931072.

78. SMITH, P.H. and MORRISON, J.C. "Scientific design of exhaust and intake systems". G.T. Foulis and Co. Ltd., 1974.

79. ANNAND, W.J.D., and ROE, G.E. "Gas flow in the internal combustion engine – power performance, emission control and silencing". G.T. Foulis and Co., 1974.

80. THOMPSON, MP. and ENGELMAN, H. "The two types of resonance in intake tuning". ASME paper 69-DGP-11, 1969.

81. BROOME, D. "Induction ram, part 1: the inertia and wave effect of ram and a summary of published work". Automobile Engineer, p 130-133, April, 1969.

82. BROOME, D. "Induction ram, part 2: inertial aspects of induction ram". Automobile Engineer, p 180-184, May, 1969.

83. BROOME, D. "Induction ram, part 3: wave phenomena and the design of ram intake systems". Automobile Engineer, p 162-267, June, 1969.

84. PROSER, T.G. "Induction ramming a motored high speed four-stroke reciprocating engine – influence of inlet port pressure waves on volumetric efficiency" I. Mech. E., vol. 188 49/74, 1974.

85. MATSUMOTA, I. and OHATA, A. "Variable induction systems to improve volumetric efficiency at low and/or medium engine speeds". SAE paper no. 860100.

86. EGUCHI, N., KUBODERA, T., OTANI, T. and USAMI, K. "Development of a variable controlled inertia charging system for naturally aspirated diesel engines in heavy trucks". Int. Journ. of Vehicle Design, vol. 7, no. 1/2, p 118-132, 1986.

87. ISOMURA, S., KURIHATA, Y., YAMASHITA, T. and KOIKE, M. "Development of variable inertia charging system for 1.6l DOHC engine". JSAE Review, vol. 8, no. 4, p 77-79, Oct. 1987.

88. LENZ, H.P. and DUELLI, H. "A new continuously variable intake manifold for achievement of optimal torque characteristic of a S.I. engine with fuel injection". ATZ Automobiltechnische Zeitschrift 89-6, p 331-332, 1987.

89. MIKULIC, L., SCHOMMERS, J., GERINGER, B., WOLF, K. and ENDERLE, C. "Variable gas exchange systems for S.I. engines – layout and experimental data". SAE paper no. 920296.

90. HATA, N. and TOSHIMITSU, L. "Improvement of two-stroke engine performance with the Yamaha power valve system (YPVS)". SAE paper no. 810922.

91. NOMURA, K., HIRANO, S., GOTOH, T. and MOTOYAMA,Y. "Improvement of fuel consumption with variable exhaust port timing in a two-stroke gasoline engine". SAE paper no. 850183.

92. Yamaha Motor (UK) Ltd. Service training information, SH/JCM/A160.

93. KRAUSE, P., WELTENS, H. and HUTCHINS, S.M. "Advanced design of automotive exhaust silencer systems". SAE paper no. 922088.

94. MIROSH, E "Reverse flow catalytic converter for natural gas fuelled diesel engine". Engine Expo Conf., Hamburg, June, 1999.

95. Opel patent for temperature control in exhaust system catalyst, European patent reference 93-406543/51.

96. WINTERBONE, D.E., WORTH,D. and NICHOLS, J.R. "A comparison of synthesis and analysis models for wave action manifolds". I. Mech. E. Int. Conf. on the Small Int. Conb. Eng., C372/037, 1989.

97. ENGELMAN, H.W. "Design of a tuned intake manifold". ASME paper 73-WA/DGP-2, 1973.

98. VORUM, P.C. "Short pipe manifold design for four-stroke engines". ASME paper 76-WA/DGP-4, 1973.

99. VORUM, P.C. "Short pipe manifold design for four-stroke engines: part II". ASME Journ. of Engineering for Power, vol. 102, p 836-841, Oct., 1980.

100. TABACZYNSKI, R.J. "Effects of inlet and exhaust system design on engine performance". SAE paper no. 821577.

101. JAMESON, R.T. and HODGINS, P.A. "Improvement of the torque characteristics of a small, high-speed engine through the design of Helmholtz tuned manifolding". SAE paper no. 900680.

102. RAMOS, J.I. "Internal combustion engine modelling". Hemisphere Publishing Co., 1989.

103. HALL, K.G. "Design optimisation of engine induction systems." Autotech new engines, components and materials seminar, C399/20, 1989.

104. PAYRI, F., DESANTES, J.M. and CORBÉRAN, J.M. "I.C. engine intake and exhaust manifold design procedure." SAE paper no. 905234.

105. LUI, J.P. "Development of design guidelines for engine intake system design from fundamental gas-dynamics studies". Ph.D. thesis, Dept. of Mech. Eng., The University of Strathclyde, Glasgow, 1995.

106. BENAJES, J., REYES, E., GALINDO, J. and PEIDRO, J. "Predesign model for intake manifolds in internal combustion engines". SAE paper no. 970055.

107. BENAJES, J., REYES, E., BERMUDEZ, J.R and SERRANO, J.R. "Pre-design criteria for exhaust manifolds in I.C. automotive engines". SAE paper no. 980783.

108. "National Engineering Laboratory engine simulation software user manual, v1.3". October, 1997

109. COURANT, R., FRIEDRICHS, K. and LEWY, H. Math. Ann. 100, 32 (1928). Translation rep. no. NYO-7689, Inst. of Math. Sci., New York University, 1956.

110. VAN WYLEN, G.J. and SONNTAG, R.E. "Fundamentals of classical thermodynamics". John Wiley and Sons, New York, 1976.

111. BINGHAM, J.F. and BLAIR, G.P. "An improved branch pipe model for multi-cylinder automotive engine calculations". Proc. I. Mech. E., vol. 199, no. D1, p 65-77, 1985.

112. ANNAND, W.J.D. "Heat transfer in the cylinders of reciprocating internal combustion engines". Proc. I. Mech. E., vol. 177, no. 36, p 973, 1963.

113. HEYWOOD, J.B. "Internal combustion engine fundamentals". McGraw-Hill Book Company, 1988.

114. BANNISTER, F.K. "Pressure waves in gases in pipes". Akroyd Stuart Memorial Lectures, 1958.

115. "Road vehicles – engines test code – net power". ISO 1585 – 1982 (E).

116. ADAMS, T.G "Effect of exhaust system design on engine performance". SAE paper number 800319.

117. TAGUCHI, G. "System of experimental design". Volume 1, Quality Resources and American Supplier Institute, Inc., 1987.

118. TAGUCHI, G. "System of experimental design". Volume 2, Quality Resources and American Supplier Institute, Inc., 1987.

119. PAYRI, F., DESANTES, J. and GALINDO, J. "One-dimensional fluid-dynamic model for catalytic converters in automotive engines." SAE paper number 950785

120. McGINNITY, F.A. "The effect of temperature on engine gas-dynamics". Ph.D. thesis, Dept. Mech. Eng., The Queen's University of Belfast, Dec., 1989.

A2.1 THE NATURAL RESONANCE FREQUENCY OF A MANIFOLD FROM DISTRIBUTED PARAMETER ACOUSTIC MODELS

The following nomenclature is applicable to section A2.1 only:

a	=	Speed of sound
f, F	=	Pipe cross sectional area
l, L	=	Pipe length
$\dot{m}$	=	Mass flowrate of unit pipe area (kg/sm^2)
n	=	Engine speed (r/min)
p	=	Pressure
t	=	Time
u	=	Particle velocity
V	=	Volume
x	=	Distance
ρ	=	Density
Δ	=	Increment of
ω	=	Angular velocity = $\frac{2\pi n}{60}$ (rad/s)

Subscripts:

0	=	Reference conditions
1 to n	=	Manifold locations
V	=	Volume conditions

Considering the unsteady flow of a non-viscous fluid in a pipe of constant cross sectional area, where the disturbing pressure is of acoustic amplitude, i.e. <<6 kPa, and the pipe flow can be considered one-dimensional, then the non-linear equations for momentum and continuity are:

$$\text{Momentum:} \quad \frac{\partial p}{\partial x} + \rho\left(\frac{\partial u}{\partial t} + u\frac{\partial u}{\partial x}\right) = 0 \qquad \text{(A2.1.1)}$$

$$\text{Continuity:} \quad \frac{\partial \rho}{\partial t} + \rho\frac{\partial u}{\partial x} + u\frac{\partial \rho}{\partial x} = 0 \qquad \text{(A2.1.2)}$$

Knowing the amplitude of the pressure disturbances, Δp, are very small, then at all points on the wave profile $p = p_0 + \Delta p$, or since $\Delta p << p_0$ then $p \approx p_0$. Similarly, the particle velocity $u \approx const$.

For a gas in equilibrium, any thermodynamic state variable can be specified by any two other state variables, thus:

$$dp = \left(\frac{\partial p}{\partial \rho}\right)_s d\rho + \left(\frac{\partial p}{\partial s}\right)_\rho ds \qquad \text{(A2.1.3)}$$

Assuming isentropic wave motion, $ds = 0$, thus:

$$dp = \left(\frac{\partial p}{\partial \rho}\right)_s d\rho \qquad \text{(A2.1.4)}$$

Considering changes of p and ρ in the x direction, then:

$$\frac{\partial p}{\partial x} = \left(\frac{\partial p}{\partial \rho}\right)_s \frac{\partial \rho}{\partial x} \qquad \text{(A2.1.5)}$$

Now substituting (A2.1.5) into (A2.1.1) gives:

$$\left(\frac{\partial p}{\partial \rho}\right)_s \frac{\partial \rho}{\partial x} + \rho\left(\frac{\partial u}{\partial t} + u\frac{\partial u}{\partial x}\right) = 0 \qquad \text{(A2.1.6)}$$

The energy equation, assuming a homentropic flow field, is:

$$\left(\frac{\partial p}{\partial \rho}\right)_s = \frac{\gamma(p_0 + \Delta p)}{\rho_0 + \Delta\rho} = \frac{\gamma p}{\rho} = a^2 \qquad \text{(A2.1.7)}$$

where $\rho = \rho_0 + \Delta\rho$. Also, since $u = u_0 + \Delta u = 0 + \Delta u = \Delta u$, substitution into (A2.1.6) gives:

$$a^2 \frac{\partial(\rho_0 + \Delta\rho)}{\partial x} + (\rho_0 + \Delta\rho)\frac{\partial(\Delta u)}{\partial t} + (\rho_0 + \Delta\rho)\Delta u \frac{\partial(\Delta u)}{\partial x} = 0 \qquad \text{(A2.1.8)}$$

Expanding gives:

$$a^2 \frac{\partial \rho}{\partial x} + \rho_0 \frac{\partial(\Delta u)}{\partial t} + \Delta\rho \frac{\partial(\Delta u)}{\partial t} + \rho_0 \Delta u \frac{\partial(\Delta u)}{\partial x} + \Delta\rho\Delta u \frac{\partial(\Delta u)}{\partial x} = 0 \qquad \text{(A2.1.9)}$$

Expanding a^2 in a Taylor's series about ρ_0:

$$a^2 = {a_0}^2 + \left(\frac{\partial a^2}{\partial \rho}\right)(\rho - \rho_0) + \ldots\ldots = {a_0}^2 + \left(\frac{\partial a^2}{\partial \rho}\right)_0 \Delta\rho + \ldots\ldots \qquad \text{(A2.1.10)}$$

and substituting into (A2.1.9) gives:

$$\left({a_0}^2 + \left(\frac{\partial a^2}{\partial \rho}\right)_0 \Delta\rho + \ldots\ldots\right)\frac{\partial \rho}{\partial x} + \rho_0 \frac{\partial(\Delta u)}{\partial t} + \Delta\rho \frac{\partial(\Delta u)}{\partial t} +$$

$$\rho_0 \Delta u \frac{\partial(\Delta u)}{\partial x} + \Delta\rho\Delta u \frac{\partial(\Delta u)}{\partial x} = 0 \qquad \text{(A2.1.11)}$$

Eliminating the second order terms gives the linear approximation for the momentum equation:

$$a_0{}^2 \frac{\partial \rho}{\partial x} + \rho_0 \frac{\partial(\Delta u)}{\partial t} = 0 \qquad \text{(A2.1.12)}$$

Similarly, for the continuity equation, the resulting linearised equation is:

$$\frac{\partial \rho}{\partial t} + \rho_0 \frac{\partial(\Delta u)}{\partial x} = 0 \qquad \text{(A2.1.13)}$$

Differentiating the momentum equation, (A2.1.12), with respect to x yields:

$$a_0{}^2 \frac{\partial^2 \rho}{\partial x^2} + \rho_0 \frac{\partial^2(\Delta u)}{\partial x \partial t} = 0 \qquad \text{(A2.1.14)}$$

and differentiating the continuity equation with respect to t yields:

$$\frac{\partial^2 \rho}{\partial t^2} + \rho_0 \frac{\partial^2(\Delta u)}{\partial x \partial t} = 0 \qquad \text{(A2.1.15)}$$

Substituting (A2.1.14) into (A2.1.15) yields the general wave equation:

$$\frac{\partial^2 \rho}{\partial t^2} = a_0{}^2 \frac{\partial^2 \rho}{\partial x^2} \qquad \text{(A2.1.16)}$$

for which the general solution is of the form:

$$\rho(x,t) = C_x f(x - a_0 t) + C_y g(x + a_0 t) \qquad \text{(A2.1.17)}$$

Since all points along the wave profile are assumed to be moving with constant velocity a_0, then (A2.1.16) can be written as:

$$\frac{\partial^2 \Theta}{\partial t^2} = a_0{}^2 \frac{\partial^2 \Theta}{\partial x^2} \qquad \text{(A2.1.18)}$$

for all general quantities Θ.

Thus, the solution to the wave equation in terms of pressure is:

$$p(x,t) = C_1 f(x - a_0 t) + C_2 g(x + a_0 t) \qquad \text{(A2.1.19)}$$

which can be written in the exponential form:

$$p(x,t) = C_1 e^{j\omega(t - x/a_0)} + C_2 e^{j\omega(t + x/a_0)} \qquad \text{(A2.1.20)}$$

This can be rearranged to give:

$$p(x,t) = \left(C_1 e^{-jkx} + C_2 e^{jkx}\right) e^{j\omega t} \qquad \text{(A2.1.21)}$$

where $k = \dfrac{\omega}{a_0}$.

For isentropic flow $\Delta u = \dfrac{p}{\rho_0 a_0}$, so for particle velocity it can be written:

$$\Delta u(x,t) = \frac{1}{Z_0}\left(C_1 e^{-jkx} - C_2 e^{+jkx}\right) e^{j\omega t} \qquad \text{(A2.1.22)}$$

where $Z_0 = \rho_0 a_0$ and is known as the characteristic impedance of the medium.

Defining a characteristic impedance for the pipe as $Y_0 = a_0 / f$, then equation (A2.1.22) can also be written in terms of acoustic mass velocity:

$$\dot{m}(x,t) = \frac{1}{Y_0}\left(C_1 e^{-jkx} - C_2 e^{+jkx}\right) e^{i\omega t} \qquad \text{(A2.1.23)}$$

Ignoring the exponential time component, equations (A2.1.21) and (A2.1.23) can be rewritten:

$$p = C_5 e^{-jkx} + C_6 e^{jkx} \qquad \text{(A2.1.24)}$$

$$\dot{m} = \frac{1}{Y_0}\left(C_5 e^{-jkx} - C_6 e^{+jkx}\right) \qquad \text{(A2.1.25)}$$

Consider the simple parallel pipe shown in Figure A2.1.1. The objective is to derive a relationship between the pressure and mass velocity characteristics at the pipe entry and exit, based on the dimensions of the pipe and the properties of the fluid contained within. At the entrance to the pipe $x = 0$, thus:

$$p_{x=0} = C_5 + C_6; \qquad \dot{m}_{x=0} = \frac{C_5 - C_6}{Y_0} \qquad \text{(A2.1.26, A2.1.27)}$$

At the pipe exit $x = l$, thus, from equations (A2.1.24) and (A2.1.25):

$$p\big|_{x=l} = C_5 e^{-jkx} + C_6 e^{jkx} = \left(C_5 + C_6\right)\cos kx - j\left(C_5 - C_6\right)\sin kx \quad \text{(A2.1.28)}$$

$$\dot{m}\big|_{x=l} = \frac{1}{Y_0}\left(C_5 e^{-jkx} - C_6 e^{+jkx}\right) = \left(\frac{C_5 - C_6}{Y_0}\right)\cos kx - j\left(\frac{C_5 + C_6}{Y_0}\right)\sin kx \quad \text{(A2.1.29)}$$

Therefore the mass flow and pressure characteristics at the pipe entry and exits can be related by substituting equations (A2.1.26) and (A2.1.27) into (A2.1.28) and (A2.1.29) respectively:

$$p\big|_{x=l} = p\big|_{x=0}\cos kx - jY_0\dot{m}\big|_{x=0}\sin kx \quad \text{(A2.1.30)}$$

$$\dot{m}\big|_{x=l} = \dot{m}\big|_{x=0}\cos kx - j\frac{p\big|_{x=0}}{Y_0}\sin kx \qquad \text{(A2.1.31)}$$

These can then be written in a matrix form that is commonly referred to as a pipe transfer matrix in acoustic theory applications:

$$\begin{bmatrix} p\big|_{x=l} \\ m\big|_{x=l} \end{bmatrix} = \begin{bmatrix} \cos kx & -jY_0\sin kx \\ -\left(j/Y_0\right)\sin kx & \cos kx \end{bmatrix} \times \begin{bmatrix} p\big|_{x=0} \\ \dot{m}\big|_{x=0} \end{bmatrix} \qquad \text{(A2.1.32)}$$

Considering the manifold network shown in Figure A2.1.2 and applying equation (A2.1.32) to manifold pipe 1, then:

$$p_{1V} = \cos\left(\frac{\omega}{a_1}l\right).p_1 - j\frac{a_1}{f_1}\sin\left(\frac{\omega}{a_1}l\right).\dot{m}_1 \qquad \text{(A2.1.33)}$$

$$\dot{m}_{1V} = -\left(j.f_1/a_1\right)\sin\left(\frac{\omega}{a_1}l\right).p_1 + \cos\left(\frac{\omega}{a_1}l\right).\dot{m}_1 \qquad \text{(A2.1.34)}$$

Since:

$$\dot{m}_2 = \dot{m}_3 = \dot{m}_4 = 0 = \sum_{i=1}^{4}\dot{m}_i - \dot{m}_1 \qquad \text{(A2.1.35)}$$

and the pressures at pipe ends adjacent to the junction are assumed equal:

$$p_{1V} = p_{2V} = p_{3V} = p_{4V} = p_V = p_{V5} \qquad \text{(A2.1.36)}$$

and also the acoustic velocities within pipes 1 to 4 are assumed equal:

$$a_1 = a_2 = a_3 = a_4 \qquad \text{(A2.1.37)}$$

then for the exhaust manifold network shown:

$$\sum_{i=1}^{4}\dot{m}_{iV} = -\left(j.f_1/a_1\right)\sin\left(\frac{\omega}{a_1}l\right).\sum_{i=1}^{4}p_i + \cos\left(\frac{\omega}{a_1}l\right).\sum_{i=1}^{4}\dot{m}_i \qquad \text{(A2.1.38)}$$

Since $\sum_{i=2}^{4}\dot{m}_i = 0$ then:

$$\sum_{i=1}^{4}\dot{m}_{iV} = -\left(j.f_1/a_1\right)\sin\left(\frac{\omega}{a_1}l\right).\sum_{i=1}^{4}p_i + \cos\left(\frac{\omega}{a_1}l\right).\dot{m}_1 \qquad \text{(A2.1.39)}$$

Applying mass conservation to the junction volume V:

Net increase of mass in junction = mass in − mass out

$$j\omega\frac{V}{a_5^{\,2}}p_V = \sum_{i=1}^{4}f_i\dot{m}_{iV} - F\dot{m}_{V5} \qquad \text{(A2.1.40)}$$

and rearranging:

$$\frac{j\omega VP_V}{a_5{}^2 f_1} + \frac{F}{f_1}\dot{m}_{V5} = \sum_{i=1}^{4}\dot{m}_{iV} \qquad \text{(A2.1.41)}$$

Substituting equation (A2.1.41) into equation (A2.1.38) for $\sum_{i=1}^{4}\dot{m}_{iV}$ gives:

$$\frac{j\omega VP_V}{a_5{}^2 f_1} + \frac{F}{f_1}\dot{m}_{V5} = -\left(\frac{jf_1}{a_1}\right)\sin\left(\frac{\omega}{a_1}l\right).\sum_{i=1}^{4}p_i + \cos\left(\frac{\omega}{a_1}l\right)\dot{m}_1 \qquad \text{(A2.1.42)}$$

Equation (A2.1.33) can be written as:

$$p_i = \frac{p_V}{\cos\left(\frac{\omega}{a_1}l\right)} + j\frac{a_1}{f_1}\tan\left(\frac{\omega}{a_1}l\right)\dot{m}_i \qquad \text{(A2.1.43)}$$

thus, since $\dot{m}_2 = \dot{m}_3 = \dot{m}_4 = 0$:

$$\sum_{i=1}^{4}p_i = \frac{4p_V}{\cos\left(\frac{\omega}{a_1}l\right)} + j\frac{a_1}{f_1}\tan\left(\frac{\omega}{a_1}l\right)\dot{m}_1 \qquad \text{(A2.1.44)}$$

Substituting equation (A2.1.44) into equation (A2.1.42) for $\sum_{i=1}^{4}p_i$ gives:

$$\frac{j\omega Vp_V}{a_5{}^2 f_1} + \frac{F}{f_1}\dot{m}_{V5} =$$

$$-\left(\frac{jf_1}{a_1}\right)\sin\left(\frac{\omega}{a_1}l\right)\left(\frac{4p_V}{\cos\left(\frac{\omega}{a_1}l\right)} + j\frac{a_1}{f_1}\tan\left(\frac{\omega}{a_1}l\right)\dot{m}_1\right) + \cos\left(\frac{\omega}{a_1}l\right)\dot{m}_1 \qquad \text{(A2.1.45)}$$

Considering the application of equation (A2.1.30) across pipe 5:

$$p_6 = \cos\left(\frac{\omega}{a_5}L\right)p_{V5} - j\frac{a_6}{F}\sin\left(\frac{\omega}{a_5}L\right)\dot{m}_{V5} \qquad \text{(A2.1.46)}$$

and since $p_6 = 0$ and pressures at pipe ends adjacent to the junction are equal:

$$\dot{m}_{V5} = \frac{F}{ja_5}\cot\left(\frac{\omega}{a_5}L\right)p_V \qquad \text{(A2.1.47)}$$

Substituting equation (A2.1.47) into equation (A2.1.45) gives:

$$\frac{j\omega V p_V}{a_5^{\,2} f_1} + \frac{F^2}{f_1 j a_5}\cot\left(\frac{\omega}{a_5}L\right)p_V =$$

$$-\left(\frac{jf_1}{a_1}\right)\sin\left(\frac{\omega}{a_1}l\right)\left(\frac{4p_V}{\cos\left(\frac{\omega}{a_1}l\right)} + j\frac{a_1}{f_1}\tan\left(\frac{\omega}{a_1}l\right)\dot{m}_1\right) + \cos\left(\frac{\omega}{a_1}l\right)\dot{m}_1 \qquad \text{(A2.1.48)}$$

Expanding, rearranging and multiplying by j gives:

$$p_V = \frac{j\dot{m}_1\left(\sin\left(\frac{\omega}{a_1}l\right)\tan\left(\frac{\omega}{a_1}l\right) + \cos\left(\frac{\omega}{a_1}l\right)\right)}{\frac{F^2}{f_1 a_5}\cot\left(\frac{\omega}{a_5}L\right) - \frac{\omega V}{a_5^{\,2} f_1} - \frac{4f_1}{a_1}\tan\left(\frac{\omega}{a_1}l\right)} \qquad \text{(A2.1.49)}$$

thus:

$$p_V = \frac{j\dot{m}_1}{\cos\left(\frac{\omega}{a_1}l\right)\left[\frac{F^2}{f_1 a_5}\cot\left(\frac{\omega}{a_5}L\right) - \frac{\omega V}{a_5^{\,2} f_1} - \frac{4f_1}{a_1}\tan\left(\frac{\omega}{a_1}l\right)\right]} \qquad \text{(A2.1.50)}$$

The natural resonance frequencies of the pipe system are determined by setting $|p_V| = \infty$ and $|\dot{m}_1| \neq 0$, which are given by the solutions to:

$$\cos\left(\frac{\omega}{a_1}l\right) = 0 \qquad \text{(A2.1.51)}$$

and:

$$\frac{F^2}{f_1 a_5}\cot\left(\frac{\omega}{a_5}L\right)-\frac{\omega V}{a_5{}^2 f_1}-\frac{4f_1}{a_1}\tan\left(\frac{\omega}{a_1}l\right)=0 \qquad \text{(A2.1.52)}$$

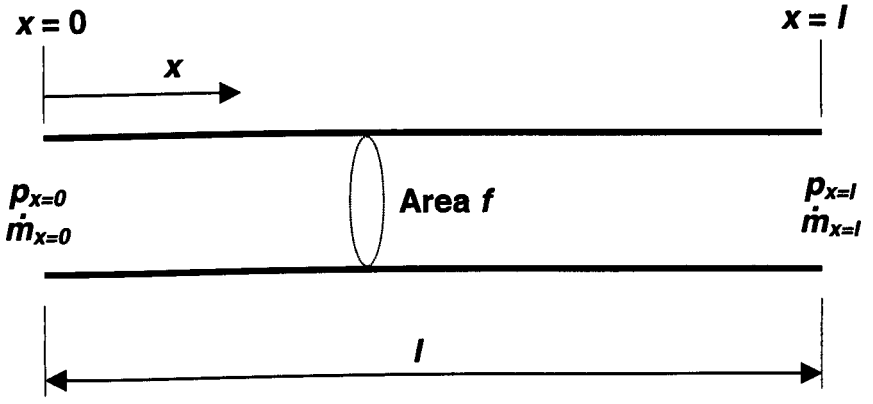

Figure 2.1.1 Simple uniform diameter tube

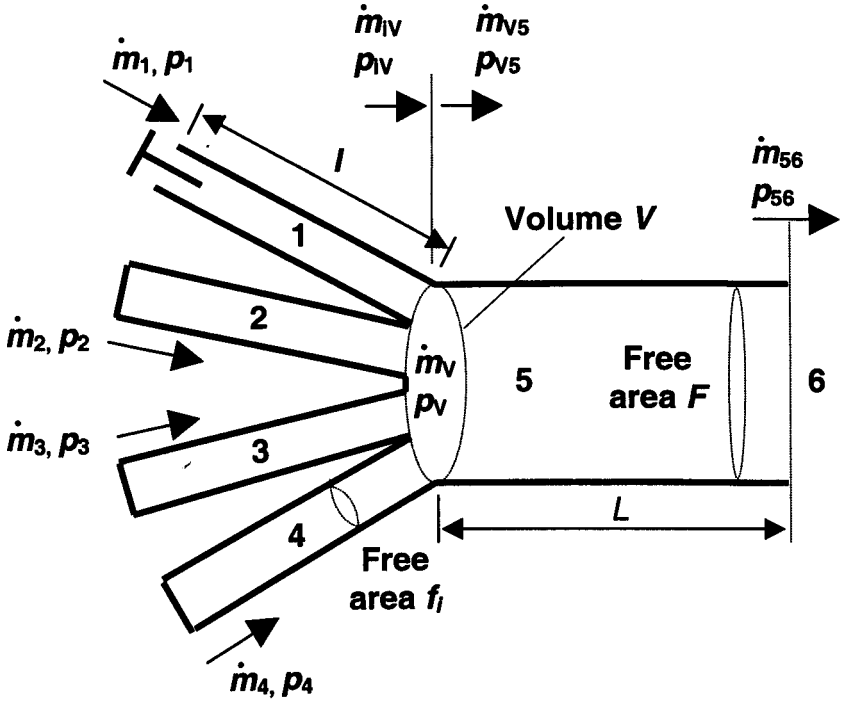

Figure 2.1.2 A 4 into 1 configuration exhaust manifold

A2.2 SPEED OF SOUND AND ENTROPY

From the second law of thermodynamics:

$$ds = \left(\frac{dQ}{T}\right)_{rev} = \frac{du}{T} + p\frac{dv}{T} \qquad \text{(A2.2.1)}$$

Assuming a perfect gas, then $pv = RT$, thus:

$$p.dv + v.dp = R.dT \qquad \text{(A2.2.2)}$$

Substituting (A2.2.2) into (A2.2.1) for $p.dv$ gives:

$$ds = \frac{du}{T} + R\frac{dT}{T} - \frac{v.dp}{T} \qquad \text{(A2.2.3)}$$

From the equations of state and internal energy, $du = C_v dT$, equation (A2.2.3) can be rewritten:

$$ds = \frac{C_v dT}{T} + R\frac{dT}{T} - R\frac{dp}{p} \qquad \text{(A2.2.4)}$$

For a perfect gas, $C_p = R + C_v$, therefore:

$$ds = C_p\frac{dT}{T} - R\frac{dp}{p} \qquad \text{(A2.2.5)}$$

At constant pressure, $dp = 0$, therefore:

$$ds = C_p\frac{dT}{T} \qquad \text{(A2.2.6)}$$

Integration between states *1* and *2* gives:

$$\frac{T_2}{T_1} = \exp\frac{s_2 - s_1}{C_p} \qquad \text{(A2.2.7)}$$

and since $a = \sqrt{\gamma RT}$, substitution yields:

$$\frac{a_2}{a_1} = \exp\frac{s_2 - s_1}{2C_p} \qquad \text{(A2.2.8)}$$

A2.3 EARNSHAW'S WAVE EQUATION AND THE SUPERPOSITION OF PRESSURE WAVES

Earnshaw's wave equation

An element of gas initially at rest, as shown in Figure A2.3.1, lying between locations b and $b+db$ and occupying volume $F.db$, moves to $b+\xi$ and now occupies volume $F(db+d\xi)$. If Δ represents the fractional change in the length of the element $\left(\frac{d\xi}{db}\right)_t$ then Earnshaw's wave equation states that for waves on a stationary background, assuming isentropic changes of properties:

$$\left(\frac{\partial^2 \xi}{\partial t^2}\right)_b = \frac{{a_0}^2}{(1+\Delta)^{\gamma+1}}\left(\frac{\partial^2 \xi}{\partial b^2}\right)_t \qquad \text{(A2.3.1)}$$

Assuming that the particle velocity, u, is a function of Δ only, then equation (A2.3.1) can be solved to give:

$$u = \left(\frac{\partial \xi}{\partial t}\right) = \pm \frac{2a_0}{\gamma - 1}\left[\left(\frac{p}{p_0}\right)^{\frac{\gamma-1}{2\gamma}} - 1\right] \qquad \text{(A2.3.2)}$$

The superposition of pressure waves

Figure A2.3.2a shows two finite amplitude pressure waves moving in opposite directions along a pipe. At some time these waves interfere with each other and the total pressure condition at this time is given by p_T. This condition is not given by the algebraic addition of pressures at points R_1 and L_1 on the wave profiles, but it has been shown by Bannister [114] that the net particle velocity is given by the addition of

the interfering components of velocity, thus, referring to Figure A2.3.2b and from equation (A2.3.2):

$$u_T = u_{R1} + u_{L1} \qquad \text{(A2.3.4)}$$

and:

$$u_{R1} = \frac{2a_0}{\gamma - 1}\left[\left(\frac{p_{R1}}{p_0}\right)^{\frac{\gamma-1}{2\gamma}} - 1\right] \qquad \text{(A2.3.5)}$$

$$u_{L1} = -\frac{2a_0}{\gamma - 1}\left[\left(\frac{p_{L1}}{p_0}\right)^{\frac{\gamma-1}{2\gamma}} - 1\right] \qquad \text{(A2.3.6)}$$

The total pressure condition is given by:

$$\left[\left(\frac{p_T}{p_0}\right)^{\frac{\gamma-1}{2\gamma}} - 1\right] = \left[\left(\frac{p_{R1}}{p_0}\right)^{\frac{\gamma-1}{2\gamma}} - 1\right] + \left[\left(\frac{p_{L1}}{p_0}\right)^{\frac{\gamma-1}{2\gamma}} - 1\right] \qquad \text{(A2.3.7)}$$

In the more general case of multiple waves interfering at a given instant in time and space:

$$\left[\left(\frac{p_T}{p_0}\right)^{\frac{\gamma-1}{2\gamma}} - 1\right] = \sum_{i=1}^{n}\left[\left(\frac{p_n}{p_0}\right)^{\frac{\gamma-1}{2\gamma}} - 1\right] \qquad \text{(A2.3.8)}$$

To incorporate these expressions in a method-of-characteristics based code, (A2.3.5) and (A2.3.6) can be written in terms of Riemann variables. From (A2.3.4), (A2.3.5) and (A2.3.6):

$$u_T = u_{R1} - \frac{2a_0}{\gamma - 1}\left[\left(\frac{p_T}{p_0}\right)^{\frac{\gamma-1}{2\gamma}} - \left(\frac{p_{R1}}{p_0}\right)^{\frac{\gamma-1}{2\gamma}}\right] \qquad \text{(A2.3.9)}$$

Since:

$$a_0 = a\left(\frac{p_0}{p}\right)^{\frac{\gamma-1}{2\gamma}} \qquad \text{(A2.3.10)}$$

then:

$$u_T + \frac{2a_T}{\gamma-1} = u_{R1} + \frac{2a_{R1}}{\gamma-1} \qquad \text{(A2.3.11)}$$

Since *R1* refers to some point on a wave profile in isolation, with pressure p_{R1} and moving with constant velocity u, then $u_{R1} + \frac{2a_{R1}}{\gamma-1} = const$, which similarly applies for all points on the rightward moving waveform, i.e.:

$$u_T + \frac{2a_T}{\gamma-1} = const \qquad \text{(A2.3.12)}$$

For leftward moving waves, i.e. $c = u - a$:

$$u_T - \frac{2a_T}{\gamma-1} = const \qquad \text{(A2.3.13)}$$

Introducing the non-dimensional parameters $U = \frac{u}{a_0}$, $A = \frac{a}{a_0}$, $Z = \frac{a_0 t}{L}$ and rearranging gives:

$$A + \frac{\gamma-1}{2}U = \lambda \qquad \text{(rightward)} \qquad \text{(A2.3.14)}$$

and:

$$A - \frac{\gamma-1}{2}U = \beta \qquad \text{(leftward)} \qquad \text{(A2.3.15)}$$

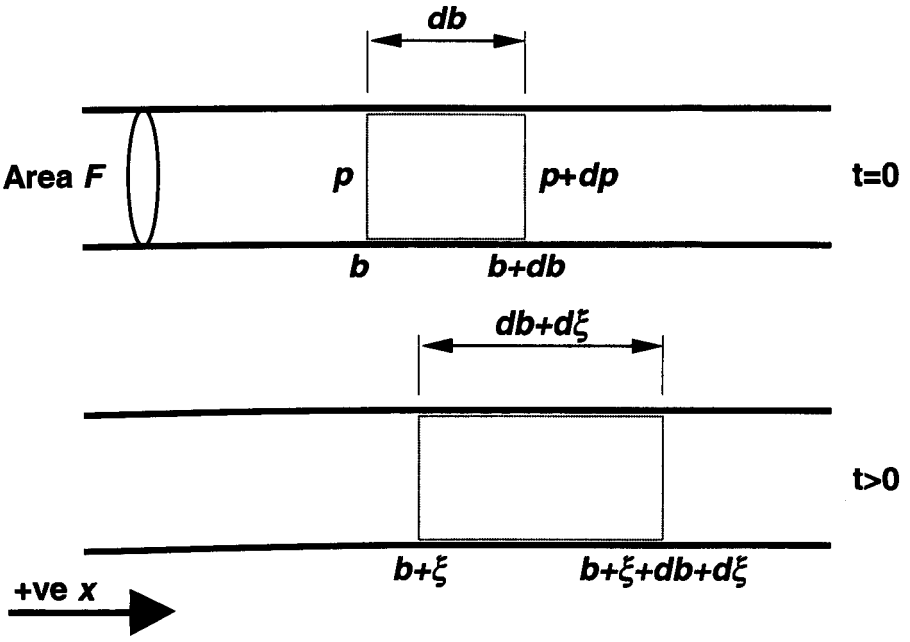

Figure A2.3.1 Displacement of fluid element

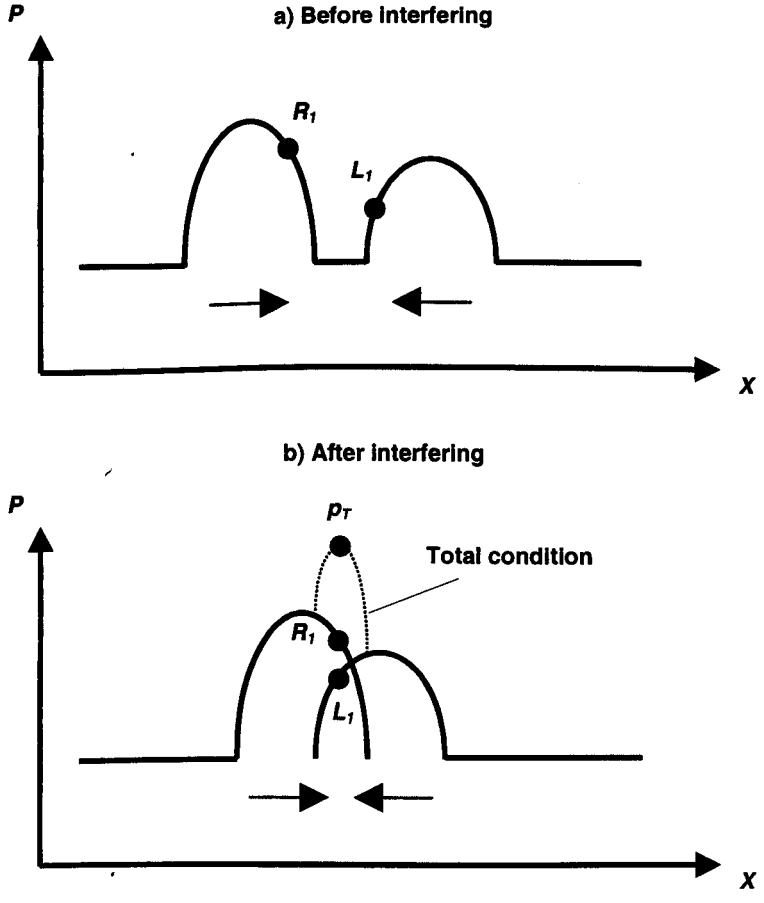

Figure A2.3.2 Superposition of pressure waves

A3.0 FIXED EXHAUST PORT PRESSURE SUBROUTINE

```
      SUBROUTINE PORTSET (A2,B2,PB1,FP,FT,G,CD,NCHK)
      COMMON /GPD/ BXI(161),AK1(21)
      COMMON /GPI/ ABXE(21,161)
      COMMON /GPT/ PA,PA1,PEN,TEN,PINR,PINR1,TINR,PEXR,PEXR1,
     1TEXR,PEX
      COMMON /GPX/ PU2(8),TU2(8),CDEG(8),N
      COMMON /C11/ NSTP
      COMMON /PB1/ PRES(721),BX3(3),A3(3),B3(3),PSET,PTEST(3)
      G6=0.5-0.5/G
      G7=1.0/G6
      AK=CD*FT/FP
      IF (AK.GT.0.99) AK=0.99
      X1=(PB1*PEXR1)**G6
      BX3(1)=0.6
      BX3(2)=1.0
      BX3(3)=1.4
5     DO 10 Q=1,3
10     B3(Q)=BX3(Q)*X1
12    DO 15 Q=1,3
       I=INT(AK*20.)+1
       J=INT((BX3(Q)-0.6)*200.)+1
       RATIOA=(AK-AK1(I))/(AK1(I+1)-AK1(I))
       ABX1J=RATIOA*(ABXE(I+1,J+1)-ABXE(I,J+1))+ABXE(I,J+1)
       ABX2J=RATIOA*(ABXE(I+1,J)-ABXE(I,J))+ABXE(I,J)
       RATIOB=(BX3(Q)-BXI(J))/(BXI(J+1)-BXI(J))
       ABX1=RATIOB*(ABX1J-ABX2J)+ABX2J
       A3(Q)=((X1+X1)*ABX1)-B3(Q)
       PTEST(Q)=PEXR*((B3(Q)+A3(Q))*0.5)**G7
15     CONTINUE
C
      DO 20 Q=1,3
       IF (ABS(PSET-PTEST(Q)) .LE. 1.0) THEN
         GO TO 50
        ELSE
        END IF
20     CONTINUE
C
      IF ((PTEST(1) .LE. PSET) .AND. (PSET .LE. PTEST(2))) THEN
30      BX3(3)=BX3(2)
        BX3(2)=BX3(1)+(BX3(2)-BX3(1))/2
       ELSE
        BX3(1)=BX3(2)
        BX3(2)=BX3(2)+(BX3(3)-BX3(2))/2
       END IF
45    CONTINUE
      GO TO 5
```

```
C
50      A2=A3(Q)
        B2=B3(Q)
        RETURN
C
        END
```

A4.0 NEWTON-RAPHSON ITERATION APPLIED TO A VARIABLE VOLUME HELMHOLTZ MODEL

To find X value which satisfies the following equation:

$$X = G(X) \qquad \text{(A4.0.1)}$$

an equation can be introduced as:

$$F(X) = X - G(X), \text{ where } F(X) = 0 \qquad \text{(A4.0.2)}$$

Assuming X_n is the trial value of X at the n^{th} step, then the $(n+1)^{th}$ trial value of X can be determined from:

$$X_{n+1} = X_n - \frac{F(X_n)}{F'(X_n)} \qquad \text{(A4.0.3)}$$

The normal form of the Helmholtz equation applied to a single manifold pipe connected a single engine cylinder is:

$$f_o(Hz) = \frac{a}{2\pi}\sqrt{\frac{A_p}{L_p\bar{V}}} \qquad \text{(A4.0.4)}$$

where, in the case of intake manifolds, it is usual to define $\bar{V} = \frac{V_s}{2} + V_{cl}$

In terms of crank angle, the period (in radians) is given by:

$$\theta_2 - \theta_1 = \frac{1}{\frac{a}{2\pi}\sqrt{\frac{A_p}{L_p\bar{V}}}}\frac{2\pi N}{60} \qquad \text{(A4.0.5)}$$

Simplifying known constants:

$$H = \frac{a}{2\pi} \qquad \text{(A4.0.6)}$$

$$K = \frac{A_p}{L_p} \qquad \text{(A4.0.7)}$$

Rearranging (A4.0.5):

$$\theta_2 - \theta_1 = H^{-1}K^{-\frac{1}{2}}\overline{V}^{\frac{1}{2}}\frac{2\pi N}{60} \qquad \text{(A4.0.8)}$$

Since at any crank angle location, the in-cylinder volume can be given as:

$$V_{\theta_i} = \left\{\left(\tfrac{S}{2} + L_R\right) - \left[\left(\tfrac{S}{2}\cos\theta_i\right) + \sqrt{{L_R}^2 - \left(\tfrac{S}{2}\sin\theta_i\right)^2}\right]\right\}A_c + V_{cl} \qquad \text{(A4.0.9)}$$

Then, to solve for θ_2 using (A4.0.3), (A4.0.8) can be written as:

$$F(X) = Y = 0 = H^{-1}K^{-\frac{1}{2}}\left(\frac{V_{\theta_1} + V_{\theta_2}}{2}\right)^{\frac{1}{2}}\frac{2\pi N}{60} + \theta_1 - \theta_2 \qquad \text{(A4.0.10)}$$

Since θ_1 is known at the beginning of each calculation, then:

$$Y = 0 = \frac{2\pi N}{60}H^{-1}K^{-\frac{1}{2}}.$$

$$\left(\frac{V_{\theta_1}}{2} + \frac{1}{2}\left[\left\{\left(\tfrac{S}{2} + L_R\right) - \left[\left(\tfrac{S}{2}\cos\theta_2\right) + \sqrt{{L_R}^2 - \left(\tfrac{S}{2}\sin\theta_2\right)^2}\right]\right\}A_c + V_{cl}\right]\right)^{\frac{1}{2}} + \theta_1 - \theta_2 \qquad \text{(A4.0.11)}$$

To find $\frac{dY}{d\theta_2}$:

$$\text{let: } M = \left(\frac{V_{\theta_1}}{2} + \frac{1}{2}\left[\left\{\left(\tfrac{S}{2} + L_R\right) - \left[\left(\tfrac{S}{2}\cos\theta_2\right) + \sqrt{{L_R}^2 - \left(\tfrac{S}{2}\sin\theta_2\right)^2}\right]\right\}A_c + V_{cl}\right]\right) \qquad \text{(A4.0.12)}$$

Then:

$$Y = \frac{2\pi N}{60} H^{-1} K^{-\frac{1}{2}} M^{\frac{1}{2}} + \theta_1 - \theta_2 \qquad \text{(A4.0.13)}$$

Thus:

$$\frac{dY}{dM} = \frac{\pi N}{60} H^{-1} K^{-\frac{1}{2}} M^{-\frac{1}{2}} \qquad \text{(A4.0.14)}$$

Now let:

$$P = \left[\left\{ \left(\tfrac{S}{2} + L_R\right) - \left[\left(\tfrac{S}{2}\cos\theta_2\right) + \sqrt{L_R{}^2 - \left(\tfrac{S}{2}\sin\theta_2\right)^2} \right] \right\} A_c + V_{cl} \right] \qquad \text{(A4.0.15)}$$

Then:

$$M = \left(\frac{V_{\theta_1}}{2} + \frac{P}{2} \right) \qquad \text{(A4.0.16)}$$

Thus:

$$\frac{dM}{dP} = \frac{1}{2} \qquad \text{(A4.0.17)}$$

Now let:

$$Q = \left\{ \left(\tfrac{S}{2} + L_R\right) - \left[\left(\tfrac{S}{2}\cos\theta_2\right) + \sqrt{L_R{}^2 - \left(\tfrac{S}{2}\sin\theta_2\right)^2} \right] \right\} \qquad \text{(A4.0.18)}$$

Then:

$$P = QA_c + V_{cl} \qquad \text{(A4.0.19)}$$

Thus:

$$\frac{dP}{dQ} = A_c \qquad \text{(A4.0.20)}$$

Now let:

$$R = \left[\left(\tfrac{S}{2} \cos\theta_2 \right) + \sqrt{L_R{}^2 - \left(\tfrac{S}{2} \sin\theta_2 \right)^2} \right] \qquad \text{(A4.0.21)}$$

Then:

$$Q = \left(\tfrac{S}{2} + L_R \right) - R \qquad \text{(A4.0.22)}$$

Thus:

$$\frac{dQ}{dR} = -1 \qquad \text{(A4.0.23)}$$

From (A4.0.21):

$$\frac{dR}{d\theta_2} = \left(-\tfrac{S}{2} \sin\theta_2 \right) + \frac{dZ}{d\theta_2} \qquad \text{(A4.0.24)}$$

where:

$$Z = \sqrt{L_R{}^2 - \left(\tfrac{S}{2} \sin\theta_2 \right)^2} \qquad \text{(A4.0.25)}$$

Now let:

$$T = L_R{}^2 - \left(\tfrac{S}{2} \sin\theta_2 \right)^2 \qquad \text{(A4.0.26)}$$

Then:

$$Z = T^{\frac{1}{2}} \qquad \text{(A4.0.27)}$$

Thus:

$$\frac{dZ}{dT} = \frac{1}{2} \left[L_R{}^2 - \left(\tfrac{S}{2} \sin\theta_2 \right)^2 \right]^{-\frac{1}{2}} \qquad \text{(A4.0.28)}$$

Now let:

$$U = \left(\tfrac{S}{2} \sin\theta_2 \right) \qquad \text{(A4.0.29)}$$

Then:

$$T = L_R{}^2 - U^2 \qquad \text{(A4.0.30)}, \qquad \text{thus } \frac{dT}{dU} - 2\left(\tfrac{S}{2}\sin\theta_2\right) \qquad \text{(A4.0.31)}$$

From (A4.0.24):

$$\frac{dR}{d\theta_2} = \left(-\tfrac{S}{2}\sin\theta_2\right) + \frac{dZ}{dT}\cdot\frac{dT}{dU}\cdot\frac{dU}{d\theta_2} \qquad \text{(A4.0.32)}$$

Thus:

$$\frac{dR}{d\theta_2} = \left[\left(-\tfrac{S}{2}\sin\theta_2\right) - \left[\left[L_R{}^2 - \left(\tfrac{S}{2}\sin\theta_2\right)^2\right]^{-\frac{1}{2}}\left(\tfrac{S}{2}\right)^2 \sin\theta_2\cos\theta_2\right]\right] \qquad \text{(A4.0.33)}$$

From (A4.0.11),(A4.0.14),(A4.0.17),(A4.0.20),(A4.0.23) and (A4.0.33):

$$\frac{dY}{d\theta_2} = \frac{dY}{dM}\cdot\frac{dM}{dP}\cdot\frac{dP}{dQ}\cdot\frac{dQ}{dR}\cdot\frac{dR}{d\theta_2} - 1 \qquad \text{(A4.0.34)}$$

Thus:

$$\frac{dY}{d\theta_2} = \frac{\pi N}{60} H^{-1} K^{-\frac{1}{2}}\left(\frac{V_{\theta_1}}{2} + \frac{1}{2}\left[\left\{\left(\tfrac{S}{2} + L_R\right) - \left[\left(\tfrac{S}{2}\cos\theta_2\right) + \sqrt{L_R{}^2 - \left(\tfrac{S}{2}\sin\theta_2\right)^2}\right]\right\}A_c + V_{cl}\right]\right)^{-\frac{1}{2}} \cdot$$

$$\left(-\frac{A_c}{2}\right)\left[\left(-\tfrac{S}{2}\sin\theta_2\right) - \left[\left[L_R{}^2 - \left(\tfrac{S}{2}\sin\theta_2\right)^2\right]^{-\frac{1}{2}}\left(\tfrac{S}{2}\right)^2 \sin\theta_2\cos\theta_2\right]\right] - 1 \qquad \text{(A4.0.35)}$$

A5.0 EXCEL VISUAL BASIC CODE FOR VARIABLE VOLUME HELMHOLTZ MODEL

```
Option Explicit

' calculates period of resonance with changing cylinder volume
' uses NR iteration: Xn+1=Xn-(F(Xn)/F'(Xn))

Dim CA1, CA2, E1, E2, DC, DP, LR, Lp, CR As Single
Dim S, C, Ac, Ap, Vcl, Vs, t1, t2 As Single
Dim a, b, e, H, K, X, i, ii, iii, iv, q As Single
Dim n, RPM, iter As Integer
Const pi = 3.141592654

Sub helmholtz()

n = 1
C = Cells(15, 3)
CA1 = Cells(5, 3) * pi / 180
CA2 = CA1 + pi / 180
E1 = Cells(10, 3) * pi / 180
E2 = Cells(11, 3) * pi / 180
DC = Cells(3, 7) / 1000
Ac = pi * DC ^ 2 / 4
S = Cells(4, 7) / 1000
DP = Cells(20, 3) / 1000
Ap = pi * DP ^ 2 / 4
Lp = Cells(25, 3)
LR = Cells(5, 7) / 1000
CR = Cells(6, 7)
RPM = Cells(13, 3)
Vs = S * pi * DC ^ 2 / 4
Vcl = Vs / (CR - 1)
t1 = 1
t2 = 2
iter = 0
  Do Until CA2 > E2
    Do Until Abs(t2 - t1) < 0.000001
      t1 = CA2
      CA2 = CA2 - (Y(CA2) / dYdX(CA2))
      t2 = CA2
      iter = iter + 1
      If iter > 10000 Then
          MsgBox ("Cannot converge on answer - check input data")
```

```
            End
        Else
        End If
    Loop
    If CA2 > E2 Then
        Range(Cells(24 + n, 5), Cells(60, 5)) = " "
        End
      Else
      End If
    Cells(24 + n, 5) = CA2 * 360 / (2 * pi)
    CA1 = CA2
    CA2 = CA1 + 2 * pi / 180
    t2 = CA2
    n = n + 1
  Loop
End Sub

Function volume(q)
a = S / 2 + LR
b = S / 2 * Cos(q)
e = (LR ^ 2 - (S / 2 * Sin(q)) ^ 2) ^ 0.5
volume = (a - (b + e)) * Ac + Vcl
End Function

Function Y(X)
H = C / (2 * pi)
K = Ap / Lp
Y = H ^ -1 * K ^ -0.5 * (volume(CA1) / 2 + volume(X) / 2) ^ 0.5 * 2 * pi * RPM / 60 +
CA1 - X
End Function

Function dYdX(X)
H = C / (2 * pi)
K = Ap / Lp
e = (LR ^ 2 - (S / 2 * Sin(X)) ^ 2) ^ 0.5
i = pi * RPM / 60 * H ^ -1 * K - 0.5
ii = (0.5 * volume(CA1) + 0.5 * volume(X)) ^ -0.5
iii = i * ii
iv = (-S / 2 * Sin(X)) - (e ^ -1 * (S / 2) ^ 2 * Sin(X) * Cos(X))
dYdX = iii * -0.5 * Ac * iv - 1
End Function

'VARIABLE LIST
'a,b,e,H,K,X,q          =       calculation variables
'i,ii,iii,iv            =       calculation variables
't1,2                   =       calculation variables
```

'Ac	=	area of cylinder
'Ap	=	area of primary pipe
'C	=	acoustic velocity
'CA1,CA2	=	start/fish of each calculated oscillation period
'CR	=	compression ratio
'DC	=	diameter of cylinder
'DP	=	diameter of primary pipe
'E1,E2	=	start/finish period of expansion sensitivity
'iter	=	iteration counter
'Lp	=	length of primary pipe
'LR	=	con rod length
'N	=	loop counter
'RPM	=	engine speed
'S	=	stroke
't1,t2	=	test values for NR iteration
'Vcl	=	clearance volume
'Vs	=	swept volume